

Characterisation of electrochemical properties of capacitive membrane electrodes



Characterisation of electrochemical properties of capacitive membrane electrodes

Determination of the relation between the electrochemical parameters and the performance of capacitive membrane electrodes with electrochemical impedance spectroscopy

by

Chérise Julia Edna Tomsjansen

to obtain the degree of Master of Science
at the Delft University of Technology
to be defended publicly on Monday November 13, 2023 at 11:00 AM

Student number:	4955331
Supervisor:	Dr. H.B. Eral
Supervisor:	Dr. R.M. Hartkamp
Daily Supervisor:	Dr. N.J.H. Boon

Preface

Dear reader,

Before you is the Master's thesis titled "Characterisation of electrochemical properties of capacitive membrane electrodes". This thesis was written to complete the study Mechanical Engineering, specializing in Energy, Flow, and Process Technology (EFPT), at Delft University of Technology. The graduation project commenced on 9 January 2023, and will conclude with a defence on 13 November 2023.

I immensely enjoyed working on this Master's thesis. The theoretical knowledge I had accumulated over the years proved to be highly valuable during the execution of this graduation project. I applied mathematical concepts from my studies, followed established design processes to design and build the EIS setup (CME meter), and benefited greatly from electrochemical courses taken in the first year of the master's program. Nevertheless, I also acquired a wealth of new knowledge during this graduation project: I worked extensively with Python, employed a new measurement system (potentiostat), and delved into the world of academia.

My journey here represents a lifelong plan, set in motion back in sixth grade when I decided to pursue a university degree. The path led me to TU Delft, where I found my academic home. I enjoyed going to the lectures and expanding my knowledge of nature. I want to express my gratitude to all my teachers, professors, colleagues, and friends who have contributed to my knowledge and personal growth over these years. I cannot believe all the years have gone by and that I'm now at the end of my Masters. I take pride in achieving this goal and am excited for the next phase, yet also feel anxious to start the rest of my life. Consequently, I've chosen to extend my academic journey and pursue a Ph.D. after completing my Master's.



I would like to express my gratitude to my supervisors, Dr. H.B. Eral and Dr. R.M. Hartkamp, for their guidance and feedback. I would also like to thank my daily supervisor, Dr. N.J.H. Boon, for his invaluable assistance in creating this graduation report, deriving formulas, and fabricating CMEs. In particular, the experience of making capacitive membrane electrodes in the laboratory was always very enjoyable. This entire graduation project would not have been possible without the support and love of my family. They have been with me from the beginning of my academic journey, supported me through thick and thin, and made compromises to assist me. Therefore, I dedicate this Master's thesis to them, as without my mother, father, and sister, I could never have achieved this.

I sincerely hope you enjoy reading this thesis report as much as I enjoyed making it,

Chérise Tomsjansen
Delft, November 2023

Abstract

Fresh water is a scarce source. Demand for freshwater is greater than supply, due to the increasing industrialisation of countries and the low natural supply of freshwater sources such as rivers and lakes. Contamination of these natural freshwater sources by industrial wastewater adds to the freshwater deficit. Throughout history, technologies have been developed to increase the supply of fresh water by desalinating other water sources into fresh water. Reverse osmosis is the most widely used desalination technology for seawater desalination, but the energy transition calls for electric-based technologies that can desalinate water using renewable energy sources. Capacitive deionisation is a relatively new desalination technology that uses electrical energy to desalinate brackish water. The capacitive deionisation cell is an electrochemical cell in which the feed water flows between two electrodes. When electricity is applied to these electrodes, ions in the water are attracted to move towards the porous electrodes where they are adsorbed within the electrical double layer. Unfortunately, the capacitive deionisation systems has some challenges: it is a batch-system, has a low fresh water production and it has not been built for large scale production. Avsalt AB, a Swedish company, has developed a new capacitive deionisation architecture to address these challenges, called the multi-channel capacitive deionisation system (MC-CDI). This system consists of two capacitive porous electrodes and several membrane-like electrodes between them, which will be referred to as capacitive membrane electrodes (CMEs). To maximise the performance of the multichannel deionisation system, the performance of the capacitive membrane electrodes should be enhanced. Therefore, the aim of his thesis is to optimise the physical properties of the capacitive membrane electrodes that affect the performance of the capacitive membrane electrodes and to gain a better understanding of how the microscopic properties of the CMEs should be carefully tailored to improve the performance.

To address these questions we can turn to Electrochemical Impedance Spectroscopy (EIS). EIS is a non-invasive measurement technique that may be regarded as a much more sophisticated resistance measurement compared to, for example, a multimeter. In contrast to the latter device, EIS measures the impedance, which is a combination of the resistance and the reactance, at a wide range of frequencies. The frequency dependency of the measured impedance can be used to find a so-called equivalent electrical circuit model (EECM). For EIS measurements on electrochemical cells, such as batteries, fuel cells, electrolyzers, the EECM elucidates the different electrochemical processes that occur at different timescales and impedance plots are used to analyse and compare these electrochemical processes. EIS has been successfully used to analyse the electrochemical processes within CDI electrodes and ion exchange membranes, but capacitive membrane electrodes used in a MC-CDI system have never been studied with an accurate and fast measurement technique such as EIS. Because CMEs do not have a solid support structure, in contrast to most CDI electrodes, ions are free to migrate through the electrodes. Therefore, the alternating current that is needed in EIS measurements can be applied on an external set of electrodes, while the response alternating voltage can be picked up at the CMEs. This 4-point impedance measurement configuration enables precise determination of the ionic resistance and capacitance of the electrode material. Therefore, an electrochemical impedance spectroscopy setup is built to determine the performance indicators of the CMEs and to gain a better understanding of the electrochemical processes taking place at the interface of the CMEs. The resulting Nyquist and Bode plots are used to analyse ion diffusion and capacitive behaviour of the electrodes. To enable the analysis, first an equivalent electrical circuit is determined for these freestanding electrodes. It was found that the CME can be represented by the Transmission-line model, which in the equivalent electrical circuit takes the form of a junction of three complex impedances. From the values of the electrochemical parameters, the performance indicators of the CME, membrane conductivity and permselectivity, were evaluated.

The CME meter presents itself as an accurate measurement system to quickly evaluate the performance indicators of the CME, with the aim of efficiently searching for the CME that will show the best performance within the MC-CDI system, without placing it within the MC-CDI system. Further research should be conducted to investigate the extent to which EIS could be used to estimate the permselectivity of the CME and whether the total measurement time to predict permselectivity is still short enough to propose EIS as an alternative measurement technique.

Table of Contents

Preface.....	3
Abstract	4
Nomenclature.....	10
Introduction.....	11
1.1 Multi-channel capacitive deionisation.....	12
1.2 Research questions and objectives	13
Theoretical Framework	16
2.1 CDI technology	17
2.1.1 Working principle of conventional CDI system	17
2.1.2 Performance and operational parameters.....	18
2.2 Electrode theory.....	20
2.2.1 Capacitors	20
2.2.2 Electrical double layer	21
2.2.3 Pore size distribution: micro-, meso- and macropores.....	23
2.3 ED technology.....	24
2.3.1 Working principle of conventional ED system	24
2.3.2 Performance and operational parameters.....	25
2.4 Ion exchange membrane theory	27
2.4.1 Donnan's Law	27
2.4.2 Concentration Polarization.....	27
2.5 Electrode material and fabrication.....	28
2.5.1 Electrode material composition	28
2.5.2 Electrode fabrication recipe	29
2.6 Applications of Electrochemical Impedance Spectroscopy.....	30
2.6.1 Electrochemical Impedance Spectroscopy for capacitive electrodes in CDI.....	30
2.6.2 Electrochemical Impedance Spectroscopy for ion exchange membranes in ED	31
2.7 Conclusion	32
Methodology	33
3.1 CME electrode materials	34
3.2 Equivalent Electrical Circuit Model for CMEs.....	35
3.2.1 Transmission-line model	35
3.2.2 Equivalent electrical circuit model of the CMEs in the CME meter	39
3.2.3 Alternative models for CME impedance equation	40
3.3 Relation between electrochemical parameters and performance indicators	43

3.3.1 Relation between permselectivity and electrochemical parameters	43
3.3.2 Relation between membrane conductivity and electrochemical parameters	44
3.4 Experimental plan.....	45
3.4.1 Experimental plan for determining the EECM of the CMEs	45
3.4.2 Experimental plan for relation between resistance and thickness	46
3.4.3 Experimental plan for determining the permselectivity	46
3.4.4 Experimental plan for relation between CME structure and performance	46
Design and Construction of the CME meter.....	48
4.1 Design of the CME meter	49
4.1.1 Programme of Requirements	49
4.1.2 Concept of the CME meter	50
4.1.3 3D CAD model of the CME meter	59
4.2 Construction of the CME meter	59
4.2.1 Bill of Material and Order list	59
4.2.2 Fabrication process of the CME meter	60
4.2.3 Fabrication recipe of the CMEs	60
4.3 Testing the CME meter	61
4.3.1 Characterising the flowrate with the pump	61
4.3.2 Check how the power supply could charge the CMEs	62
4.3.3 Determining the working procedure of the Biologic VSP-300 EIS potentiostat.....	62
4.3.4 Calibrating the conductivity meter.....	63
4.3.5 Testing for leakages inside the CME-cell.....	63
4.3.6 Testing the flow arrangement inside the CME-cell	64
4.3.7 Testing the CME meter	64
4.4 The final prototype: The CME meter.....	65
Results and Analysis	66
5.1 Determining the EECM of the CMEs.....	67
5.1.1 Varying the flowrate.....	69
5.1.2 Varying the mixing rate in the reservoir.....	70
5.1.3 Varying the concentration of KCl in the electrolyte	70
5.1.4 Varying the temperature.....	72
5.2 Relation between CME thickness and the membrane conductivity	73
5.3 Investigating the effect of charge on CME properties	77
5.4 Determining performance indicators of CMEs with different compositions	81
5.4.1 Active Material: Activated Carbon vs Graphite	83
5.4.2 Mass composition of polymeric binder: PVDF	83

5.4.3 Mass composition of conductive additive: carbon black	84
5.4.4 Mass composition of active material: graphite	84
5.4.5 Observations during the EIS measurements of all CME samples	85
Conclusion	87
Discussion and Recommendations	89
Reference List	92
List of Figures	100
List of Tables	107
Appendix A: Fundamentals of Electrochemical Impedance Spectroscopy	109
A.1 Impedance	109
A.2 Nyquist plot and Bode plots	110
A.2.1 Nyquist plot	110
A.2.2 Bode plots	111
A.3 Equivalent Electric Circuit Model	113
A.3.1 Ideal resistors, capacitors and inductors	115
A.3.2 CPE-element	115
A.3.3 Charge-transfer resistance	116
A.3.4 Warburg impedance	116
A.3.5 Transmission-line model	118
A.4 Relation between EIS and performance indicators	120
A.4.1 EIS of capacitive electrodes and performance of CDI systems	120
A.4.2 EIS of ion exchange membranes and performance of ED systems	121
A.5 Accuracy of EIS data	121
A.5.1 Accuracy Contour Plot	121
A.5.2 Kronig-Kreuner relation and quality of the fit	122
A.6 Potentiostat for EIS measurements	124
A.7 Operational parameters of EIS measurements	125
A.7.1 Concentration of the electrolyte	126
A.7.2 Flowrate of the stream	126
A.7.3 Temperature of the cell	126
A.7.4 Thickness of the specimen	126
Appendix B: Derivation of impedance equation Transmission-line Model	127
B.1 Reflective boundary condition	128
B.2 Transmissive Boundary Condition	130
Appendix C: Derivation of the equation for the Permselectivity	133
Appendix D: Python Script	135

Appendix E: EIS measurement Procedure for the CME meter.....	144
E.1 Procedure for placing the CME inside the CME-cell.....	144
E.2 Procedure for performing EIS measurement on CME sample	145
E.3 Procedure for converting the EIS data to EIS graphs	146
Appendix F: Bill of Materials.....	147
Appendix G: Additional Literature - CDI and ED.....	151
G.1 Different cell architectures of CDI	151
G.1.1 Flow arrangements: flow-by vs flow-through.....	151
G.1.2 Cell architectures: Membrane CDI, Inverted CDI and Flow-electrode CDI.....	152
G.1.3 CDI architecture based on faradaic reactions: Hybrid CDI, Cation intercalation desalination, and Desalination battery	153
G.2 Relation between physical properties and CDI performance	154
G.2.1 Nature of the electrode material.....	154
G.2.2 Applied potential	155
G.2.3 Electrolyte conditions	155
G.3 Relation between physical properties and ED performance	155
G.3.1 Ion-exchange capacity	155
G.3.2 Tortuosity and swelling.....	155
G.3.3 Membrane thickness	156
G.3.4 Initial salt concentration and Applied potential	156
G.4 Transport equations for membranes.....	156
Appendix H: Additional Results - Graphs and Tables	158
H.1 Quality of fit values of EECMs through EIS data of CME-S.....	158
H.2 Impedance plots of charged CME-AC	160
H.3 Impedance plots of charged CME-PVDF	161
H.4 Impedance plots of charged CME-CB	162
H.5 Impedance plots of charged CME-G	163

Nomenclature

Abbreviation	Full Form	Abbreviation	Full Form
AC	activated carbon or alternating current	i-CDI	inverted capacitive deionisation
ACP	Accuracy Contour plot	IEC	Ion-exchange capacity
AEM	anion exchange membrane	IEM	ion exchange membrane
ASAR	average salt adsorption rate	IHL	inner Helmholtz layer
CB	carbon black	MC-CDI	multi-channel capacitive deionisation
CC	constant current or current collector	MCDI	membrane(-based) capacitive deionisation
CDI	capacitive deionisation	MED	multi-effect distillation
CE	current efficiency	CME meter	Capacitive membrane electrode impedance meter
CE	counter electrode	MSF	multi-stage flash
CEM	cation exchange membrane	NHE	Normal Hydrogen Electrode
CID	cation intercalation	NMP	N-methyl-2-pyrrolidone
CME	capacitive membrane electrodes	NaCl	sodium chloride
CO ₂	carbon dioxide	OHL	outer Helmholtz layer
CPE	constant phase element	PSD	pore size distribution
CV	constant voltage	PTFE	polytetrafluoroethylene
DBL	diffusion boundary layer	PVDF	polyvinylidene fluoride
DD	Design Dossier	RCD	reverse current desorption
DMSO	dimethyl sulfoxide	RE	reference electrode
E _{cell}	cell voltage	RO	reverse osmosis
ED	electrodialysis	RVD	reverse voltage desorption
EDL	electric double layer	SAC	salt adsorption capacity
EECM	Equivalent electric circuit model	SSA	specific surface area
EIS	electrochemical impedance spectroscopy	TLM	Transmission-line model
ENAS	energy normalized adsorbed salt	TSEC	total specific energy consumption
FarCDI	faradaic capacitive deionisation	TU Delft	Delft University of Technology
FCDI	flow-electrode capacitive deionisation	W	Warburg impedance or infinite-length Warburg element
FLW	finite-length Warburg element	WE	working electrode
FSW	finite-space Warburg element	WR	water recovery
HCDI	hybrid capacitive deionisation	ZVD	zero voltage desorption

Symbol	Definition	Value	Symbol	Definition	Value
e ₀	elementary charge	1.602 * 10 ⁻¹⁹ C	k _B	Boltzmann constant	1.38 * 10 ⁻²³ J/K
ε ₀	permittivity of vacuum	8.854 * 10 ⁻¹² F/m	R̄	Universal gas constant	8.314 J/molK
F	Faraday's constant	96,485 C/mol			

1

Introduction

“Nothing is softer or more flexible than water, yet nothing can resist it.” — Lao Tzu

71% of the earth’s surface consist of water. That should suffice to supply humanity with all the water it needs. The United Nations predicts that 50% of the world population will have a shortage of freshwater in 2025. Water scarcity occurs when the supply of water is less than the demand, the water infrastructure is inadequate or the distribution of water is unequal [4]. The high demand for water could be explained by the food-water-energy nexus: fresh water is needed not only for domestic use, but also to produce food and energy. At the same time, energy is needed to guarantee the availability of fresh water. The UN stated that 72% of the fresh water demand is for agricultural purposes [2]. The world population is expanding, which ask for more food and freshwater. Additionally, economic development goes hand in hand with a larger energy demand. As is indicated by Figure 1, majority of the nations that are in grave danger for a water shortage in 2040 are urbanized countries with big industries [3,4].

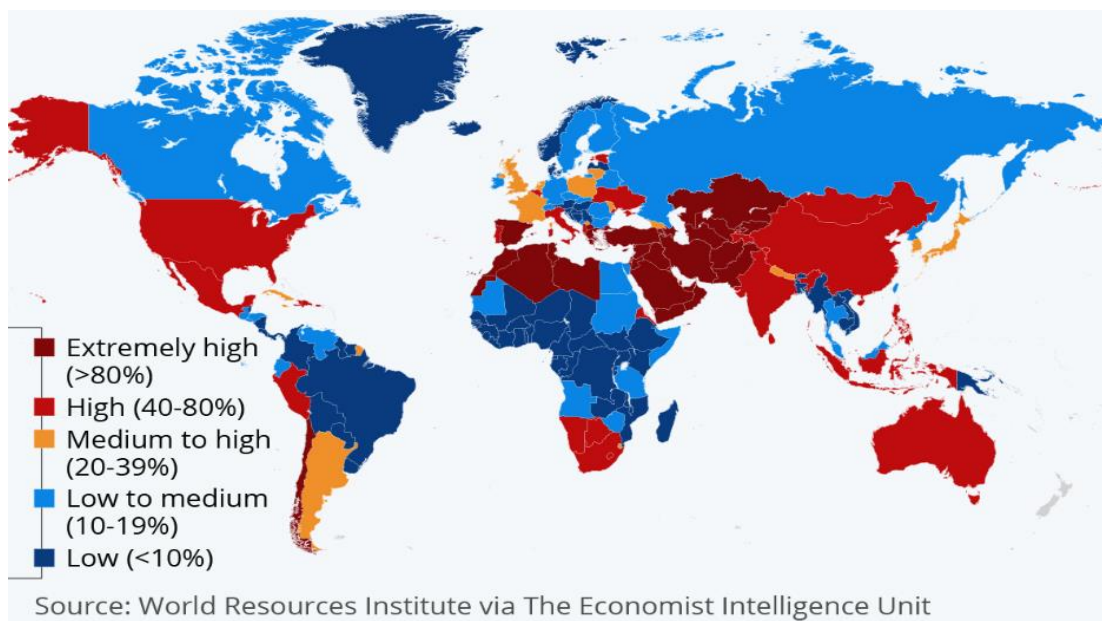


Figure 1: 33 countries will face extremely high water scarcity in 2040 according to World Resources Institute (2015, August 26). Source of the figure: Statista Infographics (2022, March 22) [4].

Not all the 71% of the water on the earth’s surface could be consumed, freshwater is specifically demanded which is only 2.5% of all the water on earth. Also, from that 2.5%, 99% is inaccessible for humans because it is stored as groundwater, permafrost and glaciers [5]. Lakes and rivers are the natural fresh water recourses that are easy accessible by humans, however, this is only 0.0075% of all the water on earth [5]. The United Nations conclude that freshwater should be recognised as a scarce resource [4]. Thus, to increase the freshwater supply, desalinated technologies were developed for the desalination of the large quantities of seawater into fresh water to increase the freshwater supply. Not only are the natural sources of fresh water limited, but the amount of fresh water is also being reduced by climate change and water pollution. Thus, reducing the contamination of water caused by agricultural, domestic and industrial use, increases the freshwater supply and reduces catastrophic effects on the environment.

Capacitive deionisation (CDI) is a desalination technology which utilizes charged electrodes to remove the salt from the water stream electrostatically. It is a very popular desalination technology in the

academic community because it is an energy efficient, cost effective and environmentally friendly system that is easy to operate [6,7]. CDI is more efficient than pressure-based desalination technologies, such as reverse osmosis, for the desalination of water with low salt concentrations (brackish water) [8]. Groundwater and industrial waste streams are examples of brackish water that could be efficiently desalinated with a CDI system. This electrical-based desalination technology is "future-proof" because "green electricity" (electricity generated from renewable energy sources) could be used to power the system, which produces desalinated water without emitting any CO_2 . The function of the electrodes in the CDI system is not only to conduct electricity and adsorb ions, they also have an additional function: selectivity. The electrodes have shown that some ions are more easily adsorbed in the electrodes than other ions [9,10]. The charge number and ion size have an effect on the amount of ions that are adsorbed [9,10]. This feature of the electrode increases the possible applications of the CDI systems. For example, the CDI system could be utilized for the selective removal of nitrate and phosphorus ions from the water stream in ditches and lakes to reduce massive fish mortality by algal bloom [11]. Another example is the contamination of ditches and rivers with industrial waste streams, which could be reduced by using the CDI system as a post-separation system to remove the toxic and harmful ions [12]. For economic reasons, CDI may potentially be used to recover scarce and rare minerals from industrial waste streams, for example Lithium-ions, which are essential for the energy-transition [13].

1.1 Multi-channel capacitive deionisation

Altogether, the CDI technology is environmental friendly, is "future-proof", ensures a circular economy, reduces water scarcity and is cost- and energy efficient. There are only a few challenges to commercialising CDI for brackish water desalination: ion removal is limited, water recovery is low, and CDI is a batch process (due to its charge-discharge cycle), which is more costly than continuous processes [14,15,16]. Therefore, to address these challenges, researchers are designing and building setups of several CDI architectures (Appendix G.1). Similarly, the Swedish company Avsalt AB has built a new CDI system that is continuous and has improved water recovery. This thesis investigates the performance of this so-called multi-channel CDI (MC-CDI) system. MC-CDI has the same working principle as conventional CDI systems, except that, similar to electrodialysis, membranes are placed between the porous electrodes. These porous electrodes are called "capacitive membrane electrodes" (CMEs), which are a combination of a capacitive porous electrode and a membrane: ions diffuse through the pores of the CME, but the charge is initiated by an external applied voltage rather than by fixed charged functional groups in the material. In a MC-CDI system, the electrodes on the outside of the cell are standard porous CDI electrodes which induce an electric field inside the cell when a voltage or current is applied. The ions inside the feed stream are attracted by this electric field and start to move towards the electrodes. An external applied voltage or current is placed upon the capacitive membrane electrodes which only let counter-ions diffuse to the next channel while co-ions stay inside the channel. A part of the counter-ions is able to reach the porous electrode where they are adsorbed

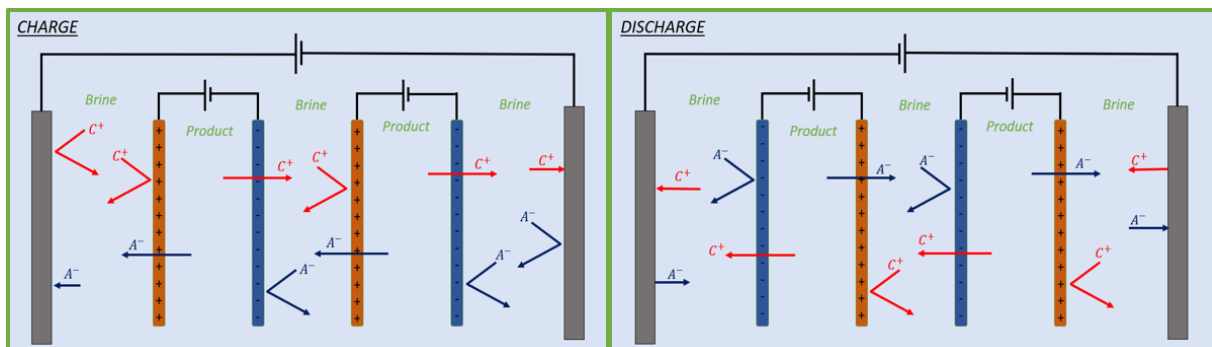


Figure 2: Multi-channel CDI system during the generation phase (left) and the discharge phase (right). The feed stream goes into the paper. Orange and blue electrodes are the positively and negatively charged capacitive membrane electrode, respectively.

inside the electric double layer. When the external capacitive electrodes are fully filled with ions, the discharge phase is initiated by switching the polarity of the capacitive electrodes and the CMEs, and subsequently, the brine channel and the product channel are maintained. Figure 2 depicts how this separation process works. The architecture and working principle of MC-CDI can be best described as a combination of CDI and electrodialysis (ED).

1.2 Research questions and objectives

The MC-CDI system has been built and already shows promising desalination performances, however, the system still needs to be optimised. The overall performance of the MC-CDI system is determined by the performance of the CMEs: if the CMEs are better in blocking co-ions while facilitation counter-ion transport, then the MC-CDI has better ion removal from the feedwater. The problem is that it is not clear what the internal structure and physical parameters of the capacitive membrane electrode should be in order to maximise the performance of the MC-CDI. Several CMEs have been fabricated and were placed inside the MC-CDI system to analyse the desalination rate and energy efficiency of the system. However, measuring the performance of the CME in the MC-CDI system is a time-consuming process. In addition, this system does not analyse the behaviour inside the CMEs, which could be used to understand the CME and develop more efficient CMEs, which would lead to better performance of the MC-CDI. Therefore, a fast measuring system capable of analysing the physical properties of CMEs is required. In this thesis, the electrochemical surface properties of CMEs are investigated. Electrochemical surface properties are e.g. capacitance and resistance. The research question is therefore:

“What are the microscopic electrochemical properties of capacitive membrane electrodes that maximise the desalination performance of multi-channel capacitive deionisation system?”

Electrochemical impedance spectroscopy (EIS) is a fast measurement tool that has been used by multiple researcher to investigate the electrochemical properties of electrochemical cells [16]. Electrochemical Impedance Spectroscopy allows for separation of processes which occur on different timescales, making it ideal for separating the electronic and ionic resistances [17]. Identifying the ionic and electronic resistances in the CDI cell is important because a part of the energy that is added to the CDI system dissipates due to these resistances [18]. The generated EIS data is also studied to investigate diffusion kinetics [17], capacitance [19] and tortuosity of the electrode [20]. Previous studies have experimentally determined the impedance of porous electrodes [19-23] and ion exchange membranes [24,25] with EIS, however, not for capacitive membrane electrodes. Therefore, an EIS setup for capacitive electrodes in CDI and ion exchange membranes in ED is adapted to measure the resistance and capacitance of CMEs. The EIS setup is not only used to analyse and characterise the processes at the CME interface, but also to check if EIS could be used in the future to determine the performance of the CME faster instead of a lab-scale MC-CDI system. The electrochemical impedance spectroscopy setup of this Thesis is called the capacitive membrane electrode impedance meter (CME meter) throughout this report. The setup should provide stable experimental conditions while measuring the behaviour of the capacitive membrane electrodes using an externally applied electric current or voltage. Although careful control of the experimental conditions is desired, ease of operation of the setup is also desired.

To answer the research question, the question is separated into multiple sub-questions and objectives. The sub-questions are a tool for breaking down the research question into smaller questions, which are answered in order to ultimately answer the research question. The sub-questions are:

- S1. *What are the performance parameters of capacitive membrane electrodes?*
- S2. *What are the interface processes occurring in the capacitive membrane electrodes?*
- S3. *How are the electrochemical properties of capacitive membranes electrodes determined with electrochemical impedance spectroscopy?*

- S4. What is the relation between the electrochemical properties of the capacitive membrane electrodes, determined with electrochemical impedance spectroscopy, and their performance?*
- S5. Which pre-defined capacitive membrane electrode, in a specific concentration, gives the best performance according to electrochemical impedance spectroscopy data?*

The objectives are the milestones which should be achieved to finish the Thesis. The objectives are:

- O1. Conduct a literature study into theories behind capacitive electrodes in capacitive deionisation systems, ion exchange membranes in electrodialysis systems, and electrochemical impedance spectroscopy.*
- O2. Design and build an electrochemical impedance spectroscopy setup that enables easy “ex-situ” measurement of the physical properties of capacitive membrane electrodes.*
- O3. Measure the impedance of pre-defined capacitive membrane electrodes with constant material composition, while they are uncharged or charged, for different thicknesses using the electrochemical impedance spectroscopy setup (CME meter) while varying operational conditions.*
- O4. Use the measured impedance data to find the electrochemical properties of the capacitive membrane electrodes and correlate these with the performance indicators.*
- O5. Measure the impedance of pre-defined capacitive membrane electrodes, with constant thicknesses, and determine the capacitive membrane electrode with the best performance.*

It takes three months to finish the in-depth investigation of the required theories to conclude Objective 1, which culminates in a literature study presentation in April. A summary of this investigation is found in the second chapter “Theoretical Framework”, where sub-questions 1, 2, and 3 are answered. To answer the first and second sub-questions, an in-depth research was done into CDI systems, capacitive electrodes, ED systems, and ion exchange membranes to understand the working principle of MC-CDI systems and CMEs. This research has been the subject of the first four sections of this chapter. This information is used to predict the performance indicators of CME, and the processes that occur at the interfaces of CMEs. A small literature research in the fabrication process of capacitive electrode for CDI application is done to understand how porous electrodes are built, and thus, how CMEs should be fabricated. The last section of the chapter Theoretical framework describes the relation between the collected EIS data and the performance of CDI electrodes and ion-exchange membranes. This is important for understanding how EIS could be applied to analyse the behaviour of capacitive membrane electrodes. Herein, sub-question 3 is answered. An in-depth investigation was done into the fundamentals of EIS, which can be found in Appendix A.

A novel EIS setup is built to measure the physical properties inside CMEs. These design steps are as follows: A programme of requirements is established, concepts are developed, the design is created in a 3D CAD programme, a prototype is built and the prototype is tested. The whole design process is explained in more detail in Chapter 4. Concluding the milestone of Objective 2, thus designing, building and testing the CME meter, is expected to take three months (May, June and July).

To answer sub-questions 4 and 5, EIS experiments are conducted on pre-defined CMEs with the CME meter. First, hypotheses on the relationship between performance indicators and measured electrochemical properties of CMEs are developed. Then, EIS experiments are performed on different CMEs with different compositions and thicknesses, while they are charged or uncharged, under different operating conditions (O3). For the first experiments, the impedance data of predefined CMEs with the same material composition are determined at different thicknesses and operating conditions while they are uncharged. In the next experiments, the EIS data of charged CMEs will be collected while keeping the thickness and material composition the same for comparison. The operating conditions such as temperature, concentration, flow rate, etc. are kept constant for these EIS experiments. The hypotheses and procedure for conducting the experiments can be found in Chapter 3 Methodology. The pre-defined CMEs are constructed with pre-defined recipes that include graphite, carbon black and PVDF, similar to what has been extensively used in (lab) test of the MC-CDI. After these experiments, the collected impedance data is plotted in Nyquist plots and Bode plots for different

thicknesses and charges. Nyquist plots and Bode plots are graphically analysed to evaluate the electrochemical properties [21]. The information obtained about the electrochemical properties of the CMEs is compared with the performance of the CME to find the desired structure of the CME that would result in higher performance (O4). The electrochemical processes and theories, that could explain this relationship, are described in the analysis of Chapter 5. Once this relationship is understood, EIS could be used in the future to determine the performance of CMEs in just an hour. This statement is tested by conducting the last EIS experiments on pre-defined CMEs where the material composition is changed, while the other parameters are kept constant (O5). The CME composition with the best performance is determined by analysing the shape of the impedance plots and using the electrochemical properties determined from these plots to estimate the performance parameters of the CME. The experiments and the analysis should take approximately two months. After analysing these experiments, the research question is answered in the Conclusion. The Thesis project should be finished in the middle of October.

2

Theoretical Framework

The principles and performance indicators of CDI systems and ED systems are investigated to understand the working principles and performance parameters of the multi-channel CDI setup. Section 2.1 and Section 2.2 give a broader understanding of these two systems. In Section 2.3 and Section 2.4, the theory behind capacitive electrodes and ion exchange membranes in the CDI and ED systems are explained in detail. Also, the physical properties that affect the performance of capacitive electrodes and ion exchange membranes are investigated. Sub-question 1 and 2 are answered in these sections. Section 2.5 is an exploratory study of different academic papers to find relevant electrodes which show high performances and are fabricated relatively easily without high-energy or high-cost equipment. Finding the CME material type which gives the best performances in the MC-CDI lies outside the scope of this Thesis, only a very limited range in material compositions will be used. Fundamental theory behind EIS is explained in Appendix A, while the application of the EIS theory on CDI electrodes and ED ion exchange membranes is explained in Section 2.6. Finally, a short conclusion summarises the chapter and gives the answers to sub-questions 1, 2 and 3.

2.1 CDI technology

Capacitive Deionisation (CDI) is a desalination technology for the desalination of brackish water which is energy-efficient, low cost and easy in operation compared to large-scale infrastructure technologies as Reverse Osmosis (RO), Electrodialysis (ED), Multi-stage Flash (MSF) and Multi-effect distillation (MED) [2]. CDI has been proposed as a useful desalination technology for wastewater treatment and recovery of resources [15]. The CDI research field has grown extremely over the years and is seen as an energy-efficient solution against worldwide water shortage and water pollution in the future [6].

2.1.1 Working principle of conventional CDI system

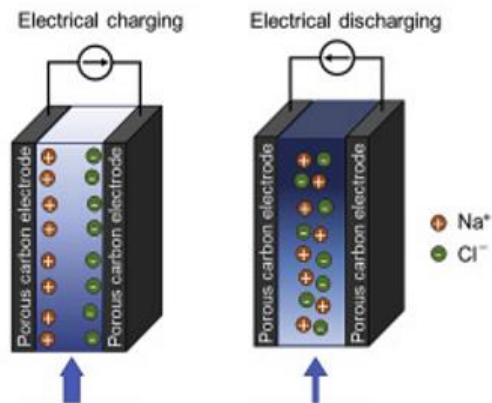


Figure 3: Charging and discharging of capacitive deionisation cells. Source: Ramachandram et al. (2019) [26].

CDI is an ion separation process using coulomb forces to attract ions in the feed water into the electrical double layer of a carbon-based electrode (electrosorption or non-faradaic reactions) or, alternatively, using redox reactions to adsorb ions onto the electrode surface (faradaic reactions) [15,27]. A CDI system consists of multiple CDI modules where one CDI module consists of multiple CDI units. The most simple CDI unit consists of a feed stream of water containing ions (electrolyte) with two porous carbon-based electrodes placed opposed to each other at the outside of the stream. A constant current (CC) or constant voltage (CV) is applied on the electrodes, forming a potential difference between the

electrodes. The positive electrode during charging is called the anode and the negative electrode during charging is called the cathode. This potential difference is the driving force of the separation process where coulomb forces move the ions of the feed stream to the electrode surface where they are adsorbed inside the electrical double layer [2]. The anode adsorbs negatively charged ions (anions) and the cathode adsorbs positively charged ions (cations) [18]. The electrode cannot adsorb an infinite amount of ions: every electrode has a limited capacity. At maximum capacity, the electrode is maximally filled with ions and a desorption step or regeneration step is needed to reuse the electrode for the next adsorption. In the desorption step, the polarity of the applied current is reversed (reverse current desorption (RCD)) or voltage is changed (zero volt desorption (ZVD) or reverse voltage desorption (RVD)) to regenerate the electrode [28]. The potential is switched and the ions previously adsorbed onto the electrode surface are released into the feed water. So, there is a charge-discharge cycle in a CDI system which introduces an extra separation step of the effluent stream because it consists of desalinated water (product) and concentrated solution (brine).

CDI has many advantages over the other desalination technologies:

- The main advantage of the CDI process is that it has a low energy consumption. Other desalination methods separate the water from the electrolyte, whereas CDI separates the salt from the electrolyte [29]. The amount of salt in the electrolyte is lower than the amount of water in the electrolyte, thus the desalination system is more efficient when salt is separated instead of the water. In addition, the total energy consumed is much lower than the energy input of the system because energy is recovered during the regeneration step [30].
- Unlike RO and ED, conventional CDI is not a membrane-based desalination process and therefore has minimal fouling problems and associated costs [7,18].
- For the energy transition from fossil fuels to renewable energy, desalination systems that use electricity as energy source are preferred to distillation desalination technologies that use natural gas. The CDI system is an environmentally friendly technology when electricity,

produced from renewable energy sources, is consumed because there are no CO₂ emissions [7].

- As CDI does not operate at high pressures or temperatures and does not require chemicals, it is also environmentally friendly and safe [15].

However, of course, there are some limitations and drawbacks of CDI:

- CDI is technically feasible, and favoured over other desalination technologies, for the deionisation of low concentrated water (brackish water). However, this low concentration in the feed causes limited ion removal because the electrical double layer could not be formed sufficiently in the electrodes [15].
- Traditional CDI uses electrosorption to adsorb ions into the pores of the electrodes. This adsorption process occurs at low applied potentials. At higher applied potentials, the electrons react with the ions in a redox reaction. This phenomenon is also known as a faradaic reaction. Faradaic reactions cause energy losses in the CDI system and are the major contributor to electrode degradation. Therefore, there is a narrow operating cell voltage range in which the CDI system is operational ($E_{cell} < 1.23V$ vs. normal hydrogen electrode, NHE) to limit the faradaic losses and increase CDI performance [15]. This limits the choice of electrode materials and the amount of ions that can be stored in the electrode [7,15].
- There is a charge-discharge cycle in the CDI process. In consequence, the outflowing stream is made up of the desalinated product and concentrated water. After the CDI process, another separation process is required to separate the product from the outflowing stream or the system needs to be paused during the regeneration step [34]. Thus, the CDI system is a batch processes and batch processes are more cost-intensive than continuous processes [14].

2.1.2 Performance and operational parameters

Performance parameters are utilized by designers of CDI systems to optimize the cost-efficiency and energy-efficiency of CDI systems.

2.1.2.1 Performance metrics

CDI is a desalination method which separates salt with a potential field in the water stream. It is fundamentally a different method than other desalination technologies because it is an electro-based process. For comparison between different desalination technologies, this difference in working principle asks for separate performance metrics:

- For comparison with other desalination technologies, the volume-based performance metrics should be used, according to Hawks et al. (2019): productivity (P) and volumetric energy consumption (E_v) [31].
- For comparison with other CDI cell architectures, the molar-based performance metrics should be used, according to Hawks et al. (2019): average salt adsorption rate (ASAR) and energy normalized adsorbed salt (ENAS) [31].

The **productivity** is the rate of desalinated water volume per projected surface area [32]. The equation of the productivity P in m³/s per m² projected surface area is,

$$P = \frac{1}{NA\Delta t_{cycle}} \int_{\Delta t_d} Q_v dt, \quad (2.1)$$

where A is the total projected surface area of the two electrodes in the cell in m², N is the amount of CDI units in the CDI cell, Δt_{cycle} is the total duration of a charge-discharge cycle in s, Δt_d is the duration for the discharge phase in s, and Q_v is the flow rate in m³/s [32].

The **volumetric energy consumption** is the total energy consumption per volume unit of desalinated water [32]. The E_v quantifies the energy efficiency of the desalination process in terms of the amount of desalinated water produced and is calculated with,

$$E_v = \frac{E_{in} - \eta E_{out}}{\int_{\Delta t_d} Q_v dt}, \quad (2.2)$$

where E_v is the volumetric energy consumption in J/m^3 , E_{in} is the total electrical energy consumed during charging step in J, E_{out} is the total energy retrieved during the discharging step in J, η is the ratio of the retrieved energy that is actually reused in the charging step and Q_v is the flow rate in m^3/s [32].

The **average salt adsorption rate (ASAR)** is the salt adsorption rate per total face area of the electrodes [30,32]. ASAR is in mol/m^2s and is calculated with the following equation,

$$ASAR = \frac{1}{NA\Delta t_{cycle}} \int_{\Delta t_d} (c_i - c_o) Q_v dt, \quad (2.3)$$

where A is the total projected surface area of the two electrodes in the cell in m^2 , N is the amount of CDI units in the CDI cell, Δt_{cycle} is the period of a charge-discharge cycle in s, c_i is the initial concentration of the salt in the feed in mol/m^3 , c_o is the salt concentration in the effluent stream in mol/m^3 , and Q_v is the flow rate in m^3/s [30].

The **energy normalized adsorbed salt (ENAS)** is the amount of adsorbed salt per joule of the total required energy. The ENAS quantifies the energy efficiency of the desalination process in terms of the amount of removed salt from the feed water [30]. To calculate the ENAS of a CDI system, use the following equation,

$$ENAS = \frac{1}{E_{in} - \eta E_{out}} \int_{\Delta t_d} (c_i - c_o) Q_v dt, \quad (2.4)$$

where $(E_{in} - \eta E_{out})$ is the total required energy of the CDI system in J [30].

Hemmatifar et al. (2016) performed experiments to find the optimal operational parameters (cell voltage and current) which generate the optimal ASAR or P (desalination speed) and ENAS or E_v (energy efficiency) of the CDI system [30]. Their conclusion is that there is a trade-off between ASAR and ENAS [30].

2.1.2.2 Performance indicators

Hawks et al. (2019) distinguish between the performance metrics of a CDI system and the performance indicators of a CDI system [31]. Performance indicators are used to better understand why a certain overall performance was achieved [31]. These performance indicators, specifically used for CDI systems, are salt adsorption capacity (SAC), charge efficiency and series resistance [31]. The performance indicators depend on the physical parameters of the electrodes.

The **salt adsorption capacity (SAC)** is the maximum amount of salt that can be removed within one purifying phase of an CDI cell [33]. The equation for calculating this performance indicator is,

$$SAC = \frac{M_w}{m_{Electrode}} \int_{\Delta t_d} (c_i - c_o) Q_v dt \quad (2.5)$$

where SAC is the salt adsorption capacity in mg salt per g electrode material, M_w is the molecular weight of the salt in g/mol, $m_{Electrode}$ is the total weight of all the electrodes in the CDI cell in g, Δt_d is the duration for the discharge phase in s, c_i is the initial concentration of the salt in the feed in mol/m^3 , c_o is the salt concentration in the effluent stream in mol/m^3 and Q_v is the flow rate in m^3/s [33].

According to Shang et al. (2017), the **charge efficiency** is defined as the amount salt removed per electric charge transferred to a given electrode [34]. The charge efficiency could also be explained as the ratio between ionic and electric current [35]. The equation for the charge efficiency is,

$$\Lambda_{charge} = \frac{F}{q_{out}} \int_{\Delta t_d} (c_i - c_o) Q_v dt, \quad (2.6)$$

where Λ_{charge} is the charge efficiency, and q_{out} is the charge transferred during the regeneration step in C [31]. The charge efficiency is negatively affected by faradaic reactions or the repulsion of co-ions, because current, which should be utilized to attract counter-ions, is utilized for other processes [34].

The **series resistance** is defined as the resistance of the external electronics, like the current collectors and threads, as well as the resistance in the separator which captures the ionic resistances in the channel of the CDI cell [49]. The equation for calculating this performance indicator is,

$$R_S = R_{\text{EER}} + R_{\text{SP}} = R_{\text{EER}} + \frac{l_{\text{SP}}\tau_{\text{SP}}}{\kappa p_{\text{SP}}}, \quad (2.7)$$

where R_S is series resistance in Ω , R_{EER} is the external electronic resistance in Ω , R_{SP} is the separator resistance or solution resistance in the separator in Ω , l_{SP} is the separator thickness in cm, τ_{SP} is the separator tortuosity, κ is the solution conductivity of the electrolyte in S/cm and p_{SP} is the porosity of the separator [49]. Reducing the series resistance directly reduces the dissipation of energy, therefore, also the total energy losses in the CDI system [30].

2.1.2.3 Operational parameters of CDI systems

The CDI has several operational parameters. These parameters can be used to understand why specific performance parameters of the CDI system are satisfying or not. There is a trade-off: improving one performance indicator often results in decreasing another performance indicator. The optimal settings for the performance depends on the required specifications of the effluent stream [35]. Huyskens et al. (2013) investigated the effect of the operational parameters on the performance indicators of a conventional CDI system and described important operational parameters: the magnitude of the applied voltage or current, the flowrate of the stream, the purification time (duration of the charging phase), the regeneration time (duration of the discharge phase), and the salt concentration of the feed stream [30,35]. The conclusion of the results of the experiments of Huyskens et al. (2013) is that the charge efficiency is an essential parameter for optimization of a CDI system and has a direct effect on the performance metrics [35]. The series resistance and the SAC are only affected by the concentration in the feed stream, because these values depend more on the physical properties of the electrodes [35].

2.2 Electrode theory

Understanding the adsorption process in porous capacitive electrodes is important for optimizing the capacitive electrodes and the operating conditions of CDI systems. This section explains the basic model of electrosorption in electrodes and transport phenomena in porous electrodes. Faradaic reactions are excluded, however, more detailed information about this topic could be found in the review of Zhang et al. (2018) [36]. The theory described in this section is limited to capacitive electrodes used in CDI systems.

2.2.1 Capacitors

Capacitors store electrical energy via charge separation by utilizing a solid dielectric. Supercapacitors (or high-capacity capacitors or electrochemical electrodes) are capacitors which can store lots of electrical energy because they have a high capacitance. Supercapacitors can be separated into two different types based on their mechanism of energy storage: capacitive electrodes and pseudocapacitors [37]. The energy storage mechanism behind capacitive electrodes is the electrosorption of ions from the electrolyte onto the surface of the electrode. The ions in the electrolyte are adsorbed when they are inside the electrical double layer (EDL) of the electrode-electrolyte interface [37]. They are not chemically bounded on the surface of the electrode with covalent bonds or VanDerWaals bonds, but are physically bounded by the electrostatic forces inside the EDL [37]. Pseudocapacitors use faradaic reactions to chemically adsorb ions onto the surface of the electrode in combination with the electrosorption of ions into the EDL of the electrode [37].

2.2.2 Electrical double layer

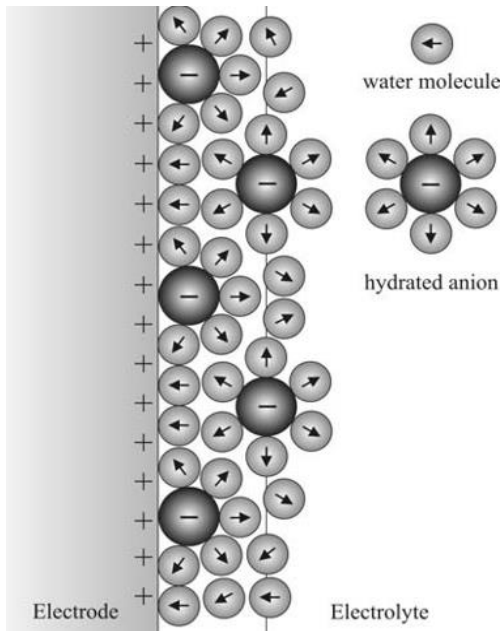


Figure 4: Metal planar electrode immersed in an electrolyte. The surface charge of the electrode attracts the anions with solvation shells and water molecules. Source: Lopatynska et al. (2008) [39].

The formation of an electrical double layer is a common phenomenon occurring at the boundary between an electrically charged material and the electrolyte [38]. To understand the concept of the electrical double layer (EDL) assume a metal electrode with flat surfaces in contact with an electrolyte consisting of anions, cations and water as solvent, see Figure 4 [39]. For now, assume that there are no redox reactions or adsorption processes at the interface of the electrode [40]. There are two bulk phases: a metallic phase and a electrolyte phase. The electrolyte and the metal are in equilibrium and must be charge-neutral, according to the electroneutrality principle. The electroneutrality principle explains that if electrons are added to the electrode, subsequently, positive ions are attracted to the interface, while negative ions are repelled. This process forms a double layer at the surface of the electrode. The double layer is also created when electrons are removed from the electrode, e.g. holes are created. Positive ions are now repelled, while negative ions are attracted.

This physical phenomena has first been described by the Helmholtz model. The ions are assumed to be point charges with no size, only charge. In this model is assumed that all the surface charge is directly compensated by the charge of the counter-ions that were attracted to the surface [41]. The potential profile is a linearly decreasing line, see Figure 5a [38]. The Helmholtz model is an ideal model where the charge efficiency is equal to unity [41]. Unfortunately, the Helmholtz model did not consider that ions have a certain mobility at temperatures above zero Kelvin thus do not densify on the electrode surface but stay moving in the solution [41]. Therefore, Gouy and Chapman developed a new model including a diffusion layer to take the thermal motions of the ions into account [38]. This Gouy-Chapman model (Figure 5b) proposed an exponentially decaying potential function inside the diffuse layer according to the Boltzmann distribution [38]. The ions are still assumed to be point charges without sizes but are concentrated around the surface of the electrode as a cloud according to Boltzmann statistics [40]. The characteristic length of the diffuse layer is the distance for the counterion concentration and potential to decay by a factor of e [41]. This distance is called the Debye length λ_D . The Debye length is an indication of the thickness of the EDL, and is calculated with the following equation,

$$\lambda_D = \sqrt{\frac{\epsilon \epsilon_0 R T}{2 c z^2 F^2}}, \quad (2.8)$$

where ϵ is the relative electrostatic permittivity of water (dimensionless), c is the concentration of the ions in the electrolyte (mol/m^3), and z is the charge number of the ion [42]. The Debye length depends on the concentration of the electrolyte, as displayed in Table 1.

Table 1: Debye length (in angstrom) for different concentrations in the electrolyte. Source: book of Schmickler & Santos (2010) [40].

Concentration (mol/L)	10^{-4}	10^{-3}	10^{-2}	10^{-1}
Debye length ($\text{\AA} = 10^{-10}\text{m}$)	304	96	30.4	9.6

A problem of this model is that the EDL capacity would become infinite when the potential is infinitely positive or negative, while, experimentally has been measured that the EDL capacity is constant [40]. So, this model was not sufficient to describe the EDL. Stern combined the Helmholtz model and the Gouy-Chapman model by including the ion monolayer from the Helmholtz model in the diffusion layer of the Gouy-Chapman model. The Stern model takes the radius of the ions into account. As the yellow line visualizes in Figure 5c, the potential decreases linearly in the Helmholtz layer and exponential in the diffuse layer [38]. The intersection between the Helmholtz plane and diffuse layer is called the Stern plane which denotes the closest distance for ions to come to the surface [41]. The capacity would converge to a constant value.

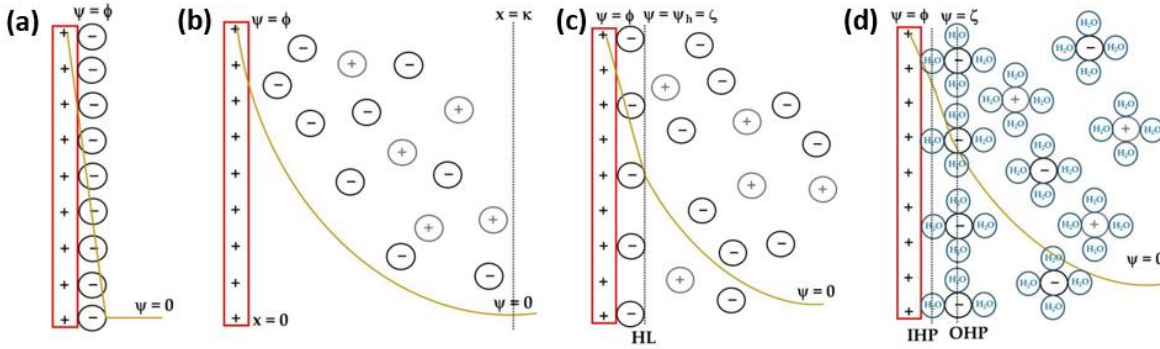


Figure 5: Electric Double Layer models developed by (a) Helmholtz, (b) Gouy and Chapman, (c) Stern and (d) Grahame. The potential in the EDL over the distance from the metal-solution interface is depicted with the yellow line. Figures were retrieved from the review paper of Dourado (2022) [38].

The last adaptation was done by Grahame: the model includes the monolayer of water molecules at the metal-solution interface due to the solvation shell of the ions [43]. Thus, Grahame adapted Stern's model by splitting the Helmholtz layer into an inner Helmholtz layer (IHL) and outer Helmholtz layer (OHL) where the IHL consists of the water molecule monolayer and the OHL is a monolayer that consists of the ion molecule with solvation shell (Figure 5d) [38]. The Helmholtz layer is now called the Stern layer. After the OHL, there is the diffusion layer of the Gouy-Chapman model. At the Stern layer, there is still a potential called the Helmholtz potential [38]. Thus, the charge compensation for the charge on the surface of the metal electrode, according to the Grahame model and electroneutrality principle, is achieved by the ions in the outer Helmholtz layer and the diffusion layer.

The potential where there are no adsorption processes at the electrode-electrolyte interface, so the electrode-electrolyte interface is not attracting any ions, is called the point of zero charge (PZC) [44,45]. To facilitate the adsorption of ions into the EDL of the electrodes, the electrodes need to be charged. Inserting an applied potential on the electrode results in adding charge in the form of adding electrons or creating holes in the electrode surface. The result of increasing the applied potential is that more ions are adsorbed into the EDL, consequently, increasing the capacitance of the electrode. The following equations show the relation between applied potential and capacitance,

$$\frac{1}{C_{\text{tot}}} = \frac{1}{C_{\text{GC}}} + \frac{1}{C_{\text{H}}}, \quad (2.9)$$

$$C_{\text{GC}} = \frac{\epsilon \epsilon_0}{\lambda_D} \cosh\left(\frac{ze_0(\phi - \phi_{\text{PZC}})}{2k_B T}\right), \quad (2.10)$$

where λ_D is the Debye length, ϵ is the relative electrostatic permittivity of water (dimensionless), z is the charge number of the ion, ϕ is the applied potential in V, ϕ_{PZC} is the potential of zero charge in V, T is the temperature in K, C_{tot} is the total capacity of the electrode in F/m^2 , C_{GC} is the Gouy-Chapman capacity which is the capacity inside the diffusion layer in F/m^2 and C_{H} is the Helmholtz capacity which is the capacity inside the Helmholtz layer in F/m^2 [40]. The cosh-term shows that the Gouy-Chapman capacitance follows a U-shaped curve where the minimum capacitance is at the point of zero charge [46]. The maximum salt adsorption capacity of an electrode is determined by the amount of ions that can be adsorbed inside the EDL. Therefore, the maximum capacity of the electrode depends on the size of the electric double layer (Debye length). For low ion concentrations in the electrolyte, the Gouy-Chapman capacity dominates, and thus, the diffusion process dominates [40,46]. For high ion

concentrations in the electrolyte, the Helmholtz capacity dominates [40,46]. The Helmholtz capacity itself is independent of the concentration of the electrolyte [40,47].

2.2.3 Pore size distribution: micro-, meso- and macropores

The EDL theory and models in the last section are utilized for flat electrodes. For porous electrodes, the EDL theory is still valid, only the pore size determines the dominance of the adsorption process. According to the International Union of Pure and Applied Chemistry (IUPAC), pore sizes are classified according to the effective pore diameter as micropores (<2nm), mesopores (2-50nm) or macropores (>50nm) [48,49]. Nanopores also exist, which have an effective pore diameter smaller than 1nm, however, different papers denote different sizes to the nanopores. For simplicity, the nanopores are not considered. The micropores of the porous electrodes provide a large surface area of active sites for adsorption, while the meso- and macropores facilitate ion transport to the micropores [48]. Finding the right balance of macro-, meso- and micropores is important to increase the adsorption of ions at the electrode surface.

2.2.3.1 Micropores

Micropores have a pore size smaller than the Debye length [48]. Micropores adsorb counterions in their EDL, thus store energy. The micropore consists of the active sites where ions could be adsorbed. Ions need to remove (a part of) their solvation shell to enter the EDL of the micropores [48]. The total capacity of the electrode is determined by the amount of active sites on the surface of the micropores (Figure 6) [36]. Improving the maximum capacity of the electrode is possible by improving the specific surface area (SSA) of the electrode by increasing the amount of micropores. Increasing the amount of micropores in the electrode surface, increases the amount of active sites, consequently, increasing the SSA.

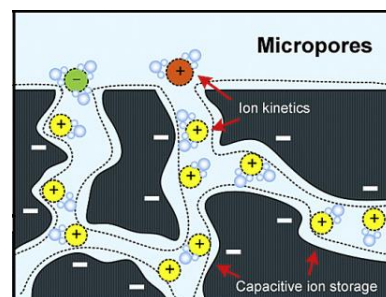


Figure 6: The adsorption of ions inside micropores. Debye lengths of the EDLs are depicted with the black dotted lines. Figure has been retrieved from the paper of Zhang et al. (2018) [36].

2.2.3.2 Macropores

Macropores in the electrode structure are also important. Macropores facilitate the transportation of ions into the meso- and micropores of the electrode surface [47]. The pore volume of the macropores is mostly filled with the electroneutral electrolyte that can be seen as salt reservoir for the the micropores [48]. The macropores improve the transport of the ions to the electrode surface, thus the macropores determine the wettability of the electrode. Macropores have a pore size that is much larger than the Debye length, so the effect of the EDL on the ions is negligible [50].

2.2.3.3 Mesopores

Mesopores have pore sizes with approximately the same diameter as the Debye length [48]. The function of the mesopores is to provide a pathway for the ions to the micropores and to store some ions inside the EDL [47]. Thus, mesopores provide both the function of the macropores and micropores. The mesopores are filled with electroneutral electrolyte, however, the counterions with solvation shell are adsorbed into the EDL while co-ions are mitigated into the diffusion layer (see Figure 7) [48,51]. More mesopores instead of macropores improves the specific surface area, while more mesopores instead of micropores improves the wettability of the electrode.

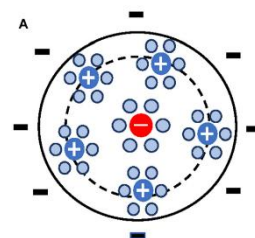


Figure 7: Model of the mesopores according to Huang & He (2013) [51]. The original figure was copied from the review paper of Gabitto & Tsouris (2023) [48].

2.3 ED technology

Electrodialysis is an electro-based desalination process that uses charge-selective membranes, referred to as ion-exchange membranes. The counter-ions are able to migrate through chemically charged membranes while co-ions are repelled by the charge in the membrane. In this section, the working principles and performance parameters of ED systems are explained in detail.

2.3.1 Working principle of conventional ED system

Electrodialysis uses ion-exchange membranes (IEMs) between two porous carbon electrodes to create alternating concentrated channels (brine) and desalinated channels (product), see Figure 8 [52,53]. There are three separate inlet streams: (1) feed stream enters the alternating product (dilute) channels where it is desalinated, (2) concentrate stream enters the brine (concentrate) channels and (3) electrode stream flows in the channel between the membrane and the electrode [54]. The channels are created by spacers. Anion exchange membranes (AEM) are positively charged ion-exchange membranes and cation exchange membranes (CEM) are negatively charged ion-exchange membranes. One unit cell includes a dilute channel, a concentrated channel, one AEM and one CEM, as depicted in Figure 8 [53]. The driving force of the desalination of the feed stream is the electrical potential difference within the system that is created by applying a DC current on the capacitive electrodes (anode and cathode in Figure 8) [53]. During the charging phase, the cathode is negatively charged and the anode is positively charged. The potential field moves the cations and anions in the feed stream in opposite directions. When a cation reaches the CEM, it can migrate through the membrane, however, after the CEM, it reaches the AEM where it will be blocked. The reverse happens for anions, where it moves through the AEM and gets blocked at the CEM surface. The anions and cations stay in the same channel which becomes highly concentrated: the brine channel. The other channel, product channel, is highly diluted. This process happens in every unit cell. The result is alternating streams of high-purity desalinated water and high-concentrated water. When the electrodes are fully filled with ions, the polarity of the DC current is switched to remove the ions from the electrodes. In this discharge phase, the alternating streams of high-purity desalinated water and high-concentrated water are also swapped.

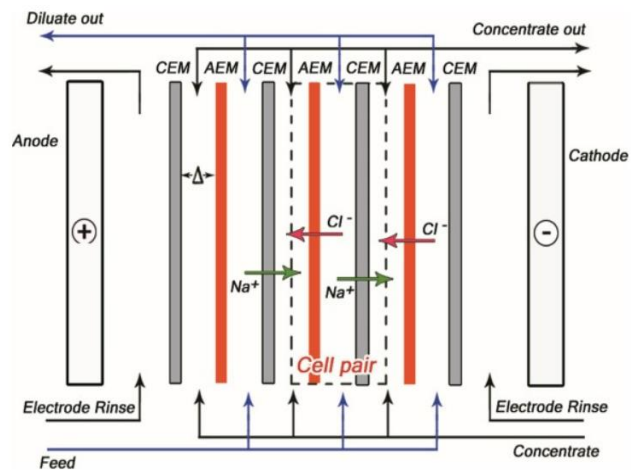


Figure 8: Schematic of a conventional electrodialysis system. The cell unit consists of one brine channel and one product channel with an AEM and an CEM. Retrieved from Qureshi et al. (2021) [53].

Unlike CDI, Electrodialysis has already multiple applications in the industry. ED is used for industrial wastewater treatment, high-purity water production and is capable of desalinating seawater [55,56]. The main advantage of ED, just like CDI, is that it removes the salts from the salt-water solution, not the water. This enables the system to remove more salts from the water with lower energy inputs. Therefore, ED is a preferred desalination process for brackish and groundwater desalination. In these low salinities of water, ED has lower energy consumption and higher water recovery than RO due to the absence of osmosis pressure limitations and better resistance to membrane fouling and scaling [54,56,57]. In addition, ED is relatively simple to operate and uses electricity as the energy input [55]. This system could be operated in a sustainable manner if electricity produced from renewable energy sources is used. Other desalination technologies need more innovation before they can be used with green electricity, thereby avoiding the need of conversion between electrical and mechanical forms of

energy. ED systems have limitations compared to other desalination systems. ED is an electro-membrane desalination technology and still uses membranes that suffer from fouling and scaling due to, respectively, adhering of organics like bacteria, viruses and toxic components, and the precipitation of ions on the membrane surface [58]. The performance of IEM is limited by fouling and scaling because the membrane pores are blocked which reduce the ion transfer through the membrane and thus reduce the purity of the water. Therefore, pre-treatment of the feed water is required and anti-scaling chemicals are induced to the feed stream to minimize fouling and scaling formation [59].

2.3.2 Performance and operational parameters

The performance metrics of ED systems are water recovery, salt removal rate and total specific energy consumption. The performance indicators are the total current efficiency, permselectivity and conductivity. The operational parameters which have effect on the performance of an ED system are external applied voltage, temperature of the feed stream, initial salt concentration in the feed stream, the pH in the channels and the physical properties of the IEMs [55]. The physical properties of the IEMs have a major influence on the performance and costs of the ED [59,60].

2.3.2.1 Performance metrics

The performance metrics of the ED are comparable to the performance metrics of the CDI. Similar to the ASAR for the CDI system, the ED system has the performance metric **salt removal rate** in mol/s to determine the salt removed from the feed stream per unit of time. According to Qureshi et al. (2021), the following equation is used to calculate the salt removal rate,

$$\dot{N}_s = N(Q_f c_i - Q_p c_o), \quad (2.11)$$

where Q_p is the flow rate of the product stream of one unit cell in m^3/s , Q_f is the flow rate of the feed stream of one unit cell in m^3/s , c_i is the initial concentration of the ion in the feed stream in mol/m^3 , c_o is the concentration of the ion in the dilute stream in mol/m^3 and N is the amount of unit cells [53]. Preferably, Q_f and Q_p would be the same, but due to osmosis and electro-osmosis, water transport could take place between the brine and product channels, however, this effect is negligible for the separation of low salinity streams [61]. Still, Al-Amshawee et al. (2020) did mention that water recovery is an important performance indicator for water streams with low salinity due to this mass transfer effect. The **water recovery** is the ratio between the flowrate of the product stream and the flowrate of the feed stream,

$$\text{WR} = \frac{Q_p}{Q_f}. \quad (2.12)$$

The **total specific energy consumption** (in J/kg) could be calculated with the following equation,

$$\text{TSEC} = \frac{\int E(t)I(t)dt}{\dot{N}_s M}, \quad (2.13)$$

where M is the molar mass of the ion in kg/mol , \dot{N}_s is the salt removal rate in mol/s , t is the duration of the operation in s , E is the voltage in V , and I is the current in A [53,62]. The total energy consumption is a measure for determining the amount of energy per removed mass of salt. The TSEC is the equivalent of $1/\text{ENAS}$ for CDI systems.

2.3.2.2 Performance indicators

The **permselectivity** is the ability of the IEM to transport counter-ions through the IEM while excluding the transport of co-ions [63]. The permselectivity is a key performance indicator because it directly shows how effective the selectivity of counter-ions is. The permselectivity is preferred to be as high as possible, thus equal to 1. The equation for the permselectivity is,

$$P = \frac{t_{\text{counter}}^m - t_{\text{counter}}^s}{1 - t_{\text{counter}}^s} \quad (2.14)$$

where P is the permselectivity, t_{counter}^m is the transport number of the counter-ion in the IEM, and t_{counter}^s is the transport number of the counter-ion in the bulk solution [64]. The transport number

could be calculated with the following equation, $t_k^i = \left[\frac{z_k D_k}{\sum_{k=0}^{n-1} z_k D_k} \right]_i$, where D_k is the diffusion coefficient of ion k and z_k is the valence number of the charge of the ion k , and i denotes the transport number of specific ion k in the solution ($_S$) or membrane ($_M$) [65].

The **ionic conductivity** denotes the ion transport in the IEM when the transport is driven by an external electrical field [66]. The ionic conductivity is a performance indicator of the IEM. The ionic conductivity performance indicator is equivalent to one over the series resistance, which is also a performance indicator for CDI systems. The ionic conductivity is calculated with,

$$\kappa_m = \frac{\delta_m}{R_m A}, \quad (2.15)$$

where κ_m is the ionic conductivity of the membrane (S/cm), δ_m is the thickness of the IEM (cm), R_m is the resistance of the membrane (Ω), and A is the cross sectional area of the membrane (cm^2) [64]. The energy-efficiency of the ED system is dominantly determined by the resistances inside the membrane, therefore, the IEMs should have low membrane resistances to increase the ion transport through the membrane [67]. For the ED system, IEMs with high permselectivity and ionic conductivity are preferred, however, there is a trade-off between these two performance indicators [68].

The **current efficiency** is, according to Sadrzadeh & Mohammadi (2009), a measure of how efficient ions are transported across the ion exchange membranes for a given applied current [69]. The equation for calculating the current efficiency is,

$$CE^k = \frac{z F Q_p (c_i^k - c_o^k)}{N \int I(t) dt} \quad (2.16)$$

where z is the charge of the ion, Q_p is the flow rate of the dilute stream of one unit cell in m^3/s , c_i is the initial concentration of the ion in the feed stream in mol/m^3 , c_o is the concentration of the ion in the dilute stream in mol/m^3 , N is the amount of unit cells, t is the duration of the operation in s , and I is the current in A [69]. The current efficiency is specific for one ion type k . The **total current efficiency** is the summation of the current efficiencies of all the ions (n) in the solution, $TCE = \sum_{k=0}^{n-1} CE^k$. Total current efficiency is also a ratio of ion current to electric current and is similar to the CDI system's performance indicator charge efficiency.

2.4 Ion exchange membrane theory

In this section, the theory behind the selective transport of ions through membranes is explained in more detail. The important Donnan theory and concentration polarization that follows from that, create three layers: bulk solution, diffusion boundary layer (DBL) and electric double layer (EDL). The theory described in this section is limited to ion exchange membranes used in ED systems.

2.4.1 Donnan's Law

Donnan's Law describes the behaviour of the ions in two electrolyte solutions that are separated by a semi-permeable membrane [70]. Examples of semi-permeable membranes are the cation exchange membrane (CEM) and the anion exchange membrane (AEM). These membranes are semi-permeable because the counter-ions are able to diffuse through them while co-ions are unable to move through the membrane [71,72]. The ion exchange membrane consist of fixed charged functional groups with a positive charge for an AEM and a negative charge for an CEM. The electroneutrality principle must be respected, so the mobile counter-ions in the solution are electrostatically attracted to move inside the membrane pores. The charged groups inside the membrane electrostatically repel the moving co-ions, consequently, the co-ions get repelled because the electrostatic forces work against the diffusion.

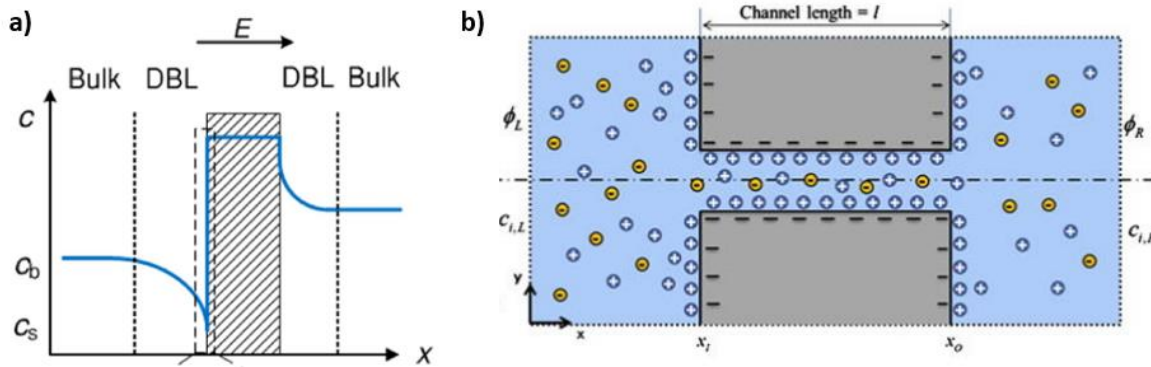


Figure 9: (a) Concentration profile of cations in a binary electrolyte with a CEM. Source: Luo et al. (2018) [73]. (b) Graphical model of an IEM. Source: Tian et al. (2015) [74].

Donnan's Law treats the IEM structure as a solution containing fixed charge functional groups simulated as immobile ions [73]. The concentration and potential in the IEM solution are constant and do not change across the thickness of the membrane [73]. There is thus a potential difference between the bulk solution and the membrane solution, so counterions are attracted by the membrane while co-ions are repelled, as depicted in Figure 9 [73,74]. The Donnan potential (φ_D) is the potential difference between the bulk solution and the ion exchange membrane solution. The Donnan potential is calculated with,

$$\varphi_D = \varphi_m - \varphi_s = \frac{RT}{z_i F} \ln \left(\frac{a_i^s}{a_i^m} \right), \quad (2.17)$$

where φ_D is the Donnan potential in V, φ_m is the potential in the membrane in V, φ_s is the potential in the bulk solution in V, z_i is the charge number of the ion, a_i^s is the activity coefficient of the ion in the solution, and a_i^m is the activity coefficient of the ion in the membrane [73]. According to the research of Tian et al. (2015), the Donnan equilibrium is not applicable for membranes with large pore sizes and large concentration differences [74].

2.4.2 Concentration Polarization

The ion exchange membranes are polymeric structures which include fixed charged groups. The charge of this groups attract the counter-ions and repel the co-ions which results in an EDL over the surface of the IEM (see Figure 9) [73,74]. When an external potential field is applied over the IEM, thus when an external potential is applied on the capacitive electrodes of the ED system, the counter-ions are able to transport through the membrane while co-ions are repelled, according to Donnan's Law [75].

Subsequently, the concentration of counter-ions on the depleted side of the membrane (left side, Figure 9a) decreases, while the concentration on the concentrated side of the membrane (right side, Figure 9a) increases [73,74]. This phenomenon is called concentration polarization: the counter-ion concentration at the interface gets more depleted in the diluted electrolyte, while the counter-ion concentration at the other side of the membrane gets more concentrated in the concentrated electrolyte [75]. Concentration polarization results in the formation of a diffusion boundary layer (DBL) at the membrane surface where this caused concentration gradient is created [76].

Concentration polarization is caused by the difference in the transport number of the counter-ion in the bulk solution and in the membrane [76]. The transport number of the counter-ion in the bulk solution is smaller than the transport number of the counter-ion in the membrane, and the difference results in the formation of DBL. The transport number denotes the fraction of the current that is carried by a type of ion and could be calculated with $t_i = \frac{z_i D_i}{\sum_{i=0}^k z_i D_i}$, where D_i is the diffusion coefficient of ion i , and z_i is the valence number of the charge of the ion i [65]. When the membrane is made selective for ion transport, the counter-ions need to carry a larger fraction of the current simply because the co-ions are not able to transport the current through the membrane. As a result, the transport number of the counter-ion in the membrane is larger than for the bulk solution because the counter-ion transport in the membrane increases while the co-ion transport decreases [76]. The transport number also changes when there is a difference in electric mobility, due to different ion types or concentrations in the solution [65].

2.5 Electrode material and fabrication

The methodology of the fabrication and the chosen electrode materials affect the morphology of the electrode resulting in enhanced electrode performances. According to the paper of Jia et al. (2016), the electrode material should have a large surface area and high electrical conductivity, thereby concluding that porous carbon is the cheapest and most commercially available material for CDI applications [47]. However, carbon is not the only electrode material. The capacitive carbon electrodes used for CDI systems are built mainly from an active material, for the porous structure that results in an increase in specific surface area, but an electroconductive additive, for enhancing the conduction of the electrons to the surface of the pores, and binder material, for merging the active material with the electroconductive additive, are also necessary to increase the capacitance of the electrode [77].

2.5.1 Electrode material composition

The main active materials can be activated carbon (AC) [77,78], carbon aerogel [79], mesoporous carbon [80], and graphene or carbon nanotube (CNT) [81,82]. Carbon aerogel, mesoporous carbon and graphene

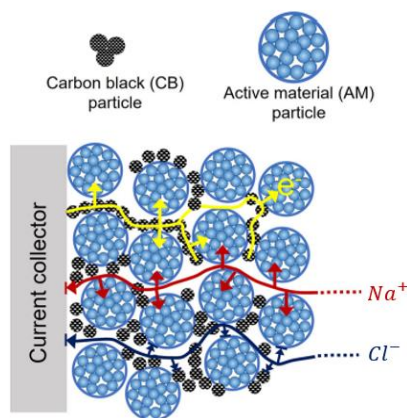


Figure 10: The electron transport and ion transport in the electrode consisting of active material and carbon black particles. Source: Qu et al. (2022) [157].

give the electrode better electrochemical performances than activated carbon, however, AC is the most commonly used active material [83]. AC has a very porous structure that is tuneable, has a large specific surface area, has a large window in which the material is electrochemically stable, is electroconductive, is environmentally friendly and is commercially available at relatively low cost [47,77]. The structure of AC consists of many micro- and nanopores which gives the electrode the large surface area and short pathways. Unfortunately, due to the absence of macro- and mesopores and the high electrical resistance of the material, the kinetics of the ions and electrons are relatively low [77]. The AC electrode material is thereby modified by adding conductive additives and binders into the slurry to optimize the performance of the electrode. Wang et al. (2020), Mubita et al. (2018), and

Nadakatti et al. (2011b), for example, added carbon black to the structure to enhance the conductivity of the electrons [84,85,86]. The polymeric binder affects the morphology of the electrode and is used to tune the pore size and pore distribution of the AC electrode material. The binder content inside an electrode has a large effect on the ion transport resistance (thus the kinetics of the ions) and acts as a glue between the active material and conductive additive [87,88]. Polyvinylidene fluoride (PVDF) or polytetrafluoroethylene (PTFE) are used as binders in the literature, but PVDF provides the most uniform morphology according to the research of Arunkumar & Paul (2017) [89]. Uniform morphologies and enhanced electroconductivity increase the maximum capacitance and adsorption rate of the AC electrode.

2.5.2 Electrode fabrication recipe

The recipe for producing capacitive electrodes consisting of AC, a conducting carbon (CB) and binder (PVDF) has been summarized by Oladunni et al. (2018) with the following steps [83]:

1. First, activated carbon powder is produced by pyrolysis of carbon powder at temperatures between 600°C and 800°C, subsequently, physically activating the product by gasification with steam, carbon dioxide or other chemically activated acids and bases.
2. The AC powder, CB and PVDF are mixed with a solvent. The slurry is stirred for 2 to 6 hours to ensure homogeneity in the mixture.
3. The slurry is smeared onto a current collector sheet (like platinum foil or graphite) until a certain thickness is reached. Another option is to dip a current collector rod into the slurry until a certain thickness and length has been reached.
4. The electrode is dried in an oven for approximately 20 till 24 hours at a specific drying temperature, so the solvent could evaporate out of the electrode. The drying temperature of the oven has an effect on the morphology of the electrode. Another method is to immerse the electrode into pure water. The solvent dissolves from the slurry hence the pore network inside the electrode is formed.

The composition of the slurry has a large effect on the desalination performance of the electrode. Park et al. (2007) concluded that the optimal capacitance and desalination performance of the porous electrode in CDI is achieved when the slurry consists of 84wt% carbon powder, 12wt% conductive carbon black and 4wt% polymeric binder [92].

Also, the chosen solvent has an effect on the pore size distribution of the electrode and the electrode preparation method. N-methyl-2-pyrrolidone (NMP) is the solvent most commonly used in the literature for electrode preparation. NMP gives the best electrochemical performance, as concluded by the research of Arunkumar & Paul (2017), due to its low viscosity, which helps in the uniform distribution of active carbon particles on the electrode surface [89]. NMP is known to be toxic and the usage has been severely restricted by the European Chemical Agency. Therefore, NMP has been replaced by a solvent with similar features: dimethyl sulfoxide (DMSO). DMSO is not toxic, environmental friendlier and cheaper than NMP [93].

Not only the solvent type, but also the drying temperature has an effect on the performance of the electrode. The solvent evaporates from the electrode when it is placed in the oven, and the evaporation rate depends on the temperature of the oven. The evaporation rate affects the pore distribution of the

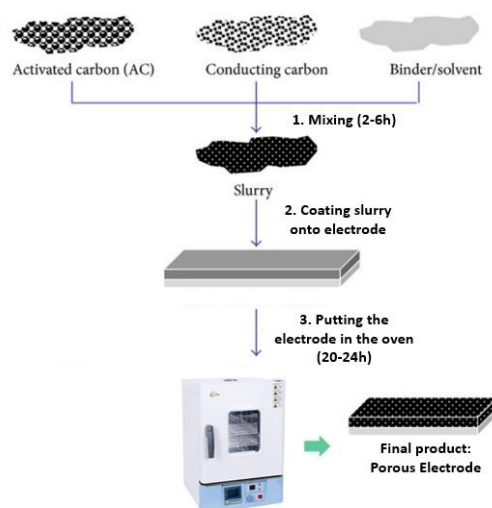


Figure 11: General fabrication of an activated carbon electrode with conducting carbon and a polymeric binder. This figure is a modified figure taken from the paper of Kim (2015) [90,91].

electrode [89]. When the evaporation rate is low, then the active material particles merge together to create larger particles with lower specific surface areas. These larger particles are called agglomerates. Increasing the drying temperature, decreases the viscosity which increases the uniform morphology of the electrode [89]. However, when the drying temperature is close to the boiling point of the solvent, then the solvent in the slurry starts to boil [89]. Boiling is a very rapid process and gives the solvent not enough time to disperse the active material uniformly [89].

2.6 Applications of Electrochemical Impedance Spectroscopy

Previous researchers have used EIS as a tool to determine the electrochemical properties of capacitive electrodes utilized in CDI and ion exchange membranes utilized in ED. In this section, the Nyquist plot of those specimen are displayed and the impedance values, that should be achieved to maximize the desalination performance of, respectively, the CDI and ED systems, are explained. The reader is expected to have some background knowledge of electrochemical impedance spectroscopy and of the graphical analysis via Nyquist and Bode plots. If you need more information about EIS, it is recommended that you read about the basics of EIS in “Fundamentals of Electrochemical Impedance Spectroscopy” in Appendix A.

2.6.1 Electrochemical Impedance Spectroscopy for capacitive electrodes in CDI

The typical Randles circuit model is the basic model for electrodes where faradaic reactions play an important role, however, for CDI electrodes, the equivalent electric circuit model (EECM) of Figure 12 is a better representation of the behaviour of the capacitive electrode [94]. The Nyquist plot consist of:

- The series resistance R_s . This resistor denotes the solution resistance of the ions in the bulk solution (R_{sp}) and the resistance of the electrons through the wires (R_{EER}). It is dominant at high frequencies. This is showed as a shifted start of the plot in the Nyquist plot. The series resistance is thus found by finding the intersection of the plot with the real axis of the Nyquist plot: the point where the plot starts. The series resistance and the resistance in the electrode are the largest contributors to the overall resistance in the CDI system, according to Kuo et al. (2020) [21].
- The semi-circle in the Nyquist plot is a parallel R element with CPE element (called R//Q-circuit element) in the EECM. The value of the resistor in the R//Q-circuit is equal to the diameter of this semi-circle [95]. This R//Q-circuit element denotes the contact resistance and contact capacitance between the current collector (CC) and the electrode [96]. The connection between the CC and the electrode is never perfect, there is always some air in between. Ideally, the CC and electrode are perfectly connected, so the semi-circle would ideally not exist, however, most EIS experiments with carbon supercapacitors result in a Nyquist plot with a small semi-circle and a phase Bode plot with a peak at high frequencies.
- The behaviour inside the electrode is described with a semi-infinite-Warburg element and an ideal capacitor placed in series [94]. The Warburg element in series with a capacitor describes the mass transfer of the ions and electrons (visualised as a 45° line) and the formation of the EDL (visualised as a 90° line) on the electrode surface.

The shape visualised in Figure 12 is the shape of capacitive electrodes used in CDI applications [94]. Some elements in the EECM could be replaced, for example, the Warburg element and capacitor in series could be replaced by a transmission-line model with reflective boundary condition or the

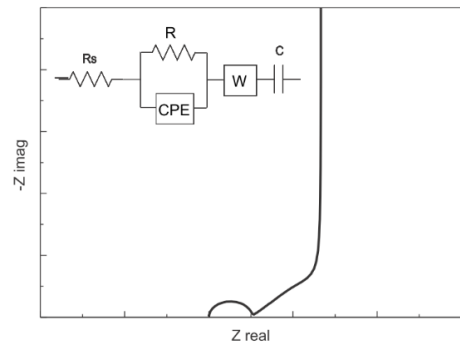


Figure 12: Typical EECM and Nyquist plot for carbon supercapacitors. The vertical line after the 45° line for the diffusion dominating region is the capacitive behaviour of the electrode dominant. There is a semi-circle due to faradaic reactions. Figure retrieved from the research paper of Dsoke et al. (2013) [94].

capacitor at the end is replaced by a CPE element. For CDI electrodes, the series resistance and contact resistance need to be as small as possible. The value of the double layer capacitance needs to be as large as possible, since this is indicative of more active sites in the CDI electrode. The slope of the line resulting from the Warburg element shows the mass transfer behaviour of the ions inside the pores and gives an indication of the pore size distribution of the CDI electrode. Ideally, this slope would be 45°, however, when the micropores are not ideally circular, this slope would be smaller.

2.6.2 Electrochemical Impedance Spectroscopy for ion exchange membranes in ED

When an ion exchange membrane is immersed in an electrolyte, there are three layers in the electrolyte: the bulk solution, the diffusion boundary layer (DBL), and the electrical double layer (EDL) [97]. These layers are formed on both sides of the membrane. The corresponding Nyquist plot (see Figure 13) of the ion exchange membranes, utilized in ED systems, consists out of the following elements [98,99]:

- The series resistance R_{MS} is a summation of the resistances in the bulk solution (R_s) and inside the membrane (R_M). This resistance is dominant at high frequencies [75]. In the Nyquist plot, the series resistance is shown as a shifted start of the plot. This resistance is indicated by a resistor.
- The semi-circle at high frequencies describes the behaviour of the EDL [99]. Thus, the EDL is modelled differently for IEM than for capacitive electrodes: the behaviour of the ions that are adsorbed in the EDL of the IEM is visualised as a R//C-circuit, and the EDL of capacitive electrodes as a capacitor.
- The semi-circle at low frequency describes the diffusion boundary layer. The DBL is displayed with an R//Q circuit. The start of the semi-circle has a 45° slope line. This semi-circle could be represented with a (finite-length) transmission-line model element [99].

The interface resistance is the summation of the resistance in the DBL (R_{DBL}) and the resistance in the EDL (R_{EDL}). The interface resistance is different for different electrolyte concentrations and ion types, even if the ionic strength is the same [76]. The series resistance, resistance in the DBL, and the resistance in the EDL need to be as small as possible. The membrane resistance (R_M) and resistance in the DBL (R_{DBL}) are the largest contributors to the overall resistance in the IEM at low salt concentrations, according to Fontananova et al. (2017) [100]. The double layer capacitance (C_{dl}) is relatively small. A large value of C_{dl} , that also increases over time, indicates that the membrane is severely affected by fouling [25].

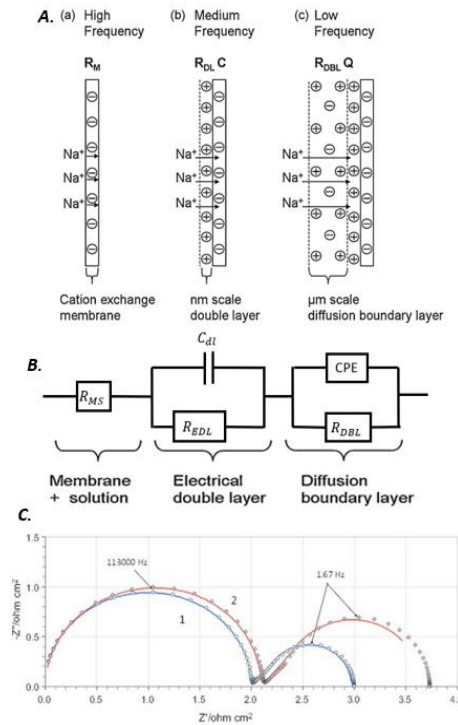


Figure 13: (B) Equivalent Electrical circuit model for an ion exchange membrane and (A) the physical behaviour in the ion exchange membrane at different frequencies. The figures are adjusted from original figures retrieved from the research paper of Długołęcki et al. (2010) [75]. (C) The Nyquist plot of an ion exchange membrane from the research paper of Nikonenko & Kozmai (2011) [99].

2.7 Conclusion

Researchers in the CDI community are continuously developing new CDI cell architectures and optimizing capacitive electrodes to improve the energy-efficiency, cost-efficiency, and freshwater production of the “conventional” CDI system. The new developed multi-channel CDI system is a new CDI cell architecture that consists of multiple membranes that are sandwiched between capacitive electrodes, just like ED systems. The difference with ion-exchange membranes is that, these so called capacitive membrane electrodes, are made of electrode material and are charged by an externally applied potential. The behaviour of the desalination of ions inside the MC-CDI is equivalent to the behaviour of ED systems, only the charging method is different. Thus, the performance metrics of MC-CDI correspond with the performance metrics of ED. The selective behaviour of the CME, for allowing the transport of counter-ions while co-ions are repelled, is also important for the performance of the MC-CDI, thus performance indicators of IEMs in ED, that describe the mobility of the ions through the membrane and how effective and efficiently that happens, corresponds with those performance indicators of CME. The performance metrics and indicators for MC-CDI systems and CMEs are summarized in Table 2.

Table 2: (left) Performance metrics of CDI, ED, and MC-CDI and (right) the performance indicators of capacitive electrodes in CDI, IEMs in ED, and CMEs in MC-CDI.

Performance Metrics		Performance Indicators	
CDI	ASAR ENAS	CDI electrodes	SAC Charge efficiency Series resistance
ED	Salt removal rate Water recovery Total specific energy consumption	IEMs	Permselectivity Conductivity Total current efficiency
MC-CDI	Salt removal rate Water recovery Total specific energy consumption	CMEs	Permselectivity Conductivity

The goal of MC-CDI designers is to construct an CME with the best performance to optimise the performance of the MC-CDI system. Still, there is a long way ahead of us, because MC-CDI systems or CMEs have not been researched by the CDI or ED community. That is why it is not certain what physical properties the CME should have to optimize the performance of the MC-CDI system. Optimising the performance of the CDI electrode, result in a better performance of the CDI system. The same is expected to be true for CMEs in MC-CDI systems, because CMEs are made from the same electrode material (active material, conductive additives and a polymeric binder) as CDI electrodes.

EIS is a very fast tool which could be used to analyse the interface processes at different timescales. This measurement system works for IEMs and CDI electrodes because the relationship between the shape of the impedance plots and the evaluated electrochemical parameters have been investigated and tested intensely by researchers in the CDI and ED community. For CMEs in MC-CDI systems, this relationship has not been investigated. Once the relationship between performance and electrochemical parameters is known, theories can be sought to explain this relationship and the structure of the CME could be optimised.

3

Methodology

The theoretical framework made clear that there is abundant information about the EIS procedure and analysis of electrodes used in CDI systems and ion-exchange membranes in ED systems. The equivalent electrical circuit model (EECM) of electrodes in CDI and IEMs in ED are modelled accurately with the EECMs explained in Chapter 2.6 and Appendix A.4, where the shape of the impedance plots could be used to predict the performance of the specimen. EIS is in this way used to compare different specimen in a relatively fast manner and find the specimen with the best electrochemical properties. Ideally, EIS would also be used to find the ideal CME structure which gives the best performance in the MC-CDI system. EIS would be faster than placing different CME specimen inside a MC-CDI setup for evaluation of the performance. However, for CMEs, no precedent literature could be found where EIS was performed on CMEs, so it is not clear what the equivalent circuit model of CMEs is and thus also not how the performance of the CME could be predicted. The goal of the experiments in this Thesis is to find out what the EECM of CMEs is, and what the relation is between the electrochemical parameters determined with EIS and the performance indicators of the CME (permselectivity and membrane conductivity). The first step is to identify possible EECMs that could physically describe the electrochemical processes in the CME. The performance of the CME could not be estimated if it is not clear how the performance indicators are evaluated with EIS, so this is the second step in the methodology. In this context, this chapter describes the EIS experiments that will be performed to answer the research question, and on which CMEs the EIS experiments will be performed.

EIS experiments are performed with a (Biologic VSP-300) potentiostat on an EIS setup called the CME meter. The CMEs are fabricated according to a pre-determined recipe. The goal of the experiments is to investigate the two hypotheses described in this chapter. During EIS experiments, EIS data is collected between a pre-defined frequency range. The EIS data consists of 7 tables with frequency, real value of the impedance, imaginary value of the impedance, magnitude of the impedance, phase angle of the impedance, real value of the capacitance, and imaginary value of the capacitance. This data is converted into an Excel file. Then, a Python script was made to analyse the EIS data by fitting the impedance equation of the EECM through the EIS data. This script could be found in Appendix D. This Python script is able to construct Nyquist plot and Bode plots from the EIS data, and, subsequently, fit the impedance equations of five EECMs through the EIS datapoints and estimate the values of electrochemical parameters membrane resistance R and membrane capacitance C . The values of R and C are changed manually while the quality of fit (χ^2) is calculated.

3.1 CME electrode materials

Only freestanding CMEs are tested in the EIS experiments. Freestanding CMEs are CMEs made from electrode material slurry that has not been smeared and dried on a current collector. Freestanding CMEs must have greater mechanical strength than CDI electrodes because the slurry is not smeared onto a current collector. The CME therefore requires more polymeric binder (PVDF) than typical CDI electrodes (~40wt%) to ensure the CME will not break after the fabrication process. The required freestanding CMEs for all the EIS experiments are summarised in Table 3. In Chapter 4.2.3, the fabrication procedure of the freestanding CMEs is explained step for step.

For the experiments, the same freestanding CME with the same composition and thickness is investigated by performing EIS measurements on the CME: Standard CME, also called CME-S. In the first experiment, the EECM for CMEs is determined by performing EIS on CME-S. This freestanding CME will have a different thickness (CME-S35 and CME-S140) to determine the relationship between thickness and resistance for the second experiment. CME-S is also investigated to determine the permselectivity of the CME by charging CME-S at different potentials in the third experiment. For the last experiment, Experiment 4, freestanding CMEs with different compositions are tested in the CME meter to determine membrane conductivity and permselectivity. These four CMEs are compared with each other and CME-S to analyse the effect of the materials on the performance indicators. Four freestanding CMEs are fabricated for this experiment: CMEs with the same mass percentages as CME-S but with a different active material namely activated carbon (Activated Carbon YEC-8A), CMEs with a lower PVDF (Polyvinylidene Fluoride) mass percentage than CME-S, CMEs with a higher carbon black (Ketjenblack EC-600JD; Weber & Schaefer) percentage in the slurry than CME-S, and CMEs with a lower graphite (Mikro-Graphit 12 micron >99% C; ProGraphite GmbH Germany) mass percentage in the slurry than CME-S. Within these five freestanding CMEs (CME-S, CME-AC, CME-PVDF, CME-CB, and CME-G), the freestanding CME with the highest permselectivity and membrane conductivity is determined.

Table 3: The different mass composition of the CMEs fabricated for the experiments.

	Material Composition	Thickness	Weight per area	Used for experiments:
CME-S	Graphite 45wt% Carbon black 8wt% PVDF 47wt%	70µm	7.1 mg/cm ²	Hypothesis 1 → Experiment 1 Hypothesis 2 → Experiment 2 (relation t-R) Hypothesis 2 → Experiment 3 (Change Charge)
CME-S35	Graphite 45wt% Carbon black 8wt% PVDF 47wt%	30µm	4.9 mg/cm ²	Hypothesis 2 → Experiment 2 (relation t-R)
CME-S140	Graphite 45wt% Carbon black 8wt% PVDF 47wt%	140µm	17.7 mg/cm ²	Hypothesis 2 → Experiment 2 (relation t-R)
CME-AC	Activated carbon 45wt% Carbon black 8wt% PVDF 47wt%	370µm	29.1 mg/cm ²	Hypothesis 2 → Experiment 4 (AC vs G)
CME-G	Graphite 29wt% Carbon black 11wt% PVDF 60wt%	65µm	8.9 mg/cm ²	Hypothesis 2 → Experiment 4 (Standard vs less G)
CME-CB	Graphite 43wt% Carbon black 14wt% PVDF 43wt%	60µm	4.2 mg/cm ²	Hypothesis 2 → Experiment 4 (Standard vs more CB)
CME-PVDF	Graphite 60wt% Carbon black 10wt% PVDF 30wt%	60µm	5.7 mg/cm ²	Hypothesis 2 → Experiment 4 (Standard vs less PVDF)

3.2 Equivalent Electrical Circuit Model for CMEs

The goal of EIS is to model the impedance of an electrochemical system by constructing an equivalent electrical circuit model (EECM) from which an impedance equation is determined. This was also done for CDI electrodes and IEMs, where examples of EECMs could be found in, respectively, Figure 12 and Figure 13B [75,94,99]. As part of the EIS measurement process, the EECM of the freestanding CME must also be developed and the accuracy of fit tested. The Transmission-Line Model (TLM) was found to give a rather accurate impedance equation for porous CDI electrodes [101]. The TLM is also expected to be suitable for freestanding CMEs, as freestanding CMEs are made from the same materials as the CDI electrode and have a similar structure. Still, the TLM for CDI electrodes needs to be adapted for freestanding CMEs, because the ions in the CDI electrode are not able to move fully through the electrode, while for freestanding CMEs, the ions are able to flow through the CME. This “alternative” Transmission-line model for CMEs is described in the sections below. Of course, other models could fit the EIS data of freestanding CMEs, perhaps even more accurately than the TLM. Thus, different EECMs were developed. In the experiments, the accuracy of the fit of the different impedance equations were tested by calculating and comparing the quality of fit value χ^2 .

3.2.1 Transmission-line model

The most simple equivalent electrical circuit model to describe the movement and adsorption of ions into an electrode is denoted with an ideal capacitor in series with a resistor. This circuit is accurate for planar electrodes, however, it describes the behaviour of the ions that move into the pores of porous electrodes insufficiently. For CDI electrodes, the diffusion and adsorption of the ions into the pores is displayed in the Nyquist plot as a 45°-line which transitions in a vertical line. The Transmission-line model, for CDI electrodes, has firstly been developed by DeLevie (1963) to more accurately model the diffusion of ions inside the pores of porous electrodes [102]. The TLM represents the resistance in the porous electrode for the diffusion of electrons inside the carbon particles of the electrode, the diffusion of the ions inside the pores of the electrodes, and the adsorption of the ions which form the EDL. The TLM describes a porous electrode as a parallel schema of perfect circular and identical cylindrical pores filled with electrolyte [103]. The equivalent electrical circuit of the impedance in one cylindrical pore, according to the TLM, is depicted in Figure 14 [104]. In the figure, the ladder-like structure of this model is noticeable.

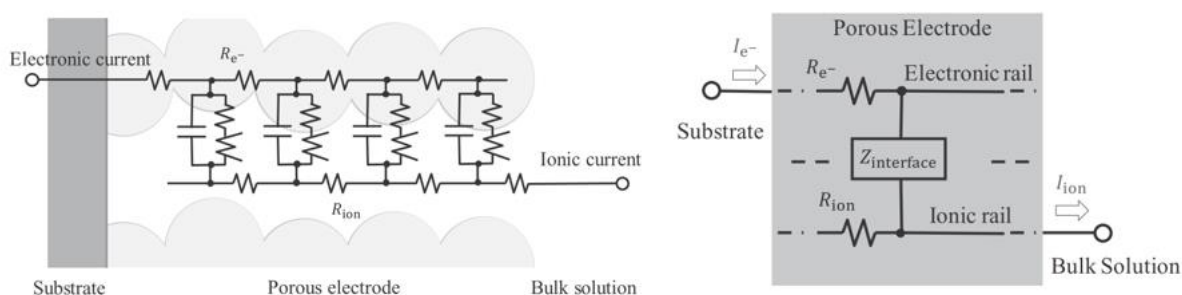


Figure 14: (left) The graphical scheme of the transmission-line model according to De Levie (1963) [102]. (right) The electronic rail and ionic rail are connected like a ladder by equivalent circuits which describe the interface impedance. The figures were retrieved from the research paper of Siroma et al. (2020) [104].

The TLM ladder-like structure consists of an electronic rail for the resistance of the electron transport through the carbon electrode, an ionic rail for the resistance of ion transport through the bulk solution, and the interface impedance to form the EDL. The interface impedance describes the interface process that occurs between an ion and a carbon particle, therefore repeats for every carbon particle, see Figure 14 [104]. The interface impedance is analogous to the step of the ladder. Examples of the interface impedance is depicted with one of the electrical circuits in Figure 15a, Figure 15b, and Figure 15c [104]. The electrical circuit of Figure 15a is chosen when an ideal double-layer capacitance is assumed, while the electrical circuit of Figure 15b more accurately describes the faradaic reactions at the interface

[104]. The electrical circuit visualised in Figure 15c is included as the interface equivalent circuit element of the TLM when the diffusion of the ions inside the particle is described [104].

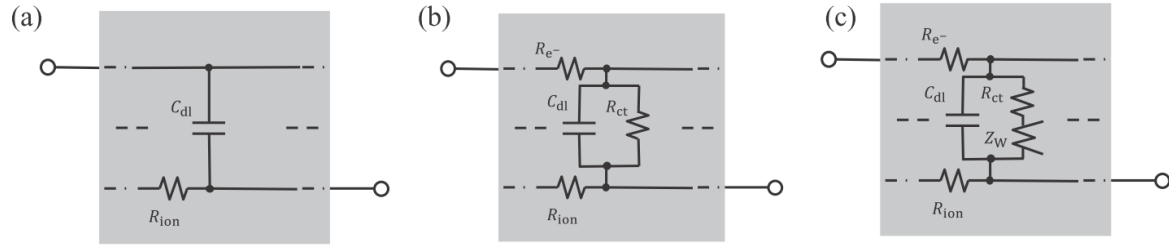


Figure 15: Equivalent circuits for the interface impedance: (a) ideal double layer capacitor, (b) faradaic reactions at the interface, (c) semi-infinite diffusion at the interface. Figure retrieved from the research paper of Siroma et al. (2020) [104].

The TLM could be simplified by assuming that the conductivity of one path is much higher than the conductivity of the other path. The path with the higher conductivity could be considered as a path without resistors. When this assumption is valid, the TLM is denoted as the one-path TLM [105]. As is shown in Figure 16, the conductivity of the electrons in the active material is assumed to be much larger than the conductivity of the ions in the electrolyte resulting in an electronic rail without resistors. The ionic resistance of the ionic rail on the ladder is separated with very small steps of repeating series placed resistors (δR), while the interface impedance is separated with very small steps of repeating parallel placed interface circuit elements (δZ_{eq}), see Figure 16a [106].

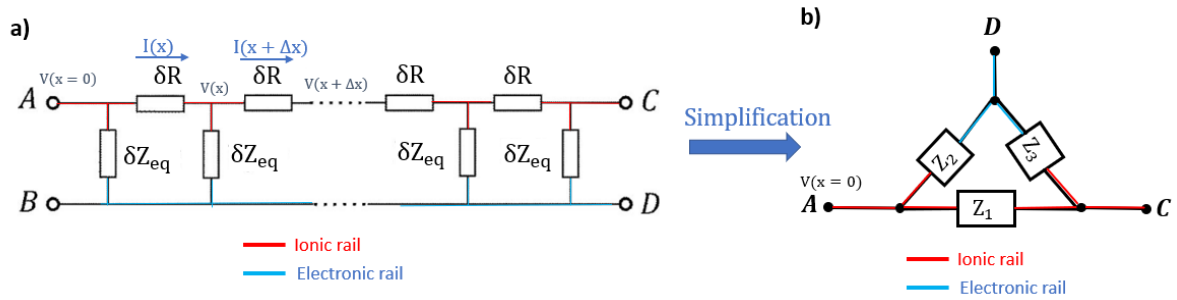


Figure 16: Electrical circuit of the finite Transmission-line model (TLM): (a) ladder-like hierarchical TLM, and (b) a simplified version of the electrical circuit of the TLM. The figure is modified from the original figure in the paper by Adamič et al. (2019) [106].

The ions move over the ionic rail (red lines in Figure 16) while the electrons move over the electronic rail (blue lines in Figure 16) [106]. The ladder-like structure of the TLM looks a bit complex, but it actually represents three different paths that the ions and electrons could take into the electrode structure. In the first path, the ions move from node A, through the resistors, to node C. The second path, the ions move from node A, though none or some resistors to the interface impedance element (see Figure 16a) [106]. The last path, the electrons move from node D to the interface impedance elements. Thus, the electrical circuit could be simplified by reducing the resistors and interface impedance blocks in three impedance blocks which describe the impedance of the electrons and ions in the electrode. In this electrical circuit, every path could be denoted with its own impedance block Z_i , as is illustrated in Figure 17b [106]. To make the electrical circuit conceptually even simpler, a $\Delta - Y$ transformation was performed, as shown in Figure 17b. In this circuit, the ions move from node A to node C through the impedance blocks z_A and z_B , while the electrons move from node D through impedance block z_C (see Figure 17b).

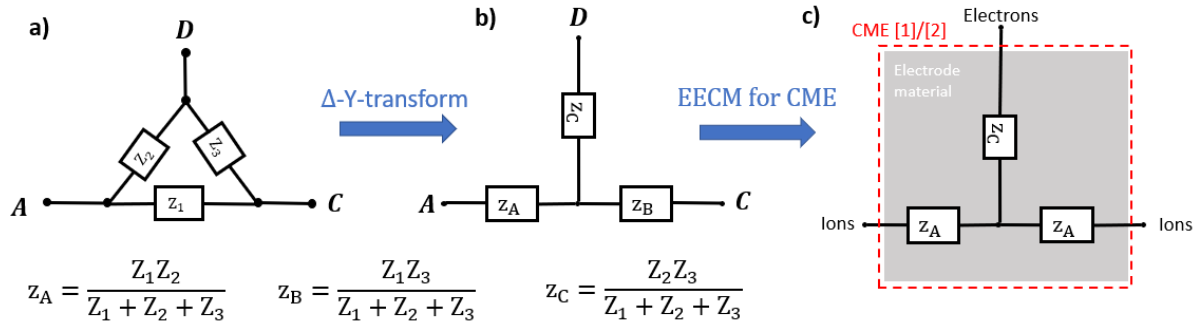


Figure 17: The electrical circuit of the Transmission-line model. (b) The Δ -Y transformation simplifies this circuit: the ions move through resistors z_A and z_B , while the electrons move through resistor z_C . (c) The equivalent electrical circuit model of the CME (EECM B: TLM), after assuming that the freestanding CMEs are homogeneous, $z_A = z_B$.

The impedance equation of the TLM is determined to fit through the EIS data. The impedance equation is derived from Kirchhoff's law by dividing the differential equation of the voltage ($V(x)$) by the differential equation of the current ($I(x)$) (Figure 16). In Appendix B, the derivation of the impedance equation of the Transmission-Line model is described in more detail. Boundary conditions are required to derive the impedance equation for the "alternative" TLM of the CME. The behaviour of the ions and electrons in the electrode structure determines the boundary conditions, and thus the impedance equation. The reflective boundary condition is applied to the TLM when the species are unable to diffuse through the electrode or are fully adsorbed in the EDL of the electrode. This boundary condition is applied for blocking electrodes, for example, CDI electrodes. With CDI electrodes, the electrode material is attached to a current collector that blocks the ions from leaving the electrode material. The impedance equation for blocking electrodes when the reflective boundary condition is applied is,

$$Z_{\text{TLM}} = \sqrt{R Z_{\text{eq}}} \coth \left(\sqrt{\frac{R}{Z_{\text{eq}}}} \right) \quad (3.1)$$

where R is the resistance in Ω , and Z_{eq} is the interface impedance. This impedance equation agrees with the transmission-line models derived in the papers of Siroma et al. (2020), Suss et al. (2013) and Huang et al. (2018) to describe the behaviour of the impedance inside porous CDI electrodes [96,101,104]. These papers only use different interface impedance equations, but they use the same impedance equation with the hyperbolic cotangent function. Figure 18a shows the electrical circuit in CDI electrodes when it is modelled according to the TLM with reflective boundary condition. The ions in the CDI electrode diffuse into the pores and are adsorbed in the active material (carbon) particles. The ions are not able to move out of the CDI electrode, because their movement is blocked when they reach the substrate (current collector). Therefore, the ions only move through one impedance block z_A , while the electrons move through the impedance block z_C , resulting in the electrical circuit showed in Figure 18a.

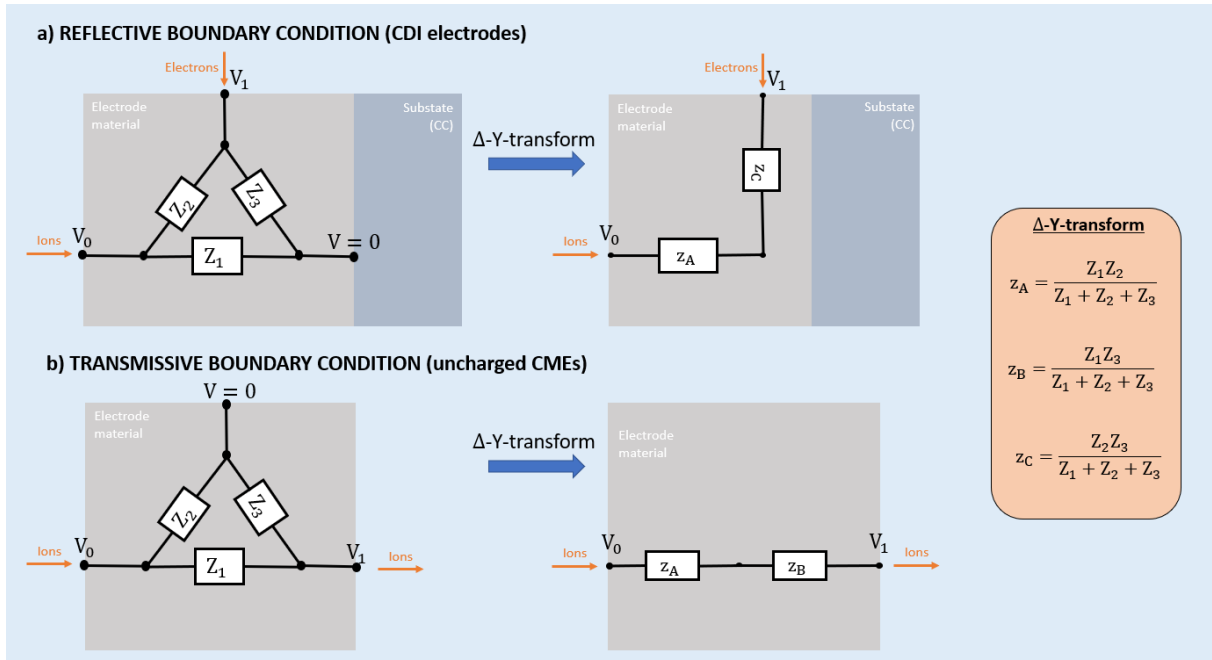


Figure 18: Equivalent electrical circuit representations of the Transmission-Line model in different electrode material structures: (a) Transmission-line model with reflective boundary condition for blocking electrodes, and (b) Transmission-line model with transmissive boundary condition for membranes made with carbon material.

If the ions are able to leave the other side of the porous electrode, then the transmissive boundary condition is applicable. The CME consists out of electrode material but acts as a membrane, so, the TLM describes the CME behaviour, where ions are adsorbed into the EDL or move fully through the thickness, when the transmissive boundary condition is applied. The derivation of the impedance equation with transmissive boundary condition is described in detail in Appendix B.2. The general impedance equation to describe uncharged CME is,

$$Z_{\text{TLM}} = \sqrt{RZ_{\text{eq}}} \tanh \left(\sqrt{\frac{R}{Z_{\text{eq}}}} \right) \quad (3.2)$$

where R is the resistance in Ω , and Z_{eq} is the interface impedance. The equivalent interface impedance is equal to an ideal capacitor ($Z_{\text{eq}} = \frac{1}{j\omega C}$) as it describes the electrical double layer formation in the pore of the electrode material. Figure 17c shows the resulting electrical circuit model for an CME, which is simplified by performing a $\Delta - Y$ transformation. The ionic current moves through blocks z_A and z_B , while the electrons move through block z_C . EIS experiments are only performed on freestanding CMEs, i.e. CMEs made from electrode material slurry that has not been smeared and dried on the current collector. The crystalline structure of the CME is assumed to be homogeneous in the x -, y -, and z -direction of the structure. When this assumption is valid, z_A could be assumed to be equal to z_B . When $z_A = z_B$, then the equations for the impedances in the TLM are,

$$z_A = \sqrt{RZ_{\text{eq}}} \tanh \left(\frac{1}{2} \sqrt{\frac{R}{Z_{\text{eq}}}} \right), \quad (3.3)$$

$$z_C = \sqrt{RZ_{\text{eq}}} \coth \left(\sqrt{\frac{R}{Z_{\text{eq}}}} \right) - \sqrt{RZ_{\text{eq}}} \tanh \left(\frac{1}{2} \sqrt{\frac{R}{Z_{\text{eq}}}} \right), \quad (3.4)$$

where R is the membrane resistance in Ω , and Z_{eq} is the interface impedance which is assumed to be equal to an ideal conductor with the impedance equation $\frac{1}{j(2\pi f)C}$ with C as the membrane capacitance in F and f the frequency in Hz. Equation 3.3 and Equation 3.4 are the impedance equations of the impedance blocks for, respectively, the ionic transport and the electronic transport. The resulting impedance equation is determined by the flow of the current through the CME. For any case, the freestanding CME is fully evaluated when the electrochemical parameters R and C are determined.

3.2.2 Equivalent electrical circuit model of the CMEs in the CME meter

With the CMEs being described by Transmission-line models, and the Transmission-line models being described by three separate impedances (z_A , z_A and z_C), we can proceed and model the full setup by an equivalent circuit. The CME-cell in the CME meter consist of stacked end electrodes (2x), spacers (3x) and CMEs (2x), as described in Chapter 4.1. The expected equivalent electrical circuit representation of the CME-cell is visualised in Figure 19. Note that the four electrodes in this circuit are each described by a TLM as well as a resistance R_{CT} and a capacitance C_{CT} to model the contact with the titanium current collector. The end electrodes act as CDI electrodes and the spacers only have a solution resistance. The impedance in the CME-cell could be measured in two different manners: 4-point measurement, or 2-point measurement.

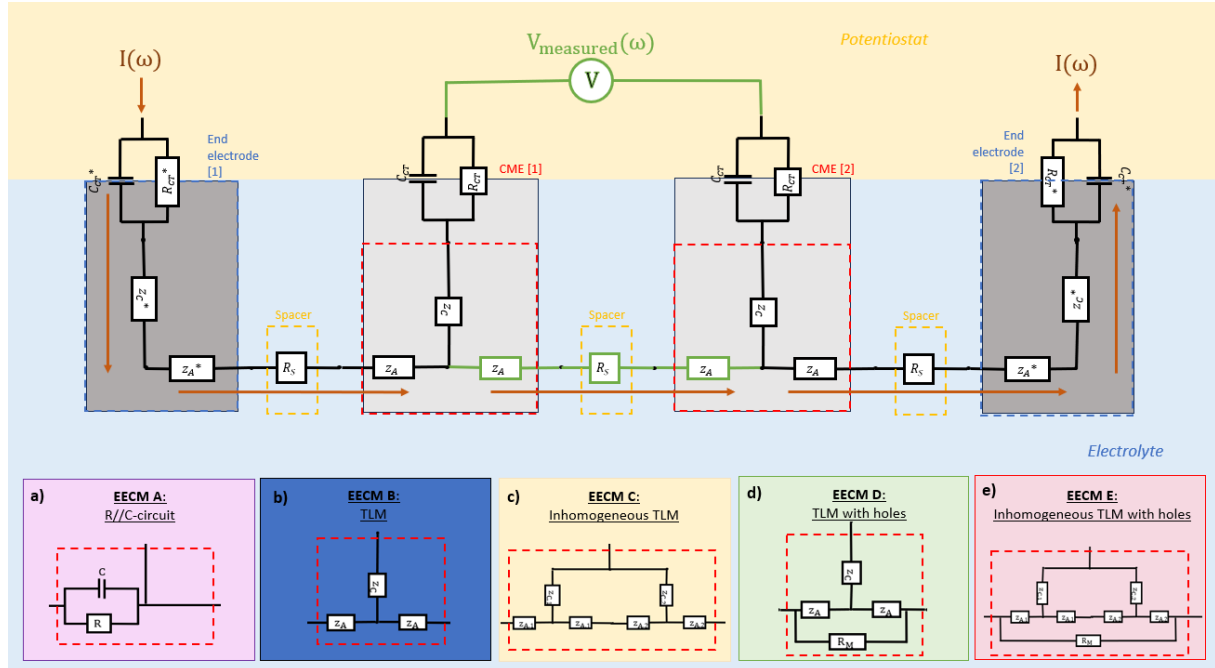


Figure 19: The predicted electrical circuit of the CME cell in the CME setup. The electrochemical behaviour of the CME could be modelled according to the TLM (EECM B). For a 4-point measurement, the current flows between the end electrodes and the potential is measured between the CMEs. In this case, the solution resistance R_s of the electrolyte in the spacer and the resistors z_A where the ions flow through are the only electrical circuit blocks that are measured (highlighted in green). In a 2-point measurement, the current flows between the CMEs and the response AC potential is measured between the CMEs. Now the contact resistance circuit, the solution resistance R_s and the resistance of the electrons z_C are measured. The 4-point measurement is preferred because the contact resistance is eliminated from the measurement. Other equivalent circuit models (EECM A, EECM C, EECM D and EECM E), whose electrical circuits are shown at the bottom of the figure in order of complexity, are also fitted through the impedance data of the CME to find the least complex but most accurate EECM. The circuit in the red dashed square is replaced by the other EECMs accordingly.

In the 4-point measurement, the current flows between the end electrodes and the potential is measured between the CMEs. Subsequently, the solution resistance R_s of the electrolyte in the spacer between the CMEs and the resistors where the ions flow through $2z_A$ are the blocks that are measured. The impedance equation is then,

$$\begin{aligned} Z_{4\text{-point}} &= 2z_A + R_s \\ &= 2\sqrt{RZ_{eq}} \tanh\left(\frac{1}{2}\sqrt{\frac{R}{Z_{eq}}}\right) + R_s, \end{aligned} \quad (3.5)$$

where R_s is the solution resistance. The resulting shape of the impedance equation in the Nyquist plot is shown in Figure 20a. Here, the plot starts with a 45°-line at high frequencies, which transitions into the semi-circle of an R//C-circuit at lower frequencies. The point, in the Nyquist plot, where the real axis is hit or the magnitude, in the Bode magnitude plot (Figure 20b), where the line converges to at lower frequencies gives the value for the electrochemical parameter R. The time taken for the ions to

travel through the CME is indicated by the peak in the Bode phase plot (Figure 20c). This value is denoted with the transport time constant τ_t , which is calculated by the following equation: $\tau_t = RC$.

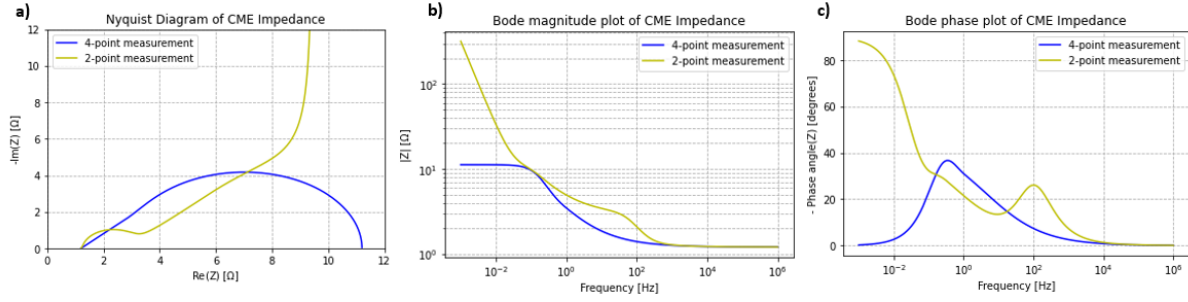


Figure 20: The (a) Nyquist plot, (b) Bode magnitude plot, and (c) Bode phase plot when a 4-point measurement (blue) and 2-point measurement (yellow) are conducted. Modelled with the impedance equation of the Transmission-line model (EECM B). Here, $R=2.2\Omega$, $C=0.5F$, $R_{CT}=0.8\Omega$, $C_{CT}=0.003F$, and $R_S=1.2\Omega$.

In the 2-point measurement, the current flows from the first CME to the second CME and the potential is also measured between the two CMEs (see Figure 19). Here, not only the solution resistance R_S and resistance for the ion movement z_A are measured, also the contact resistance and the resistance of the electron movement are measured. The impedance equation is then,

$$\begin{aligned} Z_{2\text{-point}} &= 2Z_{CT} + 2z_C + 2z_A + R_S \\ &= 2 \left(\frac{R_{CT}}{1 + R_{CT}C_{CT}j\omega} \right) + 2\sqrt{RZ_{eq}} \coth \left(\sqrt{\frac{R}{Z_{eq}}} \right) + R_S, \end{aligned} \quad (3.6)$$

where R_S is the solution resistance, Z_{CT} is the impedance caused by the contact between the titanium current collector and the end electrode, C_{CT} is the contact capacitance and R_{CT} is the contact resistance. The Nyquist plot in Figure 20a shows that there is a difference in the shape of the impedance equation for the 2-point and 4-point measurements. The 2-point measurement starts, in the Nyquist plot in yellow, with a semi-circle which denotes the contact resistance between the current collector and the cables of the potentiostat. The values of C_{CT} and R_{CT} are determined from the semi-circle in the Nyquist plot and the solution resistance is determined directly from the conductivity in the electrolyte ($R_S = \frac{t}{A\kappa}$). In the 2-point measurement, there are three processes which could be analysed in the Nyquist plot: (1) the electronic behaviour between the current collector and the cables, showed as a semi-circle at high frequencies, (2) diffusion of the ions into the pores of the CME, showed as a 45°-line in the Nyquist plot, (3) the formation of the EDL at the CME interface, shown as a vertical line going to infinity at low frequencies.

So, both the 4-point and 2-point measurements could be used to determine the two electrochemical parameters capacitance C and resistance R . However, the 4-point measurement is preferred because the contact resistance is removed from the EIS measurement, as is visualised in Figure 20 with the absence of the first semi-circle at high frequencies. The 4-point measurement illustrates the transmissive behaviour of the ions, in which we are interested, while the 2-point measurement shows the contact resistance and the capacitive behaviour of the CME, which is not of great interest for our Thesis project. The transmissive behaviour says something about the performance indicators (membrane conductivity and permselectivity) of the IEM, which are the same indicators for CMEs, while the 2-points measurement gives information to determine the performance indicators of CDI electrodes. The 4-point measurement therefore provides more information to investigate the transmission behaviour and will be used for the following EIS experiments.

3.2.3 Alternative models for CME impedance equation

The Transmission-line model is not the only EECM which could fit accurately through the EIS data. To decide whether the TLM accurately describes the behaviour inside the CME, more models are developed and fitted through the EIS data. It is not clear, yet, which impedance equation could

accurately fit through the EIS data of the CMEs, however, what is sure is that more complex Transmission-line models give an impedance equation which could fit better through the EIS data than the TLM, simply because they have more circuit elements [107]. Still, the Hypothesis is that the Transmission-line model gives an impedance equation which is accurate to fit the EIS data of the CME in the CME meter.

Hypothesis 1: The CMEs are accurately modelled with the transmission-line model and the electrochemical parameters that describe the model reflect this.

In the bottom of Figure 19, different EECMs are displayed that were fitted through the EIS data. The electrical circuits replace the Transmission-line model inserted in the dashed red square in the circuit of the CME. The first circuit is the simpler R//C-circuit (EECM A), which does not have a separate flow for the electrons and the ions, so it does not fit one-to-one into the red dashed square. If we look at the R//C-circuit, the ion branch, where the ions go out of the CME, and the electron branch, where the electrons go into the CME, follow the same branch (output branch) in the R//C-circuit. The ions enter the CME via the input branch. The electrons then go into one side of the capacitor, while the ions can go into the other side of the capacitor or leave the branch via the resistor. The circuit representing the R//C-circuit is shown in Figure 19a. Figure 21 shows the Nyquist and Bode plots of the impedance equations of the R//C-circuit (EECM A) and the Transmission-line model (EECM B). The Nyquist plot of the Transmission-line model shows a 45°-line at high frequencies that transitions in a semi-circle, while the R//C-circuit gives a semi-circle (Figure 21a). The Bode phase plot in Figure 21c shows that the peak of the TLM and R//C-circuit occur at different frequencies when the electrochemical parameters (R and C) are equal, resulting in the R//C-circuit having a higher transport time constant value τ_t than the TLM. The impedance equation of the R//C-circuit is,

$$Z_{\text{EECM A}} = R_S + \frac{R}{1 + RC(j2\pi f)}, \quad (3.7)$$

where R_S is the solution resistance, R is the membrane resistance in Ω , C is the membrane capacitance in F, and f the frequency in Hz. The impedance equation of the Transmission-line model of EECM B is,

$$Z_{\text{EECM B}} = R_S + 2\sqrt{\frac{R}{(j2\pi f)C}} \tanh\left(\frac{1}{2}\sqrt{(j2\pi f)RC}\right) = R_S + 2z_A, \quad (3.8)$$

where R_S is the solution resistance, R is the membrane resistance in Ω , C is the membrane capacitance in F, f the frequency in Hz, z_A is the general impedance equation of the TLM for ion transport calculated with Equation 3.3 in Ω .

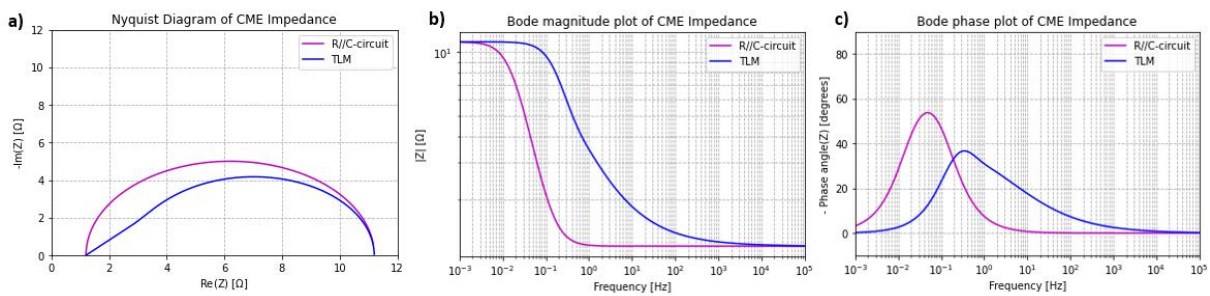


Figure 21: (a) Nyquist plot, (b) Bode magnitude plot and (c) Bode phase plot of the impedance equation of the “EECM A: R//C-circuit” (purple line) and the “EECM B: TLM” (blue line). The parameters in the impedance equations are equal, $R=10\Omega$ and $C=1.0F$.

If the electrode material slurry was dried in air during the construction of the CME, the crystalline structure of the CME may not be homogeneous. The difference in evaporation of the solvent (acetone) could result in a layered structure of the CME. The ions can be thought of as moving in two different electrode materials in succession, representing the movement through two Transmission-line models, placed in series, with separate R and C values, see EECM C in Figure 19c. The impedance equation is shown in Figure 22 in green and has the following equation,

$$Z_{\text{EECM C}} = R_S + z_{A,1} + \frac{z_{C,1}(z_{A,1} + z_{A,2})}{(z_{A,1} + z_{A,2}) + (z_{C,1} + z_{C,2})} + z_{A,2} + \frac{z_{C,2}(z_{A,1} + z_{A,2})}{(z_{A,1} + z_{A,2}) + (z_{C,1} + z_{C,2})}, \quad (3.9)$$

where R_S is the solution resistance, $z_{A,1}$ and $z_{C,1}$ are the general impedance equations of the TLM (Equation 3.3 and Equation 3.4) with values R_1 and C_1 which describe the resistance to ion transport in the first electrode material of the CME in Ω , and $z_{A,2}$ and $z_{C,2}$ are the general impedance equation of the TLM (Equation 3.3 and Equation 3.4) with values R_2 and C_2 describing the resistance to ion transport in the second electrode material in Ω . The impedance equation was derived by applying the $\Delta - Y$ transformation in the electrical circuit of Figure 22c. The inhomogeneous TLM consists, in the Nyquist plot, of two transmission-line semi-circles. When the R_1 and C_1 are approximately at the same values as R_2 and C_2 , then the two separate transmission-lines merge into one transmission-line with a dent, see the green line in Figure 22a. The inhomogeneous TLM gives two peaks in the phase plot, see Figure 22c.

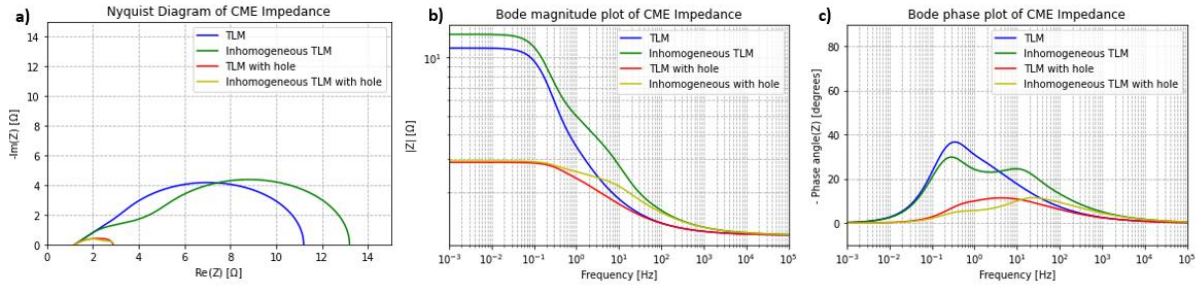


Figure 22: Transmission-line model impedance equation plotted inside (from left to right) the Nyquist plot, Bode magnitude plot and Bode phase plot for four different EECMs with TLM. “EECM B: TLM” is the Transmission-line model (blue line), “EECM C: Inhomogeneous TLM” is the model with two Transmission-line models in series with each other to denote the two-layered CME, “EECM D: TLM with hole” is the model with a Transmission-line model and a resistor for the ion transport through macropores, and “EECM E: Inhomogeneous TLM with hole” is the model of EECM C with a resistor for the ion transport through macropores. Here, $R=R_1=10\Omega$, $C=C_1=1.0F$, $R_2=5.0\Omega$, $C_2=0.2F$, $R_M=2.0\Omega$, and $R_S=0.24\Omega$. These plots result from 4-point measurements.

The CME could be inhomogeneous in the x,y -plane. This represents the case of “leaky” CMEs that have holes that allow some additional ionic current to pass through the electrode. In this case, the structure is not homogeneous. The electrical circuit then becomes like shown in Figure 19Figure 22d, and it can be calculated that the measured impedances become,

$$Z_{EECM D} = R_S + 2 \frac{R_M z_A}{2z_A + R_M}, \quad (3.10)$$

where R_S is the solution resistance, z_A and z_C are the general impedance equations of the TLM (Equation 3.3 and Equation 3.4) with values R and C which describe the resistance to transport in the electrode material of the CME in Ω , and R_M is the resistance in the hole or macropores in Ω . Also here, the $\Delta - Y$ transformation was performed to derive the impedance equation from the electrical circuit in Figure 19d. The Nyquist plot and Bode plots of the impedance equation of the TLM of this special case are shown in red in Figure 22. The resistor R_M reduces the magnitude of the semi-circle of the TLM in the Nyquist plot. Also, the 45° slope line at the start of the semi-circle, for TLM and inhomogeneous TLM, is for the TLM with hole smaller than 45° .

Finally the structure of the CME could be a combination of the heterogeneous electrode material in the z -direction and some holes, e.g. a combination of EECM C and EECM D. This circuit, EECM E, representing this case is shown in Figure 19e. Physically, this circuit describes that the CME consists of two layers, each described by the TLM, and consists of macropores where the ions could easily flow through. The Nyquist plot and Bode plots of the impedance equation of the TLM of this special case are shown in yellow in Figure 22. The $\Delta - Y$ transformation was performed (twice) to derive the impedance equation of EECM E. When $Z_{E1} = z_{A,1} + \frac{z_{C,1}(z_{A,1}+z_{A,2})}{(z_{A,1}+z_{A,2})+(z_{C,1}+z_{C,2})}$ and $Z_{E2} = z_{A,2} + \frac{z_{C,2}(z_{A,1}+z_{A,2})}{(z_{A,1}+z_{A,2})+(z_{C,1}+z_{C,2})}$, then the impedance equation of the inhomogeneous TLM with holes (EECM E) is,

$$Z_{EECM E} = R_S + \frac{R_M Z_{E1}}{Z_{E1} + Z_{E2} + R_M} + \frac{R_M Z_{E2}}{Z_{E1} + Z_{E2} + R_M} \quad (3.11)$$

where R_S is the solution resistance, $z_{A,1}$ and $z_{C,1}$ are the general impedance equations of the TLM (Equation 3.3 and Equation 3.4) with values R_1 and C_1 which describe the resistance to ion transport in the first electrode material of the CME in Ω , $z_{A,2}$ and $z_{C,2}$ are the general impedance equation of the TLM (Equation 3.3 and Equation 3.4) with values R_2 and C_2 describing the resistance to ion transport in the second electrode material in Ω , and R_M is the resistance in the hole or macropores in Ω . The impedance plots in Figure 22 of the inhomogeneous TLM with hole shows the same shape as the inhomogeneous TLM. The inhomogeneous TLM with hole has a lower overall resistance, because the plot hits the real impedance axis at a lower resistance than the inhomogeneous TLM, see Figure 22a. The macropore resistor R_M affects the magnitude of the impedance, as is showed in Figure 22b.

3.3 Relation between electrochemical parameters and performance indicators

For IEMs and CDI electrodes, it is already clear what the electrochemical parameters, determined with EIS, are that give an indication of the performance of the specimen and how it influences these performance indicators. In the chapters Theoretical framework (Chapter 2) and fundamentals of EIS (Appendix A), the relation between the electrochemical parameters and the performance indicators for electrodes in CDI and IEMs in ED are explained separately. If this relation is clear, then the performance of the specimen could be evaluated based on the shapes in the corresponding EIS plots or the value of the electrochemical parameters. For CMEs, this relationship is investigated. The electrochemical parameters are the membrane capacitance C in the TLM, and the value of the membrane resistance R in the TLM. The performance indicators are permselectivity and membrane conductivity. The membrane conductivity is determined directly from the electrochemical parameter membrane resistance, however, the relation between the permselectivity and the electrochemical parameters is still unclear.

3.3.1 Relation between permselectivity and electrochemical parameters

For CDI electrodes, a higher double layer capacitance C_{dl} improves the performance [19], while for CMEs, the influence of the membrane capacitance C on the performance is not clear. Still, the behaviour of the ions through an CME is expected to be similar to the behaviour of ions through ion-exchange membranes. For ion-exchange membranes, an important parameter is the transport time constant (τ_t), calculated from the value of the capacitance and resistance, which indicates the counter-ions transport in the membrane, according to Jiang et al. (2019) [26]. The performance indicator permselectivity is defined as the ability of the IEM to transport counter-ions through the IEM while excluding the transport of co-ions [63]. The transport constant is expected to have the same relation with the permselectivity for the CME as for the IEM: how lower the time constant, how higher the permselectivity. As was stated earlier, the time constant could be calculated with the following equation: $\tau_t = RC$.

The transport time constant could give an indication of the permselectivity, and would be an important value when the permselectivity of different CMEs are compared with each other. However, it would be very interesting if the actual value of the permselectivity could be calculated with EIS measurements. Therefore, an equation for calculating the permselectivity was derived. To calculate the permselectivity, the electrochemical parameters are determined from the fitting of the impedance equation of the Transmission-Line Model in the EIS data of the charged and uncharged CME. When the CMEs are charged, a potential has been applied between the CMEs and the end electrodes. The CME is then more positively or negatively charged, resulting in more counter-ions in the structure of the CME, while the co-ion concentration in the structure decreases [73]. As the amount of counterions in the structure increases, the resistance to counterion transport decreases. The resistance of the co-ions is assumed to be constant. The difference in the resistance in counter-ion transport and co-ion transport makes the CME (perm)selective, which is a key function of the CME in the MC-CDI system. If

the membrane resistance is assumed to be the effective resistance of the parallel resistances of the counter-ions and the co-ions in the CME, then the reduced resistance to counter-ion movement results in a lower membrane resistance. When the CME is made more negative or positive, the membrane resistance decreases and the permselectivity of the CME increases. Thus, the membrane resistance of the CME could be used to determine the permselectivity of the CME. It is therefore necessary to determine the electrochemical properties of the CME when it is uncharged and when it is charged. The equation for the permselectivity is,

$$P_+ = \frac{R_C}{R_N} - 1 \text{ and } P_- = 1 - \frac{R_C}{R_N}, \quad (3.12)$$

where P_- is the permselectivity of the cations when the applied potential difference between the CMEs and the end electrodes is negative, P_+ is the permselectivity of the anions when the applied potential difference between the CMEs and the end electrodes is positive, R_N is the membrane resistance of the uncharged CME determined from the EIS measurement in Ωcm^2 , and R_C is the membrane resistance of the charged CME determined from the EIS measurement in Ωcm^2 . The derivation of this equation could be found in Appendix C. The permselectivity of positive charged CME is P_+ , which lays between -1 and 0 , so denotes the selectivity of the anions. The permselectivity of negative charged CME is P_- , which lays between 0 and 1 , so denotes the selectivity of the cations. Charging the CME has not only an effect on the membrane resistance, but also the membrane capacitance C is affected. As the applied potential deviates from the point of zero charge of the CME, the adsorption of counter-ions in the EDL increases [44, 45]. At low ion concentrations in the electrolyte, the capacitance increases, resulting in a higher membrane capacitance for charged CMEs than for uncharged CMEs [40].

Hypothesis 2: The induced permselectivity of the CME, by applying a potential between the CME and the end electrode, could be determined by performing EIS on a charged and uncharged CME, as the charging of the CME affects the electrochemical parameters, i.e. membrane capacitance C and membrane resistance R .

3.3.2 Relation between membrane conductivity and electrochemical parameters

The membrane conductivity is defined as the mobility of the ions through the CME when an external electrical field is applied over the CME [66]. The performance indicator membrane conductivity is calculated with the following equation,

$$\kappa_m = \frac{t}{RA}, \quad (3.13)$$

where κ_m is the membrane conductivity of the CME in S/cm , t is the thickness of the CME in cm , RA is the area resistance of the CME in Ωcm^2 [64]. The area resistance is the electrochemical parameter membrane resistance R which is the electrochemical parameter estimated from the impedance equation of the Transmission-Line Model. The conductivity is higher, when the membrane resistance R of the CME is lower, according to the equation $\kappa_m = \frac{t}{RA}$. The membrane conductivity is thus directly determined when the electrochemical parameter membrane resistance (R) is estimated from the EIS measurement. Other researchers have also determined the membrane conductivity (of ion-exchange membranes) using EIS in this way, for example, Díaz & Kamcev (2021), Zheng et al. (2012), and Park et al. (2006) [66, 97, 108].

3.4 Experimental plan

The hypotheses are tested by performing some EIS experiments on predefined CMEs. The first hypothesis concerns the EECM of CMEs. The most accurate (and less complex) EECM for CMEs is expected to be the transmission line model (EECM B). Some EIS experiments are performed to fit the impedance equation of different EECMs to the EIS data and to determine the quality of the fit. Operational parameters are also varied to investigate if and how they affect the EIS measurement.

For the second hypothesis, the relationship between permselectivity and electrochemical parameters is investigated. The performance indicator permselectivity is determined by performing EIS experiments on the charged and uncharged CME. The relationship between the other performance indicator, membrane conductivity, is already known, but EIS experiments are carried out to verify this relationship. Finally, CMEs with different material compositions, resulting in different electrode structures, are determined by EIS to find the CME material with the structure that gives the highest performance indicators. During these experiments, the operational properties are kept constant. The temperature is constant at 25°C for every EIS experiment, just like the majority of the researchers did (see Table 11). The mixing speed is kept low and constant because this also has an effect on the EIS measurements. The concentration in the electrolyte is kept constant at 960mg/L, which is the average salt concentration of brackish water (salinity of 1.5 dS/m) [109]. Brackish water consist mostly out of NaCl, however, the diffusion coefficient of Cl^- is twice as large as the diffusion coefficient Na^+ [110]. Two reversely charged ions with similar diffusion coefficient would be better when the electrochemical properties of the same CME are compared for positive and negative charge, thus, for theoretical purposes, the electrolyte consist out of the ions K^+ and Cl^- which have a similar diffusion coefficient [111]. The flow rate is also an operational parameter and is kept constant at 8mL/min. In the next sub-sections, every experiment is explained in more detail.

3.4.1 Experimental plan for determining the EECM of the CMEs

To determine the EECM for the CMEs, freestanding CMEs are placed inside the CME meter where EIS is performed to construct a Nyquist plot and Bode plots from the EIS data, and, subsequently, fit the impedance equations of five different EECMs through the plots and estimate the values of electrochemical parameters resistance R and capacitance C . Only freestanding CMEs were placed inside the CME meter. 4-point EIS experiments were repeatedly conducted for determining the EIS data of CME-S. The impedance equations of five EECMs, mentioned in Chapter 3.2.1, were fitted in the EIS data: $R//C$ -circuit, TLM, inhomogeneous TLM, TLM with hole, and inhomogeneous TLM with hole. The impedance equations are fitted in the plots by using the *curvefit* command in Python which generates the values of the parameters (C and R) of the impedance equations. Subsequently, the quality of fit χ^2 is calculated according to Equation 3.14,

$$\chi^2 = \sum_{i=1}^{2n} \frac{(y_i - f(y_i))^2}{f(y_i)} * \frac{1}{\sigma_i^2} \quad (3.14)$$

where y_i is the experimental datapoint at frequency i , $f(y_i)$ is the expected value of the datapoint calculated with the impedance equation of an EECM at frequency i , σ_i is the variance of the datapoint at frequency i , and n is total number of frequencies where a measurement has been conducted [112]. The EECM is accepted as the “right” model when the value of the quality of fit χ^2 is smaller than 10^{-3} , because the error of the fit is than smaller 1% [113,114]. To calculate the quality of the fit, the value of the standard deviation (σ_i^2) is necessary. Therefore, the EIS measurement was repeated to determine the mean and standard deviation of the impedance at every frequency. To ensure that the chosen TLM is a good model for predicting the impedance of a CME, additional EIS experiments are performed on CME-S, only now the operational properties are varied. The operational parameters are changed to understand the effect of those operational parameters on the EIS measurement and the see if the chosen EECM impedance equation still fits through the EIS data with a certain accuracy ($\chi^2 < 10^{-3}$). The operational properties that are varied are: temperature, salt concentration in the electrolyte,

mixing rate, and flowrate. The composition of the electrolyte is also an operational parameter, however it is kept constant during these experiments, because the electrolyte will only consist out of the ions K^+ and Cl^- . The flowrate and mixing rate are expected to have no effect on the EIS measurement, while the temperature and concentration in the electrolyte have affect the EIS measurement. During the EIS experiment, one of the operational parameters is changed while the others are kept constant at a certain value. The temperature is kept constant at 25°C, concentration of the electrolyte is kept constant at 12.9mM, flowrate is kept constant at 8.0mL/min, and mixing rate is kept on 2.5. The varied operational parameter is changed and compared for three different values with the same interval. So, for example, EIS experiments are conducted on the same CME samples for a temperature of 25°C, 30°C, and 35°C, while the other operational variables are kept constant.

3.4.2 Experimental plan for relation between resistance and thickness

Another property that may have a large influence on the shape of the Nyquist plot is the thickness of the CME. According to the literature, the resistance increases linearly as the thickness decreases and the slope is the membrane conductivity. The conductivity inside the membrane is therefore a material property. The first part of Experiment 2 tests this relationship to ensure that it is also correct for CMEs. EIS experiments are performed on CMEs with the same composition but different thicknesses. The operating parameters are held constant. The values of the electrochemical parameters are determined from the EIS data. The membrane conductivity is calculated for every CME with the electrochemical parameter membrane resistance R in Ωcm^2 . The membrane conductivity should be of approximate equal value to conclude that the relationship between thickness and resistance is linear and that the slope of the line is equal to the membrane conductivity.

3.4.3 Experimental plan for determining the permselectivity

To test Hypothesis 2, EIS is performed at different applied potentials, at the same thickness and composition of the CME. To this extent, CMEs with a composition of the standard CME (CME-S) are fabricated where the permselectivity is expected to change by changing the applied potential on the CMEs. Prior to the EIS experiment, a potential is applied on both CMEs with the Voltcraft® Laboratory Power Supply PS-2403D. The potentials that are applied are $-1.0V$, $-0.5V$, $0V$, $+0.5V$, and $+1.0V$. After 30 minutes, the potential differences between the CMEs and the Ag/AgCl reference electrode and between the CMEs and the end electrodes are measured. After 5 minutes, the EIS experiment is conducted, because the system first need to reach steady-state at the new charge. The fitted membrane resistance R of the charged and uncharged CMEs are used to calculate the permselectivity and the transport time constant of the uncharged CME is calculated.

3.4.4 Experimental plan for relation between CME structure and performance

The CME is a membrane that consists out of active material, conductive additives and a polymeric binder. The standard CME (CME-S) is made from the active material graphite (Mikro-Graphit 12 micron >99% C; ProGraphite GmbH Germany), conductive additive carbon black (Ketjenblack EC-600JD; Weber & Schaer), and polymeric binder PVDF (Polyvinylidene Ambofluor). The influence of the structure of the CMEs on the performance parameters is investigated by performing EIS experiments and comparing the results with CME-S. First, the active material is changed from graphite to activated carbon without changing the mass percentages. The performance parameters and the time constant τ of the active carbon CME and the graphite CME are compared. The other CMEs will be made of graphite as active material, but the mass percentages are varied to see the effect of the active material, conductive additives and a polymeric binder on the CME performance. Thus, one CME with a lower graphite percentage (half the mass of graphite in the slurry than CME-S), one CME with a lower PVDF percentage (half the mass of PVDF in the slurry than CME-S), and one CME with a higher carbon black percentage (twice the mass of carbon black in the slurry than CME-S) are investigated with EIS.

The thickness was approximately equal ($\sim 65\mu\text{m}$). The fabricated CMEs with the corresponding mass percentages are denoted in Table 3.

For these constructed CMEs, the permselectivity and membrane conductivity are determined by performing multiple EIS experiments. EIS experiments on uncharged CMEs result in the value of the membrane conductivity. Then, EIS experiments are carried out on the same CMEs, however, they are now charged for 30 minutes with first -1.0V and then $+1.0\text{V}$. From the values of the membrane resistance R and the membrane capacitance C of the charged and uncharged CMEs, the permselectivity is calculated. The transport time constant of the uncharged CME-S is compared with the transport time constant of other CMEs to check if the permselectivity is actually higher if the transport time constant is lower.

4

Design and Construction of the CME meter

The multi-channel capacitive deionisation (MC-CDI) system is able to continuously desalinate brackish water. The capacitive membrane electrode (CME) inside the MC-CDI system determines the performance of the system, so after establishing that the system works, the CME materials and compositions are varied to find the CME that maximises the performance of MC-CDI. This trial-and-error process takes many hours and is not efficient. EIS could be an alternative method to determine the internal processes that happen inside the CME and could pose as a faster method to find the optimal CME structure for the MC-CDI system. For EIS, an equivalent electrical circuit model needs to be found, and, after that, the electrochemical properties that maximises the performance indicators of the CMEs could be evaluated. To answer to research question of this Thesis project, electrochemical properties of CMEs and the performance indicators of those CMEs are determined by conducting EIS experiments. Therefore, it is necessary to build a setup where EIS experiments can be performed on the CMEs, and to fabricate different CMEs with different compositions and thicknesses. This EIS setup, where CMEs are studied with EIS, is called the CME meter (Capacitive Membrane Electrode impedance meter).

This chapter is divided into three parts. Firstly, the design choices of the CME meter are explained and the 3D CAD model is shown (Section 4.1). Secondly, the manufacturing process of the components and the assembly of the CME meter is described in Section 4.2. Also the fabrication procedure of the pre-defined CMEs is briefly explained in Section 4.2.3. The material and composition of the manufactured pre-defined CMEs are defined in Table 3. Lastly, the CME meter was tested and an operating manual for the CME meter was prepared. The test plan with results can be found in Section 4.3.

4.1 Design of the CME meter

An electrochemical impedance spectroscopy (EIS) setup is built to determine the electrochemical processes of capacitive membrane electrodes (CMEs) happening at the interface by separating the electrochemical processes at different timescales. This EIS setup is called the CME meter. The design of the CME meter is explained in detail in this section. The final design is visualised in a Fusion 360 model in Section 4.1.3.

4.1.1 Programme of Requirements

The CME meter is a setup with which EIS experiments could be performed on capacitive membrane electrodes (CMEs). Figure 23 shows a schematic of the EIS setup for characterising CMEs. The CME meter consists of:

- **Potentiostat**, which performs the EIS experiments. The potentiostat applies an input AC signal and measures the AC response signal. The output of the potentiostat is EIS data consisting out of a table with seven columns: frequency, real impedance, imaginary impedance, magnitude of the impedance, angle of the impedance, real capacitance, and imaginary capacitance. The potentiostat must perform 4-point EIS measurements on the CMEs inserted in the CME-cell.
- **CME-cell**, where the CME samples are placed and inspected. The CME-cell is the system in which the CME samples are placed and pressed against a current collector. The cables of the potentiostat are connected to the current collectors. Then, the potentiostat could perform 4-point EIS experiments on the CMEs. The CME-cell must be re-usable, only the CME are replaceable. CMEs with different thicknesses and varying material compositions are able to be placed inside the CME-cell. For comparison of the EIS experiments on different CMEs, the rest of the stack in the CME cell must be fixed to ensure that the differences in the EIS measurement are only the result of the new CME in the cell. The CME cell must be leak tight, in the sense that the electrolyte must only be able to follow a predefined flow path.
- **Reservoir**, where the incoming electrolyte from the CME-cell comes from and where the outgoing electrolyte from the CME-cell goes to. The reservoir acts as a tank in which the salt concentration is controlled during the EIS measurement, as the concentration must be constant. The reservoir also acts as a thermal bath where the temperature is controlled.
- **Pump**, controls the flowrate of the electrolyte into the electrochemical cell.
- **Conductivity meter**, is used as a check, for example, to ensure that the salt concentration of the electrolyte stays constant during the EIS measurement.
- **Laptop**, used to collect the EIS data and process the EIS data into impedance plots (Nyquist and Bode plots). The EIS data is stored on the laptop as an Excel file and a Python script is used to convert it into the required impedance plots. The laptop is also used to visualise the measured conductivity of the electrolyte using the conductivity meter.
- **Power supply**, to charge the CMEs. To measure the permselectivity of the CME, the CMEs must be made selective. The CMEs are selective, for cation or anion transport, when the CME is, respectively, negatively charged or positively charged. The power supply applies a controllable DC potential to charge the CMEs.

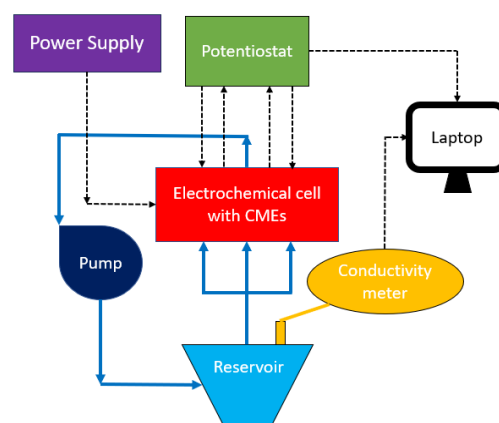


Figure 23: Schematic representations of the CME meter: electrochemical impedance spectroscopy setup for investigating CMEs.

4.1.2 Concept of the CME meter

The CME meter is a system that consists of the following sub-systems: potentiostat, power supply, CME cell, pump, conductivity meter, reservoir and laptop. A schematic of the system is visualised in Figure 24. The requirements and design choices for the sub-systems are given in the next sub-sections.

4.1.2.1 Potentiostat and power supply

The potentiostat should apply AC potential signals with frequencies between 0.001Hz and 1MHz with an perturbation amplitude of 5mV. These values correspond with the chosen frequencies and amplitudes in the literature, see Table 11. The available EIS potentiostat is the BioLogic VSP-300 stationed in the electrochemical lab of the Process and Energy department, see Figure 24 [115]. This measurement system is capable of performing EIS on multiple setups (6 in total). It has 6 electrode connections: two clamps to apply the current (P1+P2), two clamps to measure the response (S1+S3), one clamp for the reference electrode (S2), and one ground connection



Figure 24: The EIS potentiostat Biologic VSP-300 [115].

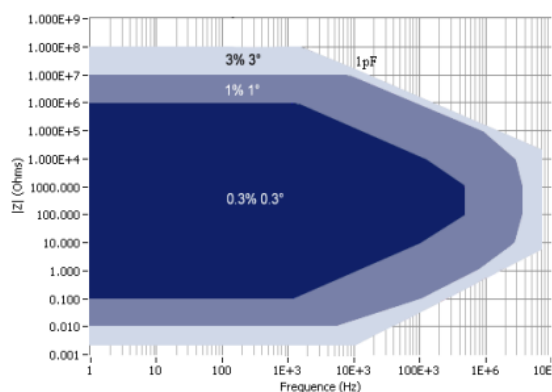


Figure 25: Accuracy Contour Plot of the Biologic VSP-300. Retrieved from the manual of the Biologic VSP-300 [115].

which will not be needed for this setup (Figure 26). The frequency range is 7 MHz (3%, 3°) down to 10 μ Hz. The frequency resolution is 1% for 10 μ Hz up to 3 MHz. The Accuracy Contour Plot (ACP) of the Biologic VSP-300 is visualised in Figure 25 [115]. The other specifications of the Biologic VSP-300 could be found on the website of Biologic and in the manual [115].

The applied current flows between the drive lead on the working electrode (P1) and the drive lead on the counter electrode (P2). The response voltage is measured between the sensing leads S1 and S3. The voltage is controlled at the drive lead on the working electrode P1 and the reference electrode

S2. Thus, for the 4-point measurement on four electrode electrochemical cell: working electrode is connected to P1, counter electrode is connected to P2, the first CME is connected to S1 and the second CME is connected to S2 and S3 (Figure 26).

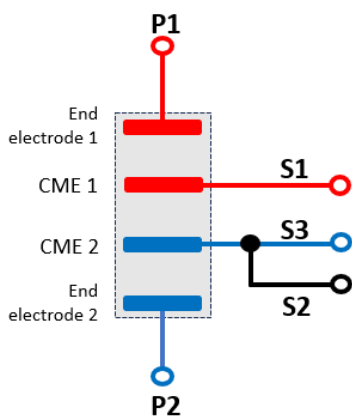


Figure 26: Four electrode connection of the potentiostat cables onto the electrodes in the CME-cell. Inspired from figures in the manual of the BioLogic VSP-300 [115].

The permselectivity, performance indicator of the CME, is determined with EIS. Therefore, the CME must be made selective. To make the CMEs selective, thus positively or negatively charged, a DC current is applied with a power supply. Unfortunately, the BioLogic potentiostat is not capable of charging the CMEs with a DC current. Therefore, another system is required that can supply the CMEs with a specific potential to charge them: Voltcraft® ps-2403d laboratory power supply. This system consists of two channels with six connections, so it has two power supplies in one system. With this system, the two CMEs could be charged at the same time. Only four clamps are needed: two negative terminals and two positive terminals. If the CME is required to be negatively charged, the negative terminal is placed on the CME and the positive terminal on the end electrode. The reverse is true if the CME has to be charged positively. An Ag/AgCl reference electrode (3M KCL) is used as a datum or a ground to determine what the absolute values of the potential are (versus the fixed potential of the Ag/AgCl reference

electrode) on the end electrodes and CMEs. The reference electrode is placed inside the reservoir during the measurements. The voltage difference between the CME and the Ag/AgCl reference electrode is measured with a multimeter, to know what the absolute value is of the potential on the CME.

4.1.2.2 CME-cell

The CMEs are placed inside the CME-cell and the EIS experiments are conducted by applying AC signals with different frequencies on the CME-cell and measuring the AC response signal. The CME cell design determines the shape of the Nyquist plot because the resistances are different for different EIS systems. The electrochemical cells, described in the literature, for porous electrodes and ion-exchange membranes were adapted to develop the CME-cell for CMEs (Długolecki et al. (2010), Gamala et al. (2016), and Zhang et al. (2020)) [24,25,75]. The resulting concept of the CME-cell is depicted in Figure 27. The potentiostat must perform 4-point EIS measurements on the CMEs. Therefore, four electrodes are necessary: working electrode, counter electrode, and two reference electrodes. In the literature, Hagar-Luggin capillaries are used as reference electrodes for 4-electrode EIS measurements on ion-exchange membranes [25,75]. The Hagar-Luggin capillaries are connected to (Ag/AgCl) reference electrodes which are connected to the sensing threads (S1, S2, and S3) of the potentiostat to measure the AC response signal. IEMs are not made of electrode material, so these separate reference electrodes were needed to measure the outgoing signal. However, a CME is an electrode and can carry a current. So, for the EIS measurement of CMEs, the Hagar-Luggin capillaries are replaced by the investigated CMEs. Two identical CMEs are thus placed inside the CME cell and work as the reference (or sensing) electrodes. The cables of the potentiostat are connected to these CMEs to measure the outgoing response signal, while the cables are connected to the working and counter electrode (end electrode 1 and end electrode 2) to induce an AC signal.

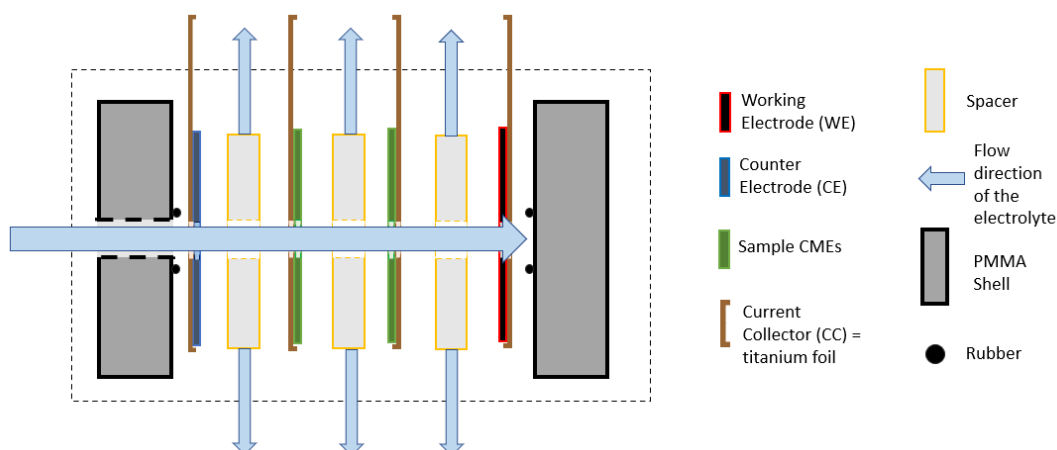


Figure 27: Sketch of the CME cell. The flow direction of the electrolyte inside the CME-cell stack is depicted with the light blue arrows. The electrolyte flows into the cell through a hole in the stack and out through the spacers.

The fiberglass spacers are placed between the electrodes to ensure that the electrolyte flows between the electrodes and to avoid short circuit. To ensure enough deionisation of the CME-cell and avoid short circuit, we choose the thickness of the spacers to be 3.0mm which is achieved by stacking multiple layers on top of each other. In principle, however, our characterisation of the CME should be independent of the choice of spacers. Rubber is placed between the current collector of the end electrodes and the shell. The rubber ensures that the electrolyte flows according to the flow arrangement, depicted in Figure 27. A circular flow path has been chosen for the electrolyte, so the electrolyte goes in via a hole in the centre of the stack and moves out of the cell via the edges of the spacers (Figure 27). The CME-cell consists of layers sandwiched between two PMMA sheets that act as a shell, see Figure 28. The corresponding layers in the PMMA shells are: rubber, working-electrode with current collector, spacer, first CME with current collector, spacer, second CME with current collector, spacer, counter-electrode with current collector, and rubber (Figure 28). To ensure alignment of the stack, a hole of 4mm in the centre of the spacers, PMMA plates, and CMEs is cut. Subsequently, the disks are aligned by stacking them, in the right order, on a 4mm diameter rod. The shell will be made of two PMMA plates which are laser cut in the desired shape. The size of the shell is 10cmx10cm with a thickness of 6mm. Bolts between the two PMMA plates induce the required pressure to clamp the electrodes, current collectors, rubber and spacers together. The 3D CAD model of the design of the CME-cell is depicted in Figure 28.

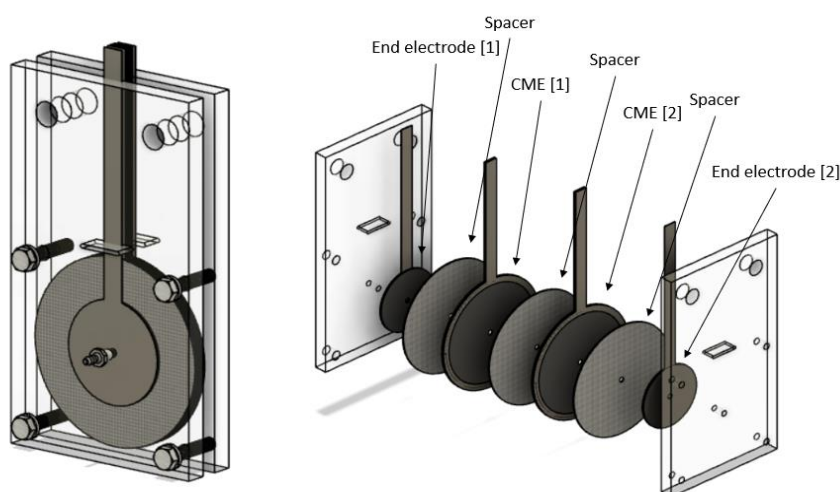


Figure 28: (left) 3D CAD model of the CME-cell and (right) the cell stack inside the PMMA plates. These models were made with Fusion360.

The current collector is made of the metal-based current collector titanium, because titanium has a high tensile strength and low electrical resistivity [116]. Additionally, Lamiel et al. (2022) state that titanium is the only metal-based current collector which may be employed as a current collector for both an anode and a cathode [116]. The titanium current collectors need to be as thin as possible. The thinnest thickness available was 0.05mm. The current collector is pressed against the end electrodes and the CME to ensure that the electrons move from the current collector into the electrodes. The design of the titanium current collector for the CMEs is showed in Figure 28. Figure 29 shows pictures

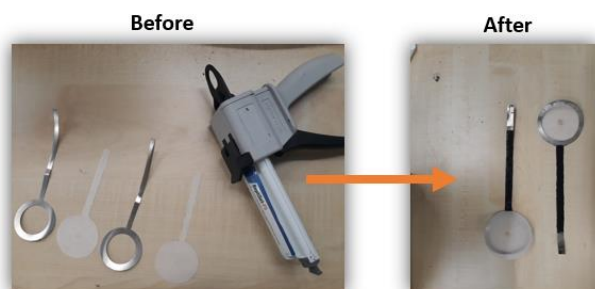


Figure 29: Design of the titanium current collectors for the CMEs. The strip of the fiberglass is glued on the titanium foil, then the silicone rubber is placed on both sides of the strip. The titanium current collector is now always aligned in the same way.

of the manufacturing process of the current collectors for the CMEs. The current collector for the CMEs is designed in this way so the CME can be removed and replaced with a new one and the ions are able to move through the CME. An additional problem needs to be solved: the current collectors of the end electrodes and CMEs are very close to each other which could induce a short circuit. To solve this issue, the titanium current collector for the CMEs is glued to a spacer to ensure that the EIS measurement could be repeated on the same CME-cell. However, the spacer cannot be glued

because the water needs to be able to flow through the spacer. Thus, the spacer is extended with a fiberglass strip which is glued onto the titanium strip of the titanium current collector, see Figure 29. The strip is, subsequently, filled with silicone rubber of RapliSet-F5 to avoid a short circuit and improve the connection between titanium current collector and the fiberglass spacer. The result is the titanium current collector for CMEs in Figure 29. With this design, the current collectors are aligned in the same way for every CME placed inside the CME-cell.

All electrodes are made of carbon material. The counter-electrode and working-electrode are identical and will be called “end electrodes” for the rest of the report. The diameter of the CMEs is not a constraint, however, the end electrodes must have a smaller diameter than the current-collector of the CMEs, because otherwise capacitive behaviour occurs at the areas where the CME is pressed against the current-collector of the end electrode.

4.1.2.3 Reservoir

The electrolyte is stored inside the reservoir which is a glass beaker. The reservoir is utilised to keep the electrolyte temperature and concentration homogeneous and constant during the EIS experiments. Additionally, the temperature and concentration must be controlled to analyse the effects of the temperature and concentration on the EIS measurements. The concentration inside the reservoir is changed manually by inserting KCl salt inside the electrolyte to increase the KCl concentration or remove electrolyte and insert water to reduce the KCl concentration. The conductivity meter measures the conductivity of the electrolyte, which result in the concentration of the electrolyte. The conductivity meter is also used to ensure that the concentration is constant during the EIS measurement. The reservoir is placed on top of the magnetic hotplate stirrer with heating option which can control the temperature of the electrolyte. The magnetic stirrer with integrated heater is the Cole-Parmer US152D-2 hotplate stirrer that is included with a SCT2 temperature controller (accuracy of $\pm 0.5^{\circ}\text{C}$) [117]. The SCT2 temperature controller (temperature sensor) could accurately control the temperature of the electrolyte in the beaker or could be used as digital thermometer [117]. The stirring of the electrolyte in the beaker ensures the homogeneous temperature and concentration in the electrolyte, however, the stirring has influence on the EIS measurements according to Długolecki et al. (2010) [75]. Therefore, the stirring of the magnet is also kept constant and at a low speed of 2.5 during the EIS experiments.

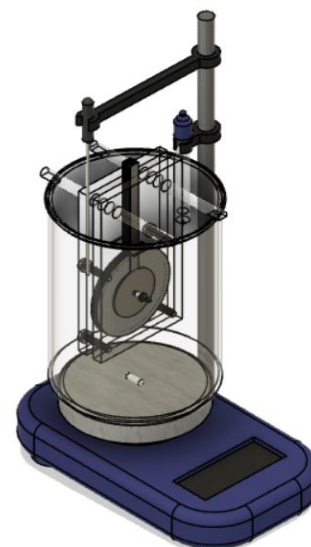


Figure 30: 3D CAD model of the reservoir sub-system with 3L glass beaker, hotplate stirrer and the CME-cell with reference electrode. Made with Fusion 360.

The CME-cell is placed inside reservoir, thus the size of the CME-cell limits the size of the glass beaker. The glass beaker must have a diameter that is larger than 150mm. The standard beaker glass with a diameter that is closest to this 150mm is the one with a volume of 3000mL, diameter of 152mm, and height of 210mm. The CME-cell is placed inside the reservoir, however, it cannot stand on the bottom of the beaker because the magnetic stirrer stands in the way. Therefore, the CME-cell “hangs” in the beaker by including PMMA support beams. The design of the CME-cell inside the beaker is illustrated in the 3D CAD model in Figure 30. PMMA was chosen because metal beams could damage the glass beaker. Additionally, calculated was that the deflection is less than 0.10 mm and the support beam will not succumb to the weight of the CME-cell when it is made of PMMA.

4.1.2.4 Pump

A fluid flow inside the CME-cell is not necessary to conduct an electrochemical impedance spectroscopy measurement. However, the electrodes inside the CME-cell consist out of carbon material that already adsorbs a few ions out of the electrolyte in the reservoir when the CME-cell is placed inside it. As a result, the salt concentration in the reservoir decreases. To keep the salt concentration during the EIS experiments constant, a fluid flow is applied within the CME-cell to purge the electrodes. A pump induces this fluid flow.

The pump pumps small volumes of fluid from the reservoir through the CME-cell, and back into the reservoir. The flowrate of the pump must be constant during the EIS experiments. The required flowrate of the pump is estimated with the following formulae: $\text{Flowrate pump} = \text{electrode area (in cm}^2\text{)} / 10$ [in mL/min]. The flowrates are thus low (lower than 10 mL/min). A peristaltic pump of Lead fluid (BT100S Basic Variable-Speed Peristaltic Pump) with a YT15 head is used for the CME meter [118]. The flowrate of the peristaltic pump is set on 8.0 mL/min (with an accuracy of $\pm 2.0\%$), however, could be changed if required during the EIS experiments. The speed accuracy is 0.5% [118]. This pump does not require an Arduino to control it, it is controlled manually.



Figure 31: Picture of the BT100S Basic Variable-Speed Peristaltic Pump. Retrieved from the website of Lead fluid [118].

The tubes for this setup need to be able to resist the salts that are present inside the electrolyte so that they will not degrade or affect the electrolyte during the measurements. The ions that could be present inside the electrolyte are Sodium, Calcium, Magnesium, Potassium and Chloride ions. PTFE tubes and silicone tubes are largely available and could resist these chemicals inside the electrolyte. Also, the tubes could resist temperatures above 200°C, so for different temperature measurements of EIS, this temperature range is large enough. Silicone tubes are less expensive than PTFE tubes, and are therefore utilised. The size of the tubing is determined by the small required flowrate and the specifications of the Lead Fluid peristaltic pump. The YT15 head only works for tubes with a minimum outer tube diameter of 13 mm, even for very low flowrates (it can have a flowrate as small as 3 mL/min) [118]. However, for the design of the CME-cell and the connection with the conductivity meter, the tube diameter must be much smaller than 13 mm: inner diameter of 2 mm and outer diameter of 4 mm. Therefore, two different size silicone tubes are used and connected with each other via a stereolithography 3D printed plastic hose connector made of watertight SLA.

4.1.2.5 Conductivity meter

The conductivity meter is not necessary to carry out the EIS experiments, however, it is useful to ensure that the concentration in the electrolyte remains constant during the EIS experiments. The TU Delft already has an inline conductivity meter which will be used to measure the conductivity of the electrolyte: eDAQ ET908 Flow-Thru Conductivity Electrode inserted in the eDAQ EPU357 Conductivity isoPod™ [119,120]. This conductivity meter is placed in the tubes and measures the conductivity of the liquid that flows through it, see Figure 32. The eDAQ Pod-Vu software is installed on the laptop, so the conductivity graphs are able to be displayed during the EIS experiments to ensure constant conductivity [121].



Figure 32: Picture of the eDAQ ET908 Flow-Thru Conductivity Electrode (left) for use of the EPU357 Conductivity isoPod™ with USB (right). Retrieved from the official website of eDAQ [119,120].

4.1.2.6 Laptop and Software

The laptop is used to analyse the data collected during the EIS experiments. Different software programmes are used to ultimately get all the data: EC-Lab® software is used to perform the EIS measurement on the CME-cell, the EIS data is copied to an Excel file, finally, a Python Script is used to

convert the EIS data to impedance graphs. The Python Script could be found in Appendix D. For the eDAQ conductivity meter, the Pod-Vu software is used to determine the conductivity, which, in combination with a formula, gives the concentration in the electrolyte.

Biologic VSP-300 potentiostat with EC-Lab® software

The EIS potentiostat, Biologic VSP-300, is connected to a computer via a LAN connection [115]. Special software of Biologic, EC-Lab® software, has been downloaded before setting up the experiments. In this software, there are multiple analysis tools, as is an EIS data modelling tool which creates the Nyquist plot during the experiments. The Nyquist and Bode plots are immediately visualised on the screen on the right when the EIS measurement is started. EC-Lab® software has its own fitting tool, but there was no possibility of fitting the Transmission-line model through the data. Therefore, the EIS data is stored in a table as a MPT file and copied to an Excel file. This file is opened with a Python script, which has the function to construct the impedance plots and fit the EECMs through the EIS data.

Before the EIS measurement could start, the settings in the EC-Lab® menu must be specified. The different options have all been tested to find the optimum settings for the EIS measurement. The specifications to be used for each EIS measurement are summarised in Appendix E. All specifications in the parameters settings are tested to find out what their influence is on the EIS measurement. The procedure to execute an EIS measurement could be found in Appendix E. For this Thesis, only the potentiostatic electrochemical impedance spectroscopy (PEIS) measurements are performed.

Design of Python script for analysing the EIS data

For the analysis of the EIS data, a script has been designed and tested to convert the data into impedance plots. The script is written in the programming language Python and executed in the programming environment Spyder® [122]. The full Python script could be found in Appendix D.

The functions of the Python script are:

- Read the Excel file with the EIS data and store the EIS data
- Fit a pre-defined EECM impedance equation through the EIS data
- Display the EIS data and fitting inside impedance plots (Nyquist and Bode plots)
- Calculate the quality of the fit value χ^2
- Determine the optimal values of the parameters inside the Transmission-line model or another EECM

First, some Python packages are imported to create the required impedance plots, generate a fit and perform mathematical operations. The used Python packages are: numpy, pandas, matplotlib.pyplot, pickle and the curve_fit of SciPy [122-126].

The first lines of code in Python are usually the constants, and the same has been done for this script. These constants are, for example, the surface area of the CME where the transmission of ions takes place, or the solution resistance needed for the transmission line model of the impedance equations. The units of the constants are placed after the value of the constant.

The EIS data in the Excel files are read and stored by using the package pandas and the command *pd.read_excel* [124]. The EIS data in the Excel files are separately stored as arrays for the frequency, real impedance, imaginary impedance, magnitude of the impedance, phase angle of the impedance, real capacitance and imaginary capacitance. The impedance is then calculated by summing the real and imaginary impedance. During the EIS experiments, the impedance is measured in Ω and not Ωcm^2 , however, for the analysis, the impedance in Ωcm^2 is preferred. Therefore, the real impedance, imaginary impedance, and magnitude impedance are multiplied by the area where transmission occurs, while the imaginary and real capacitance are divided by this area.

The impedance equations of different EECMs are inserted in the script as a definition. This comes in handy for the code to fit the impedance equation through the EIS data. Additionally, new possible EECMs could be added as a new definition which could be called upon. The goal is to find the EECM which gives the lowest chi-squared value χ^2 . But first, the equation of the optimal fit needs to be computed by finding the optimal values of the parameters to minimise χ^2 .

Therefore, a pre-defined impedance equation (in the definitions) is fitted through the EIS data with the *curve_fit* function. Python tries to find the values of the impedance equation which best fit through the EIS data. Therefore, the user must give a guess of those values. That poses a problem, because Python finds different values when the guessed values are changed. Therefore, different guesses are inserted manually in the *curve_fit* function, until the quality of the fit is as small as possible. Also, values for R and C could not be negative, even if the error is small. Then, also, new guesses need to be inserted in the *curve_fit* function.

The value of the quality of the fit χ^2 is calculated by squaring the difference between the measured imaginary impedance and fitted imaginary impedance divided by the standard deviation, squaring the difference between the measured real impedance and fitted real impedance divided by the standard deviation, and then summing these values [112]. The impedance equation is accepted as a “good fit” when the value of chi-squared χ^2 is smaller than 10^{-3} [114,115]. The standard deviation in the equation should actually be the standard deviation of the frequency of that datapoint. Thus, the array of the standard deviation should contain for every frequency another value for the standard deviation, however, in this script, all the elements in the standard deviation array contain the average value of the standard deviation of all the frequencies for one EIS measurement. Of course, this method is less accurate. In future measurements, the EIS measurements should be repeated to determine the mean and standard deviation at every frequency of the datapoint.

The body of the script is completed, now for the analysis, multiple impedance graphs are plotted. The impedance graphs that are plotted are: Nyquist plot, Bode magnitude plot, and Bode phase plot. The EIS datapoints are visualised as dotted points, while the fitted impedance equations are displayed as full lines. The impedance equation has the colour as the EIS datapoints where it is fitted through.

In the last code lines, the optimal values of the parameters inside the impedance equations are printed as are the chi-squared values of the impedance equations. When the optimal values of the parameters are negative or unphysically large or small, than the initial values are manually changed. When the optimal values are accepted, then the impedance equation of the EECM is approved as a “good fit” if the value of chi-squared is smaller than 10^{-3} .

4.1.2.7 Safety Considerations

The setup should be safe, both for the user as for the environment, at all time. Therefore, the safety of the researcher and the environment is taken into account in the design of the setup. The main design decisions related to safety are summarised below.

Station of the setup

The setup is placed inside the chemical laboratory in the Process and Energy department of 3ME of TU Delft. This laboratory is restricted for personnel of TU Delft who had finished a lab safety cursus. So, only personnel that have knowledge of laboratory safety are able to reach the setup, which excludes the possibility of unauthorised people to touch the setup. Additionally, the Biologic VSP-300 potentiostat is stationed in this lab which eliminates the need to transport the setup.

Dangers of Potassium Chloride (KCl)

Potassium chloride (KCl) is an odourless white powder inserted in the electrolyte of the setup [127]. A small amount of KCl is solved into milliQ water to produce the electrolyte. KCl is a salt, but it is not a harmless compound. According to the World Health Organisation, KCl causes irritation in the eyes, and on the skin when exposed, and, when exposed by larger concentrations, KCl could cause effects on the cardiovascular system [128]. Long-term exposure has no additional effects according to the WHO [128]. For the experiments, low concentrations of KCl are required, but, the KCl is used in a powdered form, which increases the risk of airborne KCl particles. To reduce the health risk, glasses, a lab coat and gloves are mandatory when working with or around the setup. Second measure is to put a plastic foil on top of the beaker. A creative alternative for the plastic foil is the “hoody”. The hoody is a silicone food wrapping for bowls or beakers from the IKEA® (Övermått). It has a diameter of 18cm and is light pink. The food wrapping has been used as a cap over the glass beaker for the safety requirement of the setup and to reduce the amount of water that evaporates. To make the crocodile clamps of the potentiostat reach the current collectors of the end electrodes and CMEs, 3D printed “entrances” were designed which were placed in the hoody by cutting some holes inside the silicone with a Stanley® knife. The result is visible in Figure 33. In this way, less airborne KCl particles are able to leave the electrolyte reducing the risk of irritation.



Figure 33: The hoody which will protect the researcher from airborne KCl particles and reduces the evaporation of water out of the electrolyte. The original silicone comes from IKEA®.

Disposal of the setup

After finishing this Thesis project, the setup will be dismantled. All the electric systems from the TU Delft will be reused for other projects. Other components will be thrown out or stored for recycling purposes. The Ag/AgCl reference electrode will be stored in a 3M KCl solution and stored inside a cabinet. The end electrodes, spacers, CMEs, and titanium strips are disposed in the black garbage container. The PMMA plates are also thrown in the garbage container specially reserved for PMMA parts. The glass beaker is stored in the cabinet of the electrochemical lab where other researchers could use it for their setups or experiments. The electrolyte with KCl solution is thrown in a special garbage can for chemical compounds. The KCl solution is prohibited to enter the sewage system, so, the KCl solution disposal is placed inside a jerrycan [128]. When the jerrycan is fully filled, it is emptied inside the special garbage can for chemical compounds.

4.1.3 3D CAD model of the CME meter

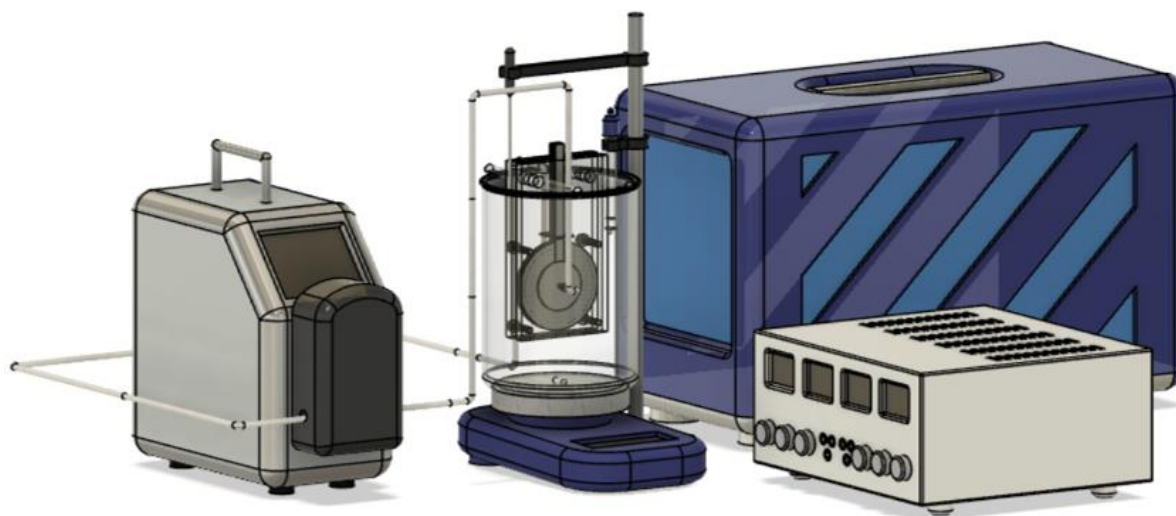


Figure 34: 3D CAD model of the CME meter for measuring the electrochemical properties of CMEs. From left to right: BT100S peristaltic pump, CME-cell in beaker on top of a hotplate stirrer, Biologic® VSP-300 potentiostat, Voltcraft® ps-2403d laboratory power supply. This model was made with Fusion360.

The final design of the CME meter is visualised in Figure 34. In this 3D CAD model, the Voltcraft® power supply, Biologic® VSP-300 potentiostat and the CME-cell in the glass beaker placed on the Cole-Parmer® Stuartth US152D-2 hotplate stirrer are visualised. The conductivity meter and the laptop are not included in this model. The conductivity meter is placed between the tubes to measure the concentration of the electrolyte. The clamps and wires between the CME-cell, the potentiostat, and Voltcraft® power supply have not been modelled. The systems are connected to the titanium strips in the CME-cell with crocodile clamps. A plastic hood is constructed from a silicone food wrapping from IKEA® (Övermätt) which is placed on top of the beaker. This hood has also not been modelled in Figure 34.

4.2 Construction of the CME meter

The design of the CME meter is fully finished and has been approved by the supervisors. The next step is building and testing the CME meter. A bill of materials has been constructed which could be found in Appendix F. After taking stock of the components already available at TU Delft, an order list was drawn up and the required components ordered. The delivery of all these components took almost three months. Some components or materials have to go through a manufacturing process. A list of all the process steps is given in Table 4. During the three months of waiting, systems such as the BioLogic® potentiostat, peristaltic pump, hotplate stirrer and conductivity meter were tested. As the components were delivered, tests were carried out. All of these tests are explained and evaluated in Section 4.3.

4.2.1 Bill of Material and Order list

After getting confirmation of the design of the CME meter, a component list has been established. The Bill of Materials is found in Appendix F. To reduce the costs of the setup and for recycling of existing measurement apparatus at the TU Delft, before ordering the components, the available components at the TU Delft are determined. The resulting Order list includes the components that are not available at the TU Delft and thus need to be ordered. The total costs of building the setup and performing EIS experiments on CMEs is approximately 1,250 euros.

4.2.2 Fabrication process of the CME meter

As some components and materials were delivered, the manufacturing process was started. This process consists of action points which should be finished before the CME-cell could be constructed. TU Delft has entities which have facilities which could laser cut, mill, 3D print, and more. These entities are: Inloop Werkplaats Werknemers (IWM), Inloop Werkplaats Studenten (IWS), and Dienst Elektronische en Mechanische Ontwikkeling (DEMO). Table 4 displays the components or materials which should be manufactured, the entity which will perform the action and some specifications of the product.

Table 4: Procedure for the manufacture of the components of the CME meter. The tools used to manufacture the components and the persons instructed to carry out the manufacturing are also specified in the table.

Action step		Manufacturing process	Entity	Specifications and notes
1.	Fabricate the hose adapters for tubes	3D printing	IWM	From 4mm to 10mm; made with SLA
2.	Cut the PMMA plate with 6mm thickness in two plates with size 100x180mm	PMMA Laser cutting	IWS	Included with holes for the rods and bolts
3.	Cut the 2 meter PMMA rod of 10mm diameter cut in 2 piece with length 180mm	Cutting machine	IWM	Afterwards filed by Chérise
4.	Tapping M6 (4 holes) and M5 (2 holes) in the two PMMA plates	"Pneumatische taparm"	DEMO	Step 2 needs to be concluded first
5.	Fabricate plastic watertight parts which serve as entrances for the titanium strips, reference electrode, temperature sensor and tubes	3D printing	IWM	For inside the plastic foil to allow the other components to get to the CME-cell and for the cell to be closed off; made with SLA
6.	Cutting holes in the Silicone wrapping (IKEA® övermätt) for the 3D printed entrances	Manually with Stanley® knife	Chérise	Diameter of the holes are smaller than the diameter of the plastic parts
7.	Fabricating the end electrodes	Laboratory	Chérise	Made with PVDF, graphite and carbon black
8.	Cutting the titanium foil in the required shape for the current collectors of the end electrodes and CMEs	"Waterstraal snijder"	DEMO	The strip has a length of 200mm and is 15mm wide; 4 pieces
9.	Spray two-part fast curing silicone rubber on the titanium current collectors for the CMEs	RepliSet-F5	Chérise	Step 8 needs to be concluded first; only for the current collectors of the CMEs
10.	Cutting fiberglass in the required shape for the spacers	Manually with Stanley® knife	Chérise	Diameter of spacer is 90mm; hole has a diameter of 4mm; 6 pieces

4.2.3 Fabrication recipe of the CMEs

The CMEs are fabricated according to a known fabrication process. The steps of this process are explained in more detail below.

The step-by-step process for making a CME is described below:

1. Determine the required weighted masses of the components (carbon material, conductive additive, binder, and solvent) of the CME from the given mass percentages.
2. Weigh the components, except the solvent, with a scale and add them in a beaker.
3. Check if the mixer, doctor blade and glass (where the CME slurry is smeared onto) are cleaned from electrode material. Place the doctor blade on the glass table and place the mixer in the fume hood. Make sure the doctor blade is placed on the right height for the CME.
4. Weight and add the solvent to the beaker to complete the slurry.
5. Mix the CME slurry. First, mix with the lowest rate, then gradually increase the mixing rate of the mixer. Place the mixer in the beaker in an angle to ensure that the top of the slurry also

get mixed and won't dry to create lumps. Be careful: the slurry starts to cook and the beaker gets hot!

6. When all the bubbles are released from the slurry, then the slurry is finished to be smeared onto the glass table. Place the slurry onto the glass table and slowly pull the doctor blade over the slurry.
7. Wait minimally 30 minutes before pulling off the material from the glass table and determine the resistance per square, the thickness and the weight per surface area of this CME material.

4.3 Testing the CME meter

The CME meter has to be tested before experiments can be performed, as several components and functions may not work properly. Several checks have been designed to ensure that the setup is working properly according to the programme of requirements. Two tests are performed to calibrate the pump and the conductivity meter. Then, two checks were carried out to check how the power supply and potentiostat are functioning, while two other tests were carried out to check if the flow of the electrolyte in the CME-cell is as designed. The last test can be seen as a general repetition where a EIS 'dummy test' is performed on two CMEs to check if the whole CME meter is fully operational. The goal of these tests is to find an operating procedure for the CME meter to perform EIS experiments on CMEs. The operating procedure of the CME meter could be found in Appendix E.

4.3.1 Characterising the flowrate with the pump

The pump must induce a flowrate of 8mL/min. Operating the pump is easily done by defining the required rotational speed in RPM. Therefore, the rotational speed that corresponds with 8mL/min flowrate of the electrolyte must be found beforehand. For this test, a new setup is designed where the following components are included: the pump, the tubes used for the CME meter, two beakers, a weight scale, and a density meter. The electrolyte with a KCl concentration of 960mg/L is placed inside the first beaker which is placed on the magnetic hotplate stirrer, while the second beaker is empty. The second beaker is placed on the scale. The temperature of the electrolyte in the first beaker is kept constant at 25°C. The pump is connected with the first beaker and the second beaker via the tubes, so when the pump is started, the electrolyte from the first beaker flows into the second. Before starting the test experiment, the mass of the second beaker is written down. After this, the pump is started at a certain RPM. A timer is used to measure the past time. After approximately 1 minute, the pump is stopped and the time is written down as is the mass of the second beaker. This test is done for rotational speeds of 1.0, 2.0, 3.0, 4.0, 5.0, 6.0, 7.0, 8.0, 9.0, and 10.0RPM. Afterwards, the density of the electrolyte is measured with the Anton Paar dma 4500 density meter which is stationed in the electrochemistry lab of the process and energy department of TU Delft. The density is measured at 25°C. During the analysis, a linear fit is fitted through the flowrates for rotational speeds of 1.0, 2.0, 3.0, 4.0, 5.0, 6.0, 7.0, 8.0, 9.0, and 10.0 RPM, subsequently, estimating the rotational speed of 8mL/min with the equation of the fit. The flowrate is calculated with the following formulae,

$$Q = \frac{m_t - m_0}{\rho \Delta t} \text{ 60s/min,}$$

where, Q is the flowrate in mL/min, m_0 is the mass of the second beaker before the experiment started in g, m_t is the mass of the second beaker after time Δt in g, ρ is the measured density of the electrolyte at 25°C in g/cm³, and Δt is the duration of the experiment measured with a timer in s. The

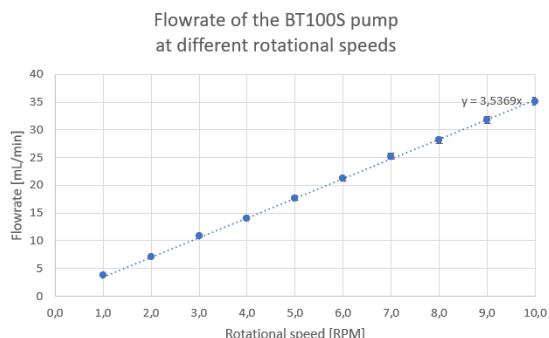


Figure 35: The relation between the rotational speed of the BT100S peristaltic pump in RPM and the flowrate of the fluid inside the tube in mL/min.

data is placed in Excel, subsequently the flowrates are calculated and a linear line is fitted through the flowrates. The output is the graph with the flowrate of the data points, the linear fit, and the estimated RPM at a flowrate of 8mL/min. The calibration test was executed as planned and the result is visualised in the graph of Figure 35. The equation of the fitting, which intersects the point (0,0), is $Q = 3.5369 \cdot \omega$ with Q in mL/min and rotational speed ω of the pump in RPM. For a flowrate of 8mL/min, the rotational speed should be 2.3RPM, and after checking this value with two tests, this has been accepted.

4.3.2 Check how the power supply could charge the CMEs

For the EIS experiments of Experiment 3, the CMEs are required to be charged. The Voltcraft® ps-2403d laboratory power supply is able to apply a specific voltage or current between two electrodes, while a multimeter is used to measure the voltage, current, or resistance between two electrodes. A test is designed to check if the power supply is able to apply a potential on the CME to charge them and what the operational procedure is to charge a CME. The test is relatively simple. The required components are: the Voltcraft® power supply, two identical previously made electrodes, titanium current collectors for CMEs, cables that connect the power supply with the electrodes, and a multimeter. The two previously made electrodes are placed adjacent to the titanium current collectors, and the cables of the power supply are connected to the titanium current collectors. A potential difference of +1.0V between the electrodes is applied by the power supply for 30 minutes. The multimeter is used to measure the potential difference between these two electrodes, during the charging. The difference must be equal to the applied potential by the power supply. Then, after 30 minutes, the difference between the two electrodes and the Ag/AgCl reference electrode is measured with the multimeter to get the absolute value of the electrodes. The output is a procedure to charge the CMEs with the Voltcraft® ps-2403d laboratory power supply.

4.3.3 Determining the working procedure of the Biologic VSP-300 EIS potentiostat

In this test, the Biologic VSP-300 system and EC-Lab® software are tested to get a feeling with the system and the software. Multiple EIS measurements are conducted in which sample electrodes are connected with the connectors of the potentiostat. The electrodes used for this test are taken from the material which is left over from the fabrication of the end electrodes. Two strips are cut from this material and are placed adjacent to the titanium current collectors. The crocodile clips of the working- and counter-electrode cables of the potentiostat are clipped on the titanium current collectors. A two point measurement is thus executed on two electrodes. In this test, the specifications of the EIS experiment in the EC-lab® software are tested and the procedure to produce the required Nyquist plot, Bode plots and complex capacitance plots is tested. The output are the specifications in the EC-lab® software which will be used for all EIS experiments. These specifications are described in the procedure for conducting EIS experiments in Appendix E. Additionally, the procedure for constructing impedance plots from the EIS data is checked.

4.3.4 Calibrating the conductivity meter

The concentration of KCl in the electrolyte is held constant during the EIS experiments. The conductivity meter displays the conductivity which determines the concentration. The conductivity meter has two functions: checking if the concentration in the electrolyte is correct and if the concentration of the electrolyte is constant during the experiments. Increase in conductivity is caused by an increase of the electrolyte concentration, which is linear. Therefore, the linear relation between conductivity and concentration must be found.

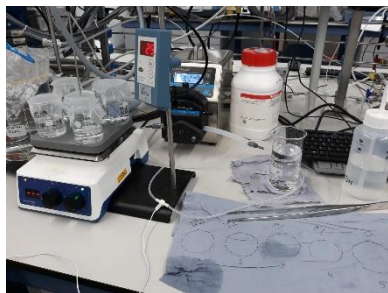


Figure 36: Picture of the test setup for calibration of the conductivity meter.

A test setup is designed with: the conductivity meter, five beakers with specified KCl concentrations, magnetic stirrer. The beakers are each filled with 50mL milliQwater. A specific amount of KCl salt is included in each beaker: 10mg, 100mg, 200mg, 500mg, 1g. This values are extracted from the average salt concentration in brackish water, which is 960mg/L [109]. One beaker is placed on top of the magnetic stirrer where the temperature is kept constant at 25°C and is stirred constantly with 2.0 (no unit defined in the specifications of the Cole-Parmer® Stuartth US152D-2 hotplate stirrer). The conductivity is measured by the conductivity meter with the Pod-Vu software for 2 minutes. The flowrate is 8mL/min.

The goal is to determine the value of the slope of the linear relation between the concentration and the conductivity. This slope is called the molar conductivity Λ_M , and is calculated with the equation $\kappa_i = \Lambda_M c_i$, where c_i is the concentration of beaker number i in mol/L and κ_i is the average conductivity measured with the conductivity meter in mS/cm. The conductivity data from Pod-Vu software is stored on the laptop, then the data is copied to Excel, where the average conductivity value is calculated. The average conductivity and the estimated concentration of the electrolyte are plotted in a graph and the data is fitted with a linear fitting. The fitting has an equation, which gives a value for the slope of the linear line, thus gives the value of the molar conductivity in kScm²/mol. The output of this test is a graph with the data, the linear fitting, the equation of that linear fitting, and the value of the slope. During the experiment, it is important to keep the temperature of the electrolyte constant because the conductivity is strongly influenced by the temperature.

The test was performed to calibrate the conductivity meter and the result is showed in Figure 37. As is visualised with the graph, the relation between the concentration and the conductivity is not linear for very small concentrations. Therefore, the molar conductivity Λ_M is not significant anymore. The polynomial fit is used as the equation to estimate the concentration inside the electrolyte:

$$c = -0.00008\kappa^2 + 0.0411\kappa + 0.0526,$$

where c is the estimated concentration inside the electrolyte in mM, and κ is the measured average conductivity during the EIS measuring time which is determined by the conductivity meter in mS/cm.

Concentration vs Conductivity plot for KCl solution

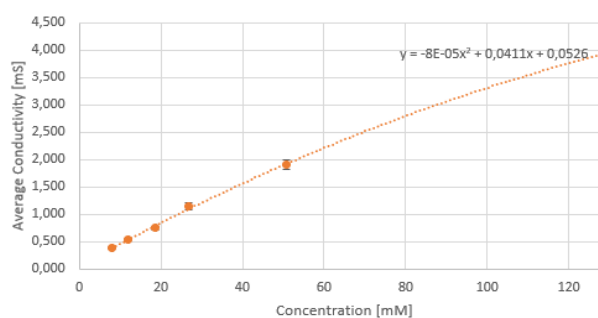


Figure 37: Concentration of the electrolyte plotted against the average measured conductivity by the conductivity meter. The

4.3.5 Testing for leakages inside the CME-cell

The tubes are connected with tubes and with hose adapters. Liquid could leak out of these connections. Leakages are best tested by placing the tube connections in water and letting nitrogen gas flow through the tubes. A new test setup is designed where the CME-cell is placed fully below water in a transparent beaker. The tubes are not connected with the pump but with a nitrogen gas

source. The plug is removed from the other side of the CME-cell. During the test, the nitrogen gas source tap is opened. Preferably, the nitrogen flows through the tubes, in the CME-cell, out of the spacer and out of the cell via the other tube. If bubbles appear at the hose connection, then there is a leak inside the hose connector. If this is the case, new hose adapters could be designed with a different shape and/or materials to eliminate the leaks. The tests were performed and there were no leaks inside the tubes or the CME-cell.

4.3.6 Testing the flow arrangement inside the CME-cell

The CME-cell has a specified flowrate as is visualised in the schematic of Figure 27. That the liquid in reality follows this flow arrangement must be checked. A test setup is designed for this test which needs the CME-cell, the pump, tubes, two beakers, and paper towels. In this test, the CME-cell is placed on a paper towel and the electrolyte is pump through the cell with 8mL/min, see Figure 38. The electrolyte therefore flows in the opposite direction to the flow through the cell in the CME meter. The different layers (rubber → end electrode → spacer → CME → spacer → CME → spacer → end electrode → rubber) are placed in turn to check if the liquid flows only out of the spacer and not between the PMMA plate and end electrode for example. The different layers that were tested and the expected output of the liquid flow in the CME-cell is summarised in Table 5. The actual output is compared with the expected output. When these two do not correspond, rubber is included between the layers to get the expected output.

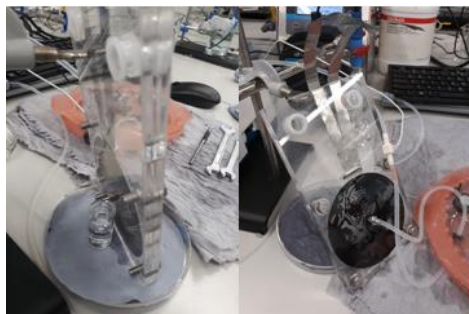


Figure 38: Picture of the test setup for testing the flow arrangement of the electrolyte through the CME-cell.

Table 5: Testing the flow arrangement inside the CME-cell (Test 6). The expected output of the flow of the liquid through the CME-cell for different layers.

TEST 6	Layer	Expected output
1.	rubber → end electrode → rubber → end electrode → rubber	Liquid flow through the cell
2.	rubber → end electrode → spacer → end electrode → rubber (without plug)	Liquid flow through the cell, and out of the spacer
3.	rubber → end electrode → spacer → end electrode → rubber (with plug)	Liquid flows only out of the spacer
4.	rubber → CME → rubber → CME → rubber	Liquid flow through the cell
5.	rubber → CME → spacer → CME → rubber (without plug)	Liquid flow through the cell, and out of the spacer
6.	rubber → CME → spacer → CME → rubber (with plug)	Liquid flows only out of the spacer
7.	rubber → end electrode → spacer → CME → spacer → CME → spacer → end electrode → rubber (with plug)	Liquid flows only out of the spacers

4.3.7 Testing the CME meter

When the specific parts of the CME meter work accordingly, there is no guarantee that the whole system will work. Therefore, the whole system is tested by conducting a “dummy test” where an EIS experiment is conducted with non-specified CMEs. This can be viewed as the general repetition before EIS experiments are conducted. The CMEs are made from already produced electrode material. It is not important what the composition of the material is, because the dummy test is only to check if the system works. The start-up procedure is executed. The electrolyte consist of 960mg/L KCl salt, which corresponds with a concentration of 12.9mmol/L. Then, the CME-cell with the CMEs is placed inside the beaker. The clamps of the potentiostat are connected with the titanium foils and the reference electrode. Then, an EIS experiment is conducted with the EC-Lab software of Biologic. During the experiments, the concentration of the electrolyte must be constant and that is checked by looking if

there are changes of the conductivity with the conductivity meter. The output of this test are important plots for data analysis, and a roadmap to perform an EIS measurement with the CME meter.

4.4 The final prototype: The CME meter

In Figure 39 is a picture showed of the final constructed prototype of the CME meter which has been built in the chemical lab of the Process and Energy department of the building 3me at TU Delft.

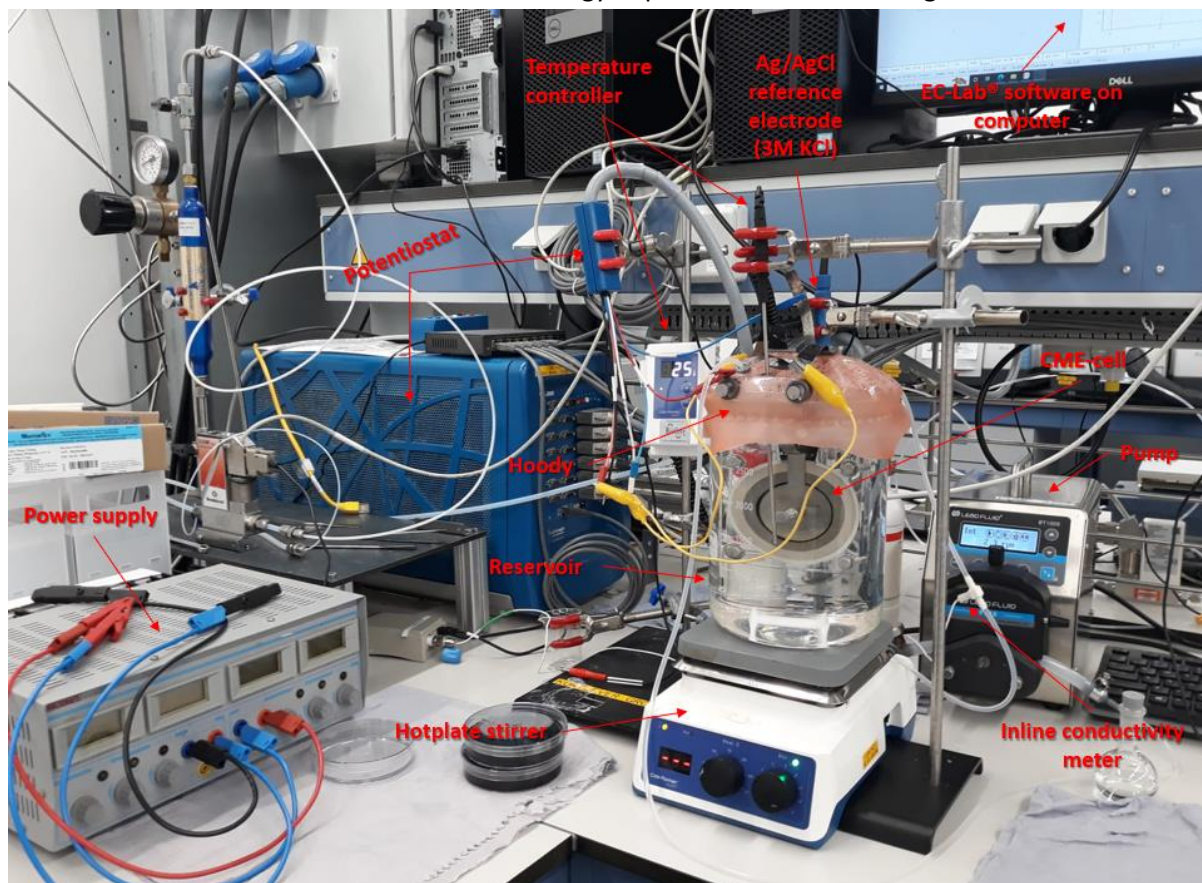


Figure 39: Pictures of the final prototype of the CME meter. The setup is located at the chemical lab of Process and Energy department of 3me at the TU Delft. The names of the different components are illustrated in the figure in red. The official names of the components are simplified (for example, pump = Lead Fluid® BT100S peristaltic pump).

5

Results and Analysis

Electrochemical impedance spectroscopy (EIS) was performed on the capacitive membrane electrodes (CMEs) in the designed EIS setup (CME meter). The results, analysis, and discussion of the EIS experiments are discussed in this chapter. Throughout the sections is EIS data presented in impedance plots.

The impedance plots are the Nyquist plot, Bode magnitude plot and Bode phase plot. The impedance (Z) is a complex number. In a Nyquist plot, the real value of the impedance ($\text{Re}(Z)$) is plotted against the negative imaginary value of the impedance ($-\text{Im}(Z)$). In the Magnitude Bode plot, the frequency is plotted against the magnitude of the impedance. In the last impedance plot, the Phase Bode plot, the frequency is plotted against the negative phase angle of the impedance. All these plots give information about the processes which occur inside the CME-cell. In the Nyquist plot and bode magnitude plot, the resistance is easily read off from the graph, whereas the capacitance is not easy to evaluate. The value of the membrane resistance is the value where the plot hits the real impedance axis, while the value of the solution resistance is the point at the real impedance axis where the plot starts. The capacitance is not easily visualised because the shape of the Nyquist plot stays the same for a larger capacitance, however, a higher membrane capacitance results in a shift of the datapoint in the shape of the Nyquist plot, so that the same point is at a higher frequency along the semicircle. To illustrate the capacitance, the Bode phase plot gives more information. In the Bode phase plot, the time constant could be visualised from the graph as it is the reciprocal of the frequency at which the peak of the plot is located. The capacitance is subsequently deduced from this time constant value and the resistance from the Nyquist plot. The Bode magnitude plot convergence at decreasing frequencies to the maximum value and at increasing frequencies to the minimum value. The minimum value gives the value of the solutions resistance in the spacers, while the maximum value indicates the magnitude of the resistance.

5.1 Determining the EECM of the CMEs

The first step in any EIS analysis is to find the model which gives an impedance equation that accurately fits the EIS data of the sample. For this purpose, EIS data has repeatedly been collected on the standard CME (CME-S) at standard operational conditions: flowrate of 8.0 mL/min, mixing rate of 2.5, temperature of 25°C and KCl concentration of approximately 1.0 mg/L. Five EECMs (described in Chapter 3 Methodology) are fitted through the EIS data. EECM A, is a single R//C-circuit. The circuit models EECM B to EECM E are the Transmission-line models, where EECM B is the “conventional” TLM and EECM C till EECM E are more complex additions to the TLM, as described in more detail in the Methodology. After fitting the impedance equation through the EIS datapoints, the quality of fit value χ^2 is determined to determine the error of the model. The EECM is accepted as “the EECM of the CMEs” if the value of χ^2 is smaller than 10^{-3} [113,114], which means that the error is smaller than 1%. In Figure 40 the impedance equation of the five EECMs has been fitted through the EIS data points of CME-S. The values of the quality of fit were determined for every EECM and could be found below the electrical circuits of the EECMs in Figure 40d till Figure 40h. Although the data shows a semi-circle in the Nyquist plot which is indicative of an R//C-circuit, the actual shape of the curve cannot be fitted accurately by the latter circuit alone: the transmission-line model, which takes the porosity of the CME into account, does a much better job at fitting the data. However, the χ^2 value of the TLM is not smaller than 10^{-3} . Therefore, more complex additional electrical circuit models of the TLM were developed (EECM C, EECM D and EECM E), their impedance equation was fitted through the EIS data, and the χ^2 -value was calculated to check if one of those EECM is a more acceptable model than the TLM. Unfortunately, all of these alternative EECMs have each a value of χ^2 which is larger than the desired 10^{-3} , so the quality of fit value is not low enough. As Figure 40 makes clear, the impedance equation of the other features of the TLM have lower χ^2 values than the TLM. This difference is very small and, according to the paper by Lazanas and Prodromidis (2023), a better EECM should only be sought after if the alternative EECM reduces the value of χ^2 by an order of 10 [107]. This is because additional elements in the electrical circuit always reduce the χ^2 values, therefore, the additional block should have physical relevance and improve the quality of fit. Otherwise, a more complex impedance equation is undesirable. This means that the χ^2 value of the alternative EECM should be 10 times smaller than the original EECM to be accepted. Thus, the values of χ^2 show that the TLM is a more accurate model to describe the behaviour through the CME-S and that other features of the TLM do not improve the quality of fit enough to be chosen as a better model. TLM is chosen as an “good model” to describe the EIS data even though the quality of fit value is not low enough. Still, a quality of fit value of $2.04 \cdot 10^{-3}$ means that the error of the impedance equation is 4.5%, which is still a low value for the error of a model.

One set of EIS data is not enough to conclude that the best EECM for the CME-S (and other CMEs) is the TLM of EECM B. Further EIS measurements have been carried out to establish what the best EECM is for the CMEs. Figure 41 to Figure 44 show the EIS data of CME-S, where the operational parameters have been varied to see the effect of the operational parameters on the collected EIS data and to conclude what is the best EECM to describe CME-S. The operational parameters which are varied are the flowrate of the electrolyte through the CME-cell, the mixing rate of the electrolyte in the reservoir, the initial salt concentration of the electrolyte, and the temperature of the electrolyte and CME-cell. In the following subsections, the results of the graphs are analysed for each varied operational parameter. What is made clear by the values of χ^2 for every EECM is that the fit of the more complex TLMs of EECM C, EECM D and EECM E (see Appendix H) are never an order more accurate than the simpler TLM of EECM B, therefore has been chosen to furtherly use the Transmission-Line Model of EECM B to fit the impedance data of the CMEs.

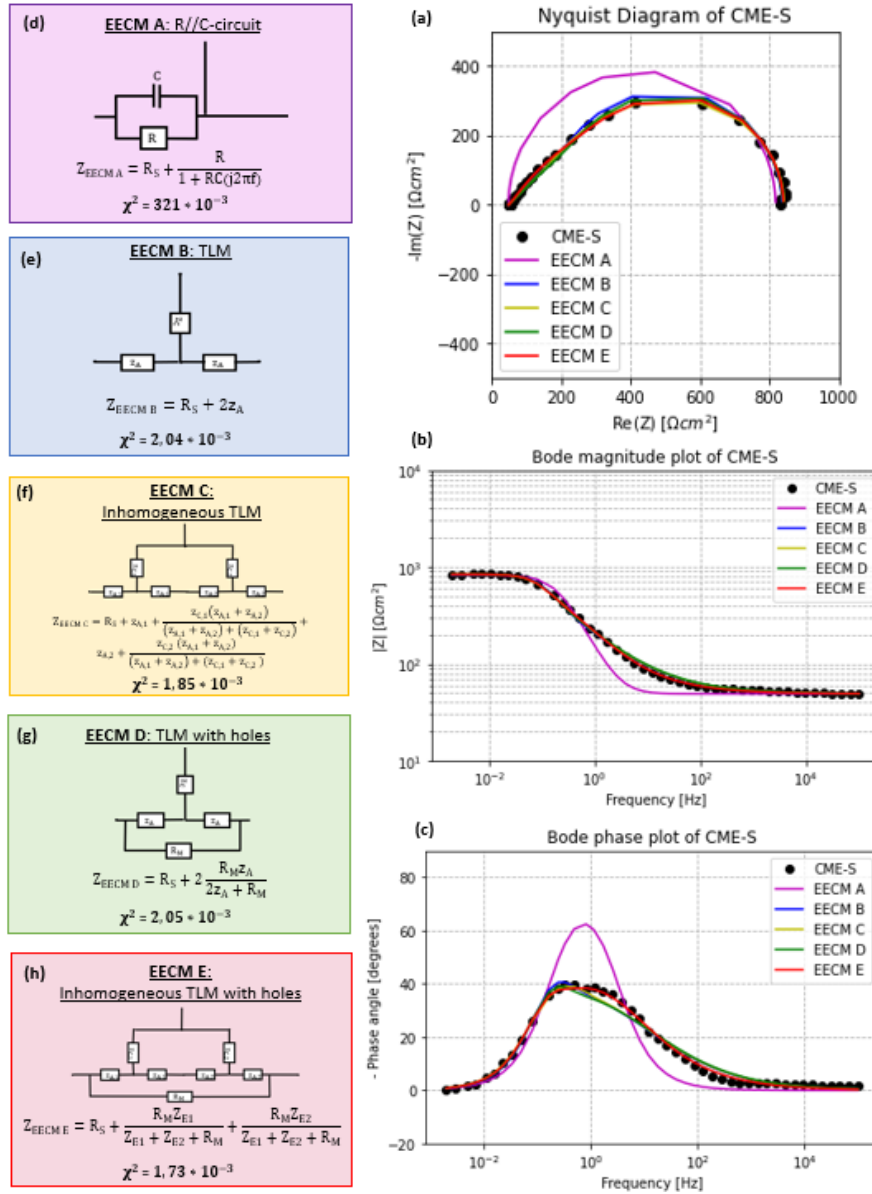
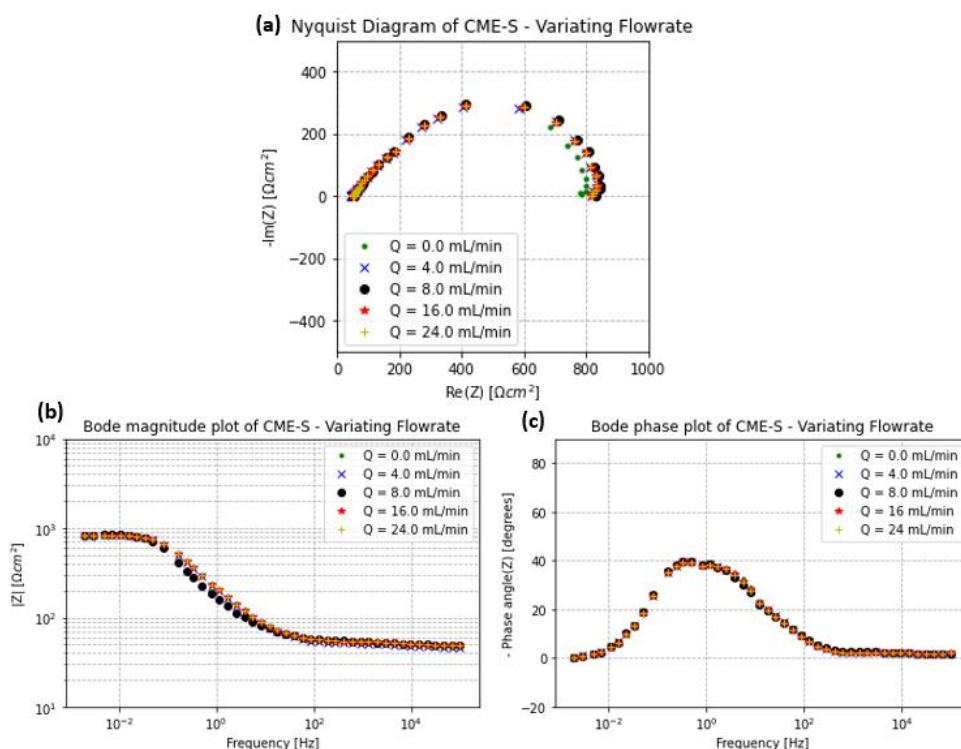


Figure 40: Electrochemical Impedance Spectroscopy measurements performed on CME-S at standard operating conditions: flowrate of 8.0mL/min, mixing rate of 2.5, temperature of 25°C and KCl concentration of approximately 1.0mg/L. (a) Nyquist diagram of CME-S, (b) Magnitude Bode Plot of CME-S, (c) Phase Bode Plot of CME-S. The coloured lines are the different impedance equations that are fitted through the EIS data of the Standard CME (black dots). The EECMs that are fitted through the EIS data are (d) EECM A: R//C-circuit (purple line), (e) EECM B: TLM (blue line which partially overlapped by the green line), (f) EECM C: inhomogeneous TLM (yellow line which partially overlapped by the green line), (g) EECM D: TLM with holes (green line), (h) EECM E: Inhomogeneous TLM with holes (red line). The impedance equations and the values of the quality of fits of the EECMs are placed below the electrical circuits. EECM E has the lowest quality of fit value.

5.1.1 Varying the flowrate



Varying the FLOWRATE		0 mL/min	4.0 mL/min	8.0 mL/min	16 mL/min	24 mL/min
EECM B TLM	R [Ωcm^2]	743	779	788	777	776
	C [F/cm^2]	0.0166	0.0181	0.0173	0.0172	0.0172
	χ^2 [10^{-3}]	2.34	2.07	2.04	2.53	2.40

Figure 41: EIS measurements performed on CME-S at different flowrates. The other operational parameters are constant: temperature is 25°C, mixing rate at 2.5, and initial salt concentration of KCl is 960mg/L. (a) The Nyquist plot of the EIS data of CME-S at different flowrates, (b) the Bode magnitude plot of the EIS data of CME-S at different flowrates, and (c) the Bode phase plot of the EIS data of CME-S at different flowrates. The different flowrates are: 0.0mL/min, 4.0mL/min, 8.0mL/min, 16mL/min, and 24mL/min. The impedance equation of five EECMs has been fitted through the EIS data in the Nyquist plot, the values of the parameters of the fit are displayed in the table below the figure.

To withhold the CMEs and end electrodes of adsorbing ions out of the electrolyte, a fluid flow is applied within the CME-cell to purge the electrodes. The flow of the electrolyte thus ensures that the salt concentration in the electrolyte stays constant during the EIS experiments. The fluid flow inside the CME-cell is therefore not expected to affect the electrochemical impedance spectroscopy measurement. To check this statement, EIS measurements are performed on CME-S at different flowrates. The EIS data in the Nyquist plot, Bode magnitude plot and Bode phase plot show that the flowrate of the electrolyte through the CME-cell has little to no effect on the EIS measurement, see Figure 41.

5.1.2 Varying the mixing rate in the reservoir

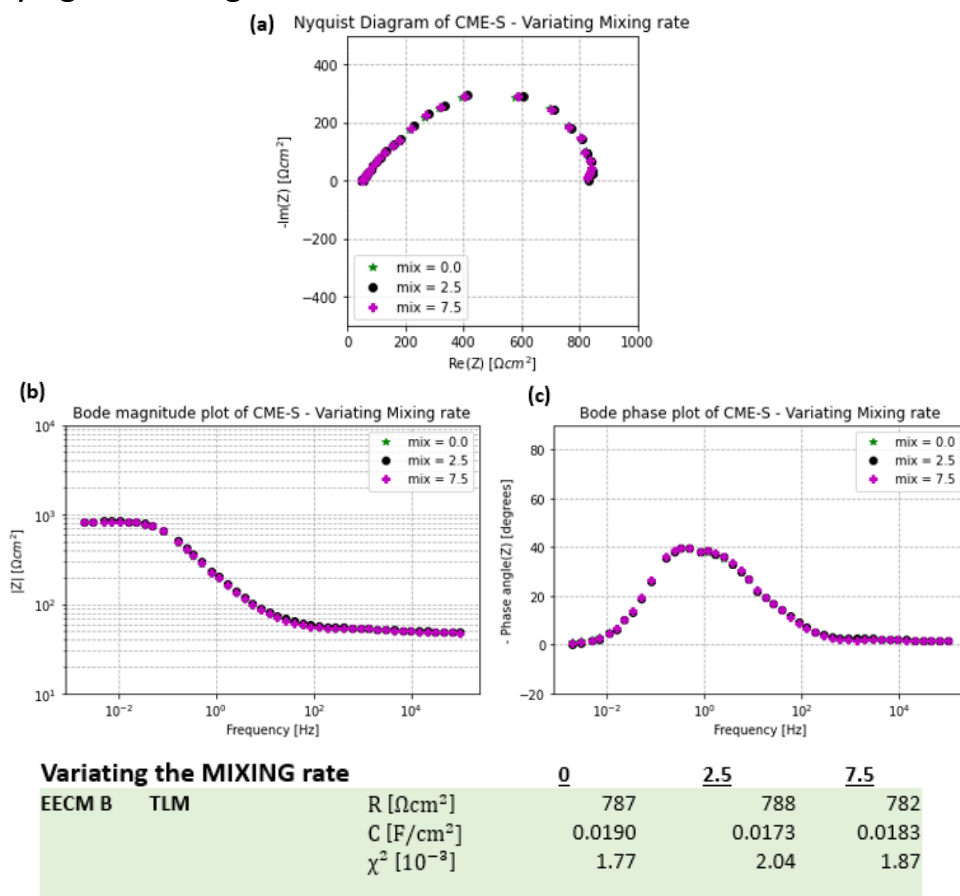


Figure 42: EIS measurements performed on CME-S at different mixing rates. The denoted number of the mixing rate is the number on the ColeParmer® Hotplate knob. The other operational parameters are constant: flowrate of 8.0mL/min, temperature is 25°C, and initial salt concentration of KCl is 960mg/L. (a) The Nyquist plot of the EIS data of CME-S at different mixing rates, (b) the Bode magnitude plot of the EIS data of CME-S at different mixing rates, and (c) the Bode phase plot of the EIS data of CME-S at different mixing rates. The different mixing rates are: 0.0, 2.5, and 7.5. The impedance equation of five EECMs has been fitted through the EIS data in the Nyquist plot, the values of the parameters of the fit are displayed in the table below the figure.

The mixing rate is defined as the rotation velocity of the magnetic stirrer in the reservoir. The mixing rate is also an operational parameter which was changed to observe the effect on the EIS data of CME-S. The mixing rate is not expected to have any influence on the EIS measurement, and as the impedance plots of Figure 42 illustrate, is this true. The EIS datapoints in the impedance plots overlap each other so the membrane resistances, membrane capacitances and transport time constants are equal. That the mixing rate has no effect on the EIS measurement is no surprise because the magnetic mixer in the design of the CME meter mixes the salt inside the electrolyte which only result in a homogeneous salt concentration in the feed stream. The pump, which inserts the electrolyte in the chemical cell, actually already ensures that the electrolyte is mixed, so the mixer is actually obsolete.

5.1.3 Varying the concentration of KCl in the electrolyte

Contrary to the mixing rate and flowrate, the concentration is expected to have a very large effect on the EIS measurements. A larger salt concentration in the electrolyte means that there are more ions inside the electrolyte, resulting in the conductivity of the ionic current to increase. The membrane resistance reduces. The membrane capacitance is expected to increase when the concentration increases, because, according to the Grahame model, the Debye length reduces at higher salt concentration, meaning more ions could be stored inside the electrical double layer of the CME [40,43].

EIS was performed on CME-S when it was emerged in a lower and a higher KCl concentration in the electrolyte and the result is showed in the impedance plots of Figure 43.

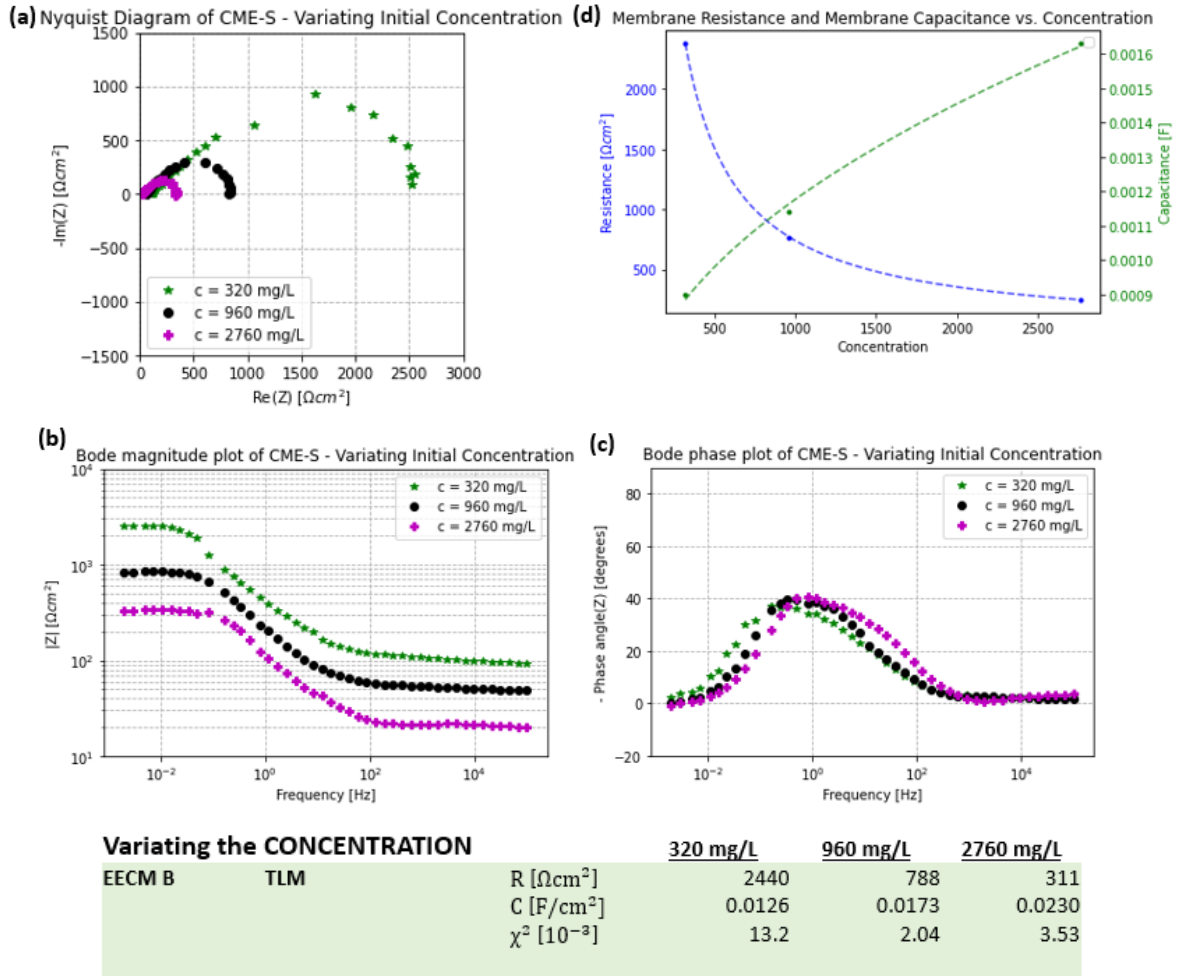


Figure 43: EIS measurements performed on CME-S at different concentrations of KCl. The different concentrations are: 320mg/L, 960mg/L, and 2760mg/L. The other operational parameters are constant: flowrate of 8.0mL/min, temperature is 25°C, and mixing rate at 2.5. (a) The Nyquist plot of the EIS data of CME-S at different concentrations of the electrolyte, (b) the Bode magnitude plot of the EIS data of CME-S at different concentrations of the electrolyte, and (c) the Bode phase plot of the EIS data of CME-S at different concentrations of the electrolyte. The impedance equation of five EECMs has been fitted through the EIS data in the Nyquist plot, the values of the parameters of the fit are displayed in the table below the figure. (d) The dual plot of the membrane resistance plotted against the concentration and the membrane capacitance plotted against the concentration. The curves are fitted to guide the eye.

The Nyquist plot, Figure 43a, illustrates the effect of the concentration on the membrane resistance: the resistance, the point in the Nyquist plot where data reaches the real impedance axis, is approximately three times smaller when the concentration is three times larger. And the reverse is true for a three times smaller salt concentration: the resistance is approximately three times larger. This was expected because a higher concentration means there are more ions in the electrolyte, resulting in more ions in the CME, causing the conductivity of the ions in the membrane to increase, reducing the membrane resistance. The Bode phase diagram in Figure 43c shows that the peak occurs at a higher frequency for higher concentrations. This means that the transport time constant τ_t is lower at higher concentrations. Still, τ_t is not as strongly affected by the concentration as the membrane resistance. This means that the membrane capacity of the CME actually increases, but less than the membrane resistance decreases, when the concentration of the electrolyte increases, because the transport time constant is calculated with $\tau_t = RC$. That the membrane capacitance increases when the concentration increases agrees with the Grahame model [43]. Important to observe is that the membrane capacity is higher when the concentration increases, but the relation is not linear, as proved

by the values in the table below Figure 43. As was explained by the book of Schmickler & Santos (2010), the capacitance of an electrode is determined by the Gouy-Chapman and the Helmholtz capacitance [40]. Increasing the concentration reduces the Debye length with the square root of the concentration. The Gouy-Chapman capacitance increases linearly with the Debye length, thus, the Gouy-Chapman capacitance depends on the square root of the concentration [40]. The Helmholtz capacitance stays constant, but at low salt concentrations, the Gouy-Chapman capacitance dominates the value of the membrane capacitance [40]. So, concentration influences the membrane resistance R , which decreases linearly with increasing concentration, and influences the membrane capacitance C , which increases with the square root of the concentration (Figure 43d). This results in a transport time constant which reduces at higher concentrations.

The quality of fit of the impedance equations are almost two orders of magnitude higher than the CME-S at standard operational conditions. This difference is directly the effect of the magnitudes of the EIS datapoints which influence the χ^2 -values. Also, the quality of the fit is influenced by the scatter of the EIS datapoints, which is clearly visible in the Nyquist plot of the CME-S with a concentration of 320mg/L (green stars).

5.1.4 Varying the temperature

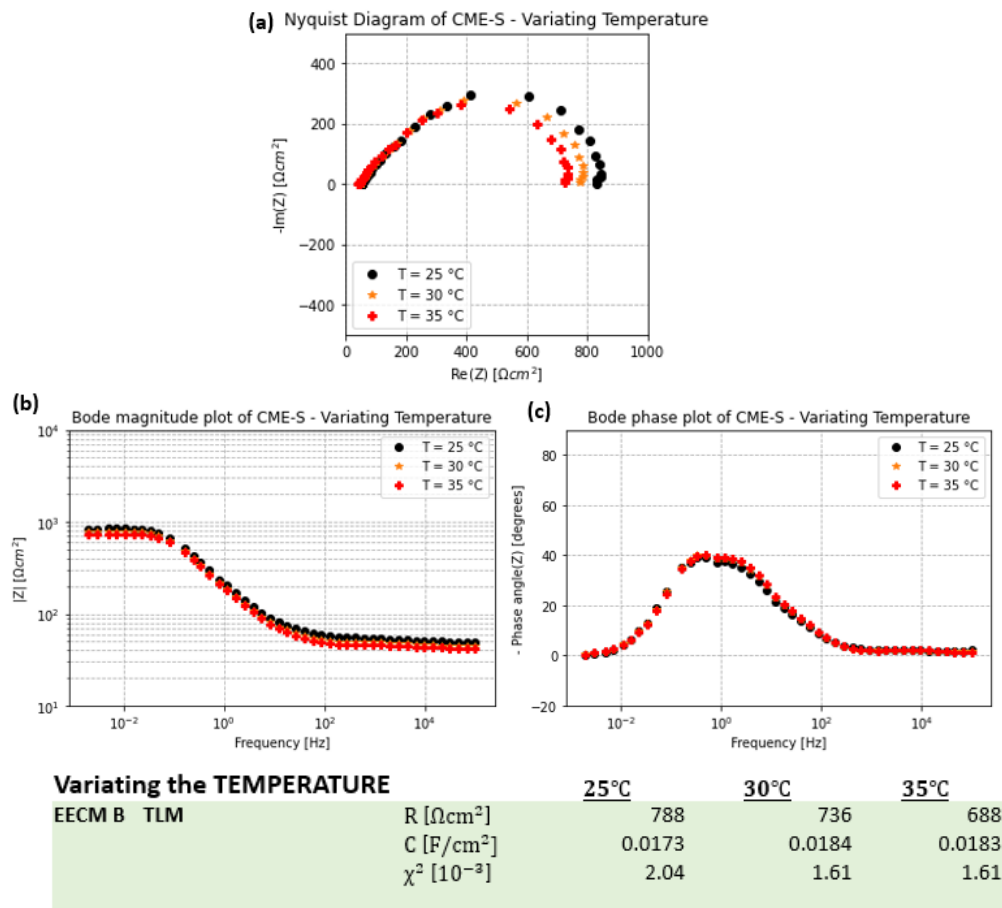


Figure 44: EIS measurements performed on CME-S at different temperatures. The other operational parameters are constant: flowrate of 8.0mL/min, mixing rate at 2.5, and initial salt concentration of KCl is 960mg/L. (a) The Nyquist plot of the EIS data of CME-S at different temperatures, (b) the Bode magnitude plot of the EIS data of CME-S at different temperatures, and (c) the Bode phase plot of the EIS data of CME-S at different temperatures. The different temperatures are: 25°C, 30°C, and 35°C. The impedance equation of five EECMs has been fitted through the EIS data in the Nyquist plot, the values of the parameters of the fit are displayed in the table below the figure.

The temperature is, just like the concentration, an operational parameter which must be held constant during the EIS measurements because it has an effect on the measured EIS data [75]. The physical

explanation is that the diffusion of the ions depends on the temperature: the higher the temperature, the faster the diffusion of ions. A higher diffusion means that the ions are faster transported into the pores of the CME, resulting in a faster adsorption rate [129]. The membrane resistance of the ions is therefore expected to decrease when the temperature increases. The Nyquist plot in Figure 44a shows that the increased temperature indeed results in a lower membrane resistance: the plot stops at the real impedance axis at a lower resistance for higher temperatures. The membrane resistance is thus lower when the temperature of the electrolyte and the cell are higher, which could also be concluded from the values of R in the table of Figure 44. A higher temperature increases the conductivity, which results in a lower membrane resistance R . The Bode phase diagram shows that the peak of the graph is at the same frequency which means that the time constant has the same value at different temperatures. This means that the capacitance must increase to give the same time constant. Only, the table below Figure 44 shows that the membrane capacitance C decreases slightly when the temperature increases. This small decrease in the membrane capacitance could be explained by the Grahame model [43]. The Gouy-Chapman capacitance depends not only on the concentration but also on the temperature: the Debye length increases with the square root of the temperature, resulting in the capacitance to decrease with the square root of the temperature [40]. Additionally, the Gouy-Chapman capacitance C_{GC} equation is a cosine hyperbolic function, in which the slope of the line decreases when the temperature increases [40]. Thus, a higher temperature result in a smaller value of the Gouy-Chapman capacitance C_{GC} , and thus also a smaller membrane capacitance [40].

5.2 Relation between CME thickness and the membrane conductivity

The membrane conductivity is expected to be a material property of the CME, calculated with the following equation (Equation 3.13),

$$\kappa_m = \frac{t}{RA}$$

Where κ_m is the membrane conductivity in $\mu S/cm$, t is the thickness of the CME, and RA is the area resistance in Ωcm^2 which is equal to the electrochemical parameter membrane resistance R which was estimated from fitting the TLM through the impedance data. To verify that the membrane conductivity is indeed a material property, the relationship between the thickness of the CME and the membrane resistance determined by EIS was investigated. Therefore, EIS measurements are performed on CMEs, made of the same material and in the same mass percentages as the standard CME (CME-S), only the thickness has been varied. The membrane resistance is determined by fitting the impedance equation of the TLM through the EIS data, then, the membrane conductivity is calculated using Equation 3.13. Expected is that the membrane conductivity is approximately equal for all the investigated CMEs because the membrane resistance increases when the thickness of the CME increases.

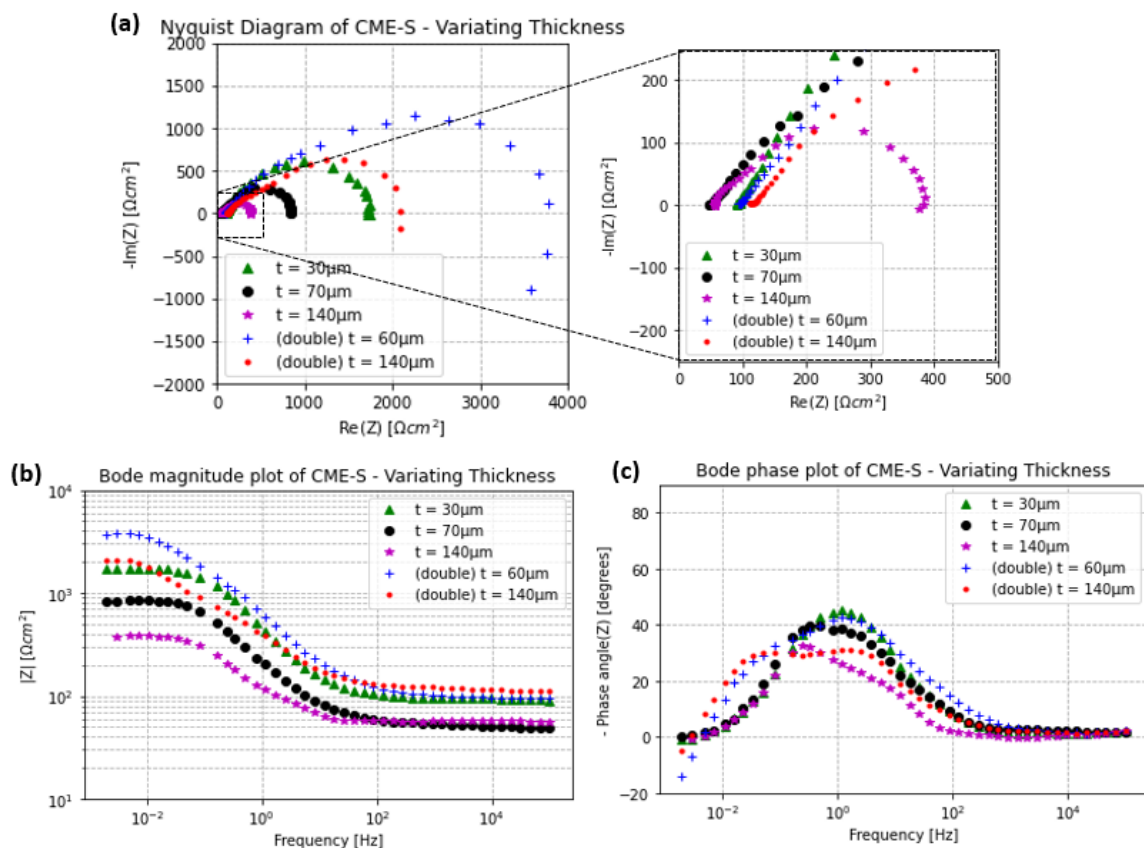


Figure 45: EIS measurements performed on CME-S with different thicknesses. The standard operating conditions are: flowrate of 8.0mL/min, mixing rate of 2.5, temperature of 25°C and KCl concentration of approximately 960mg/L. The different thickness are: 30 μm , 70 μm , and 140 μm . Additionally, the thickness of the CME was doubled by placing two instead of one CME inside the CME meter. The CME S with a thickness of 30 μm was doubled as was the CME-S with a thickness of 70 μm .

The resulting EIS data is plotted in the impedance plots in Figure 45, while the calculated membrane conductivity can be found in Table 6. The most noticeable part in the Nyquist plot in Figure 45a is that the EIS data of thicker CMEs generates a smaller semi-circle than the thinner CMEs. A smaller semi-circle means that the membrane resistance is smaller, thus the thicker CMEs have a smaller membrane resistance than the thinner CMEs. This observation is also visualised in the Bode magnitude plot by looking at the magnitude at which the line becomes constant: the magnitude at which the 30 μm thick CME becomes constant is higher than the magnitude at which the 140 μm thick CME becomes constant. The resulting values of the membrane resistance for the different thicknesses are displayed in Table 6.

That the membrane resistance is smaller when the CME is thicker is contra intuitive with the theory of the resistance and thickness relation. For any resistive medium, as the resistance usually scales linearly with the path length of the current through the medium, as is for example the case for ion exchange membranes [66,68]. The diffusional pathlength of the ions increases as the thickness increases: the ions simply have to travel over a longer distance through the membrane [108]. Note that the peak in the Bode phase plot in Figure 45c, which indicates that the ions need more time to travel through the CME when it is thicker, because the peak is at lower frequencies when the CME is thicker. The peak in the Bode phase diagram indicates the transport time constant, which is an indication of the amount of time the ions need to transport through the CME (see also Table 6 for the values of τ_t for different thicknesses) [76]. Thus the ions need more time to travel through the thicker CMEs, however, the fact remains that the resistance is much lower for thicker CMEs than thinner CMEs.

In the study of lithium-ion batteries, it has been shown that the total electrode resistance (summation of the ionic resistance, charge transfer resistance and total internal resistance) reduces when the

electrode thickness is increased until a minimum thickness is reached [108,130,131]. After this minimum thickness, the resistance increases with increasing thickness. This effect could occur when the thicker electrodes are fabricated with the same fabrication procedure as the thinner electrodes [131]. Araki et al. (2016) explained that for thicker electrodes, the binder (PVDF) and conductive additive (CB) are more homogeneously distributed, which results in the internal resistance to be smaller for ions to be adsorbed [131]. The paper of Jaiser et al. (2016) explains this process in more detail: the higher resistance for thinner CMEs is caused by the evaporation rate of acetone during the fabrication of the CME. According to their paper, the drying process of an electrode slurry has influence on the structure which has influence on the resistance [132]. High drying rates give the binder particles in the slurry not enough time to homogeneously spread themselves over the slurry [132]. If the solvent (acetone) dries is too fast, polymeric binder PVDF accumulates at the surface of the CME and has no time to equally distribute over the CME [132]. This process creates a layered electrode. PVDF is a binder and acts as a glue, when PVDF particles accumulate, pores are blocked, resulting in a larger resistance for the ions to move through the pores. Arunkumar & Paul (2017) also saw that the binder particles in the CDI electrode agglomerate when the drying temperature of the oven is close to the boiling point of the solvent, resulting in the active surface area to reduce extremely [89]. Salleh et al. (2023) explained that the reduction in active surface area is because there is too little “glue” for the carbon black particles and graphite particles to create the active sites when PVDF particles accumulate [88]. The active surface area (or active sites) of the CME thus also depends on the drying rate of the slurry, and this effect could thus be found in the value of the membrane capacitance. Table 6 indeed shows that the thicker CMEs have a higher membrane capacitance. Thus, if acetone dries is too fast, the structure of the CME consist of accumulated PVDF particles, resulting in a higher membrane resistance, because the PVDF agglomerates block pores, and a lower membrane capacitance, because the glue between the graphite and carbon black reduces resulting in less active sites. A similar effect may be going on for our CMEs as the method for making CMEs has a lot of similarities with the manufacturing method of lithium-ion battery electrodes. For CMEs, the thicker CME were made with the same electrode material slurry as the thinner CMEs, only the thickness of the doctor blade was changed. Thicker CMEs have a lower surface-to-volume ratio which means that there are less surfaces where the solvent could evaporate out of, thus the drying rate reduces. The PVDF particles have more time to equally distribute themselves over the slurry which excludes the creation of a layered structure and improves the “glue-function” of the PVDF. The result may be that the thicker CMEs have more active sites and less PVDF agglomerates which function as an obstacle, resulting in the membrane resistance of the thicker CMEs to be smaller than the thinner CMEs and the membrane capacitance of the thicker CMEs to be larger than the thinner CMEs.

The structure of the CMEs was assumed to be homogeneous, however, the paper of Jaiser et al. (2016) suggests that this may not be the case for CMEs which have one side which has been dried in air while the other side lies on glass where no acetone could evaporate out of [132]. This drying process of the

CME result in the CME having two layers: the top has a lot of PVDF particles which accumulated resulting in an increased resistance, while the bottom gets less PVDF which result in a smaller resistance [132]. To test whether this could be the case for our CMEs as well, a test was performed with the CMEs oriented in two different ways: The black curve in Figure 46 shows the original EIS trace for the pair of CMEs, while the red curve shows the result after flipping one of the CMEs around. Figure 46 shows that flipping the side of the CMEs in the cell results in a significant difference in the measured membrane resistance. The resistance of one side is thus higher than the resistance on the other side.

In principle, one should be able to measure the full impedance of the CME by having the top of one CME facing the bottom of the other CME in the setup, so that the impedance of both sides is included in the EIS data. However, the top and bottom had not been marked before as both sides were presumed to be identical. Therefore, it cannot be said with certainty what the orientation in the original and 'flipped' configuration is in Figure 46, although the figure indicates that this flipping does make difference.

The CME has a two-layer structure and each layer has its own resistance, so it is expected that the EECM inhomogeneous TLM (EECM C) would fit the EIS data of the CME better because this model consists of two TLMs, but the double transmission-line has a quality of fit value that is not one order lower than the 'conventional' TLM (EECM B). Therefore, the TLM is maintained as the chosen model to describe the impedance inside the CME.

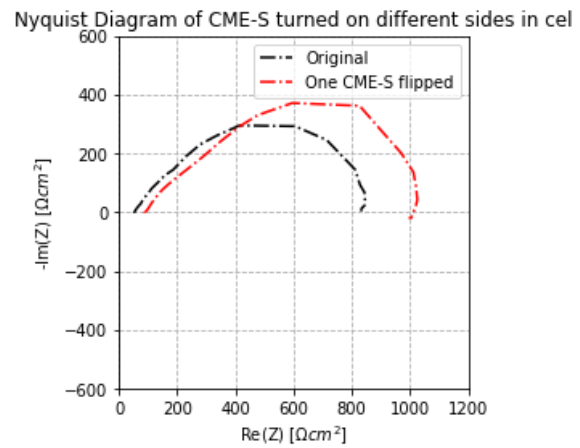


Figure 46: Difference in the measured EIS data when one CME, placed in the CME-cell of the CME meter, is rotated to the other side. The black line shows the EIS data of the original EIS trace and the red line shows the EIS data when one CME-S is flipped on the other side. The difference in membrane resistance is approximately $200\Omega\text{cm}^2$, which is quite a significant difference, proving that CME-S is not homogeneous in the z-direction.

Table 6: Values retrieved by fitting the impedance equation of the Transmission-Line Model in the EIS data of the CMEs made with the same compositions of CME-S, only with different thicknesses. χ^2 is the quality of fit, R is the membrane resistance in Ωcm^2 , C is the membrane capacitance in F/cm^2 , τ_t is the transport time constant in s, and κ_m is the membrane conductivity in $\mu\text{S}/\text{cm}$.

Varying thickness (CME-S)	R [Ωcm^2]	C [F/cm^2]	χ^2 [10^{-3}]	τ_t [s]	κ_m [$\mu\text{S}/\text{cm}$]
$t = 30\mu\text{m}$	1620	0.0068	16.1	11	4.3
$t = 70\mu\text{m}$	788	0.0173	2.04	14	8.9
$t = 140\mu\text{m}$	326	0.0401	17.2	13	21
(double) $t = 60\mu\text{m}$	3580	0.0115	482	41	2.0
(double) $t = 140\mu\text{m}$	1950	0.0321	66.9	63	3.6

Additional EIS experiments were done with the CME meter by placing twice as much of the CMEs inside the CME-cell to test if doubling the CME would also reduce the membrane resistance. The result is also illustrated in the impedance plots of Figure 45. When looking at the Nyquist plot, doubling the CME increases the membrane resistance. The membrane resistance of the (double) $t = 140\mu\text{m}$ (red crosses) CME is approximately five times larger than the $140\mu\text{m}$ CME (purple stars). The other double CME (blue dots) also shows that the semi-circle is much larger than the semi-circle of $70\mu\text{m}$ CME (black dots). Thus doubling the CMEs has not the same effect as fabricating thicker CMEs. This could also

indicate that the structure of the thicker CMEs is different to that of the thinner CMEs, but another explanation for this difference could be that there are air bubbles between the CMEs which increase the membrane resistance.

So the thickness of the slurry also affects the structure of the CME and the conductivity of the ions in the CME. The membrane conductivity is a material property, so the different values for the membrane conductivity prove that the structure of the CMEs differ from each other when the same slurry is smeared with different thicknesses on a glass plate.

5.3 Investigating the effect of charge on CME properties

EIS has been performed on the standard CME (CME-S), however, now, the CMEs have been charged. The goal of the EIS measurements on charged CMEs is to find out if the permselectivity of the investigated CME could be determined. To calculate the permselectivity, the two equations for the permselectivity of negatively and positively charged CMEs were derived (Appendix C). In this equation the membrane resistance R from the fit of the TLM of the EIS data of the uncharged CME and the charged CME was used to calculate the permselectivity. The CMEs in the CME meter are charged by applying a potential between the end electrodes and the CMEs with a power supply. Charging the CME results in the CME having a certain permselectivity, which is attempted to be determined by EIS. Expected is that the membrane resistance of the charged and uncharged CMEs relate to the value of the permselectivity according to the equations (Equation 3.12),

$$P_- = 1 - \frac{R_C}{R_N} \quad P_+ = \frac{R_C}{R_N} - 1$$

where P_- is the permselectivity of the cations when the applied potential difference between the CMEs and the end electrodes is negative, P_+ is the permselectivity of the anions when the applied potential difference between the CMEs and the end electrodes is positive, R_N is the membrane resistance of the uncharged CME determined from the EIS measurement in Ωcm^2 , and R_C is the membrane resistance of the charged CME determined from the EIS measurement in Ωcm^2 . The calculated permselectivity is displayed in Table 7.

Table 7: Values retrieved by fitting the impedance equation of the Transmission-Line Model in the EIS data of the Standard CME (CME-S). χ^2 is the quality of fit, R is the membrane resistance in Ωcm^2 , C is the membrane capacitance in F/cm^2 , τ_t is the transport time constant in s, and P is the permselectivity.

Standard CME (CME-S)	R [Ωcm^2]	C [F/cm^2]	χ^2 [10^{-3}]	τ_t [s]	P [-]
+1,0V	683	0,0140	658	9,6	-0,13
+0,5V	701	0,0141	659	9,9	-0,11
0,0V	788	0,0173	112	14	---
-0,5V	719	0,0228	734	16	+0,09
-1,0V	679	0,0200	673	14	+0,14

The impedance plots in Figure 47 show the result of the EIS measurements on CME-S when the CMEs are uncharged (No Charge), positively charged (Charge +0.5V and Charge +1.0V), and negatively charged (Charge -1.0V and Charge -0.5V). The Nyquist plot, in Figure 47a, shows that the charging of the CMEs result in a smaller membrane resistance. These findings are also displayed in Table 7 where the quality of fit value of the charged CMEs are larger than of the uncharged CME-S, while the membrane resistance is smaller. The smaller membrane resistance of the charged CMEs was expected. Charging the CME result in the increase of counter-ions concentration in the EDL of the CME structure. The ions are mobile charged particles, thus increasing the concentration of ions means that the conduction of the current increases. Subsequently, the resulting membrane resistance of the charged CMEs are smaller due to the large concentration of positive ions when the CME is positively charged or the large concentration of negative ions when the CME is negatively charged.

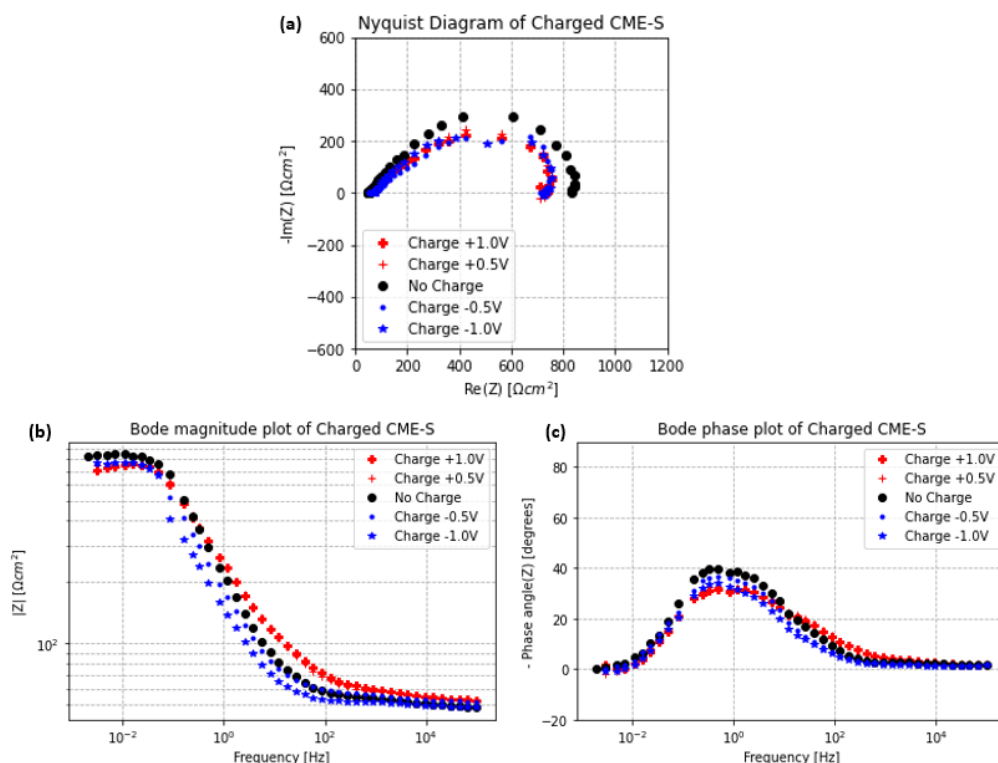


Figure 47: Electrochemical Impedance Spectroscopy performed on the Standard CME (CME-S) when it was positively charged, uncharged and negatively charged. The CME was charged by placing a potential between the CMEs and the end electrodes of +1.0V, +0.5V, -0.5V, and -1.0V. The Transmission-Line Model has been fitted through the EIS data in the Nyquist plot and the resulting values are displayed in Table 7.

The Bode phase diagram, Figure 47c, shows that the peak of the phase angle is approximately at the same frequency for the charged and uncharged CMEs, which indicates that the membrane capacitance is larger for the charged CMEs than the uncharged CMEs, because the R is smaller. Table 7 shows the values of the transport time constant τ_t and the membrane capacitance C. The membrane capacitance is larger for the negatively charged CMEs but is smaller for the positively charged CMEs. This difference could be explained by the point of zero charge (PZC). The point of zero charge is the potential where the capacitance of the electrode is at its minimum [46]. During the charging of the CMEs, the potential difference between the CMEs and the Ag/AgCl (3M KCl) reference electrode was measured after 30 minutes of charging. The electrolyte KCl concentration was low, so could be assumed that the capacitance is fully determined by the Gouy-Chapman capacitance (C_{GC}). PZC is calculated by fitting the equation of the Gouy-Chapman capacitance (Equation 2.10) through the datapoints and finding the potential where the membrane capacitance is at its minimum. The result is that the point of zero charge of CME 1 is $-0.559V$ and the point of zero charge of CME 2 is $+0.013V$, as shown in Figure 48. For adsorption of ions, the applied

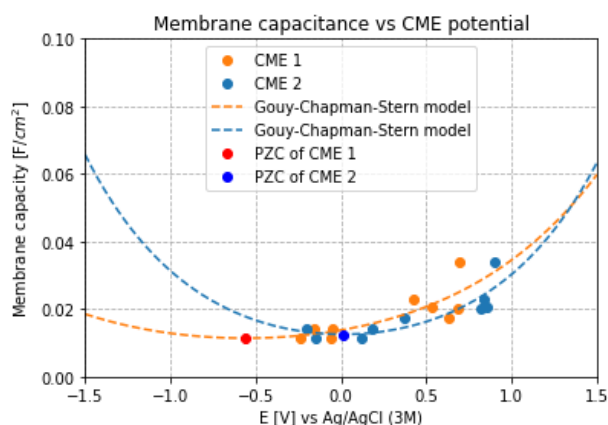


Figure 48: The point of zero charge of CME 1 and CME 2 when the electrolyte has a concentration of 960mg/L (12.8mM). The membrane capacitance plotted against the measured potential difference of the CME and the Ag/AgCl reference electrode. The membrane capacitance C is determined from the fit of the TLM in the Nyquist plot of Figure 47a at different applied potentials. The Gouy-Chapman-Stern Model has been fitted through the datapoints when is assumed that the Gouy-Chapman capacitance is dominant. The fit of figure (b) is inaccurate because there are too little datapoints. The point of zero charge of CME 1 is $-0.559V$ (red dot) and the point of zero charge of CME 2 is $+0.013V$ (blue dot).

potential on the CME must deviate from the point of zero charge, otherwise counter-ions are not attracted [45]. CME 1 has a very negative PZC which means that applying a negative potential of -1.0V between the CME 1 and end electrode 1 was not enough to make the CME more negative to become more selective for cations. CME 1 even became more positive when a potential of -1.0V was applied and attracts even anions instead of cations. Thus, when the negative potentials -1.0V and -0.5V were applied, CME 1 attracts anions while CME 2 has a low attraction for cations, see the datapoints in Figure 48. The EIS data of the negatively charged CMEs in Figure 47 and Table 7 is thus actually the EIS data of one negatively and one positively charged CME. Determining the PZC and differentiating between the applied potential on the CMEs is thus important to determine if both CMEs were actually negative or positive during the EIS measurement. Table 7 shows that the membrane conductivity increases when the CMEs are charged, no matter what the potential is, which completely agrees with the Grahame model. The Gouy-Chapman capacitance increases when a potential is applied on the electrode which deviates from the PZC [40]. Important note for Figure 48 is that there were too little EIS experiments conducted on the charged CME-S to accurately fit the Gouy-Chapman-Stern model through the datapoints. Also, it is weird that two CMEs from the same material sheet, have such a large difference between their points of zero charge. More experiments should be conducted to determine the PZC of the CMEs.

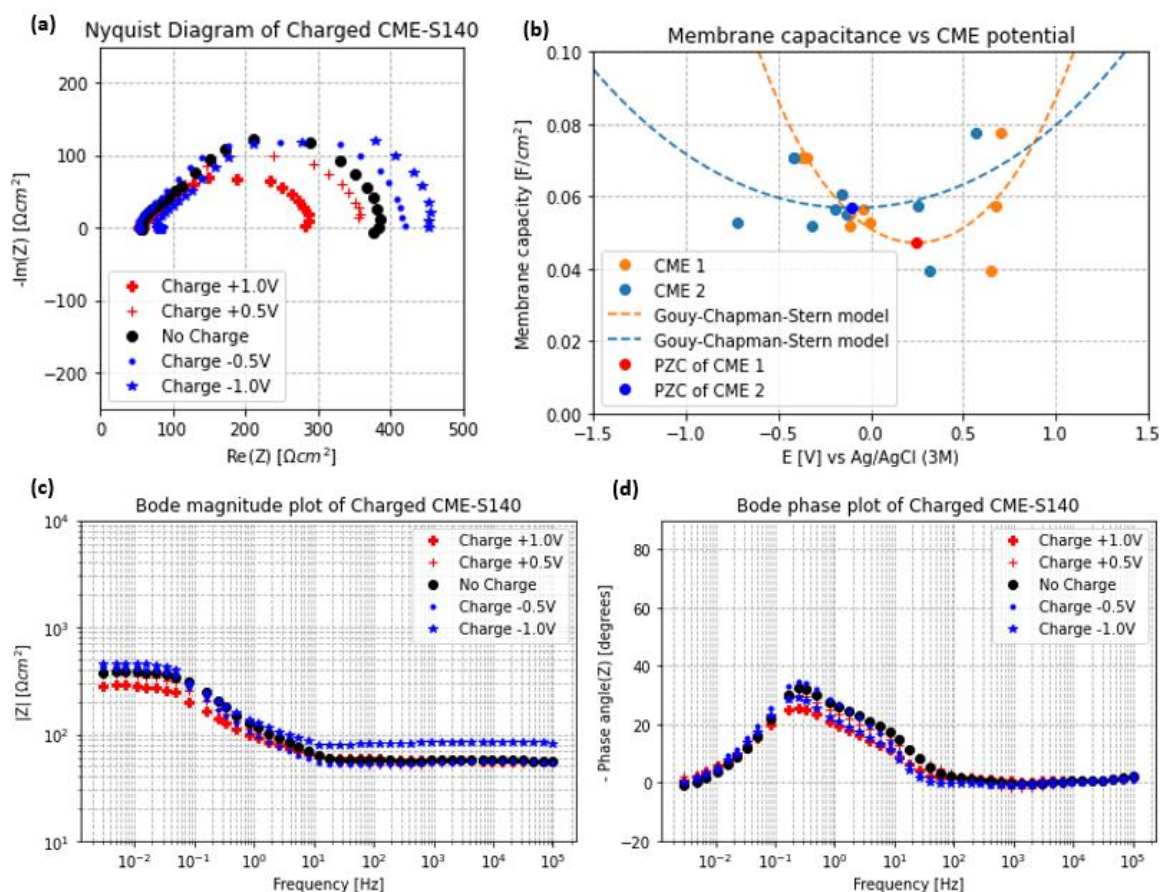


Figure 49: EIS data of the Standard CME with a thickness of 140μm (CME-S140) when it was positively charged, uncharged and negatively charged. The CME was charged by placing a potential between the CMEs and the end electrodes of +1.0V, +0.5V, -0.5V, and -1.0V. (a) Nyquist diagram of CME-S140, the (c) Magnitude Bode Plot of CME-S140, and the (d) Phase Bode Plot of CME-S140. The uncharged CME-S140 has been included in the figure for comparison with the charged ones. The Transmission-line model has been fitted through the impedance datapoints in the Nyquist plot. The PZC of CME 1 is +0.25V and the PZC of CME 2 is -0.10V.

To investigate better what happens with the EIS data when both CMEs are negatively charged, the same charge EIS experiments has been repeated on CME-S with a thickness of 140μm (CME-S140). The result of the charge EIS experiments performed on CME-S140 is displayed in Figure 49. Figure 49b

shows the membrane capacitance plotted against the measured potential difference of the CME and the Ag/AgCl reference electrode, where the PZCs of the CMEs is highlighted in the figure. As explained earlier, this figure is not accurate enough to estimate the PZCs but the graph shows that the PZCs are close to each other and that the CMEs were both negatively charged and positively charged during the charge EIS experiments. Figure 49b shows that the applied potentials on the CMEs deviated enough from the point of zero charge to attract and repel ions. So, both CMEs became negatively charged when a potential of -0.5 and -1.0 V were applied and both CMEs became positively charged when a potential of $+1.0$ V was applied. When $+0.5$ V was applied, the CMEs were both very close to their point of zero charge. The result is very surprising. The membrane resistance of the negatively charged CME is larger than the membrane resistance of the uncharged CME. This effect is not in agreement with Donnan's theory, which states that a negatively charged membrane blocks anion transport and facilitates cation transport. The cation concentration in the CME increases which results in the membrane resistance of the charged CME to be lower. The membrane resistance was therefore expected to be lower, regardless of whether the CME was positively or negatively charged. An physical explanation for this phenomena could not be found and a similar effect on either CDI electrodes nor ion exchange membranes was found in the literature. With this given, the permselectivity is calculated by using the following equation:

$$P = \frac{R_C}{R_N} - 1,$$

where the permselectivity P is positive when the CME is positively charged and the permselectivity is negative when the CME is negatively charged. The positive potentials between the CMEs and end electrodes result in smaller membrane resistances which agrees with our expectations. Figure 49a and Figure 49b show, at an applied potential of $+1.0$ V, that both CMEs are positively charged resulting in a smaller membrane resistance than the uncharged CME. Figure 49a also shows that at -0.5 V the membrane resistance is a little bit smaller than the membrane resistance of the uncharged CME, which according to Figure 49b, could be explained by the fact that this applied potential is close to the PZC of both CMEs resulting in a small attraction of counter- and small rejection of co-ions.

Table 8: Values retrieved by fitting the impedance equation of the Transmission-Line Model in the EIS data of the CME-S with a thickness of $140\mu\text{m}$ (CME-S140). χ^2 is the quality of fit, R is the membrane resistance in Ωcm^2 , C is the membrane capacitance in F/cm^2 , τ_t is the transport time constant in s, and P is the permselectivity.

Standard CME (CME-S140)	R [Ωcm^2]	C [F/cm^2]	χ^2 [10^{-3}]	τ_t [s]	P [-]
+1,0V	227	0,0775	220	16	- 0,30
+0,5V	298	0,0576	226	17	- 0,09
0,0V	326	0,0401	122	13	---
-0,5V	361	0,0605	415	22	+ 0,11
-1,0V	375	0,0563	557	21	+ 0,15

To summarise, the magnitude of the membrane resistance shows how strong the rejection of co-ions and the attraction of counter-ions is, in other words, how large the permselectivity is for a certain applied potential. Some desalination experiments should be performed to check if the calculated permselectivity of the CME from the EIS data corresponds to the actual permselectivity of the CME, however, this lies outside the scope of this Thesis project. Also, more charge EIS experiments should be conducted to conclude if the transport time constant and the permselectivity have a relation and what that relation is exactly. Therefore, more charge EIS experiments were conducted on CMEs with other compositions than CME-S in the next section.

5.4 Determining performance indicators of CMEs with different compositions

The structure of the CMEs that result in high performance indicators is still unknown, so EIS experiments are being carried out to gain a better understanding of the electrochemical processes that occur within the structure of the CME and to determine what the structure of the CME should be in order to improve the performance indicators. To this end, EIS experiments are performed on CMEs with different structures, the impedance equation of the TLM is fitted through the EIS data to estimate the electrochemical parameters and performance indicators, and then the performance indicators and electrochemical parameters are compared with those of CME-S. Other materials result in a different crystalline structure of the CME, resulting in other electrochemical parameters. All experiments were performed at standard operational conditions: flowrate of 8.0mL/min, mixing rate of 2.5, temperature of 25°C and KCl concentration of approximately 1.0mg/L. The EIS data of these different CMEs are compared with the EIS data of CME-S, thus, the influence of the combination and amount of active material, conductive additives and polymer binder in the CME structure on the measured impedance is investigated. CME-S has a mass composition of graphite (G), carbon black (CB) and PVDF of 45:8:47wt%. The different CMEs, with different materials or mass compositions than CME-S, that are placed inside the CME meter are:

- **CME-AC:** the active material is replaced by activated carbon instead of graphite (like CME-S) without changing the mass percentages. (AC:CB:PVDF=45:8:47wt%.)
- **CME-PVDF:** the mass percentage of the polymeric binder PVDF is reduced, by halving the amount of added mass of PVDF in the slurry (as compared to CME-S). (G:CB:PVDF=60:10:30wt%.)
- **CME-CB:** the mass percentage of the conductive additive carbon black is increased, by doubling the amount of added mass of carbon black in the slurry (as compared to CME-S). (G:CB:PVDF=43:14:43wt%.)
- **CME-G:** the mass percentage of the active material graphite is reduced, by halving the amount of added mass of graphite in the slurry (as compared to CME-S). (G:CB:PVDF=29:11:60wt%.)

In total four CMEs with different compositions have been placed inside the CME meter and the resulting EIS data is showed in Figure 50 together with the EIS data of CME-S. The Nyquist plot in Figure 50a shows that the four CMEs have a smaller semi-circle than CME-S resulting in a smaller membrane resistance. The peaks in the Bode phase plot of the different CME compositions are for CME-PVDF, CME-CB and CME-PVDF at higher frequencies than CME-S, resulting in smaller time constant τ_t . The peak in the Bode phase plot of CME-AC is at a much lower frequency resulting in a larger value for τ_t .

Table 9: Values retrieved by fitting the impedance equation of the Transmission-Line Model in the EIS data of different CMEs with different slurry compositions: CME-S, CME-AC, CME-PVDF, CME-CB, and CME-G. χ^2 is the quality of fit, R is the membrane resistance in Ωcm^2 , C is the membrane capacitance in F/cm^2 , τ_t is the transport time constant in s, κ_m is the membrane conductivity in $\mu\text{S}/\text{cm}$, P_+ is the permselectivity when the CME is positively charged by placing a potential of +1.0V between the CMEs and the end electrodes, and P_- is the permselectivity when the CME is negatively charged by placing a potential of -1.0V between the CMEs and the end electrodes.

CMEs with different compositions	R [Ωcm^2]	C [F/cm^2]	χ^2 [10^{-3}]	τ_t [s]	κ_m [$\mu\text{S}/\text{cm}$]	P_- [-]	P_+ [-]
CME-S	788	0.017	2.04	14	8.9	- 0.14	- 0.13
CME-AC	133	1.10	37.6	146	278	+ 0.19	- 0.27
CME-PVDF	91.6	0.024	47.2	2.2	65.5	+ 0.14	- 0.28
CME-CB	47.7	0.103	141	4.9	126	- 0.04	- 0.12
CME-G	341	0.034	55.9	12	19.1	+ 0.22	- 0.29

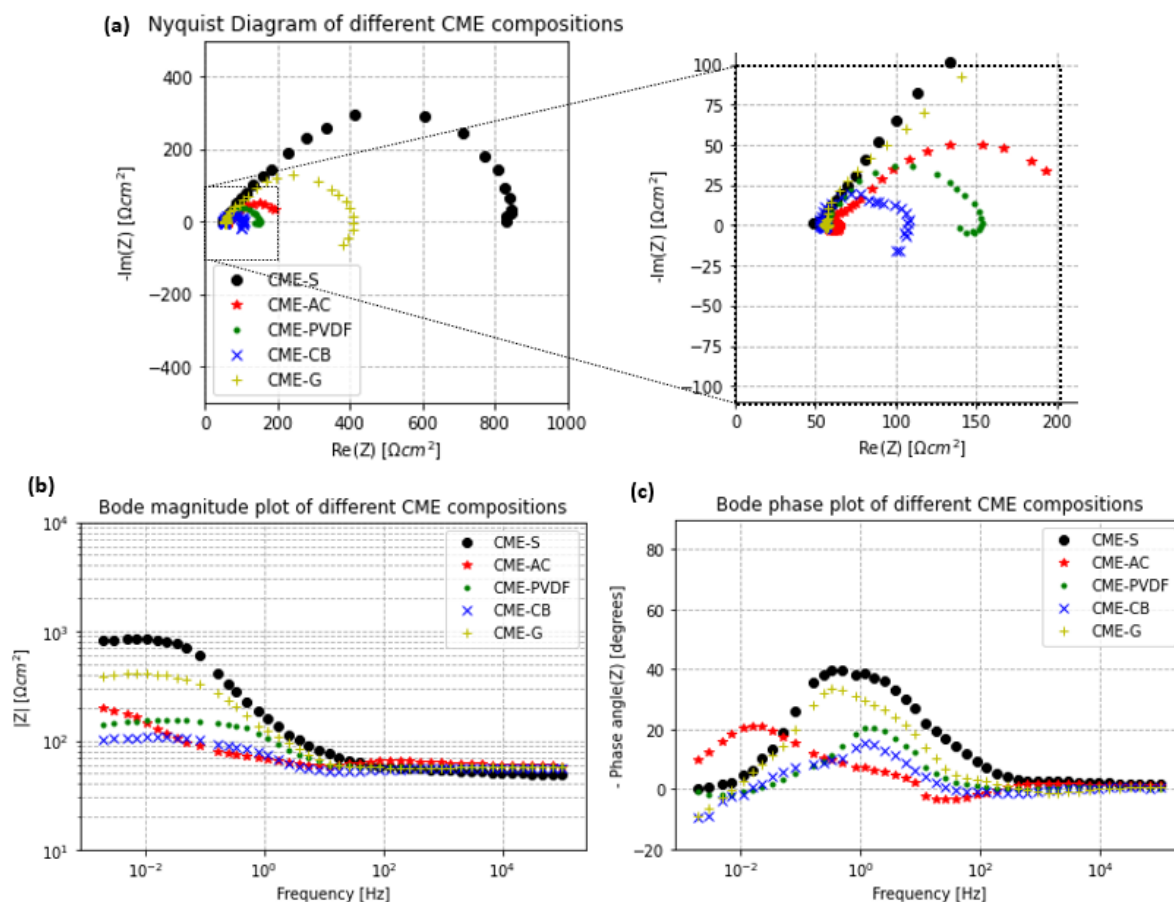


Figure 50: Impedance plots of electrochemical impedance spectroscopy measurements on CMEs with different structures. (a) Nyquist diagram of CMEs with different structures, (b) Magnitude Bode Plot of CMEs with different structures, (c) Phase Bode Plot of CMEs with different structures. The structure of the CME was varied by changing the mass percentages of the carbon black (CB), graphite (G) and the polymeric binder PVDF. The CME-S has mass percentage G:CB:PVDF=45:8:47wt%, CME-AC has active carbon instead of graphite in the same mass percentages as CME-S (AC:CB:PVDF=45:8:47wt%), CME-PVDF has twice less PVDF in the slurry than the CME-S (G:CB:PVDF=60:10:30wt%), CME-CB has twice as much carbon black as the slurry of CME-S (G:CB:PVDF=43:14:43wt%), and CME-G has twice less graphite in the slurry than CME-S (G:CB:PVDF=29:11:60wt%).

Table 9 shows the values of the electrochemical parameters of the fit of the Transmission-Line Model through the EIS datapoints and the values of the performance indicators of different CMEs that were studied here. CME-S has the lowest conductivity and a low permselectivity. CME-PVDF has the lowest transport time constant, so the time for the ions to move through the CME is the shortest. CME-AC has the highest membrane conductivity, so the transport of the ions inside the CME is the fastest, however, the transport time constant is ten times larger than the other CMEs. The calculated permselectivity of the CME when it is positively charged is the highest for the CME-G, but CME-AC and the CME-PVDF are close.

In the next subsections, the values of the permselectivity, when the different CMEs are charged, and on membrane conductivity, when the CMEs are uncharged, is investigated in more detail, individually for every CME. An attempt is made to find a physical explanation for the values of the performance indicators from the crystalline structure of the CMEs. The last section describes observations that have been observed for all the CME samples, and also looks for a physical explanation for these observations.

5.4.1 Active Material: Activated Carbon vs Graphite

The first analysed CME is called CME-AC. In this CME, the active material graphite has been replaced by activated carbon. The mass composition of the active material, conductive additive and polymeric binder are kept the same as in the standard CME to see only the effect of the difference in active material. As the Nyquist plot of Figure 50a and the membrane resistance values in Table 9 show, the resistance of CME-AC is approximately six times smaller than the resistance of CME-S with graphite. The thickness of CME-AC is also 5 times larger than the thickness of CME-S, resulting in the membrane conductivity of CME-AC to be much higher than the membrane conductivity of CME-S. Additionally, the membrane capacitance of AC is 100 times larger than the capacitance of the Standard CME, which indicates that activated carbon has a much larger active surface area than graphite. The crystalline structure of graphite consist out of multiple one-layered crystals of carbon atoms connected with VanDerWaals forces [133], while activated carbon consist of carbon atoms that contains additional functional groups to create a crystalline structure with many micropores [86]. The large number of micropores in the activated carbon increases the active surface area of the CME, resulting in high capacitance and ionic conductivity [86]. However, Nadakatti et al. (2011) also state that the performance of the activated carbon could be improved by inserting more mesopores in the structure to reduce the diffusional pathlength of the ions [77,86]. That the ions need more time to move through the CME with activated carbon (thus has a large diffusional pathways) is also visible in the Bode phase plot in Figure 50c. The Bode phase diagram shows that the peak of the phase angle of CME-AC is at a much lower frequency than the peak of the phase angle of the CME-S. This means that the transport time constant of CME-AC ($\tau_t = 146\text{s}$) is larger than the transport time constant of CME-S ($\tau_t = 14\text{s}$). Thus, the ions need 10 times more time to travel through the micropores of CME-AC with activated carbon than they need to travel through the pores of CME-S with graphite. So, the transport time constant is also an important performance parameter because even though the mobility of the ions in the CME is high, if they still need much time to travel through the CME, that means that the ions are moving in a maze or get stuck in the structure of the CME. For the ion transport in CMEs, CMEs made of activated carbon are not improving the ion transport out of the CME than CMEs made of graphite because the ions are adsorbed in the micropores and need more time to get out of the CME. The permselectivity of CME-AC was expected to be the lowest of all the CME samples, both positively and negatively charged. This expectation was predicted because activated carbon adsorbs more ions than graphite, as shown by the membrane capacitance value in Table 9, but it has many micropores that act as "dead ends" for the ions. The result is that the increased active sites (and membrane capacitance) due to the micropores in CME-AC do not contribute to the number of pores for ions to move out of the CME (mesopores), which increases the transport time of the ions. As a result, the transport time constant should be higher and the permselectivity, both for positively and negatively charged CMEs, should be lower for CME-AC than for CME-S. However, the permselectivity of CME-AC is not lower than that of CME-S, in fact it has one of the highest permselectivities.

5.4.2 Mass composition of polymeric binder: PVDF

Not only the type of materials in the CME has been changed, also the amount of the active material, conductive additives and polymeric binder has been changed to see the effect of the structure on the electrochemical parameters. The polymeric binder in the CME has been reduced in the slurry of CME-PVDF. In this CME, the amount of PVDF in CME-PVDF is twice less than the mass of PVDF in the slurry of CME-S. The type of polymeric binder is kept the same: PVDF. The polymeric binder PVDF functions as an adhesieve for the active material graphite and the conductive additive carbon black [88]. Too much PVDF could lead to the blockage of pores which reduces the active surface area thereby reducing the capacitance and hinder the movement of the ions through the CME which results in a higher membrane resistance [88]. The Nyquist plot of Figure 50a and Table 9 show that the resistance of CME-PVDF is indeed smaller than the resistance of CME-S with a higher PVDF masspercentage. This means, at approximately the same thickness, that the membrane conductivity of CME-PVDF is higher than the membrane conductivity of CME-S.

The values of the membrane capacitance in Table 9 show that the capacitance of the CME-S is lower than the capacitance of the CME-PVDF. This effect van PVDF on the membrane capacitance is that when too much PVDF is available in the structure, PVDF particles could accumulate resulting in agglomerates [132]. The PVDF particles that are “trapped” in the agglomerates are not used as “glue” for the carbon black particles and graphite particles, resulting in a reduction of active sites for ion adsorption [88]. Thus, a larger mass percentage of PVDF in the slurry results in a decreasing membrane capacitance and increasing membrane resistance of the CME. The membrane conductivity of CME-PVDF is higher than that of CME-S, which follows directly from the higher membrane resistance.

For the CME, the transport time constant is an important value to give an indication of the time needed for the ions to move through the CME. The transport time constant is lower for CME-PVDF than for CME-S. CME-PVDF even has the lowest transport time constant value. Thus, if the CME slurry is made with less PVDF, the ions take less time to be transported through the CME. A low transport time constant should result in a higher permselectivity, according to the research of Jiang et al. (2016). However, the estimated values permselectivity of the positively and negatively charged CME-PVDF result in approximately the same permselectivity as CME-G and CME-AC, which should not be the case if we look at the value of τ_t .

5.4.3 Mass composition of conductive additive: carbon black

In CME-CB, the amount of carbon black in the slurry has been doubled. This CME has been placed inside the CME meter to conduct EIS measurements on the uncharged and charged CME to investigate the effect of the carbon black on the structure of the CME. As Figure 50 shows, the EIS data in the impedance plots of CME-CB looks not as smooth as the other collected EIS data of other types of CMEs. Repeating the measurement resulted in similar shapes at high frequencies, however, at low frequencies, the datapoints had a large deviation from each other. This could also be characterised by the quality of fit of the impedance equation of the TLM because CME-CB has the highest value for the quality of the fit, which means that the Transmission-Line Model fits less accurate through the EIS datapoints of CME-CB than other CME samples. The Nyquist plot looks partly like a R//C-circuit, however, the Transmission-Line Model has a smaller quality of fit value indicating that the TLM fits better through the datapoints. EIS measurements on CME-CB do not go well, even if the CME is charged (Appendix H). It was therefore concluded that the EIS data was too scattered and imprecise to give any weight to any observation from these impedance graphs or values.

CME-CB has the highest membrane capacitance of the CMEs with graphite as active material. This was expected, because carbon black is a conductive additive which increases the access of the electrons to the active material graphite particles [134]. The active surface area increases, which results in a higher capacitance. The value of the membrane capacitance in Table 9 shows, as expected, that the extra carbon black particles in the electrode material result in a higher membrane capacitance.

CME-CB is the CME with the lowest membrane resistance, see Table 9. Doubling the amount of carbon black particles results in a membrane resistance which is approximately 20 times smaller. The paper of Jäckel et al. (2014) also observed a reduction of the resistance when more carbon black particles were mixed in the electrode slurry [135]. The small carbon black particles fit into the pores of the crystalline structure of the graphite sheets. More carbon black particles in the slurry result in more contact between the graphite particles and the carbon black particles, facilitating the access of the electrons to the graphite particles, resulting in a reduction of the resistance [135].

Charging the CME-CB does not result in a much higher permselectivity. This could be explained by the conductivity-permselectivity trade-off. The transport time constant is higher when CME-CB is positively charged but lower than CME-S when CME-CB is negatively charged. However, the EIS data from this CME is not accurate and repeatable, so it should not be used to draw any conclusions.

5.4.4 Mass composition of active material: graphite

The CME with a reduced amount of graphite, denoted as CME-G, was prepared using half the mass of graphite compared to the Standard CME. It was initially hypothesized that the membrane conductivity

and capacitance of CME-G would both be lower than CME-S, because less graphite particles directly means that the amount of active sites reduces. However, Table 9 presents values contradicting this expectation. Surprisingly, the membrane conductivity of CME-G is higher than that of CME-S, mainly because the membrane resistance in CME-G is half as low as in CME-S. Less graphite in the structure of the CME result in less particles which hinder the mobility of the ions through the pores of the CME crystalline structure. Probably, reducing the graphite particles, result in a reduced amount of graphite particles, which do not act as active surface area but as obstacles for the transport of ions through the pores. This leads to a reduced membrane resistance. Furthermore, the membrane capacitance of CME-G is higher than the capacitance of CME-S, which could be attributed to the possibility of the structure having a higher ratio of available active sites over graphite particles due to the reduced amount of graphite particles which did not benefit the amount of active sites. Less graphite particles result in a higher active surface area over total surface area of graphite particles, which resulted in an increase of the membrane capacitance (in F/cm²). The higher membrane capacitance and lower membrane resistance result in the transport time constant of the CME-G to be a little lower than that of CME-S. CME-G has the highest permselectivity for anion transport when the CME is positively charged and cation transport when the CME is negatively charged, see Table 9. However, similarly for the other CME samples, the estimated value of the permselectivity is inconclusive.

5.4.5 Observations during the EIS measurements of all CME samples

According to the research of Jiang et al. (2019), for ion exchange membranes, the transport time constant τ_t is a better indication of the permselectivity of an IEM than the resistance and could be used to compare different IEMs [76]. The value of τ_t indicates the amount of time a specific type of ion needs to move through the ion exchange membrane [76]. Larger value of τ_t indicates that the counter-ions transport is slower which result in a lower permselectivity [76]. For CMEs, this relation between permselectivity and the transport time constant has not been proved. If the conclusion of the research of Jiang et al. (2019) is also correct for CMEs, then the estimated permselectivity is higher when the transport time constant is lower [76]. However, the values of Table 9 give a different picture. For example, the permselectivity of the positively charged CME-AC is higher than the permselectivity of the positively charged CME-S, while the transport time constant of CME-AC is almost ten times larger than the transport time of CME-S. The permselectivity of CME-AC is even the second highest positive permselectivity calculated for the different CMEs, while CME-AC has the largest transport time constant. The other CMEs also show that there is no relation between the transport time constant and the permselectivity. Thus, the statement that the transport time constant is an indication of the permselectivity is dismissed.

The CME-CB has the highest value for the quality of the fit, however, all CME samples have relatively high χ^2 -values. The very high quality of fit χ^2 -values are caused by the scattering of datapoints, a depressed (or flattened) semi-circle in the datapoints, and the “curl” at low frequencies, see the Nyquist plot in Figure 50a, which is an unusual effect. At high frequencies, a negative vertical line is caused by the inductive behaviour in the cables of the potentiostat, however, for low frequencies, the negative values indicate something different [136]. The shape of the negative values at low frequencies, which appear in the positive imaginary half-plane of the Nyquist plot, looks like a “curl”. Klotz (2019) explains that this so called “inductive loop” or “low frequency hook” is not a measurement artifact but caused by temperature effects, like joule heating, or by electron transport in mixed conducting thin films when the electrode is polarised [137]. The paper of Jaiser et al. (2016) indicates that the CME could consist out of different layers which have different membrane resistance and capacitance values due to the drying process of the CME slurry [132]. This negative inductance is also visible when the CME is uncharged (see Figure 50a), so the mixed conducting CME structure could explain the resulting inductance loop. Another explanation has been given by Boukamp (2001). The inductive loop is caused when two adsorbed ions are competing for active sites which decreases the membrane capacitance until it even becomes negative [138]. Still, a brown-orange sediment was noticed on the titanium current

collectors which indicates that faradaic reactions were occurring. Hughes et al. (2020) explains that the inductive behaviour is caused by a shift in electron density in the atoms surrounding the surface of the polarised electrodes and the other atoms [139,140]. Boukamp (2001) emphasises this theory by stating that the polarised working electrode with respect to the reference electrode will result in faradaic reactions with the adsorbed oxygen species [138]. This inductive loop could thus also indicate that faradaic reactions are occurring at the surface of the CMEs. The inductive loop is probably caused by faradaic reactions happening at the surface of the CME, because, even after oxygen was blown out of the electrolyte (with nitrogen gas), there was an orange/brown settling on the titanium current collectors observed that increased over time during the charging of the CMEs. Lamoen & Perssons (1998) saw that on graphite sheets adsorption of O_2 molecules negligibly occurs [141]. However, when potassium ions (K^+) are adsorbed on the graphite surface, chemisorption of O_2 molecules (and other molecules) on the potassium sites is strongly enhanced [141,142]. When O_2 chemisorbs to the potassium, different solid molecules are created: K_2O , KO_2 , K_2O_2 , KO_x , and more [143,144]. Most potassiumoxide molecules are white solids and difficult to observe, however, the solid KO_2 has an orange colour. During the EIS measurements, small amounts of orange/brown coloured sediments were observed on the titanium current collectors after charging the CMEs. This could prove that charge transfer reactions occurred during the charging of the CME, and that the negative inductance loop in the Nyquist plot indicates this faradaic reaction.

Unfortunately, the researchers are not sure what the underlying explanation is for this inductance loop, but they know it is not a measurement mistake that could be removed [137]. The problem with this inductance loop is that the impedance equation of the EECMs cannot fit through the datapoints when the points lay in the positive imaginary plane. The fit is less accurate (quality of fit value is large) and the determined value of the membrane capacitance is smaller. There are also loops and curls at high frequencies, but this effect is only visible for the first two datapoints and it has a very small effect on the quality of fit value.

Important note is that the permselectivity, especially when the CME is negatively charged, is inconclusive. For all CME samples is showed in the Nyquist plots of Appendix H that the improved anion-transport in positive charged CME result in smaller semi-circles than the uncharged CME, while the cation-transport in negatively charged CME result larger semi-circles than the uncharged CME. According to Donnan's theory, the membrane resistance should decrease when the CME is charged, indefinitely, whether the CME is charged positively or negatively. So, another (electrochemical process) is occurring when the CME is negatively charged which does not occur when the CME is positively charged. Maybe the created potassiumoxide molecules cause the membrane resistance of the negatively charged CMEs to increase during the EIS measurement. During the negative charging of the CME, the cations K^+ are attracted to the surface of the graphite molecules and are adsorbed. According to multiple researchers, potassiumoxide molecules are created when K^+ is adsorbed on the graphite surface, because the chemisorption of O_2 molecules on the potassium sites is strongly enhanced [141-144]. This faradaic reaction result in solid salts which could block the pores, resulting in the membrane resistance of the ions to increase. The creation of potassiumoxide molecules could thus pose as the physical explanation for the increased membrane resistance during the negative charging of the CMEs. Still, the permselectivity measurements in this Thesis report are inconclusive and should be repeated to determine if Equation 3.12 could be used to predict the permselectivity of CMEs.

6

Conclusion

The Multichannel Capacitive Deionisation system is a newly designed CDI system. Multichannel capacitive deionisation avoids the regeneration phase by having product and brine channels separated at all times, such that the system can continuously produce a stream of desalinated water. Multiple capacitive membrane electrodes (CMEs), which are electrodes that act as ion exchange membranes, are placed between the CDI electrodes. The CMEs are fabricated from similar materials as normal CDI electrodes but are made selective for the counter-ions by applying a positive or negative potential across the electrode. The counter-ions are able to transport through the CME, while the co-ions are repelled to move through the pores of the CME. In this thesis report, the importance of resistance and capacitance for CME performance has been discussed. The performance indicators of the capacitive membrane electrodes were evaluated using electrochemical impedance spectroscopy. The permselectivity is the value that indicates how well the selectivity, i.e. the counter-ion transport facilitated while the co-ion transport is blocked, of the CME is. The mobility of ions through the CME is assessed by the performance indicator membrane conductivity. The performance indicators of the CME that should be maximised to maximise the performance of the MC-CDI system are therefore membrane conductivity and permselectivity.

Electrochemical impedance spectroscopy is a non-invasive measurement technique for electrochemical systems to determine the electrochemical processes taking place at the interface. This technique is relatively fast and has been used by several researchers. The EIS setup (CME meter) was designed, built and used to measure the EIS data of different CMEs. The EIS data were plotted on Nyquist and Bode plots which were analysed by fitting the Transmission-Line Model to the EIS data and determining the electrochemical parameters membrane resistance R and membrane capacitance C . The membrane resistance directly determines the value of the membrane conductivity. A higher membrane resistance means that the ions are more difficult to transport through the crystalline structure of the CME, e.g. by agglomerates or polymeric binder clogging the pores, which reduces the mobility of the ions and results in a lower membrane conductivity. The membrane conductivity of the CME should be as high as possible. However, there is a trade-off between membrane conductivity and the other performance indicator, permselectivity. Permselectivity is estimated by determining the membrane resistance of the CME when it is charged and when it is uncharged. Surprisingly, the membrane resistance decreases when the CME is positively charged and increases when the CME is negatively charged. Donnan's theory explains that the membrane resistance should decrease regardless of the positive or negative potential on the CME. However, EIS experiments on multiple CMEs show that negatively charged CMEs result in a higher membrane resistance than the uncharged CME. The membrane capacitance is not used to calculate the performance indicators, but the value gives an indication of the EDL formation in the pores of the CME.

Different CMEs with different compositions were placed in the CME meter. EIS was carried out and performance indicators were determined. The CMEs were made of an active material (activated carbon or graphite), a conductive additive (carbon black) and a polymeric binder (PVDF). The mass percentages of the components were varied to change the structure of the CME. The CME with activated carbon had a much lower membrane resistance than the CME with graphite, resulting in a higher membrane conductivity. However, the large number of micropores in the activated carbon CME resulted in a high time constant, indicating that ions were not able to leave the CME. CMEs should also have short pores that go completely through the thickness of the CME to facilitate fast transport, therefore graphite as an active material is better for the functioning of CMEs. The amount of graphite in the slurry also affects the electrochemical parameters. More graphite does not immediately mean

an increase in the number of active sites. In fact, more graphite does not contribute to the increase in active sites, but actually clogs the pores and reduces the membrane conductivity of the CME. However, too little graphite in the structure reduces the number of active sites where ions can be adsorbed, thereby reducing permselectivity. Finding the maximum amount of graphite that maximises the number of active sites while minimising the membrane resistance will maximise both permselectivity and membrane conductivity. The polymeric binder PVDF could also agglomerate and clog the pores. PVDF acts as a glue between the active material and the conductive additives, allowing electrons to reach the active material and create active sites, and generating the mechanical stability of the freestanding CME. Therefore, the mass percentage of PVDF in the slurry must always be relatively high compared with the other materials. The PVDF has a major effect on the structure of the CME: the lower the amount of PVDF, the lower the membrane resistance. PVDF acts as a glue for the carbon black and graphite particles, but also prevents the ions from moving through the pores. Therefore, the lowest mass percentage of PVDF must be found where the CME is still mechanically stable and the membrane conductivity is as high as possible. The conductive additive, carbon black, improves the membrane capacitance of the CME while creating more active sites by increasing the conductivity of the electrons. Doubling the amount of carbon black in the slurry reduces the membrane resistance by a factor of ten. It is necessary to find the mass percentage of carbon black that maximises the permselectivity while maintaining a high membrane conductivity.

To prepare the CME slurry, a solvent, acetone, is added to the slurry. The evaporation rate of the solvent affects the homogeneity of the CME. If the evaporation rate is faster, the particles have too little time to disperse evenly in the slurry, resulting in the formation of agglomerates and the PVDF moving in the direction of evaporation of the acetone. The CME then has two layers with different electrochemical parameters. The thickness of the CME also affects the rate of evaporation of the acetone, resulting in a change in structure. The membrane conductivity is therefore different for CMEs with the same composition but different thicknesses. Thickness is therefore also a variable that could be changed to improve the performance indicators of the CME.

EIS is proving to be an accurate and rapid measurement technique for gaining a better understanding of the physical processes taking place in the CME. When temperature and electrolyte concentration are controlled, EIS measurements prove to be repeatable and show that the same EIS data could be collected, indicating that the measurement has a high degree of accuracy. Conductivity could be determined with the membrane resistance by performing an EIS experiment on the CME, which takes approximately one hour. Unfortunately, estimating the permselectivity of the CMEs using EIS resulted in inconclusive data. Further research should be conducted to determine if and how permselectivity can be estimated with EIS. The CME with the best membrane conductivity and permselectivity could then be investigated with EIS.

7

Discussion and Recommendations

Further testing with the CME meter is required to determine if the permselectivity of a CME can be accurately and quickly determined with EIS. Desalination experiments should be carried out to determine the actual permselectivity of the CME and compare the results with the estimated permselectivity using EIS. In addition, the transport time constant and the actual permselectivity should be compared to see if there is a relationship between these values. Also, more EIS experiments should be carried out to determine the standard deviation for each condition separately to more accurately determine the quality of the fit. The repeatability of the EIS measurements could also be investigated. To this end, a procedure could be developed to determine the permselectivity and membrane conductivity of a CME in the shortest possible time.

The quality of the fit value was determined by using Equation 3.14 and depends on the number of the datapoints due to the standard deviation in the equation [107]. The standard deviation was calculated by repeating the EIS experiments on the CME-S eight times and summing the total imaginary standard deviation and the real standard deviation. These standard deviations were then used for all EIS experiments, even for different operational parameters, of the same CME composition to determine the quality of the fit. Of course, it would be more accurate to repeat the experiment several times for each experiment where the operational parameter or the charge is changed, in order to determine the standard deviation and the quality of the fit. Unfortunately, this was not possible due to the short time available for the thesis project. Another explanation for the high quality of fit, the CME might not be as homogeneous as was assumed. For the TLM, the pore structure of the CME was assumed to be hierarchical and homogeneous in the x-, y- and z-direction. The crystalline structure of graphite consist out of multiple one-layered carbon sheets which is very hierarchical [133]. However, in reality, the pore structure is never ideally hierarchical due to some molecules which are inserted in the structure or the layers which are rotated in the crystalline structure. Also, the fabrication process of the CME has influence on the pore structure of the CME and could never be ideal. The same is true for the assumption that the pores in the CME structure are perfectly round. In reality, the pores in the crystalline structure of the CME could never all be ideally round. Another assumption of the TLM was that the membrane resistance R was only the resistance of the transport of ions through the CME. The resistance in the electronic path was assumed to be much smaller than the resistance in the ionic path. The electronic resistance in the electronic path may have a more dominant influence to justify this assumption. However, more researchers assume that the resistance of the ions is much larger than the resistance of the electrons, that the resistance of the electrons is negligible.

The bottleneck in charging the CMEs is that, after a few charge EIS experiments, an orange sediment forms on the titanium current collectors, indicating the presence of faradaic reactions during the charging of the CMEs. It is expected that when the CME is negatively charged, the adsorbed K^+ in the graphite particles are involved in charge transfer reactions with oxygen, resulting in the formation of solid particles (KO_2) on the titanium current collector and in the spacers. This reaction is likely to be represented on the Nyquist plot as an inductance loop at low frequencies, which cannot be represented by the impedance equation of the transmission line model. Further research should be conducted to determine which faradaic reactions occur at the interface of the CME and whether these faradaic reactions can be removed from the electrochemical processes occurring at the interface of the CME. To check if the potassium ions are causing the orange sediment, several EIS experiments should be carried out on charged and uncharged CME-S when the electrolyte consists of other cations (Na^+ , Mg^{2+} , enz). Also check whether the inductive loop disappears from the Nyquist plot at low

frequencies. This would indicate that the K^+ is inducing the charge transfer processes with O^2 , resulting in the orange deposits on the titanium current collectors, and that the inductive loop is caused by these faradaic reactions.

In addition, during charging, the EIS data shows a 45° line at high frequencies, ending in a flattened (or depressed) semicircle. The chosen transmission line model does not fit the EIS data as well as another EECM would. More research should be done to find the EECM that fits the EIS data of the uncharged and charged CMEs accurately. When a flattened semi-circle was observed for CDI electrodes, it was stated to be caused by the inhomogeneities inside the electrode material, like surface roughness and porosity [96]. The non-ideal behaviour of the double layer capacitor was described with a CPE element instead of an ideal capacitor for CDI electrodes [145], the same could be done for CMEs to improve the quality of fit value by replacing the ideal capacitor in the interface impedance $Z_{\text{interface}}$ with a CPE element [104]. The EECM must comply with the following criteria: the EECM must describe electrochemical processes inside the CME (physically relevant), and the χ^2 value must be less than 10^{-3} (impedance equation fit is accurate).

A first prototype of the, in this Thesis project, designed CME meter has been built in the chemical lab. The design of the CME meter must be improved because some problems occurred during the EIS measurements: (1) the inline conductivity meter depends on the flowrate of the electrolyte through the tube; (2) the components in the CME-cell were not fixed and there were potential leaks.

(1) The result of the EIS experiments have shown that the EIS data is largely affected by the salt concentration in the electrolyte. The inline conductivity meter of eDAQ was used to determine the conductivity and to ensure that the salt concentration stayed constant during the EIS measurement. Unfortunately, this was not the case. During the EIS measurement, the conductivity could sometimes be increased by 0.020 mS/cm. What was even more difficult, the measured conductivity of the inline conductivity meter was affected by the flowrate of the electrolyte through the tubes. So, a larger flowrate resulted in a larger measured conductivity of the electrolyte. Upon lowering the flowrate, the measured conductivity also reduces. No additional salt could enter the system during the experiment, so the conclusion must be that the inline conductivity meter is sensitive to the flowrate of the electrolyte. During the calibration of the inline conductivity meter, the flowrate was not taken into account to determine the relation between the conductivity and the salt concentration in the beakers. Therefore, for all the measured concentrations during the EIS experiments of the experiments, it is unknown what the actual KCl concentration in the electrolyte was. Still, EIS data is strongly influenced by the salt concentration in the electrolyte so knowing the concentration of the electrolyte is crucial when more EIS experiments are conducted with the CME meter. Therefore, the design of the CME meter needs to be updated by removing the inline conductivity meter and inserting a conductivity probe or the inline conductivity meter needs to be calibrated for the salt concentration and the flowrate.

(2) A functional requirement in the design of the CME-cell was that the CME must be replaceable while the rest of the components in the cell (spacers, titanium current collectors, rubber) remain fixed. This problem was solved by using a 4 mm rod to align all the circular components, but the components were not fixed. The rest of the CME-cell was therefore not identical for each EIS experiment when a new CME was placed inside the CME-cell. In addition, during the permselectivity determination, when a potential was previously applied between the CMEs and the end electrodes, the potential of CME 2 decreased by more than 50% within 2 minutes, while the potential of CME 1 decreased by 20%. So there are some potential leaks in the CME cell. The design of the CME cell needs to be improved to reduce the effect of potential leakage and to ensure repeatability by keeping the components (except the CMEs) fixed.

The drying process of the CME results in the CME having two layers, according to the paper by Jaiser et al. (2016), where the resistance of one layer is higher than the resistance of the other layer [132]. The fabrication process of the CME needs to be updated to improve the drying process. In several papers,

an oven is used to dry the electrode slurry at a certain temperature. Glass could also be placed on top of the CME to distribute the particles in the slurry more homogeneously, as the acetone could not evaporate as quickly because the glass prevents the acetone from evaporating from the top of the slurry. It is still important to determine the top and bottom of the CME, especially if the CME fabrication process is not changed. Placing a dot on the CME (near the edge) with a marker to know the top of the CME could be a temporary solution until the fabrication process is adapted.

Reference List

- [1] UN (2023). *Water Scarcity | UN-Water*. UN-Water. <https://www.unwater.org/water-facts/water-scarcity>
- [2] UN-Water (2022, September 8). *Summary Progress Update 2021: SDG 6 — water and sanitation for all | UN-Water*. UN-Water. <https://www.unwater.org/publications/summary-progress-update-2021-sdg-6-water-and-sanitation-all>
- [3] Maddocks, A., Young, R. S., & Reig, P. (2015, August 26). *Ranking the World's Most Water-Stressed Countries in 2040*. World Resources Institute. <https://www.wri.org/insights/ranking-worlds-most-water-stressed-countries-2040>
- [4] Armstrong, M. (2022, March 22). *Where Water Stress Will Be Highest by 2040*. Statista Infographics. <https://www.statista.com/chart/26140/water-stress-projections-global/>
- [5] UN (2022). *Home | UN World Water Development Report 2022*. <https://www.unesco.org/reports/wwdr/2022/en>
- [6] Tang, W., Liang, J., He, D., Gong, J., Tang, L., Liu, Z., Wang, D., & Zeng, G. (2019). Various cell architectures of capacitive deionization: Recent advances and future trends. *Water Research*, 150, 225–251. <https://doi.org/10.1016/j.watres.2018.11.064>
- [7] Lee, J., Jo, K., Lee, J., Hong, S. P., Kim, S., & Yoon, J. (2018). Rocking-Chair Capacitive Deionization for Continuous Brackish Water Desalination. *ACS Sustainable Chemistry & Engineering*, 6(8), 10815–10822. <https://doi.org/10.1021/acssuschemeng.8b02123>
- [8] Sharan, P., Yoon, T. K., Jaffe, S. M., Ju, T., Currier, R., & Findikoglu, A. T. (2021). Can capacitive deionization outperform reverse osmosis for brackish water desalination? *Cleaner Engineering and Technology*, 3, 100102. <https://doi.org/10.1016/j.clet.2021.100102>
- [9] Hou, C., Taboada-Serrano, P., Yiaccoumi, S., & Tsouris, C. (2008). Electrosorption selectivity of ions from mixtures of electrolytes inside nanopores. *Journal of Chemical Physics*, 129(22). <https://doi.org/10.1063/1.3033562>
- [10] Mossad, M., & Zou, L. (2012). A study of the capacitive deionisation performance under various operational conditions. *Journal of Hazardous Materials*, 213–214, 491–497. <https://doi.org/10.1016/j.jhazmat.2012.02.036>
- [11] Stackpoole, S. M., Stets, E. G., & Sprague, L. A. (2019). Variable impacts of contemporary versus legacy agricultural phosphorus on US river water quality. *Proceedings of the National Academy of Sciences of the United States of America*, 116(41), 20562–20567. <https://doi.org/10.1073/pnas.1903226116>
- [12] Islam, R., Gupta, S. S., Jana, S. K., & Pradeep, T. (2022). Industrial Utilization of Capacitive Deionization Technology for the Removal of Fluoride and Toxic Metal Ions ($\text{As}^{3+/5+}$ and Pb^{2+}). *Global Challenges*, 6(4). <https://doi.org/10.1002/gch2.202100129>
- [13] Zavahir, S., ElMakki, T., Gulied, M., Ahmad, Z., Alsulaiti, L., Shon, H. K., Chen, Y., Park, H., Abdel-Wahab, A., & Han, D. S. (2021). A review on lithium recovery using electrochemical capturing systems. *Desalination*, 500, 114883. <https://doi.org/10.1016/j.desal.2020.114883>
- [14] Gendel, Y., Rommerskirchen, A., David, O., & Weßling, M. (2014). Batch mode and continuous desalination of water using flowing carbon deionization (FCDI) technology. *Electrochemistry Communications*, 46, 152–156. <https://doi.org/10.1016/j.elecom.2014.06.004>
- [15] Kim, N., Lee, J., Kim, S., Hong, S. P., Lee, C., Yoon, J., & Kim, C. (2020). Short Review of Multichannel Membrane Capacitive Deionization: Principle, Current Status, and Future Prospect. *Applied Sciences*, 10(2), 683. <https://doi.org/10.3390/app10020683>
- [16] Macdonald, D. D. (1990). Review of mechanistic analysis by electrochemical impedance spectroscopy. *Electrochimica Acta*, 35(10), 1509–1525. [https://doi.org/10.1016/0013-4686\(90\)80005-9](https://doi.org/10.1016/0013-4686(90)80005-9)
- [17] Ellis, C. L. C., Smith, E., Javai, H., Berns, G., & Venkataraman, D. (2018). Ion Migration in Hybrid Perovskites. *Perovskite Photovoltaics*, 163–196. <https://doi.org/10.1016/b978-0-12-812915-9.00006-x>
- [18] Volfkovich, Y. M. (2020). Capacitive Deionization of Water (A Review). *Russian Journal of Electrochemistry*, 56(1), 18–51. <https://doi.org/10.1134/s1023193520010097>
- [19] Lenz, M., Zabel, J., & Franzreb, M. (2020). New Approach for Investigating Diffusion Kinetics Within Capacitive Deionization Electrodes Using Electrochemical Impedance Spectroscopy. *Frontiers in Materials*, 7. <https://doi.org/10.3389/fmats.2020.00229>
- [20] Suthar, B., Landesfeind, J., Eldiven, A., & Gasteiger, H. A. (2018). Method to Determine the In-Plane Tortuosity of Porous Electrodes. *Journal of the Electrochemical Society*, 165(10), A2008–A2018. <https://doi.org/10.1149/2.0121810jes>
- [21] Kuo, H. A., Ramachandran, A., Oyarzun, D. I., Clevenger, E. C., Santiago, J. G., Stadermann, M., Campbell, P. G., & Hawks, S. A. (2020). Understanding resistances in capacitive deionization devices. *Environmental Science: Water Research & Technology*, 6(7), 1842–1854. <https://doi.org/10.1039/d0ew00169d>
- [22] Dykstra, J., Zhao, R., Biesheuvel, P., & van der Wal, A. (2016). Resistance identification and rational process design in Capacitive Deionization. *Water Research*, 88, 358–370. <https://doi.org/10.1016/j.watres.2015.10.006>
- [23] Landesfeind, J., Hattendorff, J., Ehrl, A., Wall, W. A., & Gasteiger, H. A. (2016). Tortuosity Determination of Battery Electrodes and Separators by Impedance Spectroscopy. *Journal of the Electrochemical Society*, 163(7), A1373–A1387. <https://doi.org/10.1149/2.1141607jes>
- [24] Galama, A., Hoog, N., & Yntema, D. (2016). Method for determining ion exchange membrane resistance for electrodialysis systems. *Desalination*, 380, 1–11. <https://doi.org/10.1016/j.desal.2015.11.018>
- [25] Zhang, L., Jia, H., Wang, J., Wen, H., & Li, J. (2020). Characterization of fouling and concentration polarization in ion exchange membrane by in-situ electrochemical impedance spectroscopy. *Journal of Membrane Science*, 594, 117443. <https://doi.org/10.1016/j.memsci.2019.117443>

- [26] Ramachandran, A., Oyarzun, D. A., Hawks, S. A., Stadermann, M., & Santiago, J. G. (2019). High water recovery and improved thermodynamic efficiency for capacitive deionization using variable flowrate operation. *Water Research*, 155, 76–85. <https://doi.org/10.1016/j.watres.2019.02.007>
- [27] Landon, J., Gao, X., Omosebi, A., & Liu, K. (2019). Progress and outlook for capacitive deionization technology. *Current Opinion in Chemical Engineering*, 25, 1–8. <https://doi.org/10.1016/j.coche.2019.06.006>
- [28] Wang, Z., Choo, K. H., Tang, C. Y., & Waite, T. D. (2022). *Electrochemical Membrane Technology for Water and Wastewater Treatment*. Elsevier Gezondheidszorg.
- [29] Yao, Q., & Tang, H. L. (2016). Occurrence of re-adsorption in desorption cycles of capacitive deionization. *Journal of Industrial and Engineering Chemistry*, 34, 180–185. <https://doi.org/10.1016/j.jiec.2015.11.004>
- [30] Hemmatifar, A., Palko, J. W., Stadermann, M., & Santiago, J. G. (2016). Energy breakdown in capacitive deionization. *Water Research*, 104, 303–311. <https://doi.org/10.1016/j.watres.2016.08.020>
- [31] Hawks, S. A., Ramachandran, A., Porada, S., Campbell, P. G., Suss, M. E., Biesheuvel, P., Santiago, J. G., & Stadermann, M. (2019). Performance metrics for the objective assessment of capacitive deionization systems. *Water Research*, 152, 126–137. <https://doi.org/10.1016/j.watres.2018.10.074>
- [32] Pan, S. Y., Snyder, S. W., Ma, H. W., Lin, Y. J., & Chiang, P. C. (2017). Development of a Resin Wafer Electrodeionization Process for Impaired Water Desalination with High Energy Efficiency and Productivity. *ACS Sustainable Chemistry & Engineering*, 5(4), 2942–2948. <https://doi.org/10.1021/acssuschemeng.6b02455>
- [33] Kang, J., Kim, T., Jo, K., & Yoon, J. (2014). Comparison of salt adsorption capacity and energy consumption between constant current and constant voltage operation in capacitive deionization. *Desalination*, 352, 52–57. <https://doi.org/10.1016/j.desal.2014.08.009>
- [34] Shang, X., Cusick, R. D., & Smith, K. C. (2017). A Combined Modeling and Experimental Study Assessing the Impact of Fluid Pulsation on Charge and Energy Efficiency in Capacitive Deionization. *Journal of the Electrochemical Society*, 164(14), E536–E547. <https://doi.org/10.1149/2.0841714jes>
- [35] Huyskens, C., Helsen, J., & de Haan, A. (2013). Capacitive deionization for water treatment: Screening of key performance parameters and comparison of performance for different ions. *Desalination*, 328, 8–16. <https://doi.org/10.1016/j.desal.2013.07.002>
- [36] Zhang, C., He, D., Ma, J., Tang, W., & Waite, T. D. (2018). Faradaic reactions in capacitive deionization (CDI) - problems and possibilities: A review. *Water Research*, 128, 314–330. <https://doi.org/10.1016/j.watres.2017.10.024>
- [37] Khalid, M., Arshid, N., & Grace, N. (2020). *Advances in Supercapacitor and Supercapattery: Innovations in Energy Storage Devices* (1st ed.). Elsevier.
- [38] Dourado, A. H. B. (2022). Electric Double Layer: The Good, the Bad, and the Beauty. *Electrochem*, 3(4), 789–808. <https://doi.org/10.3390/electrochem3040052>
- [39] Lopatynska, O., Guiver, M. D., Poperenko, L. V., Chegel, V. I., & Lashkaryov, V. (2008). Factor of interfacial potential for the surface plasmon-polariton resonance sensor response. *Semiconductor Physics, Quantum Electronics & Optoelectronics*. <https://doi.org/10.15407/spqeo11.04.329>
- [40] Schmickler, W., & Santos, E. (2010). *Interfacial Electrochemistry* (2nd ed. 2010). Springer.
- [41] Porada, S., Zhao, R., Van Der Wal, A., Presser, V., & Biesheuvel, P. (2013). Review on the science and technology of water desalination by capacitive deionization. *Progress in Materials Science*, 58(8), 1388–1442. <https://doi.org/10.1016/j.pmatsci.2013.03.005>
- [42] Xin, W., Zhang, Z., Huang, X., Hu, Y., Van Hest, J. C. M., Zhu, C., Kong, X. Z., Jiang, L., & Wen, L. (2019). High-performance silk-based hybrid membranes employed for osmotic energy conversion. *Nature Communications*, 10(1). <https://doi.org/10.1038/s41467-019-11792-8>
- [43] Grahame, D. C. (1955). Electrode processes and the electrical double layer. *Annual Review of Physical Chemistry*, 6(1), 337–358. <https://doi.org/10.1146/annurev.pc.06.100155.002005>
- [44] Parsons, R. (1974). Electrochemical nomenclature. *Pure and Applied Chemistry*, 37(4), 499–516. <https://doi.org/10.1351/pac197437040499>
- [45] Li, T., Ciampi, S., & Darwish, N. (2022). The surface potential of zero charge controls the kinetics of diazonium salts electropolymerization. *ChemElectroChem*, 9(17). <https://doi.org/10.1002/celc.202200255>
- [46] Lica, G. C., & Tong, Y. J. (2013). Electrochemical impedance spectroscopic measurement of potential of zero charge of octanethiolate-protected Au and Pd nanoparticles. *Journal of Electroanalytical Chemistry*, 688, 349–353. <https://doi.org/10.1016/j.jelechem.2012.10.008>
- [47] Jia, B., & Zhang, W. (2016). Preparation and Application of Electrodes in Capacitive Deionization (CDI): a State-of-Art Review. *Nanoscale Research Letters*, 11(1). <https://doi.org/10.1186/s11671-016-1284-1>
- [48] Gabitto, J. F., & Tsouris, C. (2023). A review of transport models in charged porous electrodes. *Frontiers in Chemical Engineering*, 4. <https://doi.org/10.3389/fceng.2022.1051594>
- [49] Rouquerol, J., Avnir, D., Fairbridge, C., Everett, D. W., Haynes, J. M., Pernicone, N., Ramsay, J. D. F., Sing, K. S. W., & Unger, K. (1994). Recommendations for the characterization of porous solids (Technical Report). *Pure and Applied Chemistry*, 66(8), 1739–1758. <https://doi.org/10.1351/pac199466081739>

- [50] Nguyen, Q. V., Lorente, S., & Duhart-Barone, A. (2018). Modeling the ionic transport in mesoporous materials. *Construction and Building Materials*. <https://doi.org/10.1016/j.conbuildmat.2018.09.155>
- [51] Huang, C., & He, J. (2013). Electrosorptive removal of copper ions from wastewater by using ordered mesoporous carbon electrodes. *Chemical Engineering Journal*, 221, 469–475. <https://doi.org/10.1016/j.cej.2013.02.028>
- [52] Tado, K., Sakai, F., Sano, Y., & Nakayama, A. (2016). An analysis on ion transport process in electrodialysis desalination. *Desalination*, 378, 60–66. <https://doi.org/10.1016/j.desal.2015.10.001>
- [53] Qureshi, B. A., Qasem, N. A., & Zubair, S. M. (2021). Normalized sensitivity analysis of electrodialysis desalination plants for mitigating hypersalinity. *Separation and Purification Technology*, 257, 117858. <https://doi.org/10.1016/j.seppur.2020.117858>
- [54] Al-Amshawee, S., Yunus, M. Y. B. M., Azoddein, A. a. M., Hassell, D. G., Dakhil, I. H., & Hasan, H. A. (2020). Electrodialysis desalination for water and wastewater: A review. *Chemical Engineering Journal*, 380, 122231. <https://doi.org/10.1016/j.cej.2019.122231>
- [55] Sedighi, M., Behvand Usefi, M. M., Ismail, A. F., & Ghasemi, M. (2023). Environmental sustainability and ions removal through electrodialysis desalination: Operating conditions and process parameters. *Desalination*, 549, 116319. <https://doi.org/10.1016/j.desal.2022.116319>
- [56] Banasiak, L. J., Kruttschnitt, T. W., & Schäfer, A. I. (2007). Desalination using electrodialysis as a function of voltage and salt concentration. *Desalination*, 205(1–3), 38–46. <https://doi.org/10.1016/j.desal.2006.04.038>
- [57] Dammak, L., Fouilloux, J., Bdiri, M., Larchet, C., Renard, E., Baklouti, L., Sarapulova, V., Kozmai, A., & Pismenskaya, N. (2021). A Review on Ion-Exchange Membrane Fouling during the Electrodialysis Process in the Food Industry, Part 1: Types, Effects, Characterization Methods, Fouling Mechanisms and Interactions. *Membranes*, 11(10), 789. <https://doi.org/10.3390/membranes11100789>
- [58] Kunrath, C. C. N., Patrocínio, D. C., Siqueira Rodrigues, M. A., Benvenuti, T., & Amado, F. D. R. (2020). Electrodialysis reversal as an alternative treatment for producing drinking water from brackish river water: A case study in the dry season, northeastern Brazil. *Journal of Environmental Chemical Engineering*, 8(2), 103719. <https://doi.org/10.1016/j.jece.2020.103719>
- [59] Nayak, S. K., Dutta, K., & Gohil, J. M. (2022). *Advancement in Polymer-Based Membranes for Water Remediation* (1st ed.). Elsevier.
- [60] Gubari, M., Zwain, H., Al-Zahiwat, M., & Alekseeva, N. (2021). Characteristics of the MK-40 and MA-40 Membranes for Industrial Wastewater Treatment – A Review. *Ecological Engineering & Environmental Technology*, 22(1), 39–50. <https://doi.org/10.12912/27197050/132095>
- [61] Qasem, N. A., Qureshi, B. A., & Zubair, S. M. (2018). Improvement in design of electrodialysis desalination plants by considering the Donnan potential. *Desalination*, 441, 62–76. <https://doi.org/10.1016/j.desal.2018.04.023>
- [62] Rajput, A., Sharma, P. P., Raj, S. K., Kumari, J., Rathore, M. S., & Kulshrestha, V. (2021). Effect of environmental temperature and applied potential on water desalination performance using electrodialysis. *Materials Today Chemistry*, 20, 100484. <https://doi.org/10.1016/j.mtchem.2021.100484>
- [63] Liu, H., & She, Q. (2022). Influence of membrane structure-dependent water transport on conductivity-permselectivity trade-off and salt/water selectivity in electrodialysis: Implications for osmotic electrodialysis using porous ion exchange membranes. *Journal of Membrane Science*, 650, 120398. <https://doi.org/10.1016/j.memsci.2022.120398>
- [64] Tian, B., Wang, X., Zhang, L., Shi, F., Zhang, Y., & Li, S. (2016). Preparation of PVDF anionic exchange membrane by chemical grafting of GMA onto PVDF macromolecule. *Solid State Ionics*, 293, 56–63. <https://doi.org/10.1016/j.ssi.2016.06.006>
- [65] Tadimeti, J. G. D., Jain, S., Chattopadhyay, S., & Bhattacharya, P. K. (2014). Selection of the Best Process Stream to Remove Ca²⁺ Ion Using Electrodialysis from Sugar Solution. *International Journal of Electrochemistry*, 2014, 1–12. <https://doi.org/10.1155/2014/304296>
- [66] Díaz, J. C., & Kamcev, J. (2021b). Ionic conductivity of ion-exchange membranes: Measurement techniques and salt concentration dependence. *Journal of Membrane Science*, 618, 118718. <https://doi.org/10.1016/j.memsci.2020.118718>
- [67] Huang, Y., Fan, H., & Yip, N. Y. (2022). Influence of electrolyte on concentration-induced conductivity-permselectivity tradeoff of ion-exchange membranes. *Journal of Membrane Science*, 668, 121184. <https://doi.org/10.1016/j.memsci.2022.121184>
- [68] Fan, H., & Yip, N. Y. (2019). Elucidating conductivity-permselectivity tradeoffs in electrodialysis and reverse electrodialysis by structure-property analysis of ion-exchange membranes. *Journal of Membrane Science*, 573, 668–681. <https://doi.org/10.1016/j.memsci.2018.11.045>
- [69] Sadrzadeh, M., & Mohammadi, T. (2009). Treatment of sea water using electrodialysis: Current efficiency evaluation. *Desalination*, 249(1), 279–285. <https://doi.org/10.1016/j.desal.2008.10.029>
- [70] Donnan, F. G. (1924). The theory of membrane equilibria. *Chemical Reviews*, 1(1), 73–90. <https://doi.org/10.1021/cr60001a003>
- [71] Ran, J., Wu, L., He, Y., Yang, Z., Wang, Y., Jiang, C., Ge, L., Bakangura, E., & Xu, T. (2017). Ion exchange membranes: New developments and applications. *Journal of Membrane Science*, 522, 267–291. <https://doi.org/10.1016/j.memsci.2016.09.033>
- [72] Sarkar, S., SenGupta, A. K., & Prakash, P. (2010). The Donnan Membrane Principle: Opportunities for Sustainable Engineered Processes and Materials. *Environmental Science & Technology*, 44(4), 1161–1166. <https://doi.org/10.1021/es9024029>
- [73] Luo, T., Abdu, S., & Wessling, M. (2018). Selectivity of ion exchange membranes: A review. *Journal of Membrane Science*, 555, 429–454. <https://doi.org/10.1016/j.memsci.2018.03.051>
- [74] Tian, H., Zhang, L., & Wang, M. (2015). Applicability of Donnan equilibrium theory at nanochannel–reservoir interfaces. *Journal of Colloid and Interface Science*, 452, 78–88. <https://doi.org/10.1016/j.jcis.2015.03.064>

- [75] Długofęcki, P., Ogonowski, P., Metz, S. J., Saakes, M., Nijmeijer, K., & Wessling, M. (2010). On the resistances of membrane, diffusion boundary layer and double layer in ion exchange membrane transport. *Journal of Membrane Science*, 349(1–2), 369–379. <https://doi.org/10.1016/j.memsci.2009.11.069>
- [76] Jiang, W., Lin, L., Xu, X., Wang, H., & Xu, P. (2019). Physicochemical and electrochemical characterization of cation-exchange membranes modified with polyethyleneimine for elucidating enhanced monovalent permselectivity of electrodialysis. *Journal of Membrane Science*, 572, 545–556. <https://doi.org/10.1016/j.memsci.2018.11.038>
- [77] Ntakirutimana, S., Tan, W., Anderson, M. A., & Wang, Y. (2020). Editors' Choice—Review—Activated Carbon Electrode Design: Engineering Tradeoff with Respect to Capacitive Deionization Performance. *Journal of the Electrochemical Society*, 167(14), 143501. <https://doi.org/10.1149/1945-7111/abfd7>
- [78] Thom, N. T., Anh, V., Trang, N. T. T., Phuong, N. T., Thanh, D. T. M., Dang, L. S., Lam, T. D., & Nam, P. C. (2022). Study on the functionalization of activated carbon and the effect of binder toward capacitive deionization application. *Green Processing and Synthesis*, 11(1), 830–841. <https://doi.org/10.1515/gps-2022-0049>
- [79] Zhang, C., Wang, H., Gao, Y., & Wan, C. (2022). Cellulose-derived carbon aerogels: A novel porous platform for supercapacitor electrodes. *Materials & Design*, 219, 110778. <https://doi.org/10.1016/j.matdes.2022.110778>
- [80] Zhang, H., Tian, J., Cui, X., Li, J., & Zhu, Z. (2022). Highly mesoporous carbon nanofiber electrodes with ultrahigh specific surface area for efficient capacitive deionization. *Carbon*, 201, 920–929. <https://doi.org/10.1016/j.carbon.2022.10.002>
- [81] Liu, L., Liao, L., Meng, Q., & Cao, B. (2015). High performance graphene composite microsphere electrodes for capacitive deionisation. *Carbon*, 90, 75–84. <https://doi.org/10.1016/j.carbon.2015.04.009>
- [82] Zhang, S., Wang, Y., Han, X., Cai, Y., & Xu, S. (2018). Optimizing the fabrication of carbon nanotube electrode for effective capacitive deionization via electrophoretic deposition strategy. *Progress in Natural Science*, 28(2), 251–257. <https://doi.org/10.1016/j.pnsc.2018.02.010>
- [83] Oladunni, J., Zain, J. H., Hai, A., Banat, F., Bharath, G., & Alhseinat, E. (2018). A comprehensive review on recently developed carbon based nanocomposites for capacitive deionization: From theory to practice. *Separation and Purification Technology*, 207, 291–320. <https://doi.org/10.1016/j.seppur.2018.06.046>
- [84] Wang, Y., Vázquez-Rodríguez, I., Santos, C., García-Quismondo, E., Palma, J., Anderson, M. A., & Lado, J. J. (2020). Graphite felt 3D framework composites as an easy to scale capacitive deionization electrode for brackish water desalination. *Chemical Engineering Journal*, 392, 123698. <https://doi.org/10.1016/j.cej.2019.123698>
- [85] Mubita, T., Porada, S., Biesheuvel, P., Van Der Wal, A., & Dykstra, J. (2018). Capacitive deionization with wire-shaped electrodes. *Electrochimica Acta*, 270, 165–173. <https://doi.org/10.1016/j.electacta.2018.03.082>
- [86] Nadakatti, S. M., Tendulkar, M. S., & Kadam, M. (2011b). Use of mesoporous conductive carbon black to enhance performance of activated carbon electrodes in capacitive deionization technology. *Desalination*, 268(1–3), 182–188. <https://doi.org/10.1016/j.desal.2010.10.020>
- [87] Mistry, A., Trask, S. E., Dunlop, A. R., Jeka, G. T., Polzin, B. J., Mukherjee, P. P., & Srinivasan, V. (2021). Quantifying Negative Effects of Carbon-Binder Networks from Electrochemical Performance of Porous Li-Ion Electrodes. *Journal of the Electrochemical Society*, 168(7), 070536. <https://doi.org/10.1149/1945-7111/ac1033>
- [88] Salleh, N. A., Kheawhom, S., Hamid, N. a. A., Rahiman, W., & Mohamad, A. A. (2023). Electrode polymer binders for supercapacitor applications: A review. *Journal of Materials Research and Technology*, 23, 3470–3491. <https://doi.org/10.1016/j.jmrt.2023.02.013>
- [89] Arunkumar, M. A., & Paul, A. (2017). Importance of Electrode Preparation Methodologies in Supercapacitor Applications. *ACS Omega*, 2(11), 8039–8050. <https://doi.org/10.1021/acsomega.7b01275>
- [90] Kim, K. H. (2015). High Operating Voltage Supercapacitor Using PPy/AC Composite Electrode Based on Simple Dipping Method. *Journal of Chemistry*, 2015, 1–7. <https://doi.org/10.1155/2015/314893>
- [91] Carlsson Technologies Sdn Bhd (n.d.). *ZX Instruments - Thermal Blast Drying Oven Laboratory Equipments Melaka, Malaysia, Ayer Keroh Supplier, Suppliers, Supply, Supplies | Carlsson Technologies (Malaysia) Sdn Bhd*. https://www.carlsson-tech.com/index.php?ws=showproducts&products_id=3059938
- [92] Park, K., Lee, J., Park, P., Yoon, S., Moon, J., Eum, H., & Lee, C. (2007). Development of a carbon sheet electrode for electrosorption desalination. *Desalination*, 206(1–3), 86–91. <https://doi.org/10.1016/j.desal.2006.04.051>
- [93] Nyongombe, G. E., Bello, I. T., Otun, K. O., Kabongo, G. L., Mothudi, B. M., Noto, L., & Dhlamini, M. S. (2022). Unveiling the benefits of dimethyl sulfoxide as a binder solvent on the electrochemical performance of layered double hydroxides. *Electrochimica Acta*, 419, 140386. <https://doi.org/10.1016/j.electacta.2022.140386>
- [94] Dsoke, S., Tian, X., Täubert, C., Schlüter, S., & Wohlfahrt-Mehrens, M. (2013). Strategies to reduce the resistance sources on Electrochemical Double Layer Capacitor electrodes. *Journal of Power Sources*, 238, 422–429. <https://doi.org/10.1016/j.jpowsour.2013.04.031>
- [95] Lasia, A. (2014). *Electrochemical Impedance Spectroscopy and its Applications*. Springer Publishing.
- [96] Huang, Q. A., Li, Y., Tsay, K. C., Sun, C., ChangpingYang, Zhang, L., & Zhang, J. (2018). Multi-scale impedance model for supercapacitor porous electrodes: Theoretical prediction and experimental validation. *Journal of Power Sources*, 400, 69–86. <https://doi.org/10.1016/j.jpowsour.2018.07.108>
- [97] Park, J., Choi, J., Woo, J., & Moon, S. (2006). An electrical impedance spectroscopic (EIS) study on transport characteristics of ion-exchange membrane systems. *Journal of Colloid and Interface Science*, 300(2), 655–662. <https://doi.org/10.1016/j.jcis.2006.04.040>

- [98] Du, C., & Pan, N. (2006). High power density supercapacitor electrodes of carbon nanotube films by electrophoretic deposition. *Nanotechnology*, 17(21), 5314–5318. <https://doi.org/10.1088/0957-4484/17/21/005>
- [99] Nikonenko, V., & Kozmai, A. (2011). Electrical equivalent circuit of an ion-exchange membrane system. *Electrochimica Acta*, 56(3), 1262–1269. <https://doi.org/10.1016/j.electacta.2010.10.094>
- [100] Fontananova, E., Messina, D., Fontananova, E., Nicotera, I., Kosma, V., Curcio, E., Van Baak, W., & Drioli, E. (2017). Effect of solution concentration and composition on the electrochemical properties of ion exchange membranes for energy conversion. *Journal of Power Sources*, 340, 282–293. <https://doi.org/10.1016/j.jpowsour.2016.11.075>
- [101] Suss, M. E., Baumann, T. F., Worsley, M. A., Rose, K. A., Jaramillo, T. F., Stadermann, M., & Santiago, J. G. (2013). Impedance-based study of capacitive porous carbon electrodes with hierarchical and bimodal porosity. *Journal of Power Sources*, 241, 266–273. <https://doi.org/10.1016/j.jpowsour.2013.03.178>
- [102] De Levie, R. (1963). On porous electrodes in electrolyte solutions. *Electrochimica Acta*, 8(10), 751–780. [https://doi.org/10.1016/0013-4686\(63\)80042-0](https://doi.org/10.1016/0013-4686(63)80042-0)
- [103] Barcia, O. E., D'Elia, E., Frateur, I., Mattos, O. R., Pébère, N., & Tribollet, B. (2002). Application of the impedance model of de Levie for the characterization of porous electrodes. *Electrochimica Acta*, 47(13–14), 2109–2116. [https://doi.org/10.1016/s0013-4686\(02\)00081-6](https://doi.org/10.1016/s0013-4686(02)00081-6)
- [104] Siroma, Z., Fujiwara, N., Yamazaki, S. I., Asahi, M., Nagai, T., & Ioroi, T. (2020). Multi-rail transmission-line model as an equivalent circuit for electrochemical impedance of a porous electrode. *Journal of Electroanalytical Chemistry*, 878, 114622. <https://doi.org/10.1016/j.jelechem.2020.114622>
- [105] Illig, J., Ender, M., Weber, A. C., & Ivers-Tiffée, E. (2015). Modeling graphite anodes with serial and transmission line models. *Journal of Power Sources*, 282, 335–347. <https://doi.org/10.1016/j.jpowsour.2015.02.038>
- [106] Adamič, M., Talian, S. D., Sinigoj, A. R., Humar, I., Moškon, J., & Gaberšček, M. (2019). A Transmission Line Model of Electrochemical Cell's Impedance: Case Study on a Li-S System. *Journal of the Electrochemical Society*, 166(3), A5045–A5053. <https://doi.org/10.1149/2.0061903jes>
- [107] Lazanas, A. C., & Prodromidis, M. I. (2023). Electrochemical Impedance Spectroscopy—A Tutorial. *ACS Measurement Au*. <https://doi.org/10.1021/acsmeasuresci.2c00070>
- [108] Zheng, H., Li, J., Song, X., Liu, G., & Battaglia, V. (2012b). A comprehensive understanding of electrode thickness effects on the electrochemical performances of Li-ion battery cathodes. *Electrochimica Acta*, 71, 258–265. <https://doi.org/10.1016/j.electacta.2012.03.161>
- [109] Shevah, Y. (2014). Adaptation to Water Scarcity and Regional Cooperation in the Middle East. In *Elsevier eBooks* (pp. 40–70). <https://doi.org/10.1016/b978-0-12-382182-9.00004-9>
- [110] Aqion (2013). *Table of diffusion coefficients*. <https://www.aqion.de/site/diffusion-coefficients>
- [111] Tanaka, Y. (2004). Concentration polarization in ion-exchange membrane electrodialysis: The events arising in an unforced flowing solution in a desalting cell. *Journal of Membrane Science*, 244(1–2), 1–16. <https://doi.org/10.1016/j.memsci.2004.02.041>
- [112] Lindemuth, J. R., Rodgers, R. & Fosdick, L. (1985). *The Evaluation of Electrochemical Corrosion Data by a Non-Linear X² Minimization*. The Electrochemical Society, Pennington, NJ. <https://electrochemistryresources.com/fitting-eis-data-adding-components/>
- [113] Oje, A. I., Ogwu, A. A., & Oje, A. (2021). Effect of temperature on the electrochemical performance of silver oxide thin films supercapacitor. *Journal of Electroanalytical Chemistry*, 882, 115015. <https://doi.org/10.1016/j.jelechem.2021.115015>
- [114] Assis, S. L., Wolyneć, S., & Costa, I. (2006). Corrosion characterization of titanium alloys by electrochemical techniques. *Electrochimica Acta*, 51(8–9), 1815–1819. <https://doi.org/10.1016/j.electacta.2005.02.121>
- [115] BioLogic. (2022a, March 2). VSP-300 Potentiostat - BioLogic. <https://www.biologic.net/products/vsp-300/>
- [116] Lamiel, C., Hussain, I., Ma, X., & Zhang, K. (2022). Properties, functions, and challenges: current collectors. *Materials Today Chemistry*, 26, 101152. <https://doi.org/10.1016/j.mtchem.2022.101152>
- [117] Cole-Parmer Instrument Company, LLC (2021). *Hotplates, Stirrers & Hotplate Stirrers with BioCote® antimicrobial protection*. <https://pim-resources.coleparmer.com/data-sheet/04807-58-65-90-91-cp-bro-stuart-undergrad-a4-2021-final-uk.pdf>
- [118] Lead Fluid. (2023, January 11). BT100S Basic Variable-Speed Peristaltic Pump - Lead Fluid. <https://leadfluid.com/product/bt100s-basic-variable-speed-peristaltic-pump/>
- [119] eDAQ (n.d.). ET908 Flow-Thru Conductivity Electrode (93 µL) - eDAQ. <https://www.edaq.com/ET908>
- [120] eDAQ (n.d.). EPU357 Conductivity isoPodTM with USB - eDAQ. <https://www.edaq.com/EPU357>
- [121] eDAQ (n.d.). isoPods: Streaming Meters for Recording Temperature, pH, Conductivity and Dissolved Oxygen - eDAQ. <https://www.edaq.com/isopods-miniature-electrically-isolated-meters>
- [122] Van Rossum, G., & Drake Jr, F. L. (1995). *Python reference manual*. Centrum voor Wiskunde en Informatica Amsterdam.
- [123] Harris, C.R., Millman, K.J., van der Walt, S.J. et al. *Array programming with NumPy*. *Nature* 585, 357–362 (2020). <https://doi.org/10.1038/s41586-020-2649-2>.
- [124] McKinney, W. (2010). Data structures for statistical computing in Python. *Proceedings of the Python in Science Conferences*. <https://doi.org/10.25080/majora-92bf1922-00a>
- [125] Hunter, J. (2007). Matplotlib: a 2D Graphics environment. *Computing in Science and Engineering*, 9(3), 90–95. <https://doi.org/10.1109/mcse.2007.55>

- [126] Virtanen, P., Gommers, R., Oliphant, T. E., Haberland, M., Reddy, T., Cournapeau, D., Burovski, E., Peterson, P., Weckesser, W., Bright, J., Van Der Walt, S. J., Brett, M., Wilson, J., Millman, K. J., Mayorov, N., Nelson, A., Jones, E. D., Kern, R., Larson, E. B., . . . Oshima, T. (2020). SciPy 1.0: fundamental algorithms for scientific computing in Python. *Nature Methods*, 17(3), 261–272. <https://doi.org/10.1038/s41592-019-0686-2>
- [127] CarlRoth (2017, January 17). *Safety Data Sheet: Potassium chloride solution*. <https://www.carlroth.com/medias/SDB-5346-NL-NL.pdf?context=bWFzdGVyfHNIY3VyaXR5RGFOYXNoZWV0c3wyMjUwNTZ8YXBwbGliYXRpb24vcGRmfHNIY3VyaXR5RGFOYXNoZVV0cy9oODgvaDRhLzkwNDExODI1NTYxOTAucGRmfDM3ZTNjOTNiODIhYzZM2ZTgxNzQyNjIwMDc5NmU0NiA2ZTA5OWlyZjIzNDBiMDU4M2I0NjY0N2IiMjc0ZWYxYWM>
- [128] International Labour Organization & World Health Organization (2021). *ICSC 1450 - POTASSIUM CHLORIDE*. http://www.ilo.org/dyn/icsc/showcard.display?p_card_id=1450&p_version=2&p_lang=en
- [129] Rica, R. A., Brogioli, D., Ziano, R., Salerno, D., & Mantegazza, F. (2012). Ions transport and adsorption mechanisms in porous electrodes during Capacitive-Mixing Double Layer Expansion (CDLE). *Journal of Physical Chemistry C*, 116(32), 16934–16938. <https://doi.org/10.1021/jp3059849>
- [130] Lu, W., Jansen, A. N., Dees, D. W., Nelson, P., Veselka, N. R., & Henriksen, G. L. (2011b). High-energy electrode investigation for plug-in hybrid electric vehicles. *Journal of Power Sources*, 196(3), 1537–1540. <https://doi.org/10.1016/j.jpowsour.2010.08.117>
- [131] Araki, C., Tsubouchi, S., Noie, A., Nishimura, E., Suzuki, S., & Makino, S. (2016b). Influence of decreasing electrode thickness on its structure and resistance for Lithium-Ion batteries. *Meeting Abstracts*. <https://doi.org/10.1149/ma2016-02/3/325>
- [132] Jaiser, S., Müller, M., Baunach, M., Bauer, W., Scharfer, P., & Schabel, W. (2016). Investigation of film solidification and binder migration during drying of Li-Ion battery anodes. *Journal of Power Sources*, 318, 210–219. <https://doi.org/10.1016/j.jpowsour.2016.04.018>
- [133] Yang, S., & Li, H. (2020). Effect of temperature on composite films made with activated carbon, graphite, or graphene oxide (GO) in a gelatin matrix. *Bioresources*, 16(1), 77–95. <https://doi.org/10.15376/biores.16.1.77-95>
- [134] Burnat, B., Brycht, M., Leniart, A., & Skrzypek, S. (2022). Carbon black-modified carbon ceramic electrode – Its fabrication, characterization, and electroanalytical performance. *Diamond and Related Materials*, 130, 109513. <https://doi.org/10.1016/j.diamond.2022.109513>
- [135] Jäckel, N., Weingarh, D., Zeiger, M., Aslan, M., Grobelsek, I., & Presser, V. (2014). Comparison of carbon onions and carbon blacks as conductive additives for carbon supercapacitors in organic electrolytes. *Journal of Power Sources*, 272, 1122–1133. <https://doi.org/10.1016/j.jpowsour.2014.08.090>
- [136] Orazem, M. E., & Tribollet, B. (2017). *Electrochemical impedance spectroscopy*. John Wiley & Sons, Incorporated.
- [137] Klotz, D. (2019). Negative capacitance or inductive loop? – A general assessment of a common low frequency impedance feature. *Electrochemistry Communications*, 98, 58–62. <https://doi.org/10.1016/j.elecom.2018.11.017>
- [138] Boukamp, B. A. (2001). Interpretation of an “inductive loop” in the impedance of an oxygen ion conducting electrolyte/metal electrode system. *Solid State Ionics*, 143(1), 47–55. [https://doi.org/10.1016/S0167-2738\(01\)00832-3](https://doi.org/10.1016/S0167-2738(01)00832-3)
- [139] Lauvstad, G. Ø., Tunold, R., & Sunde, S. (2002). Electrochemical Oxidation of CO on Pt and Ni Point Electrodes in Contact with an Yttria-Stabilized Zirconia Electrolyte. *Journal of the Electrochemical Society*, 149(12), E497. <https://doi.org/10.1149/1.1518484>
- [140] Hughes, M., Allen, J. A., & Donne, S. W. (2020). Characterization of carbonate derived carbons through electrochemical impedance spectroscopy. *Electrochimica Acta*, 338, 135847. <https://doi.org/10.1016/j.electacta.2020.135847>
- [141] Lamoén, D., & Persson, B. N. J. (1998). Adsorption of potassium and oxygen on graphite: A theoretical study. *Journal of Chemical Physics*, 108(8), 3332–3341. <https://doi.org/10.1063/1.475732>
- [142] Sjövall, P., & Kasemo, B. H. (1993). A TDS study of oxygen, water and carbon dioxide coadsorption with potassium on graphite. *Surface Science*, 290(1–2), 55–68. [https://doi.org/10.1016/0039-6028\(93\)90588-b](https://doi.org/10.1016/0039-6028(93)90588-b)
- [143] Chang, J. S., Lauderback, L., & Falconer, J. L. (1991). Aes and sims analysis of potassium/ graphite surfaces. *Carbon*, 29(4–5), 645–652. [https://doi.org/10.1016/0008-6223\(91\)90132-3](https://doi.org/10.1016/0008-6223(91)90132-3)
- [144] Chakarov, D., Sjövall, P., & Kasemo, B. H. (1993). The interaction of potassium with oxygen on graphite as studied by high-resolution electron energy loss spectroscopy and thermal desorption spectroscopy. *Journal of Physics: Condensed Matter*, 5(18), 2903–2912. <https://doi.org/10.1088/0953-8984/5/18/012>
- [145] Magar, H. S., Hassan, R. Y. A., & Mulchandani, A. (2021). Electrochemical Impedance Spectroscopy (EIS): Principles, Construction, and Biosensing Applications. *Sensors*, 21(19), 6578. <https://doi.org/10.3390/s21196578>
- [146] Pang, T., Marken, F., Zhang, D., Mattia, D., & Shen, J. (2022). Linking macroscopic surface morphology of activated carbon fibres and electrosorption performance: An electrochemical impedance spectroscopy and capacitive deionization study. *Applied Surface Science*, 609, 155397. <https://doi.org/10.1016/j.apsusc.2022.155397>
- [147] DuToit, M., Ngaboyamahina, E., & Wiesner, M. (2021). Pairing electrochemical impedance spectroscopy with conducting membranes for the in situ characterization of membrane fouling. *Journal of Membrane Science*, 618, 118680. <https://doi.org/10.1016/j.memsci.2020.118680>
- [148] Itagaki, M., Suzuki, S. O., Shitanda, I., & Watanabe, K. (2007). Electrochemical Impedance and Complex Capacitance to Interpret Electrochemical Capacitor. *Electrochemistry*, 75(8), 649–655. <https://doi.org/10.5796/electrochemistry.75.649>
- [149] Taberna, P., Simon, P., & Fauvarque, J. (2003). Electrochemical Characteristics and Impedance Spectroscopy Studies of Carbon-Carbon Supercapacitors. *Journal of the Electrochemical Society*, 150(3), A292. <https://doi.org/10.1149/1.1543948>

- [150] Huang, J., Li, Z., Liaw, B. Y., & Zhang, J. (2016). Graphical analysis of electrochemical impedance spectroscopy data in Bode and Nyquist representations. *Journal of Power Sources*, 309, 82–98. <https://doi.org/10.1016/j.jpowsour.2016.01.073>
- [151] Macdonald, R. J., & Barsoukov, E. (2018). *Impedance Spectroscopy: Theory, Experiment, and Applications* (3rd ed.). Wiley.
- [152] Qu, D., & Shi, H. (1998). Studies of activated carbons used in double-layer capacitors. *Journal of Power Sources*, 74(1), 99–107. [https://doi.org/10.1016/S0378-7753\(98\)00038-X](https://doi.org/10.1016/S0378-7753(98)00038-X)
- [153] Scipioni, R., Jørgensen, P. M., Graves, C. R., Hjelm, J., & Jensen, S. H. (2017). A Physically-Based Equivalent Circuit Model for the Impedance of a LiFePO₄/Graphite 26650 Cylindrical Cell. *Journal of the Electrochemical Society*, 164(9), A2017–A2030. <https://doi.org/10.1149/2.1071709jes>
- [154] Kizilyalli, M., Corish, J. & Metselaar, R. (1999). Definitions of terms for diffusion in the solid state (IUPAC Recommendations 1999). *Pure and Applied Chemistry*, 71(7), 1307–1325. <https://doi.org/10.1046/j.1365-3075.1999.00263.x>
- [155] Hilario, F., Roche, V., Jorge, A. M., & Nogueira, R. P. (2017). Application of the transmission line model for porous electrodes to analyse the impedance response of TiO₂ nanotubes in physiological environment. *Electrochimica Acta*, 253, 599–608. <https://doi.org/10.1016/j.electacta.2017.09.045>
- [156] Gao, P., Tsai, W., Daffos, B., Taberna, P., Pérez, C. R., Gogotsi, Y., Simon, P., & Favier, F. (2015). Graphene-like carbide derived carbon for high-power supercapacitors. *Nano Energy*, 12, 197–206. <https://doi.org/10.1016/j.nanoen.2014.12.017>
- [157] Qu, D., Ji, W., & Qu, H. (2022). Probing process kinetics in batteries with electrochemical impedance spectroscopy. *Communications Materials*, 3(1). <https://doi.org/10.1038/s43246-022-00284-w>
- [158] Lucas, É., Han, L., Sullivan, I. D., Atwater, H. A., & Xiang, C. (2022). Measurement of ion transport properties in ion exchange membranes for photoelectrochemical water splitting. *Frontiers in Energy Research*, 10. <https://doi.org/10.3389/fenrg.2022.1001684>
- [159] Zhao, Z., Shi, S., Cao, H., & Li, Y. (2017). Electrochemical impedance spectroscopy and surface properties characterization of anion exchange membrane fouled by sodium dodecyl sulfate. *Journal of Membrane Science*, 530, 220–231. <https://doi.org/10.1016/j.memsci.2017.02.037>
- [160] Gamry Instruments. (n.d.). *Accuracy Contour Plots ACP: Potentiostat EIS Performance*. <https://www.gamry.com/application-notes/EIS/accuracy-contour-plots-measurement-and-discussion/>
- [161] Pine Research Instrumentation Store (2023, January 4). *EIS Basic Background Theory*. <https://pineresearch.com/shop/kb/theory/eis-theory/basic-background-theory/>
- [162] Stevenson, H., Shanmugam, N. R., Selvam, A. P., & Prasad, S. (2018). The Anatomy of a Nonfaradaic Electrochemical Biosensor. *Journal of Laboratory Automation*, 23(1), 5–15. <https://doi.org/10.1177/2472630317738700>
- [163] Kanoun, O. (2016). *Progress Reports on Impedance Spectroscopy: Measurements, Modeling, and Application*. De Gruyter.
- [164] Boukamp, B. A. (1995). A Linear Kronig-Kramers Transform Test for Immittance Data Validation. *Journal of the Electrochemical Society*, 142(6), 1885–1894. <https://doi.org/10.1149/1.2044210>
- [165] Agarwal, P., Orazem, M. E., & Garcia-Rubio, L. H. (1995). Application of Measurement Models to Impedance Spectroscopy: III. Evaluation of Consistency with the Kramers-Kronig Relations. *Journal of the Electrochemical Society*, 142(12), 4159–4168. <https://doi.org/10.1149/1.2048479>
- [166] Matsubara, Y. (2021). A small yet complete framework for a potentiostat, galvanostat, and electrochemical impedance spectrometer. *Journal of Chemical Education*, 98(10), 3362–3370. <https://doi.org/10.1021/acs.jchemed.1c00228>
- [167] Ahdab, Y. D., & Lienhard, J. H. (2020). Desalination of brackish groundwater to improve water quality and water supply. *Elsevier eBooks*, 559–575. <https://doi.org/10.1016/B978-0-12-818172-0.00041-4>
- [168] Kim, J., & Pyun, S. I. (2011). Comparison of transmissive permeable and reflective impermeable interfaces between electrode and electrolyte. *Journal of Solid State Electrochemistry*, 15(11–12), 2447–2452. <https://doi.org/10.1007/s10008-011-1393-9>
- [169] Siroma, Z., Fujiwara, N., Yamazaki, S., Asahi, M., Nagai, T., & Ioroi, T. (2015). Mathematical solutions of comprehensive variations of a transmission-line model of the theoretical impedance of porous electrodes. *Electrochimica Acta*, 160, 313–322. <https://doi.org/10.1016/j.electacta.2015.02.065>
- [170] Hawks, S. A., Knipe, J. M., Campbell, P. G., Loeb, C. K., Hubert, M. A., Santiago, J. G., & Stadermann, M. (2018). Quantifying the flow efficiency in constant-current capacitive deionization. *Water Research*, 129, 327–336. <https://doi.org/10.1016/j.watres.2017.11.025>
- [171] Guyes, E. N., Shocron, A. N., Simanovski, A., Biesheuvel, P., & Suss, M. E. (2017). A one-dimensional model for water desalination by flow-through electrode capacitive deionization. *Desalination*, 415, 8–13. <https://doi.org/10.1016/j.desal.2017.03.013>
- [172] Jeon, S., Park, H., Yeo, J., Yang, S., Cho, C., Han, M. H., & Kim, D. (2013). Desalination via a new membrane capacitive deionization process utilizing flow-electrodes. *Energy and Environmental Science*, 6(5), 1471. <https://doi.org/10.1039/c3ee24443a>
- [173] Gao, X., Omosibi, A., Landon, J., & Liu, K. (2015). Surface charge enhanced carbon electrodes for stable and efficient capacitive deionization using inverted adsorption–desorption behavior. *Energy and Environmental Science*, 8(3), 897–909. <https://doi.org/10.1039/c4ee03172e>
- [174] Lee, J., Kim, S., & Kim, C. (2014). Hybrid capacitive deionization to enhance the desalination performance of capacitive techniques. *Energy and Environmental Science*, 7(11), 3683–3689. <https://doi.org/10.1039/c4ee02378a>

- [175] Yang, H., Shi, Q., Zhang, Y., Xie, S., Jiang, D., Zhang, F., Yu, C., Tu, B., & Zhao, D. (2002). Synthesis of ordered mesoporous carbon monoliths with bicontinuous cubic pore structure of Ia3d symmetry. *Chemical Communications*, 23, 2842–2843. <https://doi.org/10.1039/b209233f>
- [176] Noked, M., Okashy, S., Zimrin, T., & Aurbach, D. (2012). Composite Carbon Nanotube/Carbon Electrodes for Electrical Double-Layer Super Capacitors. *Angewandte Chemie*, 51(7), 1568–1571. <https://doi.org/10.1002/anie.201104334>
- [177] Kalluri, R. K., Biener, M. M., Suss, M. E., Merrill, M. D., Stadermann, M., Santiago, J. G., Baumann, T., Biener, J., & Striolo, A. (2013). Unraveling the potential and pore-size dependent capacitance of slit-shaped graphitic carbon pores in aqueous electrolytes. *Physical Chemistry Chemical Physics*, 15(7), 2309. <https://doi.org/10.1039/c2cp43361c>
- [178] Seo, M., Kim, J., Han, J. Y., Kang, S., Ihm, J., & Kim, D. (2013). Tunable and selective formation of micropores and mesopores in carbide-derived carbon. *Carbon*, 60, 299–306. <https://doi.org/10.1016/j.carbon.2013.04.041>
- [179] Suss, M. E., Porada, S., Sun, X., Biesheuvel, P., Yoon, J., & Presser, V. (2015b). Water desalination via capacitive deionization: what is it and what can we expect from it? *Energy and Environmental Science*, 8(8), 2296–2319. <https://doi.org/10.1039/c5ee00519a>
- [180] Zhang, W., Ma, J., Wang, P., Wang, Z., Shi, F., & Liu, H. (2016). Investigations on the interfacial capacitance and the diffusion boundary layer thickness of ion exchange membrane using electrochemical impedance spectroscopy. *Journal of Membrane Science*, 502, 37–47. <https://doi.org/10.1016/j.memsci.2015.12.007>

List of Figures

Figure 1: 33 countries will face extremely high water scarcity in 2040 according to World Resources Institute (2015, August 26). Source of the figure: Statista Infographics (2022, March 22) [4].....	11
Figure 2: Multi-channel CDI system during the generation phase (left) and the discharge phase (right). The feed stream goes into the paper. Orange and blue electrodes are the positively and negatively charged capacitive membrane electrode, respectively.	12
Figure 3: Charging and discharging of capacitive deionisation cells. Source: Ramachandram et al. (2019) [26].	17
Figure 4: Metal planar electrode immersed in an electrolyte. The surface charge of the electrode attracts the anions with solvation shells and water molecules. Source: Lopatynska et al. (2008) [39].	21
Figure 5: Electric Double Layer models developed by (a) Helmholtz, (b) Gouy and Chapman, (c) Stern and (d) Grahame. The potential in the EDL over the distance from the metal-solution interface is depicted with the yellow line. Figures were retrieved from the review paper of Dourado (2022) [38].	22
Figure 6: The adsorption of ions inside micropores. Debye lengths of the EDLs are depicted with the black dotted lines. Figure has been retrieved from the paper of Zhang et al. (2018) [36].	23
Figure 7: Model of the mesopores according to Huang & He (2013) [51]. The original figure was copied from the review paper of Gabitto & Tsouris (2023) [48].	23
Figure 8: Schematic of a conventional electrodialysis system. The cell unit consists of one brine channel and one product channel with an AEM and an CEM. Retrieved from Qureshi et al. (2021) [53].	24
Figure 9: (a) Concentration profile of cations in a binary electrolyte with a CEM. Source: Luo et al. (2018) [73]. (b) Graphical model of an CEM. Source: Tian et al. (2015) [74].	27
Figure 10: The electron transport and ion transport in the electrode consisting of active material and carbon black particles. Source: Qu et al. (2022) [157].	28
Figure 11: General fabrication of an activated carbon electrode with conducting carbon and a polymeric binder. This figure is a modified figure taken from the paper of Kim (2015) [90,91].	29
Figure 12: Typical EECM and Nyquist plot for carbon supercapacitors. The vertical line after the 45° line for the diffusion dominating region is the capacitive behaviour of the electrode dominant. There is a semi-circle due to faradaic reactions. Figure retrieved from the research paper of Dsoke et al. (2013) [94].	30
Figure 13: (B) Equivalent Electrical circuit model for an ion exchange membrane and (A) the physical behaviour in the ion exchange membrane at different frequencies. The figures are adjusted from original figures retrieved from the research paper of Długolecki et al. (2010) [75]. (C) The Nyquist plot of an ion exchange membrane from the research paper of Nikonenko & Kozmai (2011) [99].	31
Figure 14: (left) The graphical scheme of the transmission-line model according to De Levie (1963) [102]. (right) The electronic rail and ionic rail are connected like a ladder by equivalent circuits which describe the interface impedance. The figures were retrieved from the research paper of Siroma et al. (2020) [104].	35
Figure 15: Equivalent circuits for the interface impedance: (a) ideal double layer capacitor, (b) faradaic reactions at the interface, (c) semi-infinite diffusion at the interface. Figure retrieved from the research paper of Siroma et al. (2020) [104].	36
Figure 16: Electrical circuit of the finite Transmission-line model (TLM): (a) ladder-like hierarchical TLM, and (b) a simplified version of the electrical circuit of the TLM. The figure is modified from the original figure in the paper by Adamič et al. (2019) [106].	36
Figure 17: The electrical circuit of the Transmission-line model. (b) The Δ -Y transformation simplifies this circuit: the ions move through resistors z_A and z_B , while the electrons move through resistor z_C .	

(c) The equivalent electrical circuit model of the CME (EECM B: TLM), after assuming that the freestanding CMEs are homogeneous, $z_A=z_B$	37
Figure 18: Equivalent electrical circuit representations of the Transmission-Line model in different electrode material structures: (a) Transmission-line model with reflective boundary condition for blocking electrodes, and (b) Transmission-line model with transmissive boundary condition for membranes made with carbon material.....	38
Figure 19: The predicted electrical circuit of the CME cell in the CME setup. The electrochemical behaviour of the CME could be modelled according to the TLM (EECM B). For a 4-point measurement, the current flows between the end electrodes and the potential is measured between the CMEs. In this case, the solution resistance R_s of the electrolyte in the spacer and the resistors z_A where the ions flow through are the only electrical circuit blocks that are measured (highlighted in green). In a 2-point measurement, the current flows between the CMEs and the response AC potential is measured between the CMEs. Now the contact resistance circuit, the solution resistance R_s and the resistance of the electrons z_C are measured. The 4-point measurement is preferred because the contact resistance is eliminated from the measurement. Other equivalent circuit models (EECM A, EECM C, EECM D and EECM E), whose electrical circuits are shown at the bottom of the figure in order of complexity, are also fitted through the impedance data of the CME to find the least complex but most accurate EECM. The circuit in the red dashed square is replaced by the other EECMs accordingly.....	39
Figure 20: The (a) Nyquist plot, (b) Bode magnitude plot, and (c) Bode phase plot when a 4-point measurement (blue) and 2-point measurement (yellow) are conducted. Modelled with the impedance equation of the Transmission-line model (EECM B). Here, $R=2.2\Omega$, $C=0.5F$, $R_{CT}=0.8\Omega$, $C_{CT}=0.003F$, and $R_s=1.2\Omega$	40
Figure 21: (a) Nyquist plot, (b) Bode magnitude plot and (c) Bode phase plot of the impedance equation of the “EECM A: R//C-circuit” (purple line) and the “EECM B: TLM” (blue line). The parameters in the impedance equations are equal, $R=10\Omega$ and $C=1.0F$	41
Figure 22: Transmission-line model impedance equation plotted inside (from left to right) the Nyquist plot, Bode magnitude plot and Bode phase plot for four different EECMs with TLM. “EECM B: TLM” is the Transmission-line model (blue line), “EECM C: Inhomogeneous TLM” is the model with two Transmission-line models in series with each other to denote the two-layered CME, “EECM D: TLM with hole” is the model with a Transmission-line model and a resistor for the ion transport through macropores, and “EECM E: Inhomogeneous TLM with hole” is the model of EECM C with a resistor for the ion transport through macropores. Here, $R=R_1=10\Omega$, $C=C_1=1.0F$, $R_2=5.0\Omega$, $C_2=0.2F$, $R_M=2.0\Omega$, and $R_s=0.24\Omega$. These plots result from 4-point measurements.....	42
Figure 23: Schematic representations of the CME meter: electrochemical impedance spectroscopy setup for investigating CMEs.....	49
Figure 24: The EIS potentiostat Biologic VSP-300 [115].	50
Figure 25: Accuracy Contour Plot of the Biologic VSP-300. Retrieved from the manual of the Biologic VSP-300 [115].	50
Figure 26: Four electrode connection of the potentiostat cables onto the electrodes in the CME-cell. Inspired from figures in the manual of the BioLogic VSP-300 [115].	51
Figure 27: Sketch of the CME cell. The flow direction of the electrolyte inside the CME-cell stack is depicted with the light blue arrows. The electrolyte flows into the cell through a hole in the stack and out through the spacers.	52
Figure 28: (left) 3D CAD model of the CME-cell and (right) the cell stack inside the PMMA plates. These models were made with Fusion360.....	52

Figure 29: Design of the titanium current collectors for the CMEs. The strip of the fiberglass is glued on the titanium foil, then the silicone rubber is placed on both sides of the strip. The titanium current collector is now always aligned in the same way.....	53
Figure 30: 3D CAD model of the reservoir sub-system with 3L glass beaker, hotplate stirrer and the CME-cell with reference electrode. Made with Fusion 360.....	54
Figure 31: Picture of the BT100S Basic Variable-Speed Peristaltic Pump. Retrieved from the website of Lead fluid [¹¹⁸].....	55
Figure 32: Picture of the eDAQ ET908 Flow-Thru Conductivity Electrode (left) for use of the EPU357 Conductivity isoPod™ with USB (right). Retrieved from the official website of eDAQ [^{119,120}].	55
Figure 33: The hood which will protect the researcher from airborne KCl particles and reduces the evaporation of water out of the electrolyte. The original silicone comes from IKEA®	58
Figure 34: 3D CAD model of the CME meter for measuring the electrochemical properties of CMEs. From left to right: BT100S peristaltic pump, CME-cell in beaker on top of a hotplate stirrer, Biologic® VSP-300 potentiostat, Voltcraft® ps-2403d laboratory power supply. This model was made with Fusion360.	59
Figure 35: The relation between the rotational speed of the BT100S peristaltic pump in RPM and the flowrate of the fluid inside the tube in mL/min.	62
Figure 36: Picture of the test setup for calibration of the conductivity meter.	63
Figure 37: Concentration of the electrolyte plotted against the average measured conductivity by the conductivity meter. The relation is not linear.	63
Figure 38: Picture of the test setup for testing the flow arrangement of the electrolyte through the CME-cell.....	64
Figure 39: Pictures of the final prototype of the CME meter. The setup is located at the chemical lab of Process and Energy department of 3me at the TU Delft. The names of the different components are illustrated in the figure in red. The official names of the components are simplified (for example, pump = Lead Fluid® BT100S peristaltic pump).....	65
Figure 40: Electrochemical Impedance Spectroscopy measurements performed on CME-S at standard operating conditions: flowrate of 8.0mL/min, mixing rate of 2.5, temperature of 25°C and KCl concentration of approximately 1.0mg/L. (a) Nyquist diagram of CME-S, (b) Magnitude Bode Plot of CME-S, (c) Phase Bode Plot of CME-S. The coloured lines are the different impedance equations that are fitted through the EIS data of the Standard CME (black dots). The EECMs that are fitted through the EIS data are (d) EECM A: R//C-circuit (purple line), (e) EECM B: TLM (blue line which partially overlapped by the green line), (f) EECM C: inhomogeneous TLM (yellow line which partially overlapped by the green line), (g) EECM D: TLM with holes (green line), (h) EECM E: Inhomogeneous TLM with holes (red line). The impedance equations and the values of the quality of fits of the EECMs are placed below the electrical circuits. EECM E has the lowest quality of fit value.	68
Figure 41: EIS measurements performed on CME-S at different flowrates. The other operational parameters are constant: temperature is 25°C, mixing rate at 2.5, and initial salt concentration of KCl is 960mg/L. (a) The Nyquist plot of the EIS data of CME-S at different flowrates, (b) the Bode magnitude plot of the EIS data of CME-S at different flowrates, and (c) the Bode phase plot of the EIS data of CME-S at different flowrates. The different flowrates are: 0.0mL/min, 4.0mL/min, 8.0mL/min, 16mL/min, and 24mL/min. The impedance equation of five EECMs has been fitted through the EIS data in the Nyquist plot, the values of the parameters of the fit are displayed in the table below the figure.	69
Figure 42: EIS measurements performed on CME-S at different mixing rates. The denoted number of the mixing rate is the number on the ColeParmer® Hotplate knob. The other operational parameters are constant: flowrate of 8.0mL/min, temperature is 25°C, and initial salt concentration of KCl is 960mg/L. (a) The Nyquist plot of the EIS data of CME-S at different mixing rates, (b) the Bode	

- magnitude plot of the EIS data of CME-S at different mixing rates, and (c) the Bode phase plot of the EIS data of CME-S at different mixing rates. The different mixing rates are: 0.0, 2.5, and 7.5. The impedance equation of five EECMs has been fitted through the EIS data in the Nyquist plot, the values of the parameters of the fit are displayed in the table below the figure. 70
- Figure 43: EIS measurements performed on CME-S at different concentrations of KCl. The different concentrations are: 320mg/L, 960mg/L, and 2760mg/L. The other operational parameters are constant: flowrate of 8.0mL/min, temperature is 25°C, and mixing rate at 2.5. (a) The Nyquist plot of the EIS data of CME-S at different concentrations of the electrolyte, (b) the Bode magnitude plot of the EIS data of CME-S at different concentrations of the electrolyte, and (c) the Bode phase plot of the EIS data of CME-S at different concentrations of the electrolyte. The impedance equation of five EECMs has been fitted through the EIS data in the Nyquist plot, the values of the parameters of the fit are displayed in the table below the figure. (d) The dual plot of the membrane resistance plotted against the concentration and the membrane capacitance plotted against the concentration. The curves are fitted to guide the eye. 71
- Figure 44: EIS measurements performed on CME-S at different temperatures. The other operational parameters are constant: flowrate of 8.0mL/min, mixing rate at 2.5, and initial salt concentration of KCl is 960mg/L. (a) The Nyquist plot of the EIS data of CME-S at different temperatures, (b) the Bode magnitude plot of the EIS data of CME-S at different temperatures, and (c) the Bode phase plot of the EIS data of CME-S at different temperatures. The different temperatures are: 25°C, 30°C, and 35°C. The impedance equation of five EECMs has been fitted through the EIS data in the Nyquist plot, the values of the parameters of the fit are displayed in the table below the figure. 72
- Figure 45: EIS measurements performed on CME-S with different thicknesses. The standard operating conditions are: flowrate of 8.0mL/min, mixing rate of 2.5, temperature of 25°C and KCl concentration of approximately 960mg/L. The different thickness are: 30µm, 70µm, and 140µm. Additionally, the thickness of the CME was doubled by placing two instead of one CME inside the CME meter. The CME S with a thickness of 30µm was doubled as was the CME-S with a thickness of 70µm. 74
- Figure 46: Difference in the measured EIS data when one CME, placed in the CME-cell of the CME meter, is rotated to the other side. The black line shows the EIS data of the original EIS trace and the red line shows the EIS data when one CME-S is flipped on the other side. The difference in membrane resistance is approximately 200Ωcm², which is quite a significant difference, proving that CME-S is not homogeneous in the z-direction. 76
- Figure 47: Electrochemical Impedance Spectroscopy performed on the Standard CME (CME-S) when it was positively charged, uncharged and negatively charged. The CME was charged by placing a potential between the CMEs and the end electrodes of +1.0V, +0.5V, -0.5V, and -1.0V. The Transmission-Line Model has been fitted through the EIS data in the Nyquist plot and the resulting values are displayed in Table 7. 78
- Figure 48: The point of zero charge of CME 1 and CME 2 when the electrolyte has a concentration of 960mg/L (12.8mM). The membrane capacitance plotted against the measured potential difference of the CME and the Ag/AgCl reference electrode. The membrane capacitance C is determined from the fit of the TLM in the Nyquist plot of Figure 47a at different applied potentials. The Gouy-Chapman-Stern Model has been fitted through the datapoints when is assumed that the Gouy-Chapman capacitance is dominant. The fit of figure (b) is inaccurate because there are too little datapoints. The point of zero charge of CME 1 is -0.559V (red dot) and the point of zero charge of CME 2 is +0.013V (blue dot). 78
- Figure 49: EIS data of the Standard CME with a thickness of 140µm (CME-S140) when it was positively charged, uncharged and negatively charged. The CME was charged by placing a potential between the CMEs and the end electrodes of +1.0V, +0.5V, -0.5V, and -1.0V. (a) Nyquist diagram of

CME-S140, the (c) Magnitude Bode Plot of CME-S140, and the (d) Phase Bode Plot of CME-S140. The uncharged CME-S140 has been included in the figure for comparison with the charged ones. The Transmission-line model has been fitted through the impedance datapoints in the Nyquist plot. The PZC of CME 1 is +0.25V and the PZC of CME 2 is -0.10V.	79
Figure 50: Impedance plots of electrochemical impedance spectroscopy measurements on CMEs with different structures. (a) Nyquist diagram of CMEs with different structures, (b) Magnitude Bode Plot of CMEs with different structures, (c) Phase Bode Plot of CMEs with different structures. The structure of the CME was varied by changing the mass percentages of the carbon black (CB), graphite (G) and the polymeric binder PVDF. The CME-S has mass percentage G:CB:PVDF=45:8:47wt%, CME-AC has active carbon instead of graphite in the same mass percentages as CME-S (AC:CB:PVDF=45:8:47wt%), CME-PVDF has twice less PVDF in the slurry than the CME-S (G:CB:PVDF=60:10:30wt%), CME-CB has twice as much carbon black as the slurry of CME-S (G:CB:PVDF=43:14:43wt%), and CME-G has twice less graphite in the slurry than CME-S (G:CB:PVDF=29:11:60wt%).....	82
Figure 51: Nyquist plot of a three-electrode electrochemical cell with a working electrode where electrosorption and faradaic reactions occur. Source: Magar et al. (2021) [145].	110
Figure 52: (Up) Nyquist plot (right) of an electrode according to the simplified Randles equivalent model (left). (Down) Bode plots of Randles equivalent circuit model: (left) magnitude vs frequency plot and (right) phase angle vs frequency plot. Figures are copied from the book of Lasia (2014) [95].	111
Figure 53: The correlation between the Nyquist plot (left) and the Nyquist Incline Frequency plot (right) for an capacitive carbon electrode. Source: Lenz et al. (2020) [19].	112
Figure 54: Frequency ranges where diffusion is dominant for electrode materials Activated Carbon (ACC20) and Carbon Aerogel (PO921617). Source: Lenz et al. (2020) [19].	112
Figure 55: Nyquist plots for different equivalent electrical circuit models: (A) ideal capacitor, (B) RC-element, (C) R//C-circuit, (D) R//C-circuit in series with a resistor. (E) shows that the frequencies in a Nyquist plot decrease from left to right. Typical EECMs for membranes with in the EECM additionally to a R//C-circuit there is in series (F) R//C-circuit and (G) Finite-Length Warburg (FLW) element. Picture retrieved from Chapter 6 of the book of Ellis et al. (2018) [17].	113
Figure 56: Nyquist plots of EECMs including a CPE element (A) in series with a resistor and (B) in parallel with a resistor. The θ in the figure is equal to the α in Equation A.17. The figure could be found in the paper of Lazanas & Prodromidis (2023) [107].	115
Figure 57: Nyquist plot (left) and Bode plots (right) of the Randles circuit with Warburg element. The dotted line a is the shape when an semi-infinite-length Warburg element is used, b is the shape of a finite-length Warburg element (FLW), and c is the shape of a finite-space Warburg element (FSW). The figures have been retrieved from the book of Lasia (2014) [95].	116
Figure 58: The concept of De Levie's transmission-line model for porous electrodes. The pores are assumed to be perfectly cylindrical (same radius), identical (same length), and equally distributed (finite number of pores). Original figure can be found in the paper of Scipioni et al. (2017) [153].	118
Figure 59: (left) The graphical scheme of the transmission-line model according to De Levie (1963). (right) The electronic rail and ionic rail are connected like a ladder by equivalent circuits which describe the interface impedance. The figures were retrieved from the research paper of Siroma et al. (2020) [104].	118
Figure 60: Equivalent circuits for the interface impedance: (a) ideal double layer capacitor, (b) faradaic reactions at the interface, (c) semi-infinite diffusion at the interface. Figure retrieved from the research paper of Siroma et al. (2020) [104].	119
Figure 61: The shape of the Nyquist plot for different equivalent circuits in one-path TLM. Figure has been retrieved from the research paper of Hilario et al. (2017) [155].	119

Figure 62: Complex capacitance plots: (left) real capacitance vs frequency and (right) imaginary capacitance vs frequency. Source: Arunkumar & Paul (2017) [89].	120
Figure 63: EIS Accuracy Contour Plot (ACP) for a potentiostat retrieved from the website of Pine Research [161]. The error of the impedance measurement is $\pm 1\%$ for the magnitude and $\pm 1^\circ$ for the phase angle (blue), $\pm 2\%$ for the magnitude and $\pm 2^\circ$ for the phase angle (green), and $\pm 5\%$ for the magnitude and $\pm 5^\circ$ for the phase angle (yellow).	122
Figure 64: Voigt circuit with n RC-elements. Such an R//C-element is also called a Voigt element. Figure is originally displayed in the book of Lasia (2014) [95].	123
Figure 65: (left) potentiostat electrical circuit for performing 3-point measurements on an electrochemical cell, and (right) functions of potentiostat and frequency response analyser (FRA) to construct the EIS data of an electrochemical cell. Left figure was retrieved from Orazem & Tribollet (2017) and right figure was retrieved from Lazanas & Prodromidis (2023) [107,136].	124
Figure 66: : Electrical circuit of the finite transmission-line model (TLM). The equivalent circuit is depicted below. The impedance of the system is measured between A and D for the reflective boundary condition and between A and C for the transmissive boundary condition. The figure is modified from the original figure in the paper by Adamič et al. (2019) [106].	127
Figure 67: (left) Transmission-line model with reflective boundary condition and (right) the equivalent electrical circuit. The figures were retrieved from the papers of Kim & Pyun (2011) and Siroma et al. (2015) [168,169].	128
Figure 68: (left) Transmission-line model with reflective boundary condition and (right) the equivalent electrical circuit. The figures were retrieved from the papers of Kim & Pyun (2011) and Siroma et al. (2015) [168,169].	130
Figure 69: Schematic of the ion transport when the CME is negatively charged. The anion resistance (R_-) stays equal to R_0 while the cation resistance (R_+) decreases.	133
Figure 70: The impedance equation of the Transmission-line Model, when the CME is uncharged (green) and the CME is positively or negatively charged (red).	133
Figure 71: Specifications of the Parameters Setting to perform an EIS measurement at a frequency range of 100kHz to 1.00mHz. Screenshot of the EC-Lab® programme on the computer.	145
Figure 72: Cell architectures and flow arrangements of CDI systems: (a) Flow-by CDI, (b) Membrane CDI (MCDI), (c) Flow-through CDI, (d) Inverted CDI (i-CDI), (e) Flow-electrode CDI (FCDI), (f) Hybrid CDI (HCDI), (g) Cation intercalation desalination (CID), and (h) Desalination battery. Source: Tang et al. (2019) [6].	152
Figure 73: Nyquist plots of the EIS data of CME-S when the operational parameters are varied. Impedance equations of five EECMs (EECM A: R//C-circuit, EECM B: TLM, EECM C: Inhomogeneous TLM, EECM D: TLM with holes, EECM E: Inhomogeneous TLM with holes) have been fitted through the EIS data (not visible) and the quality of fit value was calculated. The χ^2 -values of the five EECMs have been displayed in the table below the Nyquist plots. The Nyquist plots are equal to the ones in Figure 41a to Figure 44a.	158
Figure 74: Electrochemical impedance spectroscopy performed on the CME with activated carbon instead of graphite as active material (AC:CB:PVDF=45:8:47wt%). The CMEs were made selective for anions by placing a potential between the CMEs and the end electrodes of +1.0V for 30 minutes. The CMEs were made selective for cations by charging them with the electrons of the end electrodes by placing a potential between them of -1.0V for 30 minutes. The EIS data is visualised as the (a) Nyquist diagram of the CME-AC, the (c) Magnitude Bode Plot of CME-AC, and the (d) Phase Bode Plot of CME-AC. The uncharged CME-AC has been included in the figure for comparison with the charged ones.	160
Figure 75: Electrochemical impedance spectroscopy performed on CMEs with a lower mass percentage of the binder PVDF than CME-S. The slurry mass composition of CME-PVDF is	

G:CB:PVDF=60:10:30wt%. The CMEs were made selective for anions by placing a potential between the CMEs and the end electrodes of +1.0V for 30 minutes. The CMEs were made selective for cations by charging them with the electrons of the end electrodes by placing a potential between them of -1.0V for 30 minutes. The EIS data is visualised as the (a) Nyquist diagram of the CME-PVDF, the (b) Magnitude Bode Plot of CME-PVDF, and the (c) Phase Bode Plot of CME-PVDF. The EIS data of the uncharged CME-PVDF has been included in the figure for comparison with the charged ones. 161

Figure 76: Electrochemical impedance spectroscopy performed on CMEs with a higher mass percentage of carbon black (CB) than CME-S. The slurry mass composition of the CME-CB has twice as much carbon black in the slurry as CME-S (G:CB:PVDF=43:14:43wt%). The CMEs were made selective for anions by placing a potential between the CMEs and the end electrodes of +1.0V for 30 minutes. The CMEs were made selective for cations by charging them with the electrons of the end electrodes by placing a potential between them of -1.0V for 30 minutes. The EIS data is visualised as the (a) Nyquist diagram of the CME-CB, the (b) Magnitude Bode Plot of CME-CB, and the (c) Phase Bode Plot of CME-CB. 162

Figure 77: Electrochemical impedance spectroscopy performed on CMEs with a lower mass percentage of graphite than CME-S. The slurry mass composition of CME-G has twice less graphite in the slurry than CME-S (G:CB:PVDF=29:11:60wt%). The CMEs were made selective for anions by placing a potential between the CMEs and the end electrodes of +1.0V for 30 minutes. The CMEs were made selective for cations by charging them with the electrons of the end electrodes by placing a potential between them of -1.0V for 30 minutes. The EIS data is visualised as the (a) Nyquist diagram of CME-G, the (b) Magnitude Bode Plot of CME-G, and the (c) Phase Bode Plot of CME-G. The EIS data of the uncharged CME-G has been included in the figure for comparison with the charged ones. 163

List of Tables

Table 1: Debye length (in angstrom) for different concentrations in the electrolyte. Source: book of Schmickler & Santos (2010) [40].....	21
Table 2: (left) Performance metrics of CDI, ED, and MC-CDI and (right) the performance indicators of capacitive electrodes in CDI, IEMs in ED, and CMEs in MC-CDI.	32
Table 3: The different mass composition of the CMEs fabricated for the experiments.	34
Table 4: Procedure for the manufacture of the components of the CME meter. The tools used to manufacture the components and the persons instructed to carry out the manufacturing are also specified in the table.	60
Table 5: Testing the flow arrangement inside the CME-cell (Test 6). The expected output of the flow of the liquid through the CME-cell for different layers.	64
Table 6: Values retrieved by fitting the impedance equation of the Transmission-Line Model in the EIS data of the CMEs made with the same compositions of CME-S, only with different thicknesses. χ^2 is the quality of fit, R is the membrane resistance in Ωcm^2 , C is the membrane capacitance in F/cm^2 , τ_t is the transport time constant in s, and κ_m is the membrane conductivity in $\mu\text{S}/\text{cm}$	76
Table 7: Values retrieved by fitting the impedance equation of the Transmission-Line Model in the EIS data of the Standard CME (CME-S). χ^2 is the quality of fit, R is the membrane resistance in Ωcm^2 , C is the membrane capacitance in F/cm^2 , τ_t is the transport time constant in s, and P is the permselectivity.	77
Table 8: Values retrieved by fitting the impedance equation of the Transmission-Line Model in the EIS data of the CME-S with a thickness of $140\mu\text{m}$ (CME-S140). χ^2 is the quality of fit, R is the membrane resistance in Ωcm^2 , C is the membrane capacitance in F/cm^2 , τ_t is the transport time constant in s, and P is the permselectivity.	80
Table 9: Values retrieved by fitting the impedance equation of the Transmission-Line Model in the EIS data of different CMEs with different slurry compositions: CME-S, CME-AC, CME-PVDF, CME-CB, and CME-G. χ^2 is the quality of fit, R is the membrane resistance in Ωcm^2 , C is the membrane capacitance in F/cm^2 , τ_t is the transport time constant in s, κ_m is the membrane conductivity in $\mu\text{S}/\text{cm}$, P_+ is the permselectivity when the CME is positively charged by placing a potential of +1.0V between the CMEs and the end electrodes, and P. is the permselectivity when the CME is negatively charged by placing a potential of -1.0V between the CMEs and the end electrodes.	81
Table 10: Different circuit elements and their impedance equation, which are used for constructing equivalent electrical circuit models for electrochemical systems. The physical effect, that gives an explanation for the existence of the circuit element in the EECM, is also depicted in the table. The way in which the circuit element could be recognised in the Nyquist plot is also indicated in the table.	114
Table 11: Conditions and parameters of previous EIS setups in the literature.....	125
Table 12: The connection of the cables clamps of the BioLogic® VSP-300 potentiostat on the different electrodes in the CME-cell.....	145
Table 13: Values retrieved by fitting the impedance equation of the Transmission-Line Model in the EIS data of the CME with activated carbon as active material at different potentials. χ^2 is the quality of fit, R is the membrane resistance in Ωcm^2 , C is the membrane capacitance in F/cm^2 , τ_t is the transport time constant in s, and P is the calculated permselectivity when the CME is positively charged by placing a potential of +1.0V or negatively charged by placing a potential of -1.0V between the CMEs and the end electrodes.	160
Table 14: Values retrieved by fitting the impedance equation of the Transmission-Line Model in the EIS data of the CME with half the amount of polymeric binder PVDF in the slurry as CME-S at	

different potentials. χ^2 is the quality of fit, R is the membrane resistance in Ωcm^2 , C is the membrane capacitance in F/cm^2 , τ_t is the transport time constant in s, and P is the calculated permselectivity when the CME is positively charged by placing a potential of +1.0V or negatively charged by placing a potential of -1.0V between the CMEs and the end electrodes.	161
Table 15: Values retrieved by fitting the impedance equation of the Transmission-Line Model in the EIS data of the CME with twice as much carbon black in the slurry as CME S at different potentials. χ^2 is the quality of fit, R is the membrane resistance in Ωcm^2 , C is the membrane capacitance in F/cm^2 , τ_t is the transport time constant in s, and P is the calculated permselectivity when the CME is positively charged by placing a potential of +1.0V or negatively charged by placing a potential of -1.0V between the CMEs and the end electrodes.	162
Table 16: Values retrieved by fitting the impedance equation of the Transmission-Line Model in the EIS data of the CME with half the amount of graphite in the slurry as CME-S at different potentials. χ^2 is the quality of fit, R is the membrane resistance in Ωcm^2 , C is the membrane capacitance in F/cm^2 , τ_t is the transport time constant in s, and P is the calculated permselectivity when the CME is positively charged by placing a potential of +1.0V or negatively charged by placing a potential of -1.0V between the CMEs and the end electrodes.	163

Appendix A: Fundamentals of Electrochemical Impedance Spectroscopy

Electrochemical Impedance Spectroscopy (EIS) is a non-destructive tool to examine interface processes at, for example, the electrode or membrane interface. The phenomena that occur at interfaces of the system, e.g. non-faradaic processes, faradaic processes, mass transfer processes, occur at different timescales [95]. With EIS, these processes are decoupled at different time scales, so the different mechanisms that happen in the system could be obtained. EIS is able to characterize interfacial processes, geometric effects and the stability of the system [95]. Majority of the researchers investigated the kinetics (diffusion), resistances and capacitance of electrodes and membranes within CDI systems.

The standard roadmap for executing an Electrochemical Impedance Spectroscopy measurement on electrode is summarized below (according to the review of Magar et al., 2021) [145]:

1. Apply a potential wave on the working electrode and record the resulting wave.
2. Extract the real impedance (Z_{real}), imaginary impedance (Z_{imag}), magnitude of the impedance ($|Z|$) and phase angle of the impedance (Φ).
3. Repeat step 1 and 2 for different frequencies ($f = \text{range}(1\text{mHz} - 1\text{MHz})$, $A = 10\text{mV}$)
4. Construct the Nyquist plot and Bode plots.
5. Construct the equivalent electrical circuit model (EECM) from the shape of the Nyquist plot.
6. Collect the series resistance, charge-transfer resistance, and Warburg impedance.

A.1 Impedance

With EIS, an AC potential or current is applied on the system. The output is the impedance of the system that is measured at different frequencies [146]. Impedance is analogous to resistance, but depends on the frequency. Impedance is a complex number with a real and imaginary part. The real part is denoted with the resistance of the system that is independent of the frequency (resistor) and the imaginary part denotes the resistance due to capacitive or/and inductive processes within the system (capacitor, inductor). The AC potential or current is shifted by the elements within the system: capacitors result in -90° phase shifts and inductors inside the system result in 90° phase shifts. The EIS measures the AC response (current or potential). The AC response has the same frequency but a different phase than the applied AC signal due to capacitors and inductors within the electrochemical system. The impedance is determined by dividing the AC potential with the AC current, see Equation A.3. The EIS is called the potentiostatic EIS when the AC potential is the input and the AC current is the output, while the EIS is called the galvanic EIS when the AC current is the input and the AC potential is the output.

$$V(t) = V_0 \sin(\omega t) \quad (\text{A.1})$$

$$I(t) = I_0 \sin(\omega t + \varphi) \quad (\text{A.2})$$

$$Z(\omega) = \frac{V(t)}{I(t)} = Z_{\text{real}} + iZ_{\text{imag}} = Z_0(\cos(\varphi) - j\sin(\varphi)) \quad (\text{A.3})$$

During the EIS experiments, multiple AC potential (or current) signals are applied to the electrochemical system. The frequency of the applied AC potential (or current) signal is reduced at every experiment (logarithmic descending from 1 MHz to 1 mHz), while the amplitude of the signals stay constant (~ 5 mV) [145]. The output AC current (or potential) signal is measured for every input signal. The EIS data is subsequently plotted in potential vs time plots and current vs time plots for every frequency. The Laplace transform or Fast Fourier Transfer (FFT) is applied to convert the plots to the

magnitude vs frequency and phase angle vs frequency plots, also referred to as the Bode plots [95]. More detailed explanation about the Bode plots is given in Section A1.2. When the EIS data is expressed with polar coordinates, Nyquist plot is constructed which shape gives information about the physical processes that occur inside the electrochemical system. Thus, the EIS data, data collected during the electrochemical impedance spectroscopy experiments, consists of five columns of measured data: frequency (f), real impedance (Z_{real}), imaginary impedance (Z_{imag}), magnitude of the impedance ($|Z|$) and phase angle of the impedance (φ).

$$|Z| = \sqrt{Z_{\text{real}}^2 + Z_{\text{imag}}^2} = Z_0 = \frac{V_0}{I_0} \quad (\text{A.4})$$

$$\varphi = \arctan\left(\frac{Z_{\text{imag}}}{Z_{\text{real}}}\right) \quad (\text{A.5})$$

$$Z_{\text{real}} = Z'(\omega) = |Z|\cos(\varphi) \quad (\text{A.6})$$

$$Z_{\text{imag}} = Z''(\omega) = |Z|\sin(\varphi) \quad (\text{A.7})$$

A.2 Nyquist plot and Bode plots

The experimentally determined impedance data, at different frequencies, is analysed via graphical methods. The EIS data is presented in Nyquist plots and Bode plots.

A.2.1 Nyquist plot

Nyquist plots are plotted to analyse the resistive processes within a system [145]. The Nyquist plot is a graph with the real part of the impedance on the x-axis and the negative imaginary part of the impedance on the y-axis. Figure 51 illustrates an example of the Nyquist plot of an EIS measurement in a three-electrode electrochemical cell of an electrode where electrosorption and redox reactions occur [145]. The shape of the Nyquist plot evaluates the processes that happen inside the electrode. The real axis shows the resistances that are related according to Ohm's law. The positive y-axis in the Nyquist plot is the negative imaginary impedance axis and this relates to the inductive and capacitive behaviour in the electrode. High frequencies are depicted on the left of the Nyquist plot while low frequencies are depicted on the right of the Nyquist plot. So, the frequency decreases when you follow the line to the right. The Nyquist plot contains information about the electronic and ionic processes [17]. Electronic processes dominate at high frequencies or low time scales, while ionic processes dominate at low frequencies or high time scales. The middle frequencies correspond to a combination of ionic and electronic processes which depend on the system design [17].

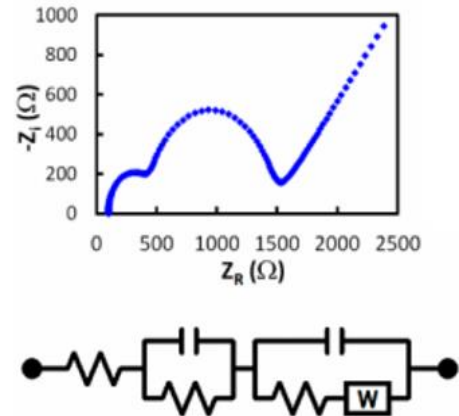


Figure 51: Nyquist plot of a three-electrode electrochemical cell with a working electrode where electrosorption and faradaic reactions occur. Source: Magar et al. (2021) [145].

The Nyquist plot is essential for the analysis of an electrochemical system with EIS, because all researcher, using EIS to investigate an electrode or membrane, used the plot to determine the physical phenomena happening inside electrochemical systems. First, the value of the specific resistances inside electrodes and membranes are determined with the Nyquist plot. Kuo et al. (2020) and Dykstra et al. (2016) decoupled the resistances inside an electrochemical system into the contact resistance between the electrode and current collector, the external electronic resistances inside the cables of the electrochemical system, the solution resistance in the electrolyte (spacer channel), the resistance of the electrode and the resistance of the membrane [21,22]. Subsequently, the specific capacitances is calculated with the collected EIS data. DuToit et al. (2021) investigated with an EIS setup if conducting membranes could be used to decrease the fouling [147]. They extracted the specific capacitances from

the impedance data and analyzed how these capacitances decrease with increasing fouling. The output plot was a plot of the total capacitance and the permeate flux decline. The total capacitance (C_{tot}) of the conducting membrane was calculated with Equation A.8 [148]. Other parameters, like the tortuosity, were also calculated with the collected impedance data: Landesfeind et al. (2016) decoupled the resistances within the electrode to determine the tortuosity of battery electrodes and separators [23].

$$C_{\text{tot}} = C_{\text{real}} + jC_{\text{imag}} = \frac{1}{j\omega Z_{\text{imag}}} \quad (\text{A.8})$$

A.2.2 Bode plots

Bode plots are for the analysis of capacitive processes within a system [145]. Bode plots are additionally analysed because the Nyquist plot does not show at what frequency which process occurs. The Bode plots consist of two plots: impedance magnitude vs frequency plot and impedance phase angle versus frequency plot. The magnitude axis in the magnitude vs frequency Bode plot is logarithmic, while the phase angle axis in the phase vs frequency Bode plot is linear and negative, see Figure 52 for an example of the Bode plots for a Randles circuit [95].

The magnitude vs frequency plot is analysed to find the specific capacities of the electrochemical system. The total complex capacitance could be calculated with the collected EIS data with Equation A.9 to A.12 [149]. How higher the magnitude of the impedance, how lower the value for the real and imaginary capacitance. The real capacitance ($C'(\omega)$) is the capacitance of the electrochemical system, while the imaginary capacitance ($C''(\omega)$) corresponds to the energy dissipation of dielectric losses [149]. The slope of the line in the magnitude vs frequency plot is for ideal capacitors equal to -1 and for ideal inductors equal 1 .

$$C(\omega) = \frac{1}{j\omega Z(\omega)} \quad (\text{A.9})$$

$$C(\omega) = C'(\omega) - jC''(\omega) \quad (\text{A.10})$$

$$C_{\text{real}} = C'(\omega) = -\frac{Z''(\omega)}{\omega|Z(\omega)|^2} \quad (\text{A.11})$$

$$C_{\text{imag}} = C''(\omega) = \frac{Z'(\omega)}{\omega|Z(\omega)|^2} \quad (\text{A.12})$$

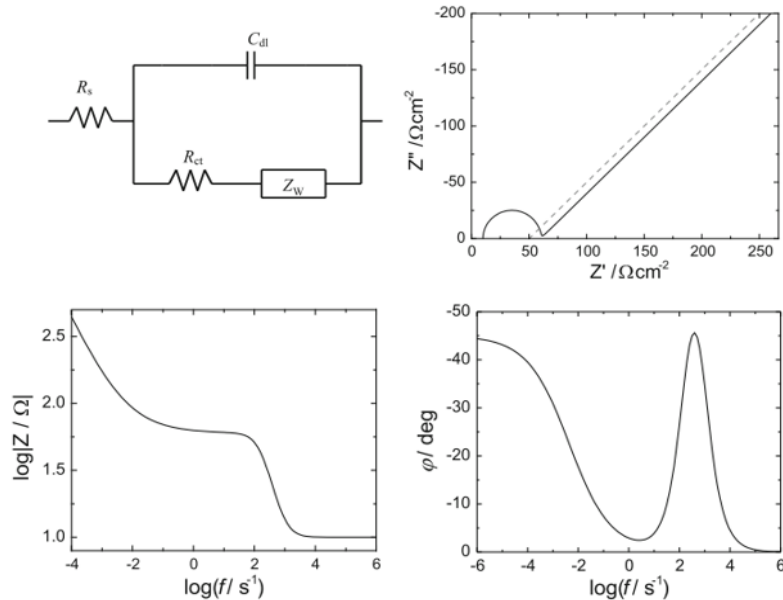


Figure 52: (Up) Nyquist plot (right) of an electrode according to the simplified Randles equivalent model (left). (Down) Bode plots of Randles equivalent circuit model: (left) magnitude vs frequency plot and (right) phase angle vs frequency plot. Figures are copied from the book of Lasia (2014) [95].

As stated earlier, an ideal capacitor corresponds with a phase angle of -90° and an ideal inductor corresponds with a phase angle of 90° . All values between these two angles show that the equivalent electrical circuit consists of a combination of ideal and non-ideal capacitors and inductors. The phase Bode plots are usually used to find the equivalent electrical model of a system, especially to identify if R//Q-circuits or R//C-circuits are required in the EECM [95]. The R//C- and R//Q-elements are visualised as a semi-circle in the Nyquist plot and corresponds with the peak in the phase vs frequency plot [150]. This peak in the phase Bode plot indicates capacitive behaviour [146]. The elements are explained in more detail in Section A1.3. In Figure 52, at a frequency of 10^3 Hz, there is a peak in the phase vs frequency plot that shows that the Randles equivalent circuit model consists of an R//Q-circuit [95]. The peak or plateau at very low frequencies shows the total capacitive behaviour between the electrolyte and the electrode [146]. For example, in Figure 52, there is a plateau at 45° and a frequency of 10^{-6} Hz, that denotes ideal capacitive behaviour in the Randles circuit [95].

The Nyquist Incline Frequency plot (NIF) is an alternative plot for presenting the EIS data and is utilized for the analysis of the kinetics within a system. The NIF has firstly been proposed by Lenz et al. (2020) and is an adjusted Nyquist plot to show the time domain at which the physical phenomena dominate (Figure 53) [19]. The plot has actually the same shape as a phase Bode plot, only the angles are positive instead of negative. The NIF was used to give a fast prediction of the kinetics of the electrode material, which in turn gives information about the structure of the electrode. The same analysis could be utilized for analysing phase Bode plots. For electrode material with a pore size distribution with many micropores, plateaus at 90° are reached which denotes purely capacitive behaviour [19]. Perfect cylindrical pores give a 45° plateau in the NIF

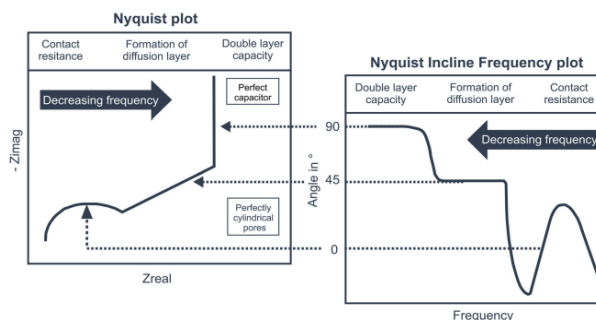


Figure 53: The correlation between the Nyquist plot (left) and the Nyquist Incline Frequency plot (right) for an capacitive carbon electrode. Source: Lenz et al. (2020) [19].

which indicates dominating diffusion effects [19]. Diffusion occurs dominantly between an angle of 20° and 60° , as defined by Lenz et al, resulting in a frequency range where diffusion is dominant [19]. This frequency range shifts towards lower ranges for lower electrolyte concentrations, see Figure 54 [19]. The conclusion of their research was that the electrode material shows faster electrosorption kinetics when the left boundary of the frequency range is at a lower frequency. The electrosorption kinetics of different materials could be compared in this manner.

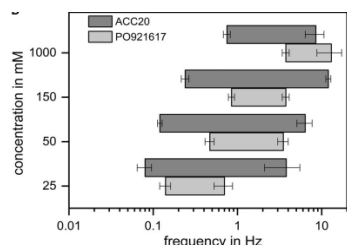


Figure 54: Frequency ranges where diffusion is dominant for electrode materials Activated Carbon (ACC20) and Carbon Aerogel (PO921617). Source: Lenz et al. (2020) [19].

A.3 Equivalent Electric Circuit Model

The impedance data retrieved from the EIS is modelled by establishing the accurate equivalent electronic circuit (EECM) and fitting the model through the experimental data. Each circuit element of the EECM corresponds to a physical phenomenon inside the system [17]. The EECM gives thus all the information about the physical phenomena that occur inside a system. The impedance of the circuit elements (Table 10), the EECM, and Kirchhoff's laws lead to the corresponding impedance equation for the EECM that shows the relationship between the frequency and the impedance. The experimental impedance data is fitted with this impedance equation. After fitting the EECM in the EIS data, the separate resistances inside the electrochemical system are determined and, if necessary, the value of physical parameters are calculated and the kinetics are determined [145].

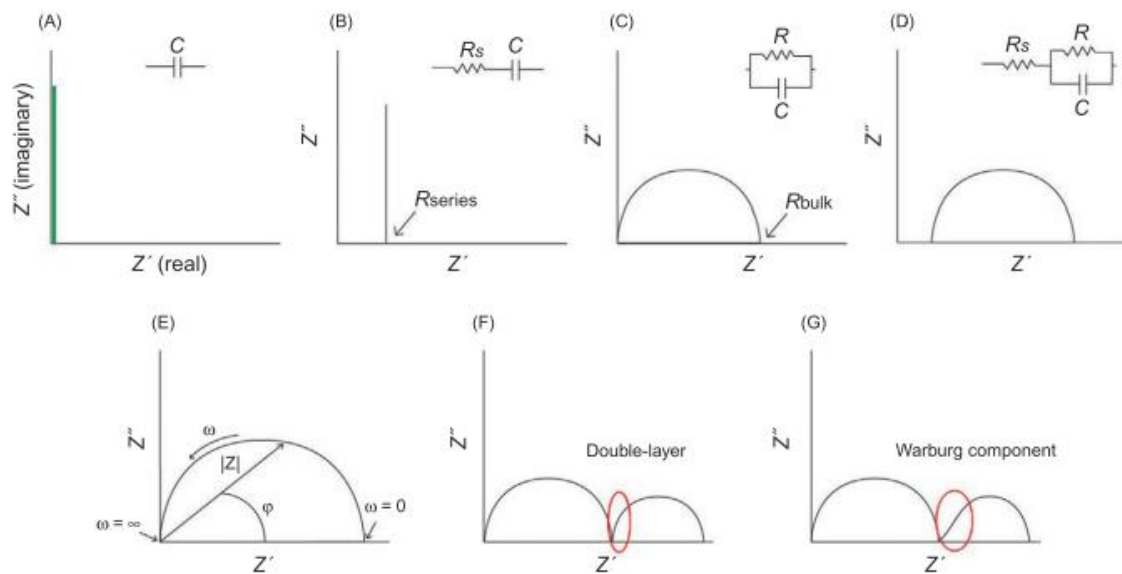

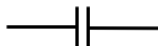
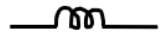
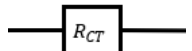


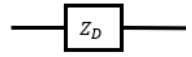
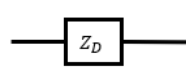
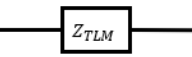

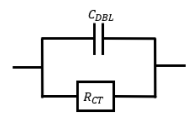
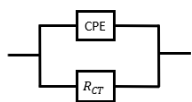
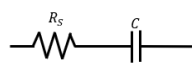


Figure 55: Nyquist plots for different equivalent electrical circuit models: (A) ideal capacitor, (B) RC-element, (C) R//C-circuit, (D) R//C-circuit in series with a resistor. (E) shows that the frequencies in a Nyquist plot decrease from left to right. Typical EECMs for membranes with in the EECM additionally to a R//C-circuit there is in series (F) R//C-circuit and (G) Finite-Length Warburg (FLW) element. Picture retrieved from Chapter 6 of the book of Ellis et al. (2018) [17].

The EECM is constructed by analysing the shape of the Nyquist plot. An typical and simple EECM used for electrochemical systems is called the simplified Randles equivalent circuit model (Figure 52) [95]. The ions must move from the bulk solution to the electrode surface and (a part of) the series resistance shows this behaviour. When the ions reach the electrode, the ions diffuse into the meso- and micropores and are utilized in the faradaic reaction. The ions need to diffuse into the micro- and mesopores before they can react, this is denoted with the Warburg impedance. A part of the ions that diffused into the pores of the electrode are adsorbed in the EDL. These physical phenomena are illustrated with the elements of the electrical circuit.

Table 10: Different circuit elements and their impedance equation, which are used for constructing equivalent electrical circuit models for electrochemical systems. The physical effect, that gives an explanation for the existence of the circuit element in the EECM, is also depicted in the table. The way in which the circuit element could be recognised in the Nyquist plot is also indicated in the table.

Name of circuit element	Corresponding shape in Nyquist plot	Physical effect	Impedance equation	Equivalent circuit element
Ideal resistor	Plot shifted from the imaginary axis	Electron transfer and ion transfer in bulk solution	$Z_R(\omega) = R$	
Ideal capacitor	Vertical line in the positive direction	Storage of ions in the EDL (non-faradaic reactions); ideal	$Z_C(\omega) = \frac{1}{j\omega C}$	
Ideal inductor	Vertical line in the negative direction	Stray inductance	$Z_L(\omega) = j\omega L$	
Charge-transfer resistance	(Part of a) semi-circle	Faradaic reactions	$Z_f(\omega) = R_{CT}$	
Constant phase element (CPE)	Straight line with a slope smaller than 90°	Storage of ions in the EDL (non-faradaic reactions); non-ideal	$Z_Q(\omega) = \frac{1}{Q(j\omega)^\alpha}$	
(semi-infinite-length) Warburg element	Straight line with a slope of 45°	Infinite length diffusion of ions and electrons.	$Z_W(\omega) = \frac{W}{\sqrt{\omega}} (1 - j)$	
Finite-length Warburg element (FLW)	Straight line with a slope of 45° at high frequencies, semi-circle at low frequencies	Finite length diffusion of ions. Ions can leave the other end.	$Z_{FLW}(\omega) = Z_0 \frac{1}{\sqrt{j\omega RC}} \tan(\sqrt{j\omega RC})$	
Finite-space Warburg element (FSW)	Straight line with a slope of 45° at high frequencies, vertical line at low frequencies	Finite length diffusion of ions. Ions cannot leave the other end: they are blocked.	$Z_{FSW}(\omega) = Z_0 \frac{1}{\sqrt{j\omega RC}} \coth(\sqrt{j\omega RC})$	
Transmission-line Model (TLM) (finite space, reflective BC)	Straight line with a slope of 45° at high frequencies, vertical line at low frequencies	Ambipolar diffusion in the electrolyte, electrode material and interface of blocking electrodes	$Z_{TLM}(\omega) = \sqrt{RZ_{eq}} \coth\left(\sqrt{\frac{R}{Z_{eq}}}\right)$	
Transmission-line Model (TLM) (finite length, transmissive BC)	Straight line with a slope of 45° at high frequencies, semi-circle at low frequencies	Ambipolar diffusion in the electrolyte, material and interface of membranes	$Z_{TLM}(\omega) = \sqrt{RZ_{eq}} \tanh\left(\sqrt{\frac{R}{Z_{eq}}}\right)$	
Resistor and capacitor in parallel (R//C-circuit)	Semi-circle	Ideal capacitive behaviour → Ions are adsorbed in the EDL (non-faradaic reactions) and faradaic reactions occur	$Z(\omega) = \frac{R_{CT}}{1 + R_{CT}C(j\omega)}$	
Resistor and constant phase element in parallel (R//Q-circuit)	Depressed or tilted semi-circle	Non-ideal capacitive behaviour → Ions are adsorbed in the EDL (non-faradaic reactions) and faradaic reactions occur	$Z(\omega) = \frac{R_{CT}}{1 + R_{CT}Q(j\omega)^\alpha}$	
Resistor and capacitor in series	Vertical line shifted on the real axis of the Nyquist plot	Capacitive behaviour of the electrode	$Z(\omega) = R_s + \frac{1}{j\omega C_{el}}$	

A.3.1 Ideal resistors, capacitors and inductors

The building blocks of the EECMs are shown in Table 10. Resistors are represented by a block with the letter R, capacitance by two equal vertical lines with the letter C and inductance by a coil with the letter L. Figure 55 shows different shapes in the Nyquist plot that corresponds to different electrical circuits [17]. Resistors are equivalent to the real component of the impedance while inductors and capacitors indicate the behaviour of the imaginary part of the impedance. Vertical lines in the positive axis direction of the Nyquist plots indicate purely capacitive behaviour, which is indicated by a capacitor element in series with a resistor (RC-element). Vertical lines in the negative axis direction of the Nyquist plots indicate purely inductive behaviour, which is indicated by an inductor element with a resistor.

$$Z(\omega) = R \quad (\text{A.13})$$

$$Z(\omega) = \frac{1}{j\omega C} = -\frac{1}{\omega C}j \quad (\text{A.14})$$

$$Z(\omega) = j\omega L \quad (\text{A.15})$$

The semi-circle corresponds to a parallel resistor and capacitor (R//C-circuit). In an electrode, the semi-circle corresponds to a coupling of the parallel placed charge-transfer resistance and the parallel plate capacitor (Figure 55) [17]. Resistors placed in series shift the semi-circles and vertical lines on the real impedance axis of the Nyquist plots (Figure 55B and Figure 55D) [17]. For electrodes, this resistor is called the series resistance. A resistor in series with a capacitor denotes the ideal capacitive behaviour inside the electrode, thus the transfer of ions and electrons to the surface of the pores of the electrode and the formation of the EDL in the ideal case. Figure 55C shows the corresponding Nyquist shape of the RC-element [17]. The ideal capacitor is called the electrical double layer capacitor and is calculated with Equation A.16 where λ_D is the Debye length of the EDL. In the Nyquist plot, the behaviour of the electrical double layer is ideally depicted as a vertical line of 90°, see Figure 55B [17].

$$C_{dl} = \frac{\epsilon\epsilon_0}{\lambda_D} \quad (\text{A.16})$$

A.3.2 CPE-element

In the Nyquist plot, the behaviour of the electrical double layer is ideally depicted as a vertical line of 90°, but for electrodes, the slope of this line is lower than 90°. The double layer capacitor then reveals non-ideal behaviour. This non-ideal behaviour is caused by the inhomogeneities inside the electrode-material like surface roughness and porosity [96]. Instead of an ideal capacitor, a constant phase element (CPE) is added in series with the resistor to model the non-ideal behaviour of the double layer capacitor [145]. This electrical circuit is then called an R//Q circuit [97]. The CPE is determined according to the following equation,

$$\text{CPE: } Z_{CPE} = \frac{1}{Q(j\omega)^\alpha} \quad (\text{A.17})$$

When α is equal to 1, the CPE element is an ideal capacitor, while when α is equal to 0, the CPE element acts as a resistor. Thus, the α in the equation for CPE gives an indication of the non-ideality of the system when $\alpha \neq 1$ or $\alpha \neq 0$. Equation A.18 and A.19 are utilized by DuToit et al. (2021) to calculate the specific capacitance of the CPE element in an R//Q circuit and CPE element in series with an ideal resistor, respectively [147]. In the Nyquist plot, the resistor in series with a CPE element shows a straight line with a slope smaller than 90° and the resistor in parallel with a CPE element shows a depressed or tilted semi-circle.

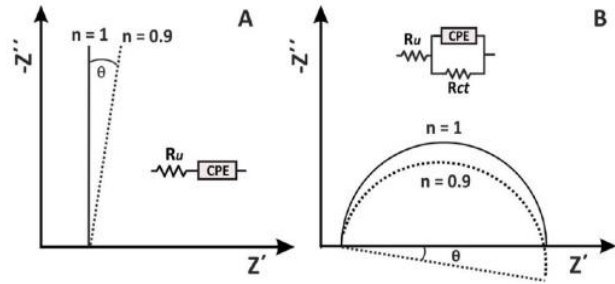


Figure 56: Nyquist plots of EECMs including a CPE element (A) in series with a resistor and (B) in parallel with a resistor. The θ in the figure is equal to the α in Equation A.17. The figure could be found in the paper of Lazanas & Prodromidis (2023) [107].

$$C_{dl,R/Q} = \frac{(CPE \cdot R)^{\frac{1}{\alpha}}}{R} \quad (A.18)$$

$$C_{dl,RQ} = (CPE \cdot R^{-(\alpha-1)})^{\frac{1}{\alpha}} \quad (A.19)$$

A.3.3 Charge-transfer resistance

If faradaic reactions occur in electrodes, then the resistor in the R//Q-circuit is replaced with a charge-transfer resistance element. The charge-transfer resistance provides information about the kinetics of the faradaic reaction [95]. In the Nyquist plot, faradaic reactions are dominant at lower frequencies while the double layer capacitance is dominant at higher frequencies. When the frequency limits zero, the capacitive resistances become infinite, which makes the faradaic reactions dominant. The charge-transfer resistance is determined by finding the intersection of the semi-circle with the real axis and subtracting the series resistance from that value. Higher concentrations in the bulk solution result in a lower charge-transfer resistance.

$$RE(Z_f) = R_{CT} \quad (A.20)$$

A.3.4 Warburg impedance

Like the ideal capacitor, the ideal resistor is not a sufficiently accurate way of modelling the behaviour of the real resistor in a system, because the real resistor will always have some capacitance and inductance. In fact, a real resistor acts like a transmission line, which is best explained as the behaviour of an electrical output having a delayed response compared to the input [151]. This delay is caused by the resistor that is distributed over a finite length, instead of, in the case of an ideal resistor, localized in a point [151]. The equivalent circuit element that describes this distribution of the resistor is given by the distribution elements. Examples of distribution elements are the Transmission-Line Model (TLM) or the Warburg elements [152]. The processes that are best described by these distribution elements are: the resistance for the diffusion of ions into the pores of the electrode, the resistance for the electrons to reach the surface of electrodes with rough surfaces, the resistance for the electrons to reach the surface of electrode with electrode-material that is inhomogeneous, and the resistance for counter-ion-hopping on the surface of the electrode [73,95,151].

The Warburg element represents the resistance against mass transfer. The Warburg element could be a confusing element because it has different equations for the impedance that result in different shapes in the plots. Also in the literature are Warburg elements mistakenly used. There are three Warburg elements: infinite-length Warburg element (W), finite-length Warburg element (FLW), and finite-space Warburg element (FSW). The boundary conditions determine which Warburg element should be used to describe the impedance due to the diffusion of ions inside electrodes and membranes.

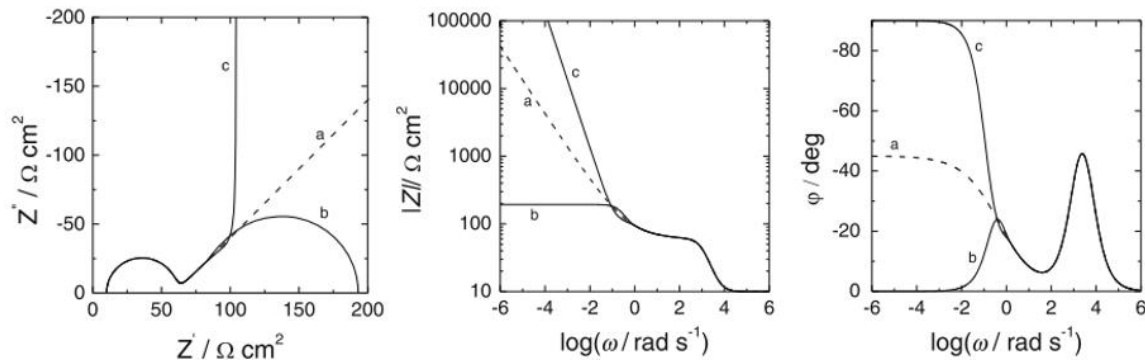


Figure 57: Nyquist plot (left) and Bode plots (right) of the Randles circuit with Warburg element. The dotted line a is the shape when an semi-infinite-length Warburg element is used, b is the shape of a finite-length Warburg element (FLW), and c is the shape of a finite-space Warburg element (FSW). The figures have been retrieved from the book of Lasia (2014) [95].

Semi-infinite-length Warburg element

Semi-infinite-length Warburg elements are included in the EECM when the diffusion has no limitations. The semi-infinite-length Warburg element (W) describes the diffusion according to Fick's Law. This diffusion impedance assumes that the length of the electrode goes to infinity. Thus, the species keep diffusing infinitely without limitations in the electrode, hence, the diffusion is independent of the length. In the Nyquist plot, this Warburg element is visualised as a straight line with a slope of 45° at low frequencies. In the phase vs frequency plot is a plateau visible at 45° . Equation A.21 gives the impedance equation of the semi-infinite-length Warburg element. When the α in the equation for CPE is equal to 0.5, then the semi-infinite Warburg element corresponds with the CPE element. The Warburg impedance is small at high frequencies because the ions don't have to move far, while at low frequencies, the Warburg impedance is large [145]. The Warburg impedance depends on the electrolyte concentration and the applied electrode potential [95].

$$Z_W = \frac{Z_0}{\sqrt{\omega}} (1 - j) \quad (\text{A.21})$$

finite-length Warburg element

When there are diffusion limitations, the Warburg element is replaced by other Warburg elements: finite-length Warburg element and finite-space Warburg element. The length of the electrode is assumed to be finite, resulting in diffusion limitations. The finite-length Warburg (FLW) impedance uses the transmissive boundary condition, which is used when ions penetrate the electrode and are able to leave the electrode at the other side [95]. The behaviour of, for example, membranes could be described by the finite-length Warburg impedance. The FLW is showed in a Nyquist plot as a straight line with a slope of 45° at high frequencies and a semi-circle at low frequencies. The impedance equation of the FLW is given below:

$$Z_{FLW} = \frac{Z_0}{\sqrt{j\omega\tau}} \tanh(\sqrt{j\omega\tau}), \quad (\text{A.22})$$

where $\tau = RC$ is the time constant in s, R is the resistance of the resistor (Ω), C is the capacitance of the capacitor (F), ω is the frequency (1/s), T is the temperature (K), c is the concentration in the electrolyte (mol/m^3) and L is the length of the electrode (m). When the frequency goes to infinity, Equation A.22 becomes Equation A.21. In the Nyquist plot, at high frequencies, the infinite-length Warburg element and the finite-length Warburg element have the same shape, see Figure 57 [95]. The shape deviates as the frequency is decreased. At low frequencies, the Nyquist plot shape of the FLW is visualized as a semi-circle. This shows that as the frequency tends toward zero, the FLW element has the same impedance response as a $R//C$ -circuit element. For very low frequencies, the finite-length Warburg element could be replaced by a parallel placed resistor and capacitor. When the transmissive impedance is not strictly capacitive, then the capacitor could be changed into a CPE-element. The FLW is then called the generalized finite-length Warburg element. In this case is the semi-circle in the Nyquist plot depressed.

finite-space Warburg element

For blocking electrodes, the finite-space Warburg element is used to describe the diffusion of the ions into the electrode which assumes a reflective boundary condition. The reflective boundary condition is used when the ions are not able to leave the electrode at the other side [95]. The species are then blocked from leaving the electrode.

$$Z_{FSW} = \frac{Z_0}{\sqrt{j\omega\tau}} \coth(\sqrt{j\omega\tau}) \quad (\text{A.23})$$

When the frequency goes to infinity, Equation A.23 becomes Equation A.21. This behaviour is also visible in the Nyquist plot as a straight line with a slope of 45° . Decreasing the frequency, the straight line with a slope of 45° transitions into a vertical line in the Nyquist plot, see Figure 57 [95]. The vertical line has a real Warburg impedance value of $\lim_{\omega \rightarrow 0} \text{Re}(Z_{FSW}) = \frac{Z_0}{3}$. What is also noticeable is that the vertical line in the Nyquist plot for the finite-space Warburg element at high frequencies has exactly

the same shape in the Nyquist plot as a resistor and capacitor in series. So, for frequencies going to zero, the FSW element could be replaced by a resistor in series with a capacitor. Identical to the FLW, when the reflective impedance is not strictly capacitive, then the capacitor could be changed into a CPE-element. The FSW is then called the generalized finite-space Warburg element.

A.3.5 Transmission-line model

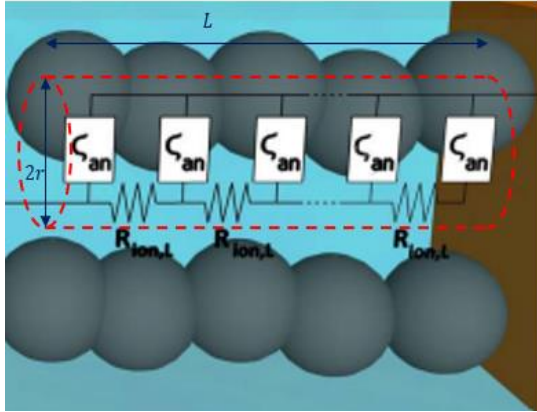


Figure 58: The concept of De Levie's transmission-line model for porous electrodes. The pores are assumed to be perfectly cylindrical (same radius), identical (same length), and equally distributed (finite number of pores). Original figure can be found in the paper of Scipioni et al. (2017) [153].

Siroma et al. (2020), Suss et al. (2013) and Huang et al. (2018) use the transmission-line model to describe the behaviour of the impedance inside porous electrodes [96,101,104]. De Levie (1963) was the first who developed the Transmission-Line Model (TLM) for modelling the microstructure of porous electrodes [102]. The transmission line model shows the same response as the finite-space Warburg element: for both elements is a straight line with a slope of 45° visible that transitions into a vertical line (Figure 58) [153]. This is not weird because the TLM describes the resistance for the mass transfer inside the electrode, e.g. it represents the ambipolar diffusion of the electrons and ions. Ambipolar diffusion is defined by IUPAC (1999) as 'diffusion in systems with two (or more) diffusing species with opposite electrical charge' [154]. The TLM thus represents the resistance in the porous electrode for

the diffusion of electrons inside the carbon particles of the electrode, for the diffusion of the counter-ions inside the pores of the electrodes, and to form an EDL.

The geometric parameters inside the porous capacitive electrodes have a large influence on the impedance in the electrochemical system. The TLM describes a porous electrode as a parallel schema of perfect circular and identical cylindrical pores filled with electrolyte [103]. The assumptions of the TLM, according to Barcia et al. (2002) [103], are:

- (1) solution resistivity is independent of the coordinate along the pore axis x
- (2) The conductivity of the solid phase is infinite
- (3) the local impedance is independent of x

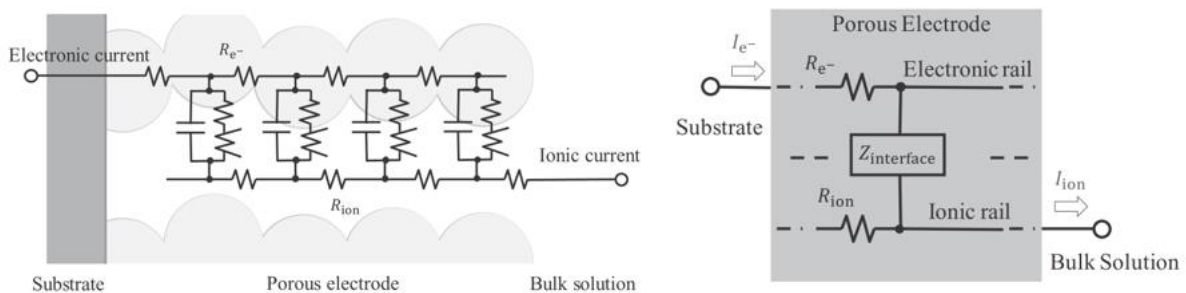


Figure 59: (left) The graphical scheme of the transmission-line model according to De Levie (1963). (right) The electronic rail and ionic rail are connected like a ladder by equivalent circuits which describe the interface impedance. The figures were retrieved from the research paper of Siroma et al. (2020) [104].

The equivalent electrical circuit of the impedance in one cylindrical pore, according to the TLM, is depicted in Figure 59 [104]. In the figure, the ladder-like structure of this model is noticeable. This ladder structure is finite, however, the ladder is assumed to consist of infinite steps where one ladder step represents all steps of the ladder [104]. The TLM structure consists of an electronic rail for the

impedance of the electrons through the carbon electrode, an ionic rail for the impedance of ions through the bulk solution and the interface resistance between the electrolyte and the carbon particles. The ionic and electronic path resistances are depicted with resistors, while the interface resistance is depicted with one of the depicted equivalent electrical circuits in Figure 60a, Figure 60b, and Figure 60c [104]. The electrical circuit of Figure 60a is chosen when an ideal double-layer capacitance is assumed, while the electrical circuit of Figure 60b more accurately describes the faradaic reactions at the interface [104]. The electrical circuit visualised in Figure 60c is included inside the equivalent circuit of the TLM when the diffusion of the ions inside each particle of the pore is described [104]. The Warburg impedance included in the interface circuit effectively describes this behaviour.

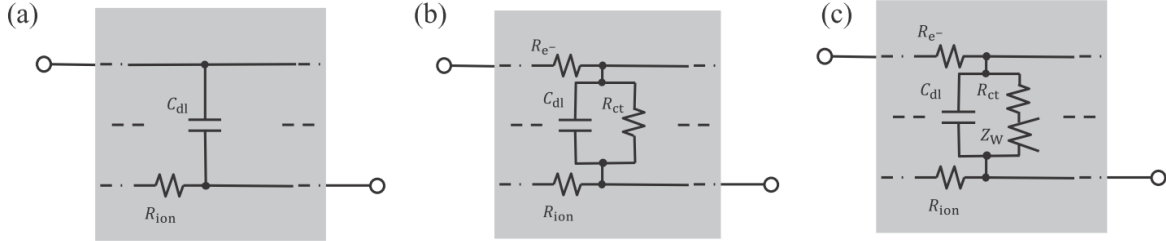


Figure 60: Equivalent circuits for the interface impedance: (a) ideal double layer capacitor, (b) faradaic reactions at the interface, (c) semi-infinite diffusion at the interface. Figure retrieved from the research paper of Siroma et al. (2020) [104].

The TLM could be simplified by assuming that the conductivity of one path is much higher than the conductivity of the other path. The path with the higher conductivity could be considered as a path without resistors. When this assumption is valid, the TLM is denoted as the one-path TLM [105]. For example, suppose that the conductivity of the electrons through the electrode is much higher than the conductivity of the ions in the electrolyte. The resistance of the electronic rail is then assumed to be very small and the resistors on the electronic rail are removed from the TLM. Figure 61 shows the effect that the different equivalent electrical circuits has on the shape in the Nyquist plot of the one-path TLM for porous electrodes [155]. The equivalent electrical circuit determines the equivalent impedance equation (Z_{eq}).

Just like the Warburg elements, the TLM impedance equation is derived with different boundary conditions: reflective and transmissive boundary conditions. Equation A.24 is the impedance equation of the finite-transmission-line model with reflective boundary condition and Equation A.25 is the impedance equation of the finite-transmission-line model with transmissive boundary condition. Appendix B gives the whole derivation of these impedance equations. If the ions are not allowed to leave the other side of the porous electrode (in the case of porous electrodes), then the reflective boundary condition is applicable. If the ions are able to leave the other side of the porous electrode (in the case of ion exchange membranes), then the transmissive boundary condition is applicable. The equations of the TLMs and Warburg elements are similar, they are identical when the equivalent interface element is equal to an ideal capacitor ($Z_{eq} = \frac{1}{j\omega C}$).

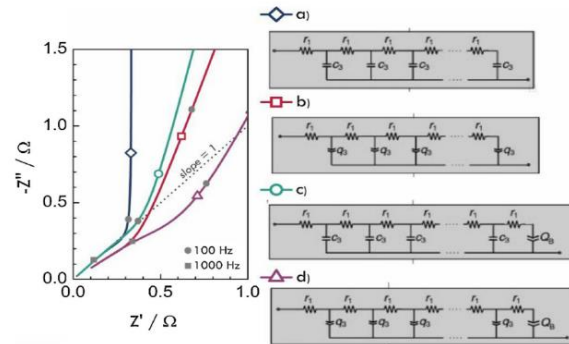


Figure 61: The shape of the Nyquist plot for different equivalent circuits in one-path TLM. Figure has been retrieved from the research paper of Hilario et al. (2017) [155].

$$Z_{TLM} = \sqrt{RZ_{eq}} \coth \left(\sqrt{\frac{R}{Z_{eq}}} \right) \quad (A.24)$$

$$Z_{TLM} = \sqrt{RZ_{eq}} \tanh \left(\sqrt{\frac{R}{Z_{eq}}} \right) \quad (A.25)$$

The power of the TLM is that the model could be used to predict the geometrical parameters of the porous electrode. The impedances are dominant at different time scales, therefore, EIS could be used

to decouple these different impedances. Barcia et al. (2002) and Hilario et al. (2017) fitted a modification of Equation A.24 in the impedance data, collected from EIS, resulting in acquiring geometrical parameters of the porous electrode as the average radius of the cylindrical pore, the average pore length and the number of pores [103,155].

A.4 Relation between EIS and performance indicators

A.4.1 EIS of capacitive electrodes and performance of CDI systems

The capacitance of the electrode indicates the maximum amount of ions that can be adsorbed inside the EDL, thus for EIS, the capacitance of the EDL (C_{dl}) equivalently describes the capacitance of the electrode. The most common way of determining the specific capacitance is by graphical analysing the semi-circles in the Nyquist plot and the peaks in the phase Bode plot. The specific capacitance between CC and electrode is denoted with a peak in the high frequency domain of the phase Bode plot, and the specific capacitance between the electrode and the electrolyte is denoted with a peak or plateau in the low frequency domain of the phase Bode plot. Another way is to construct a complex capacitance plots with which the whole electrode capacitance is directly determined [89,148]. The real capacitance is plotted against the frequency and the imaginary capacitance is plotted against the frequency, see Figure 62. How higher the real capacitance at low frequency ($\omega \rightarrow \infty$), how higher the double layer capacity [89]. The capacitance created between the current collector and electrode are disregarded in this calculation. A high value of the double layer capacitance directly states that the electrode could adsorb many ions in the EDL, thus the SAC of the CDI system is high when this electrode is included in the design of the system.

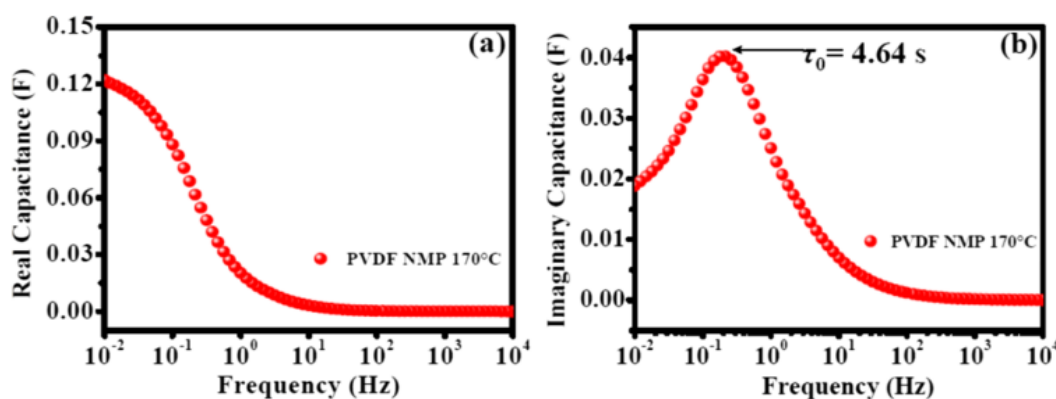


Figure 62: Complex capacitance plots: (left) real capacitance vs frequency and (right) imaginary capacitance vs frequency. Source: Arunkumar & Paul (2017) [89].

The maximum in the imaginary capacitance vs frequency plot is at the frequency f_0 which provides the value of the dielectric relaxation time constant $\tau_0 = 1/f_0$ [89,156]. According to Arunkumar and Paul (2017), τ_0 corresponds to the time needed for the supercapacitor to be filled for 50% of the total double layer capacitance with ions [89]. Additionally, according to Gao et al. (2015), τ_0 corresponds with the transition between the capacitive and resistive behaviour of the capacitive electrode [156]. At high frequencies, the supercapacitor behaves resistive because all the power is dissipated, and at low frequencies, the supercapacitor behaves capacitive because all the power is converted in reactive power [149]. The time constant τ_0 is the frequency where the supercapacitor has equally resistive as capacitive behaviour [149]. Electrodes with a low time constant and a high double layer capacitance (or real capacitance at low frequencies) are preferred because this indicates that the electrode has a high adsorption rate [89].

Additionally, the kinetics of the species inside the electrode could be analyzed by looking at the corresponding shape of the Nyquist plot. Arunkumar & Paul (2017) compared the diffusion by ions in the electrolyte of different electrodes by determining the “knee frequency” [89]. The knee frequency is the frequency at the transition point, which is the point in the Nyquist plot where the semi-circle stops

and the 45° line begins [89]. The higher the knee frequency, the faster the diffusion of ions in the pores of the electrode [89].

A.4.2 EIS of ion exchange membranes and performance of ED systems

For ion exchange membranes, the transport time constant τ indicates the amount of time an specific type of ion needs to move through the membrane [76]. The transport time constant is different for different types of ions with different ionic strengths, therefore, it is used to estimate the ability of the ion to move through the membrane [76]. The transport time constant is determined by finding the frequency f_m of the first peak in the phase Bode plot (at low frequency) and then calculating the time constant with the equation $\tau_t = 1/f_m$. Permselectivity cannot be explained with resistance measurements, according to Jiang et al. (2019), however, the same authors conclude that the transport time constant is a more suitable indicator for evaluating the permselectivity of different counter-ions than the resistance [76]. A lower transport time constant, thus the first peak in the phase Bode plot is at a higher frequency, indicates that the counter-ions transport is faster resulting in higher permselectivity.

The conductivity is the length multiplied by the reciprocal of the overall resistances in the IEM times the surface area of the IEM. The overall resistances include the R_{EDL} , R_{DBL} , and R_M [67]. For low concentrations, the R_{EDL} is relatively very low, while R_{DBL} is large and R_M is lower than the R_{DBL} . The overall resistance in the membrane have a direct effect on the conductivity: how lower the summation of all resistances, how higher the conductivity. The conductivity directly means that the mobility of the ions through the membrane is high. Thus, when the membrane and interface resistances are high, the mobility of the ions are lower [157]. Fontananova et al. (2017) investigated the effect of combined NaCl solutions with $MgCl_2$, Na_2SO_4 , and $CaCl_2$ on the measured impedance with EIS [100]. According to the authors, the valence of the ions (monovalent or multivalent) also affect the interface impedances and membrane resistance where it has a stronger effect on the membrane resistance than on the interface impedances [100]. The larger hydrated radius of the bivalent Mg^{2+} ion towards the monovalent Na^+ ion results in a lower mobility of the Mg^{2+} ion [100].

Membrane fouling is an issue for IEMs and has been investigated by multiple researchers [25,63,147,159]. According to Zhang et al. (2020), a sharply increasing R_{EDL} over time indicates that the membrane is fouled [25]. In the Nyquist plot, the first semi-circle, at high frequencies, increases in width and height, while the second semi-circle, at lower frequencies, decreases and even disappears over time [158].

A.5 Accuracy of EIS data

A.5.1 Accuracy Contour Plot

The potentiostat used for measuring the EIS data of an electrochemical cell is not capable to measure the impedance at all frequencies with a high accuracy. Especially at high frequencies, the accuracy of the collected data is limited. The accuracy at different applied frequencies and measured impedances is summarized in the Accuracy Contour Plot (ACP). The logarithmic frequency is placed on the x-axis and the logarithmic magnitude of the impedance is placed on the y-axis. According to the website of Gamry instruments, the ACP graph is constructed by measuring the impedances of ideal capacitors with known capacities between 10 pF and 100 μ F in logarithmic increasing steps and resistors between 1 T Ω and 10 m Ω in logarithmic decreasing steps [160]. AC potential is applied at different frequencies between the maximum and minimum frequency of the instrumentation with logarithmic decreasing steps. The collected EIS data is shown graphically in Bode plots where accuracy limits are placed. The accuracy limit at different measured impedances at a specific frequency is used to construct the Accuracy Contour Plot. The instrument, thus the potentiostat, has to be calibrated beforehand [160]. The ACP is specific for every potentiostat: even the cable length has an influence on the accuracy. Figure 63 shows a typical Accuracy Contour Plot for a potentiostat [161]. The regions in the ACP show the ranges of applied frequencies and measured impedances where the accuracy is the same. Thus, the ACP could be used to determine the uncertainty of the collected EIS data.

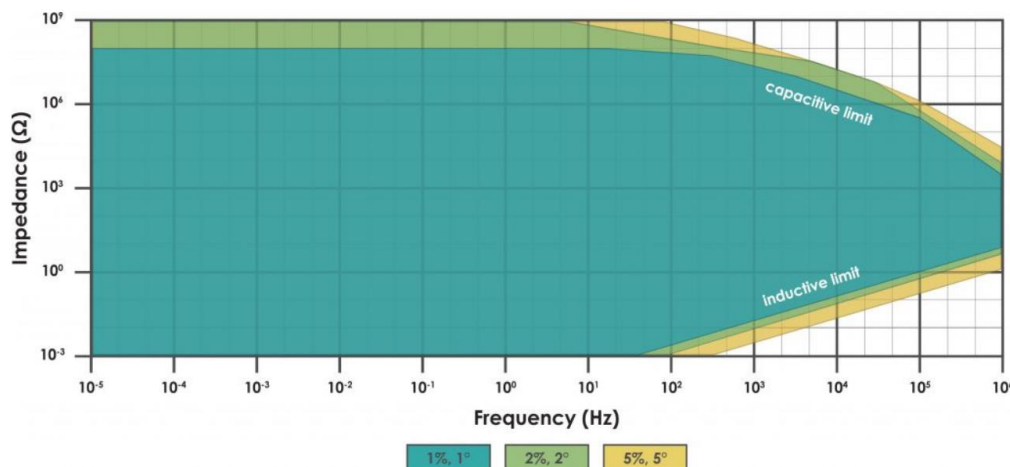


Figure 63: EIS Accuracy Contour Plot (ACP) for a potentiostat retrieved from the website of Pine Research [161]. The error of the impedance measurement is $\pm 1\%$ for the magnitude and $\pm 1^\circ$ for the phase angle (blue), $\pm 2\%$ for the magnitude and $\pm 2^\circ$ for the phase angle (green), and $\pm 5\%$ for the magnitude and $\pm 5^\circ$ for the phase angle (yellow).

At high frequencies, the range of measured impedances, where the accuracy is small, reduces. This effect is caused by the capacitive limit at high impedances and the inductive limit at low impedances. The capacitive limit is caused by the influence of stray capacitance in the EIS system, while the inductive limit is caused by the influence of stray inductance in the EIS system [161]. Stray capacitance is caused by the clips, at the end of the cell cable, that act as a parallel plate capacitor with the air as the dielectric [160]. The effect of stray capacitance is minimized by connecting the clips radially to the electrochemical system [160]. Stray inductance is caused by the magnetic fields induced by the current through the cables of the working and counter electrode. Physically twisting the working and counter-electrode cables around each other reduces the magnetic field because the current in the WE cable moves in the opposite direction to the CE cable [160]. This action thus reduces the stray inductance. Pick-up is another phenomenon that has effect on the stray inductance. When the reference electrodes sense the magnetic field of the WE and CE cables, a current starts flowing inside the RE cables. This effect contributes to the stray inductance. The distance between the reference electrodes and working- and counter-electrode must be maximized, while the distance between the reference electrodes should be as small as possible by physically twisting these cables around each other, to minimize the stray inductance [160].

EIS measurements of membranes occur in the high impedance region, thus therefore, electrochemical cells with membranes are high impedance systems [160]. The limit of the measurable impedance of the instrument is, at high impedances, determined by the drift inside the potentiostat. Drift is caused by the instrument's internal resistance or measurement circuit, resulting in an additional phase shift [160]. The accuracy thus reduces. Increasing the amplitude of the applied signal solves this problem, because the magnitude of the impedance becomes independent of the frequency, however, this could make the linearity condition invalid. Samples with high impedances result in small current flows, which are easily inaccurate due to noise effects. A Faraday cage avoids the influence of external electrical fields which improves the accuracy of the EIS data points [75].

A.5.2 Kronig-Kreuner relation and quality of the fit

The ACP gives information about the errors in the measured data caused by the potentiostat, however, the applied signal itself could be invalid. The impedance data is invalid when one or more of these conditions is not met: (1) stability, (2) causability, (3) linearity, (4) finiteness [161].

1. **Stability** - The system is stable if the energy produced in the system does not excite the total energy input [95]. The impedance data must additionally be stationary, which means that the

measured impedance is time independent. This condition is checked by repeating the measurements and compare the obtained results, which should be identical [95]. The electrochemical system must thus be able to return to the initial state without further oscillations once the applied signal is terminated [161]. This includes the positioning of the electrodes inside the electrochemical cell that should maintain their position for all the impedance measurements [162]. This needs to be considered during the design of the EIS setup. The stability condition also demands that there are no negative impedances in the system [95].

2. **Causality** - The resulting signal is only caused by the applied signal [161]. If this condition is true, then the causality condition is valid. Noise generated independently of the applied signal makes this condition invalid [95]. Observed oscillations, after the applied signal has been terminated, indicate the presence of noise. With the Fast Fourier transform, the noise component is isolated from the other frequencies and could be eliminated [163]. Also, measuring the impedance at different cycles and then averaging the impedance, reduces the noise effect [163].
3. **Linearity** - The resulting signal must exhibit a linear response to the applied signal [161]. Electrochemical systems are usually non-linear, so, to ensure linearity, the applied signal amplitude must be small enough to obtain linearisation of the impedance equations [95]. However, too small amplitudes will not excite the system, so there is a range in which the amplitude of the applied perturbation must be to ensure valid impedance data. The effective range is around 5-20mV for potentiostatic EIS measurements [161]. Linearity is ensured by checking if the amplitude of the measured current is doubled when the amplitude of the applied potential is made twice as large.
4. **Finiteness** – The real and imaginary part of the measured impedance must have a finite value over the entire frequency range ($0 < \omega < \infty$) [95].

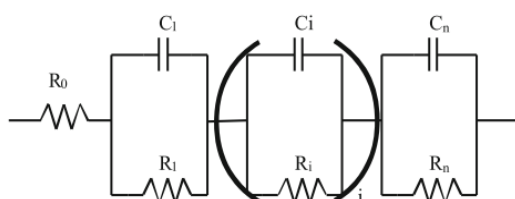


Figure 64: Voigt circuit with n RC-elements. Such an R//C-element is also called a Voigt element. Figure is originally displayed in the book of Lasia (2014) [95].

These conditions for validity are investigated, after the impedance data has been collected, by using the Kramers-Kronig transforms. The Kramers-Kronig transforms are mathematical relations that allow one to calculate the real part and imaginary part of a complex function separately from one and other, see Equation A.26 and A.27 [95]. Unfortunately, the mathematical application of these Kramers-Kronig relations to real impedance data is in practice impossible because it entails analysis between zero

and infinite frequency limits, which are physically impossible to measure [161]. Therefore, Boukamp (1995) proposed to replace the Kramers-Kronig transform with an approximation by using the Voigt circuit that could represent any linear circuit [164]. The Voigt circuit is an EECM consisting of a number of R//C-elements that result in an impedance equation which is fitted through the collected impedance data to check its validity. Determining the necessary amount of Voigt elements (see Figure 64) is important for this method, because the CPE and Warburg elements can only be approximated when there are sufficient RC-elements inside the circuit [95, 165]. The correct number of Voigt elements n depends on the system random errors: lower system random errors, means more Voigt elements are necessary [95]. A deviation between experimental impedance data and Kramers-Kronig fit with the Voigt circuit, as well as a value of the quality of fit more than two orders of magnitude higher than the collected impedance data, suggests that the EIS data is not valid [161].

$$Z_{\text{real}} = Z'(\omega) = Z'(\infty) + \frac{2}{\pi} \int_0^{\infty} \frac{xZ'(x) - \omega Z''(\omega)}{x^2 - \omega^2} dx \quad (\text{A.26})$$

$$Z_{\text{imag}} = Z''(\omega) = -\left(\frac{2\omega}{\pi}\right) \int_0^{\infty} \frac{Z'(x) - Z'(\omega)}{x^2 - \omega^2} dx \quad (\text{A.27})$$

The value of chi-square χ^2 indicates the quality of the equivalent electrical circuit model, thus how well the impedance equation of the EECM fits through the measured EIS data [107, 113, 136]. The chi-square is

therefore referred to as the goodness of the fit or quality of the fit [107,161]. The quality of fit (χ^2) is calculated by summing the squared residuals between the experimental impedance data and the fit equation of an EECM or the Voigt circuit [107,161]. The equation is given as

$$\chi^2 = \sum_{i=1}^{2n} \frac{(y_i - f(y_i))^2}{f(y_i)} * \frac{1}{\sigma_i^2}, \quad (\text{A.28})$$

where y_i is the experimental datapoint at frequency i , $f(y_i)$ is the expected value of the datapoint calculated with the impedance equation of an EECM at frequency i , σ_i is the variance of the datapoint at frequency i , and n is total number of frequencies where a measurement has been conducted [112]. The chi-square value needs to be as low as possible, however the EECM could be accepted as a “good model” to fit through the experimental impedance data if the chi-square value is lower than 10^{-3} [113,114]. The goal is to find the EECM which has the lowest quality of fit value. Increasing the elements inside the EECM always results in a lower chi-squared, however, the EECM still needs to be physically relevant. A rule of thumb is therefore that increasing the elements inside the EECM is only acceptable if the chi-squared value decreases with an order, with the condition that the additional elements could correlate to electrochemical physical behaviour [107].

A.6 Potentiostat for EIS measurements

The devices designed to perform EIS measurements are potentiostats or galvanostats, which are combined with a frequency response analyser (FRA). The devices are equivalent and usually result in the same impedance diagrams, only the input and response signals are different. For the potentiostat, the voltage difference between the working electrode and reference electrode is controlled to be zero, so the voltage at the working and reference electrode are equal. The input signal is an AC signal, with a perturbation amplitude that is determined by the researcher, while the AC current response is measured between the sensing leads [136]. For the galvanostat, the input and output are switched, where the perturbation amplitude and frequency of the AC current is controlled while the voltage over the sensing leads is measured [136]. Most electrochemical devices consist of both a potentiostatic mode and a galvanostatic mode [107], this is also the case for the Biologic VSP-300 system. Potentiostats are used for materials with a high impedance and galvanostat is used for samples with a low impedance [166]. For supercapacitors and membranes, usually the potentiostat is used to perform EIS measurements, therefore, in this thesis report, the focus will lay in the understanding and usage of the potentiostat.

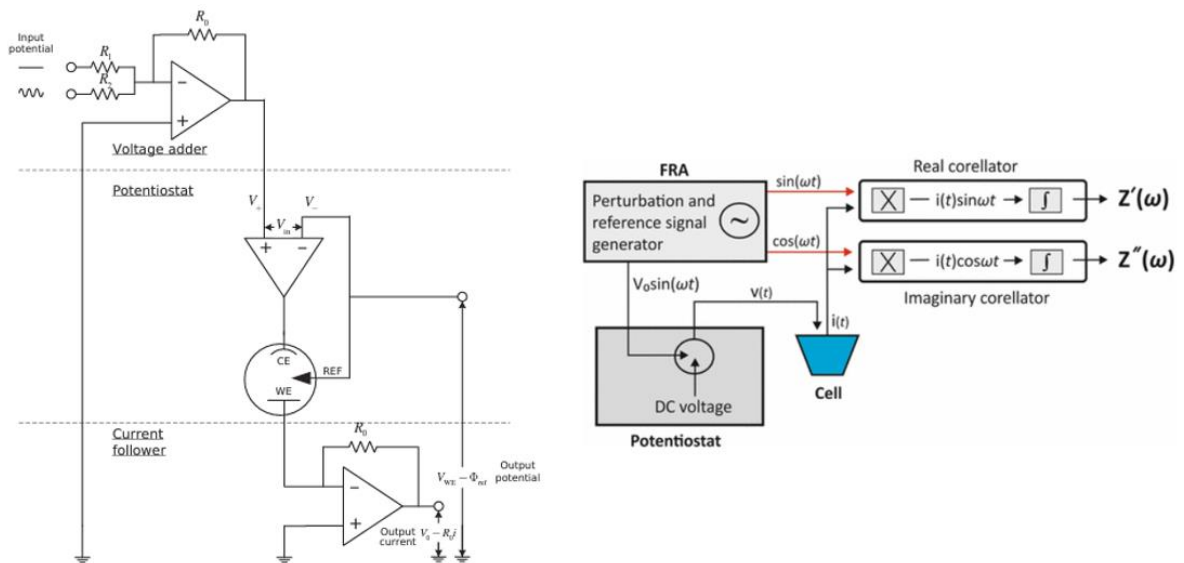


Figure 65: (left) potentiostat electrical circuit for performing 3-point measurements on an electrochemical cell, and (right) functions of potentiostat and frequency response analyser (FRA) to construct the EIS data of an electrochemical cell. Left figure was retrieved from Orazem & Tribollet (2017) and right figure was retrieved from Lazanas & Prodromidis (2023) [107,136].

In Figure 65a is the basic structure of the potentiostat visualised [136]. The potentiostat inputs a DC voltage signal. To make an AC voltage signal, the system of the potentiostat is included with a frequency response analyser (FRA) which ensures that a sine-wave perturbation signal goes into the potentiostat [107]. The voltage adder, Figure 65a, is used to add the AC sine-wave of the FRA with the DC voltage of the potentiostat [136]. Then, the constant AC voltage signal goes into the electrochemical cell where the working and reference electrode voltage are controlled by the operational amplifier. This operational amplifier is called a voltage follower and keeps the input voltage of the working electrode and the output voltage of the reference electrode equal [136]. A small current flows between the counter electrode and the working electrode. Then another operational amplifier, the current follower, Figure 65a, is used to measure the current response, which has the same frequency but another phase than the AC voltage [136]. The output response signal is determined in the current follower. The potential difference over the sensing leads (for 4-point measurement) is measured with a voltmeter, which is placed in parallel with a resistor with a known value. Then, the AC response current is determined with Ohm's law from that potential and known resistance. The FRA analyses the response and transforms the data into its real and imaginary components [107]. This process is clearly illustrated in Figure 65b [107].

A.7 Operational parameters of EIS measurements

The salt concentration in the electrolyte, flowrate of the solution flow, temperature in the electrochemical cell, and the thickness of the membrane are operational parameters that influence the impedance measurement of the EIS system. The influence of some of these parameters are investigated during the experiments while the other parameters are kept constant.

Table 11: Conditions and parameters of previous EIS setups in the literature.

Researchers	Potentiostat	Electrode Configuration	Frequency range	Perturbation Amplitude	Operating parameters and variables	Electrochemical system investigated
Park et al. (2006) [92]	AutoLab, Model PGSTAT 30	Four-electrode	1,000,000Hz – 0.001 Hz	???	Temperature: $25^{\circ}\text{C} \pm 1^{\circ}\text{C}$; Concentration KCl: 0.005M, 0.01M, 0.025M, 0.05M	Ion exchange membranes in two compartment cell
Długołęcki et al. (2010) [25]	Iviumstat (Potentiostat/galvanostat)	Four-electrode	1,000Hz – 0.001Hz	3mA	Concentration NaCl: 0.017 M and 0.5 M; Flowrate: 100mL/min, 400mL/min, 800mL/min; Temperature: $25^{\circ}\text{C} \pm 0.2^{\circ}\text{C}$	Ion exchange membranes (CEM and AEM)
Suss et al. (2013) [101]	Biologic potentiostat	Three-electrode	10,000Hz – 0.010Hz	5mV	Concentration NaCl: 0.5M, 2.5 M	Hierarchical carbon aerogel electrodes
Landesfeind et al. (2016) [23]	Biologic VMP3 potentiostat/galvanostat	Two-electrode	200,000Hz – 0.5Hz	5mV and 10mV	Temperature: 25°C ; Conductivity: 0.41 – 12.5 mS/cm	Porous separators and electrodes in a three cell setup
Gamala et al. (2016) [24]	Ivium Technologies (Galvanostat)	Two-electrode + four-electrode	100,000Hz – 0.1Hz	10mA – 1A	Temperature: $25^{\circ}\text{C} \pm 0.5^{\circ}\text{C}$; Concentration NaCl: 0.001M – 5.0M	Ion exchange membranes in two and six compartment cells
Lenz et al. (2020) [19]	Interface 5000E, Gamry Instruments	Two-electrode	10,000Hz – 0.01Hz	10mV	Concentration sodium chloride: 25mM; Flowrate: 0.2 mL/min	Flow-by CDI setup with symmetric electrodes
Kuo et al. (2020) [24]	BioLogic VSP-300 potentiostat	Two-electrode + four-electrode	700,000Hz – 0.040Hz	10mV	Concentration NaCl: 0.015M – 2M; Thickness: 355 μm , 600 μm , and 1025 μm ;	Flow-through electrode CDI cell with hierarchical carbon aerogel monolith electrodes
Zhang et al. (2020) [25]	AutoLab, PGSTAT204, Metrohm	Four-electrode	1,000,000Hz – 0.010Hz	500mV	Temperature: $25^{\circ}\text{C} \pm 2^{\circ}\text{C}$; Concentration NaCl: 0.01M	Fouling of anion exchange membrane in a four compartment cell
DuToit et al. (2021) [147]	Gamry Reference 600 Potentiostat	Three-electrode + four-electrode	100,000Hz – 0.1Hz	10mV _{rms}	Concentration phosphate buffered saline (PBS): 0.01M	Fouling effects of ion exchange membranes

A.7.1 Concentration of the electrolyte

The salt concentration in the bulk solution has a direct effect on the impedance: higher initial salt concentrations reduce the resistance in the bulk solution (R_{bulk}). Higher salt concentration means that there are more ions inside the bulk which increases the conductivity of the ions. During an EIS measurement, the series resistance reduces for higher initial salt concentrations. If the concentration is varied during the EIS experiments or not, for every applied signal frequency, the concentration must stay constant. This is achieved by flowing the electrolyte, with the correct salt concentration, along the examined specimen. The investigated specimen must be placed inside a thermic bath of the electrolyte solution for at least 24 hours before the experiments start, just like Długolecki et al. (2010) did for their investigated ion exchange membranes, to ensure that the initial salt concentration inside the specimen is equal to the salt concentration in the bulk solution [75]. The concentration in the stream is measured with a conductivity meter. Majority of the researchers (Table 11) execute the EIS experiments with electrolytes consisting of NaCl with a concentration between 0.001M and 5M. Brackish water is defined to have a salinity of 500 mg/L – 20,000 mg/L, according to the review paper of Ahdab & Lienhard (2020), which would correspond with a salt concentration of 8.5mM – 0.034M NaCl [167].

A.7.2 Flowrate of the stream

The flowrate has an effect on the measured impedance: higher flowrates reduce the resistance in the bulk solution (R_{bulk}). However, the research of Długolecki et al. (2010) has concluded that increasing the flow rate has no effect on the resistance for ion exchange membranes working in electrochemical systems when the electrolyte has a very high ion concentration [75]. The resistance inside the membrane dominates, thus reducing the resistance in the bulk solution has no large influences on the resistance. The concentrations in the CDI systems are small because brackish water is desalinated, therefore, the flowrate has an effect on the measured impedance. The flowrate is controlled with a pump.

A.7.3 Temperature of the cell

The electrochemical cell needs to be isothermal for EIS experiments, meaning, the experiments are conducted under constant temperature. Many researchers, see Table 11, experimented at an operating temperature of 25°C. Almost all researchers used a thermic bath to control the temperature of the compartments [19,21,23,24,25,75,97,101,147].

A.7.4 Thickness of the specimen

Decreasing the thickness of the membranes or the electrodes results in respectively lower membrane resistance and lower electronic resistance inside the electrode [21]. Thus, the series resistance is lower for smaller membranes and electrodes. However, the thickness could not be decreased indefinitely: the specimen needs to have some mechanical strength [27].

Appendix B: Derivation of impedance equation Transmission-line Model

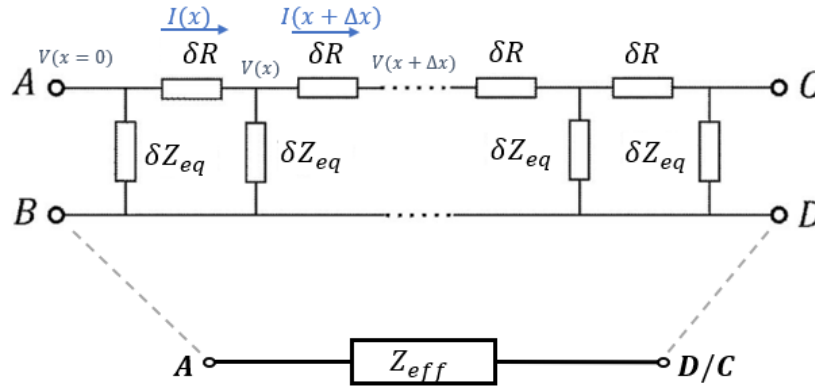


Figure 66: : Electrical circuit of the finite transmission-line model (TLM). The equivalent circuit is depicted below. The impedance of the system is measured between A and D for the reflective boundary condition and between A and C for the transmissive boundary condition. The figure is modified from the original figure in the paper by Adamič et al. (2019) [106].

Assume the Transmission-line Model could be applied for an electrode with a length L . Figure 66 shows the equivalent circuit of the TLM [106]. As is visible from the figure, the TLM consists of an ionic rail with resistors placed in series, an electronic rail without resistors, and an interface impedance. Thus the conductivity of the electrons in the active material is assumed to be much larger than the conductivity of the ions in the electrolyte. This ladder is separated with very small steps of repeating parallel placed resistor (δR) and interface impedance (δZ_{eq}). Assume the amount of steps N to be very large, so one step has length $\Delta x = \frac{L}{N}$. Then is valid for the resistors placed in series and the interface impedances placed parallel, that:

$$R = \delta R + \delta R + \dots + \delta R = N\delta R \rightarrow \delta R = \frac{R}{N} = \frac{R}{L} \Delta x$$

$$\frac{1}{Z_{eq}} = \frac{1}{\delta Z_{eq}} + \frac{1}{\delta Z_{eq}} + \dots + \frac{1}{\delta Z_{eq}} = \frac{N}{\delta Z_{eq}} \rightarrow \delta Z_{eq} = NZ_{eq} = \frac{L}{\Delta x} Z_{eq}$$

Kirchoff's laws give the equation for the potential which depend on x :

$$V(x) - V(x + \Delta x) = I(x + \Delta x)\delta R = I(x)\delta R = I(x)\frac{R}{L} \Delta x$$

$$\frac{V(x) - V(x + \Delta x)}{\Delta x} = I(x)\frac{R}{L}$$

The differential equation of the potential is then:

$$\frac{dV(x)}{dx} = \frac{V(x + \Delta x) - V(x)}{\Delta x} = -I(x)\frac{R}{L}$$

Kirchoff's laws also give then the equations for the current which depend on x :

$$I(x) - I(x + \Delta x) = \frac{V(x)}{\delta Z_{eq}} = V(x)\frac{1}{Z_{eq}L} \Delta x$$

$$\frac{I(x) - I(x + \Delta x)}{\Delta x} = V(x)\frac{1}{Z_{eq}L}$$

The differential equation of the current is then:

$$\frac{dI(x)}{dx} = \frac{I(x + \Delta x) - I(x)}{\Delta x} = -V(x) \frac{1}{Z_{eq}L}$$

The differential equations could be inserted together to get:

$$\begin{aligned} \frac{d^2V(x)}{dx^2} &= -\frac{dI(x)}{dx} * \frac{R}{L} \\ \frac{d^2V(x)}{dx^2} &= V(x) \frac{R}{Z_{eq}L^2} \end{aligned}$$

The homogeneous solution of the second order differential equation is:

$$V(x) = c_1 \exp\left(\sqrt{\frac{R}{Z_{eq}}} * \frac{x}{L}\right) + c_2 \exp\left(-\sqrt{\frac{R}{Z_{eq}}} * \frac{x}{L}\right)$$

Then, the solution of the equation for the current is:

$$I(x) = -\frac{L}{R} * \frac{dV(x)}{dx} = -\sqrt{\frac{1}{RZ_{eq}}} \left(c_1 \exp\left(\sqrt{\frac{R}{Z_{eq}}} * \frac{x}{L}\right) - c_2 \exp\left(-\sqrt{\frac{R}{Z_{eq}}} * \frac{x}{L}\right) \right)$$

The values of c_1 and c_2 depend on the boundary conditions. Two boundary conditions, reflective and transmissive, are worked out because they are utilized for supercapacitors and electric conducting membranes, respectively.

B.1 Reflective boundary condition

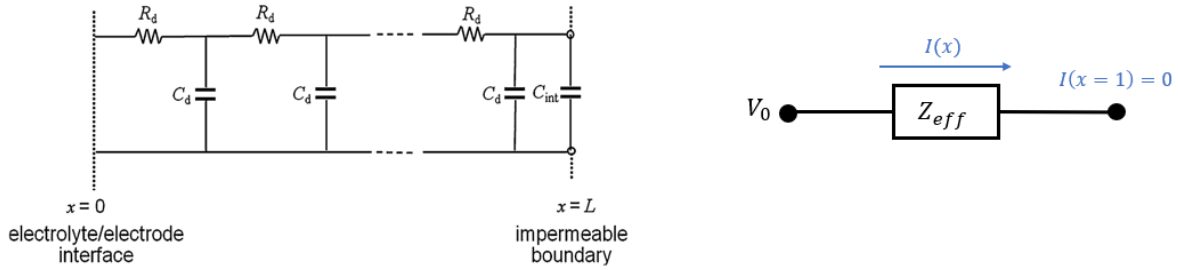


Figure 67: (left) Transmission-line model with reflective boundary condition and (right) the equivalent electrical circuit. The figures were retrieved from the papers of Kim & Pyun (2011) and Siroma et al. (2015) [168,169].

The reflective boundary condition is applied to the TLM when the species are unable to diffuse through the electrode (blocking) or are fully adsorbed in the EDL of the electrode. This boundary condition is applied, for example, for supercapacitors with a current collector foil glued at the back of the electrode. The corresponding boundary conditions are:

$$\text{RBC 1: } V(x=0) = V_0$$

$$\text{RBC 2: } I(x=L) = 0$$

Solving the first boundary condition RBC 1 gives:

$$V(x=0) = V_0$$

$$c_1 + c_2 = V_0$$

Solving the second boundary condition RBC 2 gives:

$$I(x=L) = -\sqrt{\frac{1}{RZ_{eq}}} \left(c_1 \exp\left(\sqrt{\frac{R}{Z_{eq}}}\right) - c_2 \exp\left(-\sqrt{\frac{R}{Z_{eq}}}\right) \right) = 0$$

$$c_1 \exp\left(\sqrt{\frac{R}{Z_{eq}}}\right) - c_2 \exp\left(-\sqrt{\frac{R}{Z_{eq}}}\right) = 0$$

$$c_1 = c_2 \exp\left(-2 \sqrt{\frac{R}{Z_{eq}}}\right)$$

Substituting RBC 1 and RBC 2 result in the formulas of the constants c_1 and c_2 :

$$c_1 = V_0 \left(\frac{1}{1 + \exp\left(2 \sqrt{\frac{R}{Z_{eq}}}\right)} \right)$$

$$c_2 = V_0 \left(\frac{1}{1 + \exp\left(-2 \sqrt{\frac{R}{Z_{eq}}}\right)} \right)$$

The general solution of the differential equation is:

$$V(x) = V_0 \left(\frac{\exp\left(\sqrt{\frac{R}{Z_{eq}}}\left(\frac{x}{L} - 1\right)\right) + \exp\left(-\sqrt{\frac{R}{Z_{eq}}}\left(\frac{x}{L} - 1\right)\right)}{\exp\left(\sqrt{\frac{R}{Z_{eq}}}\right) + \exp\left(-\sqrt{\frac{R}{Z_{eq}}}\right)} \right)$$

$$I(x) = -\frac{V_0}{\sqrt{RZ_{eq}}} \left(\frac{\exp\left(\sqrt{\frac{R}{Z_{eq}}}\left(\frac{x}{L} - 1\right)\right) - \exp\left(-\sqrt{\frac{R}{Z_{eq}}}\left(\frac{x}{L} - 1\right)\right)}{\exp\left(\sqrt{\frac{R}{Z_{eq}}}\right) + \exp\left(-\sqrt{\frac{R}{Z_{eq}}}\right)} \right)$$

The impedance equation is the equation of the effective impedance of the electrical circuit. All the impedances could be replaced with one effective impedance, see Figure 67 [[168,169](#)]. The impedance is calculated with Ohm's law:

$$Z_{eff} = \frac{V(x=0) - V(x=L)}{I(x=0)} = \frac{V(x=0)}{I(x=0)}$$

$$\begin{aligned}
 Z_{\text{eff}} &= V_0 * \left(-\frac{V_0}{\sqrt{RZ_{\text{eq}}}} \left(\frac{\exp\left(-\sqrt{\frac{R}{Z_{\text{eq}}}}\right) - \exp\left(\sqrt{\frac{R}{Z_{\text{eq}}}}\right)}{\exp\left(\sqrt{\frac{R}{Z_{\text{eq}}}}\right) + \exp\left(-\sqrt{\frac{R}{Z_{\text{eq}}}}\right)} \right) \right)^{-1} \\
 &= \sqrt{RZ_{\text{eq}}} \left(\frac{\exp\left(\sqrt{\frac{R}{Z_{\text{eq}}}}\right) + \exp\left(-\sqrt{\frac{R}{Z_{\text{eq}}}}\right)}{\exp\left(\sqrt{\frac{R}{Z_{\text{eq}}}}\right) - \exp\left(-\sqrt{\frac{R}{Z_{\text{eq}}}}\right)} \right) = \sqrt{RZ_{\text{eq}}} \left(\frac{\cosh\left(\sqrt{\frac{R}{Z_{\text{eq}}}}\right)}{\sinh\left(\sqrt{\frac{R}{Z_{\text{eq}}}}\right)} \right) \\
 &= \sqrt{RZ_{\text{eq}}} \coth\left(\sqrt{\frac{R}{Z_{\text{eq}}}}\right)
 \end{aligned}$$

Thus when the interface impedance Z_{eq} is denoted as an ideal capacitance with impedance equation, $Z_{\text{eq}} = \frac{1}{j\omega C}$, then the impedance equation of the TLM with reflective boundary condition is:

$$Z_{\text{eff}} = \sqrt{\frac{R}{j\omega C}} \coth(\sqrt{j\omega RC})$$

B.2 Transmissive Boundary Condition

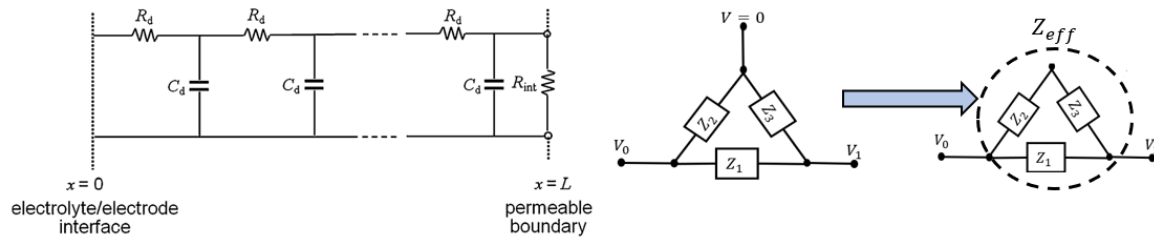


Figure 68: (left) Transmission-line model with reflective boundary condition and (right) the equivalent electrical circuit. The figures were retrieved from the papers of Kim & Pyun (2011) and Siroma et al. (2015) [168,169].

The transmissive boundary condition is applied to the TLM when the species are able to diffuse through the electrode. The TLM with transmissive boundary condition is applied to describe the ion diffusion inside electric conducting membranes, for example. There is now also a voltage at the end of the electrode (V_1). The equivalent circuit looks like Figure 68 [168,169]. The corresponding boundary conditions are:

$$\begin{aligned}
 \text{TBC 1: } &V(x=0) = V_0 \\
 \text{TBC 2: } &V(x=L) = V_1 \\
 \text{TBC 3: } &I(x=0) = \frac{V(x=0)}{Z_2} + \frac{V(x=0) - V(x=L)}{Z_1} \\
 \text{TBC 4: } &I(x=L) = \frac{-V(x=L)}{Z_3} + \frac{V(x=0) - V(x=L)}{Z_1} \\
 \text{TBC 5: } &Z_2 = Z_3
 \end{aligned}$$

Due to symmetry:

Solving the boundary conditions TBC 1 and TBC 2 gives:

$$\begin{aligned}
 V(x=0) &= c_1 + c_2 = V_0 \\
 V(x=L) &= c_1 \exp\left(\frac{R}{Z_{\text{eq}}}\right) + c_2 \exp\left(-\frac{R}{Z_{\text{eq}}}\right) = V_1
 \end{aligned}$$

Substituting TBC 1 and TBC 2 result in the formulas of the constants c_1 and c_2 :

$$c_1 = \frac{V_1 - V_0 \exp\left(-\sqrt{\frac{R}{Z_{eq}}}\right)}{\exp\left(\sqrt{\frac{R}{Z_{eq}}}\right) - \exp\left(-\sqrt{\frac{R}{Z_{eq}}}\right)}$$

$$c_2 = \frac{V_0 \exp\left(\sqrt{\frac{R}{Z_{eq}}}\right) - V_1}{\exp\left(\sqrt{\frac{R}{Z_{eq}}}\right) - \exp\left(-\sqrt{\frac{R}{Z_{eq}}}\right)}$$

The general solution of the differential equation is:

$$V(x) = V_0 \left(\frac{\exp\left(\sqrt{\frac{R}{Z_{eq}}}\left(1 - \frac{x}{L}\right)\right) - \exp\left(\sqrt{\frac{R}{Z_{eq}}}\left(\frac{x}{L} - 1\right)\right)}{\exp\left(\sqrt{\frac{R}{Z_{eq}}}\right) - \exp\left(-\sqrt{\frac{R}{Z_{eq}}}\right)} \right)$$

$$+ V_1 \left(\frac{\exp\left(\sqrt{\frac{R}{Z_{eq}}}\frac{x}{L}\right) - \exp\left(-\sqrt{\frac{R}{Z_{eq}}}\frac{x}{L}\right)}{\exp\left(\sqrt{\frac{R}{Z_{eq}}}\right) - \exp\left(-\sqrt{\frac{R}{Z_{eq}}}\right)} \right)$$

$$I(x) = \frac{V_0}{\sqrt{RZ_{eq}}} \left(\frac{\exp\left(\sqrt{\frac{R}{Z_{eq}}}\left(1 - \frac{x}{L}\right)\right) + \exp\left(-\sqrt{\frac{R}{Z_{eq}}}\left(1 - \frac{x}{L}\right)\right)}{\exp\left(\sqrt{\frac{R}{Z_{eq}}}\right) - \exp\left(-\sqrt{\frac{R}{Z_{eq}}}\right)} \right)$$

$$- \frac{V_1}{\sqrt{RZ_{eq}}} \left(\frac{\exp\left(\sqrt{\frac{R}{Z_{eq}}}\frac{x}{L}\right) + \exp\left(-\sqrt{\frac{R}{Z_{eq}}}\frac{x}{L}\right)}{\exp\left(\sqrt{\frac{R}{Z_{eq}}}\right) - \exp\left(-\sqrt{\frac{R}{Z_{eq}}}\right)} \right)$$

Solving the boundary condition TBC 3 gives:

$$I(x=0) = \frac{V(x=0)}{Z_2} + \frac{V(x=0) - V(x=1)}{Z_1}$$

$$V_0 \left(\frac{1}{Z_2}\right) + (V_0 - V_1) \left(\frac{1}{Z_1}\right) = \frac{V_0}{\sqrt{RZ_{eq}}} \left(\frac{\cosh\left(\sqrt{\frac{R}{Z_{eq}}}\right) - 1}{\sinh\left(\sqrt{\frac{R}{Z_{eq}}}\right)} \right) + \frac{V_0 - V_1}{\sqrt{RZ_{eq}}} \left(\frac{1}{\sinh\left(\sqrt{\frac{R}{Z_{eq}}}\right)} \right)$$

Calculate Z_1 and Z_2 :

$$\frac{1}{Z_1} = \frac{1}{\sqrt{RZ_{eq}}} \frac{1}{\sinh\left(\sqrt{\frac{R}{Z_{eq}}}\right)} \rightarrow Z_1 = \sqrt{RZ_{eq}} \sinh\left(\sqrt{\frac{R}{Z_{eq}}}\right)$$

$$\frac{1}{Z_2} = \frac{1}{\sqrt{RZ_{eq}}} \left(\frac{\cosh\left(\sqrt{\frac{R}{Z_{eq}}}\right) - 1}{\sinh\left(\sqrt{\frac{R}{Z_{eq}}}\right)} \right) \rightarrow Z_2 = \sqrt{RZ_{eq}} \left(\frac{\sinh\left(\sqrt{\frac{R}{Z_{eq}}}\right)}{\cosh\left(\sqrt{\frac{R}{Z_{eq}}}\right) - 1} \right) = \sqrt{RZ_{eq}} \coth\left(\frac{1}{2} \sqrt{\frac{R}{Z_{eq}}}\right)$$

Boundary condition TBC 5 gives: $Z_3 = Z_2 = \sqrt{RZ_{eq}} \coth\left(\frac{1}{2} \sqrt{\frac{R}{Z_{eq}}}\right)$

All the impedances could be replaced with one effective impedance:

$$\frac{1}{Z_{eff}} = \frac{1}{Z_1} + \frac{1}{2Z_2}$$

$$\frac{1}{Z_{eff}} = \frac{1}{\sqrt{RZ_{eq}}} \left(\frac{1}{\sinh\left(\sqrt{\frac{R}{Z_{eq}}}\right)} + \frac{\cosh\left(\sqrt{\frac{R}{Z_{eq}}}\right) - 1}{2 \sinh\left(\sqrt{\frac{R}{Z_{eq}}}\right)} \right) = \frac{1}{\sqrt{RZ_{eq}}} \left(\frac{\cosh\left(\sqrt{\frac{R}{Z_{eq}}}\right) + 1}{2 \sinh\left(\sqrt{\frac{R}{Z_{eq}}}\right)} \right)$$

$$Z_{eff} = 2 \sqrt{RZ_{eq}} \left(\frac{\sinh\left(\sqrt{\frac{R}{Z_{eq}}}\right)}{\cosh\left(\sqrt{\frac{R}{Z_{eq}}}\right) + 1} \right) = 2 \sqrt{RZ_{eq}} \tanh\left(\frac{1}{2} \sqrt{\frac{R}{Z_{eq}}}\right)$$

Thus when the interface impedance Z_{eq} is denoted as an ideal capacitance with impedance equation, $Z_{eq} = \frac{1}{j\omega C}$, then the impedance equation of the TLM with transmissive boundary condition is:

$$Z_{eff} = 2 \sqrt{\frac{R}{j\omega C}} \tanh\left(\frac{1}{2} \sqrt{j\omega RC}\right)$$

Appendix C: Derivation of the equation for the Permselectivity

The Permselectivity is also calculated with the electrochemical parameters derived from the fitting of the impedance equation of the Transmission-Line Model. The equation for the permselectivity is,

$$P = \frac{t_+ - t_-}{t_+ + t_-}$$

where P is the permselectivity of the ion exchange membrane and t is the transport number of an anion or cation [64]. The transport number is calculated with $t_i = \frac{z_i J_i}{\sum_i z_i J_i}$, where J_i is the molar flux of cation or anion i in $\text{mol}/\text{m}^2\text{s}$ and z_i is the valence of the charge of cation or anion i [65]. The molar flux is calculated with $J_i = \frac{j_i}{F}$, where j_i is the electrical current density in $\text{C}/\text{m}^2\text{s}$ and F is Faraday's constant ($= 96485 \text{ C/mol}$). The equation for the permselectivity could be rewritten to become,

$$P = \frac{j_+ - j_-}{j_+ + j_-},$$

where P is the permselectivity of the ion exchange membrane and j is the electrical current density of an anion or cation in $\text{C}/\text{m}^2\text{s}$. Ohm's law gives $j_i = \frac{\Delta V_m}{R_i}$ where R_i is the area resistance of the cation or anion i to move through the CME in Ωcm^2 and ΔV_m is the potential difference between the membrane potential and the potential of the end electrode (Figure 69) in V . ΔV_m is negative when a negative potential is applied between the CME and the end electrode, and ΔV_m is positive when a positive potential is applied between the CME and the end electrode. Then, if the membrane potential is constant, the permselectivity becomes,

$$P = \left(\frac{\frac{\Delta V_m}{R_+} - \frac{\Delta V_m}{R_-}}{\frac{\Delta V_m}{R_+} + \frac{\Delta V_m}{R_-}} \right) = \frac{R_- - R_+}{R_+ + R_-},$$

Where R_+ is the area resistance of the cations to move through the charged CME in Ωcm^2 and R_- is the area resistance of the anions to move through the charged CME in Ωcm^2 . The permselectivity now depends on the resistance of the anions and the cations to move through the CME.

The current that flows between the membrane could be calculated with Ohm's law. The total current could be separated in the current of the anions and the current of the cations $I = I_+ + I_-$. Assume all cations go through the cation resistor R_+ and all anions go through the anion resistor R_- , see

Figure 69. The total

resistance R could then be calculated by assuming that the resistors are placed in parallel, so $R = \frac{R_- R_+}{R_- + R_+}$. When $\Delta V_m = 0$, thus the CME is uncharged, assume that the cation resistor is equal to the anion resistor, so $R_+ = R_- = R_0$. The total resistance is then equal to $R = \frac{R_0}{2}$, where is the membrane resistance when the CME is uncharged. This value is denoted with R_N . If the CME is charged by placing a potential over the CME (and for example the end electrode), $\Delta V_m \neq 0$, assume the resistance of the co-ion stays R_0 , while the resistor of the counter-ion decreases. As a result, the total membrane resistance reduces when the CME is charged, which is denoted with R_C (see Figure 70).

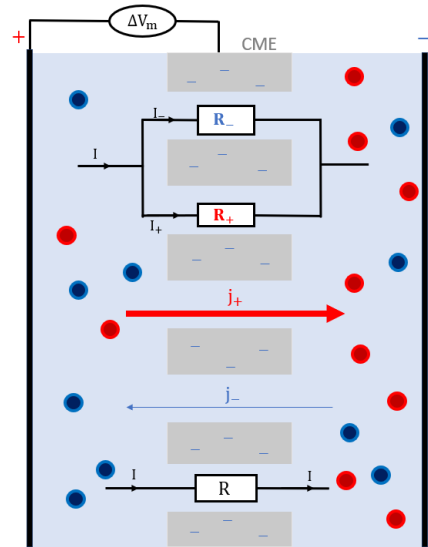


Figure 69: Schematic of the ion transport when the CME is negatively charged. The anion resistance (R_-) stays equal to R_0 while the cation resistance (R_+) decreases.

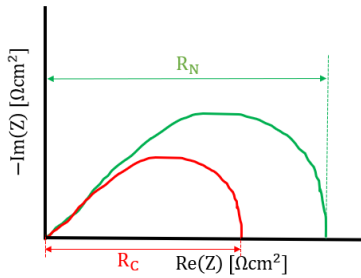


Figure 70: The impedance equation of the Transmission-line Model, when the CME is uncharged (green) and the CME is positively or negatively charged (red).

Thus:

$$\begin{aligned}
 \text{If } \Delta V_m < 0 & \rightarrow R_- = R_0 \text{ and } R_+ < R_0 & \rightarrow R_+ = R_0 \frac{1-P_-}{1+P_-} \\
 \text{If } \Delta V_m = 0 & \rightarrow R_- = R_+ = R_0 & \rightarrow R_N = \frac{R_0}{2} \\
 \text{If } \Delta V_m > 0 & \rightarrow R_- < R_0 \text{ and } R_+ = R_0 & \rightarrow R_- = R_0 \frac{1+P_+}{1-P_+}
 \end{aligned}$$

Inserting the equation for the anion and cation resistance in the total resistance of the CME when it is charged, subsequently, dividing the total resistance of the charged CME with the total resistance of the uncharged CME gives the equation for the permselectivity:

For $\Delta V_m < 0 \rightarrow R_+ = R_0 \frac{1-P_-}{1+P_-}$, $R_C = \frac{R_0 R_+}{R_0 + R_+}$ and $R_N = \frac{R_0}{2}$ gives:

$$\frac{R_C}{R_N} = \frac{R_0 R_+}{R_0 + R_+} * \frac{2}{R_0} = \frac{2R_+}{R_0 + R_+} = \frac{2R_+}{R_+ \left(\frac{1+P_-}{1-P_-} \right) + R_+} = 1 - P_-$$

$$P_- = 1 - \frac{R_C}{R_N}$$

Where P_- is the permselectivity of the cations to move through the membrane when the CME is charged with a negative membrane potential. Thus, the permselectivity for the cations is $0 < P_- < 1$.

For $\Delta V_m > 0 \rightarrow R_- = R_0 \frac{1+P_+}{1-P_+}$, $R_C = \frac{R_- R_0}{R_- + R_0}$ and $R_N = \frac{R_0}{2}$ gives:

$$\frac{R_C}{R_N} = \frac{R_0 R_-}{R_0 + R_-} * \frac{2}{R_0} = \frac{2R_-}{R_0 + R_-} = \frac{2R_-}{R_- \left(\frac{1-P_+}{1+P_+} \right) + R_-} = 1 + P_+$$

$$P_+ = \frac{R_C}{R_N} - 1$$

Where P_+ is the permselectivity of the anions to move through the membrane when the CME is charged with a positive membrane potential. Thus, the permselectivity for the anions is $-1 < P_+ < 0$.

Appendix D: Python Script

```
# -*- coding: utf-8 -*-
"""
Created on Tue Jun 13 13:31:22 2023
@author: joohk
"""

import pandas as pd
import numpy as np
import matplotlib.pyplot as plt
from scipy.optimize import curve_fit
import pickle
plt.close('all')
#####
#Determine with Z-fit the value of the blocks in the EECM and write them down for the fit later
R_TLM1 = 14.72      # Resistance in ohms of TLM1
C_TLM1 = 0.636      # Capacitance in Farads of TLM1
R_TLM2 = 12.4       # Resistance in ohms of TLM2
C_TLM2 = 15.0       # Capacitance in Farads of TLM2
R_M = 71.43         # Resistance in ohms of the holes in the CME
R_CT = 0.75         # Resistance in ohms
C_CT = 2.2e-3       # Capacitance in Farads
R_s = 53            # Resistance in ohms
alpha = 1           # factor in CPE equation
L = 0.2e-6          # Inductance in Henry
d = 7               # inner diameter tinaniumstrip of CME in cm
error_m = 0.01      # magnitude error according to the ACP
error_ang = 1       # phase error according to the ACP in degC
A = 0.25*np.pi*d**2 # surface area of the CME in cm^2
#####
# Read the Excel file
data1 = pd.read_excel('Experiment 5 - CME 11 Sept #2 AC - 4-point PLASTIC EIS data.xlsx', sheet_name=0)
data2 = pd.read_excel('Experiment 5 - CME 11 Sept #2 AC - 4-point PLASTIC EIS data.xlsx', sheet_name=1)
data3 = pd.read_excel('Experiment 5 - CME 11 Sept #2 AC - 4-point PLASTIC EIS data.xlsx', sheet_name=2)
data4 = pd.read_excel('Experiment 5 - CME 11 Sept #2 AC - 4-point PLASTIC EIS data.xlsx', sheet_name=3)
data5 = pd.read_excel('Experiment 5 - CME 11 Sept #2 AC - 4-point PLASTIC EIS data.xlsx', sheet_name=4)
data6 = pd.read_excel('Experiment 5 - CME 11 Sept #2 AC - 4-point PLASTIC EIS data.xlsx', sheet_name=5)
data7 = pd.read_excel('Experiment 5 - CME 11 Sept #2 AC - 4-point PLASTIC EIS data.xlsx', sheet_name=6)
data8 = pd.read_excel('Experiment 5 - CME 11 Sept #2 AC - 4-point PLASTIC EIS data.xlsx', sheet_name=7)
data9 = pd.read_excel('Experiment 5 - CME 11 Sept #2 AC - 4-point PLASTIC EIS data.xlsx', sheet_name=8)
data10 = pd.read_excel('Experiment 5 - CME 11 Sept #2 AC - 4-point PLASTIC EIS data.xlsx', sheet_name=9)
data11 = pd.read_excel('Experiment 5 - CME 11 Sept #2 AC - 4-point PLASTIC EIS data.xlsx', sheet_name=10)
data12 = pd.read_excel('Experiment 5 - CME 11 Sept #2 AC - 4-point PLASTIC EIS data.xlsx', sheet_name=11)
n=-1
# Extract the required columns
# EIS data of datasheet 1
frequency1 = data1['freq'][0:n]
real_impedance1 = data1['Re(Z)'][0:n]*A
imaginary_impedance1 = -data1['Im(Z)'][0:n]*A
phase_angle1 = data1["Phase(Z)"][0:n]
magnitude_impedance1 = data1["|Z|"][0:n]*A
real_capacitance1 = data1['Re(C)'][0:n]*10**-9/A
imaginary_capacitance1 = data1['Im(C)'][0:n]*10**-9/A
impedance1 = real_impedance1 + 1j*imaginary_impedance1
# EIS data of datasheet 2
frequency2 = data2['freq'][0:n]
real_impedance2 = data2['Re(Z)'][0:n]*A
imaginary_impedance2 = -data2['Im(Z)'][0:n]*A
phase_angle2 = data2["Phase(Z)"][0:n]
magnitude_impedance2 = data2["|Z|"][0:n]*A
real_capacitance2 = data2['Re(C)'][0:n]*10**-9/A
imaginary_capacitance2 = data2['Im(C)'][0:n]*10**-9/A
impedance2 = real_impedance2 + 1j*imaginary_impedance2
# EIS data of datasheet 3
frequency3 = data3['freq'][0:n]
real_impedance3 = data3['Re(Z)'][0:n]*A
imaginary_impedance3 = -data3['Im(Z)'][0:n]*A
phase_angle3 = data3["Phase(Z)"][0:n]
```

```

magnitude_impedance3 = data3["|Z|"][0:n]*A
real_capacitance3 = data3['Re(C)'][0:n]*10**-9/A
imaginary_capacitance3 = data3['Im(C)'][0:n]*10**-9/A
impedance3 = real_impedance3 + 1j*imaginary_impedance3
# EIS data of datasheet 4
frequency4 = data4['freq'][0:n]
real_impedance4 = data4['Re(Z)'][0:n]*A
imaginary_impedance4 = -data4['Im(Z)'][0:n]*A
phase_angle4 = data4["Phase(Z)"][0:n]
magnitude_impedance4 = data4["|Z|"][0:n]*A
real_capacitance4 = data4['Re(C)'][0:n]*10**-9/A
imaginary_capacitance4 = data4['Im(C)'][0:n]*10**-9/A
impedance4 = real_impedance4 + 1j*imaginary_impedance4
# EIS data of datasheet 5
frequency5 = data5['freq'][0:n]
real_impedance5 = data5['Re(Z)'][0:n]*A
imaginary_impedance5 = -data5['Im(Z)'][0:n]*A
phase_angle5 = data5["Phase(Z)"][0:n]
magnitude_impedance5 = data5["|Z|"][0:n]*A
real_capacitance5 = data5['Re(C)'][0:n]*10**-9/A
imaginary_capacitance5 = data5['Im(C)'][0:n]*10**-9/A
impedance5 = real_impedance5 + 1j*imaginary_impedance5
# EIS data of datasheet 6
frequency6 = data6['freq'][0:n]
real_impedance6 = data6['Re(Z)'][0:n]*A
imaginary_impedance6 = -data6['Im(Z)'][0:n]*A
phase_angle6 = data6["Phase(Z)"][0:n]
magnitude_impedance6 = data6["|Z|"][0:n]*A
real_capacitance6 = data6['Re(C)'][0:n]*10**-9/A
imaginary_capacitance6 = data6['Im(C)'][0:n]*10**-9/A
impedance6 = real_impedance6 + 1j*imaginary_impedance6
# EIS data of datasheet 7
frequency7 = data7['freq'][0:n]
real_impedance7 = data7['Re(Z)'][0:n]*A
imaginary_impedance7 = -data7['Im(Z)'][0:n]*A
phase_angle7 = data7["Phase(Z)"][0:n]
magnitude_impedance7 = data7["|Z|"][0:n]*A
real_capacitance7 = data7['Re(C)'][0:n]*10**-9/A
imaginary_capacitance7 = data7['Im(C)'][0:n]*10**-9/A
impedance7 = real_impedance7 + 1j*imaginary_impedance7
# EIS data of datasheet 8
frequency8 = data8['freq'][0:n]
real_impedance8 = data8['Re(Z)'][0:n]*A
imaginary_impedance8 = -data8['Im(Z)'][0:n]*A
phase_angle8 = data8["Phase(Z)"][0:n]
magnitude_impedance8 = data8["|Z|"][0:n]*A
real_capacitance8 = data8['Re(C)'][0:n]*10**-9/A
imaginary_capacitance8 = data8['Im(C)'][0:n]*10**-9/A
impedance8 = real_impedance8 + 1j*imaginary_impedance8
# EIS data of datasheet 9
frequency9 = data9['freq'][0:n]
real_impedance9 = data9['Re(Z)'][0:n]*A
imaginary_impedance9 = -data9['Im(Z)'][0:n]*A
phase_angle9 = data9["Phase(Z)"][0:n]
magnitude_impedance9 = data9["|Z|"][0:n]*A
real_capacitance9 = data9['Re(C)'][0:n]*10**-9/A
imaginary_capacitance9 = data9['Im(C)'][0:n]*10**-9/A
impedance9 = real_impedance9 + 1j*imaginary_impedance9
# EIS data of datasheet 10
frequency10 = data10['freq'][0:n]
real_impedance10 = data10['Re(Z)'][0:n]*A
imaginary_impedance10 = -data10['Im(Z)'][0:n]*A
phase_angle10 = data10["Phase(Z)"][0:n]
magnitude_impedance10 = data10["|Z|"][0:n]*A
real_capacitance10 = data10['Re(C)'][0:n]*10**-9/A
imaginary_capacitance10 = data10['Im(C)'][0:n]*10**-9/A
impedance10 = real_impedance10 + 1j*imaginary_impedance10
# EIS data of datasheet 11
frequency11 = data11['freq'][0:n]
real_impedance11 = data11['Re(Z)'][0:n]*A
imaginary_impedance11 = -data11['Im(Z)'][0:n]*A

```



```

phase_angle11 = data11["Phase(Z)"][0:n]
magnitude_impedance11 = data11["|Z|"][0:n]*A
real_capacitance11 = data11['Re(C)'][0:n]*10**-9/A
imaginary_capacitance11 = data11['Im(C)'][0:n]*10**-9/A
impedance11 = real_impedance11 + 1j*imaginary_impedance11
# EIS data of datasheet 12
frequency12 = data12['freq'][0:n]
real_impedance12 = data12['Re(Z)'][0:n]*A
imaginary_impedance12 = -data12['Im(Z)'][0:n]*A
phase_angle12 = data12["Phase(Z)"][0:n]
magnitude_impedance12 = data12["|Z|"][0:n]*A
real_capacitance12 = data12['Re(C)'][0:n]*10**-9/A
imaginary_capacitance12 = data12['Im(C)'][0:n]*10**-9/A
impedance12 = real_impedance12 + 1j*imaginary_impedance12
#####
# Determine the mean of the data
N = 8      #Number of performed EIS experiments at 0.0V
mean_frequency = (frequency1 + frequency2 + frequency3 + frequency4 + frequency5 + frequency6 + frequency7 + frequency8)/N
mean_impedance = (impedance1 + impedance2 + impedance3 + impedance4 + impedance5 + impedance6 + impedance7 + impedance8)/N
mean_real_impedance = (real_impedance1 + real_impedance2 + real_impedance3 + real_impedance4 + real_impedance5 +
real_impedance6 + real_impedance7 + real_impedance8)/N
mean_imaginary_impedance = (imaginary_impedance1 + imaginary_impedance2 + imaginary_impedance3 + imaginary_impedance4 +
imaginary_impedance5 + imaginary_impedance6 + imaginary_impedance7 + imaginary_impedance8)/N
mean_magnitude_impedance = (magnitude_impedance1 + magnitude_impedance2 + magnitude_impedance3 + magnitude_impedance4 +
magnitude_impedance5 + magnitude_impedance6 + magnitude_impedance7 + magnitude_impedance8)/N
mean_phase_angle = (phase_angle1 + phase_angle2 + phase_angle3 + phase_angle4 + phase_angle5 + phase_angle6 + phase_angle7 +
phase_angle8)/N
mean_real_capacitance = (real_capacitance1 + real_capacitance2 + real_capacitance3 + real_capacitance4 + real_capacitance5 +
real_capacitance6 + real_capacitance7 + real_capacitance8)/N
mean_imaginary_capacitance = (imaginary_capacitance1 + imaginary_capacitance2 + imaginary_capacitance3 + imaginary_capacitance4 +
imaginary_capacitance5 + imaginary_capacitance6 + imaginary_capacitance7 + imaginary_capacitance8)/N
SD_real = np.sqrt(((real_impedance1 - mean_real_impedance)**2 + (real_impedance2 - mean_real_impedance)**2 + (real_impedance3 -
mean_real_impedance)**2 + (real_impedance4 - mean_real_impedance)**2 + (real_impedance5 - mean_real_impedance)**2 +
(real_impedance6 - mean_real_impedance)**2 + (real_impedance7 - mean_real_impedance)**2 + (real_impedance8 -
mean_real_impedance)**2) / (N-1))
SD_imaginary = np.sqrt(((imaginary_impedance1 - mean_imaginary_impedance)**2 + (imaginary_impedance2 -
mean_imaginary_impedance)**2 + (imaginary_impedance3 - mean_imaginary_impedance)**2 + (imaginary_impedance4 -
mean_imaginary_impedance)**2 + (imaginary_impedance5 - mean_imaginary_impedance)**2 + (imaginary_impedance6 -
mean_imaginary_impedance)**2 + (imaginary_impedance7 - mean_imaginary_impedance)**2 + (imaginary_impedance8 -
mean_imaginary_impedance)**2) / (N-1))
SD_real_tot = np.sum(SD_real)
SD_imaginary_tot = np.sum(SD_imaginary)
#####
# Determine the mean of the data of -1.0V
mean_frequency_minoneV = frequency9
mean_impedance_minoneV = impedance9
mean_real_impedance_minoneV = real_impedance9
mean_imaginary_impedance_minoneV = imaginary_impedance9
mean_magnitude_impedance_minoneV = magnitude_impedance9
mean_phase_angle_minoneV = phase_angle9
mean_real_capacitance_minoneV = real_capacitance9
mean_imaginary_capacitance_minoneV = imaginary_capacitance9
# Determine the mean of the data of +1.0V
mean_frequency_plusoneV = frequency10
mean_impedance_plusoneV = impedance10
mean_real_impedance_plusoneV = real_impedance10
mean_imaginary_impedance_plusoneV = imaginary_impedance10
mean_magnitude_impedance_plusoneV = magnitude_impedance10
mean_phase_angle_plusoneV = phase_angle10
mean_real_capacitance_plusoneV = real_capacitance10
mean_imaginary_capacitance_plusoneV = imaginary_capacitance10
#####
# Open the EIS data of CME-S
with open('standard_impedance.pkl', 'rb') as file:
    standard_impedance = pickle.load(file)
with open('standard_frequency.pkl', 'rb') as file:
    standard_frequency = pickle.load(file)
with open('standard_real_impedance.pkl', 'rb') as file:
    standard_real_impedance = pickle.load(file)
with open('standard_imaginary_impedance.pkl', 'rb') as file:
    standard_imaginary_impedance = pickle.load(file)

```

```

with open('standard_phase_angle.pkl', 'rb') as file:
    standard_phase_angle = pickle.load(file)
with open('standard_magnitude_impedance.pkl', 'rb') as file:
    standard_magnitude_impedance = pickle.load(file)
with open('standard_real_capacitance.pkl', 'rb') as file:
    standard_real_capacitance = pickle.load(file)
with open('standard_imaginary_capacitance.pkl', 'rb') as file:
    standard_imaginary_capacitance = pickle.load(file)
# Open the EIS data of CME-AC
with open('AC_impedance.pkl', 'wb') as file:
    pickle.dump(impedance8, file)
with open('AC_frequency.pkl', 'wb') as file:
    pickle.dump(frequency8, file)
with open('AC_real_impedance.pkl', 'wb') as file:
    pickle.dump(real_impedance8, file)
with open('AC_imaginary_impedance.pkl', 'wb') as file:
    pickle.dump(imaginary_impedance8, file)
with open('AC_phase_angle.pkl', 'wb') as file:
    pickle.dump(phase_angle8, file)
with open('AC_magnitude_impedance.pkl', 'wb') as file:
    pickle.dump(magnitude_impedance8, file)
with open('AC_real_capacitance.pkl', 'wb') as file:
    pickle.dump(real_capacitance8, file)
with open('AC_imaginary_capacitance.pkl', 'wb') as file:
    pickle.dump(imaginary_capacitance8, file)
#####
# Defining the impedance equations of the different EECMs
def R_C_Circuit(freq, R, C):
    Z = R_s + (R/(1+R*C*(1j*2*np.pi*freq)))
    return Z
def TLM(freq, R, C):
    Zeq = 1/(1j*2*np.pi*freq*C)
    Z_A = np.sqrt(R*Zeq)*((np.tanh(0.5*np.sqrt(R/Zeq))))
    Z_C = np.sqrt(R*Zeq)*(1/(np.tanh(np.sqrt(R/Zeq))))-np.sqrt(R*Zeq)*((np.tanh(0.5*np.sqrt(R/Zeq))))
    Z_CT = (R_CT/(1+R_CT*C_CT*(1j*2*np.pi*freq)))
    Z = 2*Z_A + R_s
    return Z
def inhomogeneous(freq, R1, C1, R2, C2):
    Zeq1 = 1/(1j*2*np.pi*freq*C1)
    Zeq2 = 1/(1j*2*np.pi*freq*C2)
    Z_A1 = np.sqrt(R1*Zeq1)*((np.tanh(0.5*np.sqrt(R1/Zeq1))))
    Z_C1 = np.sqrt(R1*Zeq1)*(1/(np.tanh(np.sqrt(R1/Zeq1))))-np.sqrt(R1*Zeq1)*((np.tanh(0.5*np.sqrt(R1/Zeq1))))
    Z_A2 = np.sqrt(R2*Zeq2)*((np.tanh(0.5*np.sqrt(R2/Zeq2))))
    Z_C2 = np.sqrt(R2*Zeq2)*(1/(np.tanh(np.sqrt(R2/Zeq2))))-np.sqrt(R2*Zeq2)*((np.tanh(0.5*np.sqrt(R2/Zeq2))))
    Z_CT = (R_CT/(1+R_CT*C_CT*(1j*2*np.pi*freq)))
    Z = 1*R_s + 2*(0.5*((Z_A1+Z_A2)+((Z_A1+Z_A2)*(Z_C1+Z_C2)/(Z_A1+Z_A2+Z_C1+Z_C2)))) + 0*((Z_C1*Z_C2)/(Z_A1+Z_A2+Z_C1+Z_C2)) +
    0*Z_CT
    return Z
def holeTLM(freq, R, C, RM):
    Zeq = 1/(1j*C*(2*np.pi*freq))
    Z = R_s + 2*(np.sqrt(R*Zeq)*((np.tanh(0.5*np.sqrt(R/Zeq))))*RM)/(2*np.sqrt(R*Zeq)*((np.tanh(0.5*np.sqrt(R/Zeq))))+RM)
    return Z
def inhomogeneousHole(freq, R1, C1, R2, C2, RM):
    Zeq1 = 1/(1j*2*np.pi*freq*C1)
    Zeq2 = 1/(1j*2*np.pi*freq*C2)
    Z_A1 = np.sqrt(R1*Zeq1)*((np.tanh(0.5*np.sqrt(R1/Zeq1))))
    Z_C1 = np.sqrt(R1*Zeq1)*(1/(np.tanh(np.sqrt(R1/Zeq1))))-np.sqrt(R1*Zeq1)*((np.tanh(0.5*np.sqrt(R1/Zeq1))))
    Z_A2 = np.sqrt(R2*Zeq2)*((np.tanh(0.5*np.sqrt(R2/Zeq2))))
    Z_C2 = np.sqrt(R2*Zeq2)*(1/(np.tanh(np.sqrt(R2/Zeq2))))-np.sqrt(R2*Zeq2)*((np.tanh(0.5*np.sqrt(R2/Zeq2))))
    Z_CT = (R_CT/(1+R_CT*C_CT*(1j*2*np.pi*freq)))
    ZT = (Z_C1*Z_C2)/(Z_A1+Z_A2+Z_C1+Z_C2)
    ZV = Z_A1 + ((Z_A1+Z_A2)*Z_C1)/(Z_A1+Z_A2+Z_C1+Z_C2)
    ZW = Z_A2 + ((Z_A1+Z_A2)*Z_C2)/(Z_A1+Z_A2+Z_C1+Z_C2)
    ZX = (ZV*RM)/(ZV+ZW+RM)
    ZY = (ZW*RM)/(ZV+ZW+RM)
    ZN = (ZV*ZW)/(ZV+ZW+RM)
    ZZ = ZT + ZN
    Z = R_s + 2*(0.5*(ZX + ZY))
    return Z
#####

```

```
#####
#####
# Fit the impedance equations of the EECMs through the EIS datapoint of Charged CME with -1.0V
R_s = 54
# EECM B --> TLM
popt1_1, pcov1_1 = curve_fit(TLM, mean_frequency_minoneV, mean_impedance_minoneV, p0=[200, 1.0], method='lm')
perr1_1 = np.sqrt(np.diag(pcov1_1))
R_opt11, C_opt11 = popt1_1
funcdata11 = TLM(mean_frequency_minoneV, R_opt11, C_opt11)
chi_square_real11 = abs(((mean_real_impedance_minoneV - np.real(funcdata11))/SD_real_tot)**2/np.real(funcdata11))
chi_square_imag11 = abs(((mean_imaginary_impedance_minoneV - np.imag(funcdata11))/SD_imaginary_tot)**2/np.imag(funcdata11))
chi_square_sum11 = np.sum(chi_square_real11) + np.sum(chi_square_imag11)
# EECM C --> inhomogeneous TLM
popt2_1, pcov2_1 = curve_fit(inhomogeneous, mean_frequency_minoneV, mean_impedance_minoneV, p0=[80, 0.1, 60, 1.0],
method='lm')
perr2_1 = np.sqrt(np.diag(pcov2_1))
R1_opt21, C1_opt21, R2_opt21, C2_opt21 = popt2_1
funcdata21 = inhomogeneous(mean_frequency_minoneV, R1_opt21, C1_opt21, R2_opt21, C2_opt21)
chi_square_real21 = abs(((mean_real_impedance_minoneV - np.real(funcdata21))/SD_real_tot)**2/np.real(funcdata21))
chi_square_imag21 = abs(((mean_imaginary_impedance_minoneV - np.imag(funcdata21))/SD_imaginary_tot)**2/np.imag(funcdata21))
chi_square_sum21 = np.sum(chi_square_real21) + np.sum(chi_square_imag21)
# EECM D --> TLM with holes
popt3_1, pcov3_1 = curve_fit(holeTLM, mean_frequency_minoneV, mean_impedance_minoneV, p0=[300, 1.0, 600], method='lm')
perr3_1 = np.sqrt(np.diag(pcov3_1))
R_opt31, C_opt31, R_M_opt31 = popt3_1
funcdata31 = holeTLM(mean_frequency_minoneV, R_opt31, C_opt31, R_M_opt31)
chi_square_real31 = abs(((mean_real_impedance_minoneV - np.real(funcdata31))/SD_real_tot)**2/np.real(funcdata31))
chi_square_imag31 = abs(((mean_imaginary_impedance_minoneV - np.imag(funcdata31))/SD_imaginary_tot)**2/np.imag(funcdata31))
chi_square_sum31 = np.sum(chi_square_real31) + np.sum(chi_square_imag31)
# EECM E --> inhomogeneous TLM with holes
popt4_1, pcov4_1 = curve_fit(inhomogeneousHole, mean_frequency_minoneV, mean_impedance_minoneV, p0=[300, 1.0, 100, 0.5, 600],
method='lm')
perr4_1 = np.sqrt(np.diag(pcov4_1))
R1_opt41, C1_opt41, R2_opt41, C2_opt41, R_M_opt41 = popt4_1
funcdata41 = inhomogeneousHole(mean_frequency_minoneV, R1_opt41, C1_opt41, R2_opt41, C2_opt41, R_M_opt41)
chi_square_real41 = abs(((mean_real_impedance_minoneV - np.real(funcdata41))/SD_real_tot)**2/np.real(funcdata41))
chi_square_imag41 = abs(((mean_imaginary_impedance_minoneV - np.imag(funcdata41))/SD_imaginary_tot)**2/np.imag(funcdata41))
chi_square_sum41 = np.sum(chi_square_real41) + np.sum(chi_square_imag41)
# EECM A --> R//C-circuit
popt5_1, pcov5_1 = curve_fit(R_C_Circuit, mean_frequency_minoneV, mean_impedance_minoneV, p0=[150, 1.0], method='lm')
perr5_1 = np.sqrt(np.diag(pcov5_1))
R_opt51, C_opt51 = popt5_1
funcdata51 = R_C_Circuit(mean_frequency_minoneV, R_opt51, C_opt51)
chi_square_real51 = abs(((mean_real_impedance_minoneV - np.real(funcdata51))/SD_real_tot)**2/np.real(funcdata51))
chi_square_imag51 = abs(((mean_imaginary_impedance_minoneV - np.imag(funcdata51))/SD_imaginary_tot)**2/np.imag(funcdata51))
chi_square_sum51 = np.sum(chi_square_real51) + np.sum(chi_square_imag51)
#####
# Fit the impedance equations of the EECMs through the EIS datapoint of Charged CME with +1.0V
R_s = 54
# EECM B --> TLM
popt1_2, pcov1_2 = curve_fit(TLM, mean_frequency_plusoneV, mean_impedance_plusoneV, p0=[100, 1.0], method='lm')
perr1_2 = np.sqrt(np.diag(pcov1_2))
R_opt12, C_opt12 = popt1_2
funcdata12 = TLM(mean_frequency_plusoneV, R_opt12, C_opt12)
chi_square_real12 = abs(((mean_real_impedance_plusoneV - np.real(funcdata12))/SD_real_tot)**2/np.real(funcdata12))
chi_square_imag12 = abs(((mean_imaginary_impedance_plusoneV - np.imag(funcdata12))/SD_imaginary_tot)**2/np.imag(funcdata12))
chi_square_sum12 = np.sum(chi_square_real12) + np.sum(chi_square_imag12)
# EECM C --> inhomogeneous TLM
popt2_2, pcov2_2 = curve_fit(inhomogeneous, mean_frequency_plusoneV, mean_impedance_plusoneV, p0=[200, 0.3, 50, 20.0],
method='lm')
perr2_2 = np.sqrt(np.diag(pcov2_2))
R1_opt22, C1_opt22, R2_opt22, C2_opt22 = popt2_2
funcdata22 = inhomogeneous(mean_frequency_plusoneV, R1_opt22, C1_opt22, R2_opt22, C2_opt22)
chi_square_real22 = abs(((mean_real_impedance_plusoneV - np.real(funcdata22))/SD_real_tot)**2/np.real(funcdata22))
chi_square_imag22 = abs(((mean_imaginary_impedance_plusoneV - np.imag(funcdata22))/SD_imaginary_tot)**2/np.imag(funcdata22))
chi_square_sum22 = np.sum(chi_square_real22) + np.sum(chi_square_imag22)
# EECM D --> TLM with holes
popt3_2, pcov3_2 = curve_fit(holeTLM, mean_frequency_plusoneV, mean_impedance_plusoneV, p0=[250, 1.5, 200], method='lm')
perr3_2 = np.sqrt(np.diag(pcov3_2))
R_opt32, C_opt32, R_M_opt32 = popt3_2
funcdata32 = holeTLM(mean_frequency_plusoneV, R_opt32, C_opt32, R_M_opt32)
```

```

chi_square_real32 = abs(((mean_real_impedance_plusoneV - np.real(funcdata32))/SD_real_tot)**2/np.real(funcdata32))
chi_square_imag32 = abs(((mean_imaginary_impedance_plusoneV - np.imag(funcdata32))/SD_imaginary_tot)**2/np.imag(funcdata32))
chi_square_sum32 = np.sum(chi_square_real32) + np.sum(chi_square_imag32)
# EECM E --> inhomogeneous TLM with holes
popt4_2, pcov4_2 = curve_fit(inhomogeneousHole, mean_frequency_plusoneV, mean_impedance_plusoneV, p0=[200, 0.3, 60, 20.0, 200],
method='lm')
perr4_2 = np.sqrt(np.diag(pcov4_2))
R1_opt42, C1_opt42, R2_opt42, C2_opt42, R_M_opt42 = popt4_2
funcdata42 = inhomogeneousHole(mean_frequency_plusoneV, R1_opt42, C1_opt42, R2_opt42, C2_opt42, R_M_opt42)
chi_square_real42 = abs(((mean_real_impedance_plusoneV - np.real(funcdata42))/SD_real_tot)**2/np.real(funcdata42))
chi_square_imag42 = abs(((mean_imaginary_impedance_plusoneV - np.imag(funcdata42))/SD_imaginary_tot)**2/np.imag(funcdata42))
chi_square_sum42 = np.sum(chi_square_real42) + np.sum(chi_square_imag42)
# EECM A --> R//C-circuit
popt5_2, pcov5_2 = curve_fit(R_C_Circuit, mean_frequency_plusoneV, mean_impedance_plusoneV, p0=[100, 1.0], method='lm')
perr5_2 = np.sqrt(np.diag(pcov5_2))
R_opt52, C_opt52 = popt5_2
funcdata52 = R_C_Circuit(mean_frequency_plusoneV, R_opt52, C_opt52)
chi_square_real52 = abs(((mean_real_impedance_plusoneV - np.real(funcdata52))/SD_real_tot)**2/np.real(funcdata52))
chi_square_imag52 = abs(((mean_imaginary_impedance_plusoneV - np.imag(funcdata52))/SD_imaginary_tot)**2/np.imag(funcdata52))
chi_square_sum52 = np.sum(chi_square_real52) + np.sum(chi_square_imag52)
#####
# Fit the impedance equations of the EECMs through the EIS datapoint of Uncharged CME with 0.0V
R_s = 59
# EECM B --> TLM
popt1_3, pcov1_3 = curve_fit(TLM, frequency8, impedance8, p0=[160, 1.0], method='lm')
perr1_3 = np.sqrt(np.diag(pcov1_3))
R_opt13, C_opt13 = popt1_3
funcdata13 = TLM(frequency8, R_opt13, C_opt13)
chi_square_real13 = abs(((real_impedance8 - np.real(funcdata13))/SD_real_tot)**2/np.real(funcdata13))
chi_square_imag13 = abs(((imaginary_impedance8 - np.imag(funcdata13))/SD_imaginary_tot)**2/np.imag(funcdata13))
chi_square_sum13 = np.sum(chi_square_real13) + np.sum(chi_square_imag13)
# EECM C --> inhomogeneous TLM
popt2_3, pcov2_3 = curve_fit(inhomogeneous, frequency8, impedance8, p0=[150, 1.0, 50, 0.5], method='lm')
perr2_3 = np.sqrt(np.diag(pcov2_3))
R1_opt23, C1_opt23, R2_opt23, C2_opt23 = popt2_3
funcdata23 = inhomogeneous(frequency8, R1_opt23, C1_opt23, R2_opt23, C2_opt23)
chi_square_real23 = abs(((real_impedance8 - np.real(funcdata23))/SD_real_tot)**2/np.real(funcdata23))
chi_square_imag23 = abs(((imaginary_impedance8 - np.imag(funcdata23))/SD_imaginary_tot)**2/np.imag(funcdata23))
chi_square_sum23 = np.sum(chi_square_real23) + np.sum(chi_square_imag23)
# EECM D --> TLM with holes
popt3_3, pcov3_3 = curve_fit(holeTLM, frequency8, impedance8, p0=[300, 1.0, 500], method='lm')
perr3_3 = np.sqrt(np.diag(pcov3_3))
R_opt33, C_opt33, R_M_opt33 = popt3_3
funcdata33 = holeTLM(frequency8, R_opt33, C_opt33, R_M_opt33)
chi_square_real33 = abs(((real_impedance8 - np.real(funcdata33))/SD_real_tot)**2/np.real(funcdata33))
chi_square_imag33 = abs(((imaginary_impedance8 - np.imag(funcdata33))/SD_imaginary_tot)**2/np.imag(funcdata33))
chi_square_sum33 = np.sum(chi_square_real33) + np.sum(chi_square_imag33)
# EECM E --> inhomogeneous TLM with holes
popt4_3, pcov4_3 = curve_fit(inhomogeneousHole, frequency8, impedance8, p0=[300, 1.0, 50, 0.5, 600], method='lm')
perr4_3 = np.sqrt(np.diag(pcov4_3))
R1_opt43, C1_opt43, R2_opt43, C2_opt43, R_M_opt43 = popt4_3
funcdata43 = inhomogeneousHole(frequency8, R1_opt43, C1_opt43, R2_opt43, C2_opt43, R_M_opt43)
chi_square_real43 = abs(((real_impedance8 - np.real(funcdata43))/SD_real_tot)**2/np.real(funcdata43))
chi_square_imag43 = abs(((imaginary_impedance8 - np.imag(funcdata43))/SD_imaginary_tot)**2/np.imag(funcdata43))
chi_square_sum43 = np.sum(chi_square_real43) + np.sum(chi_square_imag43)
# EECM A --> R//C-circuit
popt5_3, pcov5_3 = curve_fit(R_C_Circuit, frequency8, impedance8, p0=[160, 1.0], method='lm')
perr5_3 = np.sqrt(np.diag(pcov5_3))
R_opt53, C_opt53 = popt5_3
funcdata53 = R_C_Circuit(frequency8, R_opt53, C_opt53)
chi_square_real53 = abs(((real_impedance8 - np.real(funcdata53))/SD_real_tot)**2/np.real(funcdata53))
chi_square_imag53 = abs(((imaginary_impedance8 - np.imag(funcdata53))/SD_imaginary_tot)**2/np.imag(funcdata53))
chi_square_sum53 = np.sum(chi_square_real53) + np.sum(chi_square_imag53)
#####
# Plot the Nyquist plot
fig, ax = plt.subplots()
ax.plot(mean_real_impedance_plusoneV, -mean_imaginary_impedance_plusoneV, 'P', color='r', label='Charge +1.0V')
# ax.plot(real_impedance10, -imaginary_impedance10, 'P', color='r', label='Charge +1.0V')
# ax.plot(real_impedance12, -imaginary_impedance12, '+', color='r', label='Charge +1.0V')
# ax.plot(np.real(funcdata12), -np.imag(funcdata12), 'r', label='TLM: Charge +1.0V')
# ax.plot(np.real(funcdata22), -np.imag(funcdata22), 'y', label='EECM B')

```

```

# ax.plot(np.real(funcdata32), -np.imag(funcdata32), 'g', label='EECM C')
# ax.plot(np.real(funcdata42), -np.imag(funcdata42), 'r', label='EECM D')
# ax.plot(np.real(funcdata52), -np.imag(funcdata52), 'm', label='EECM E')
# ax.plot(mean_real_impedance, -mean_imaginary_impedance, '--', color='k', label='No Charge')
ax.plot(real_impedance8, -imaginary_impedance8, 'o', color='grey', label='No Charge')
# ax.plot(np.real(funcdata13), -np.imag(funcdata13), 'grey', label='TLM: No Charge')
# ax.plot(np.real(funcdata23), -np.imag(funcdata23), 'y', label='EECM B')
# ax.plot(np.real(funcdata33), -np.imag(funcdata33), 'g', label='EECM C')
# ax.plot(np.real(funcdata43), -np.imag(funcdata43), 'r', label='EECM D')
# ax.plot(np.real(funcdata53), -np.imag(funcdata53), 'm', label='EECM E')
ax.plot(mean_real_impedance_minoneV, -mean_imaginary_impedance_minoneV, '*', color='b', label='Charge -1.0V')
# ax.plot(real_impedance9, -imaginary_impedance9, '*', color='b', label='Charge -1.0V')
# ax.plot(real_impedance11, -imaginary_impedance11, '.', color='b', label='Charge -1.0V')
# ax.plot(np.real(funcdata11), -np.imag(funcdata11), 'b', label='TLM: Charge -1.0V')
# ax.plot(np.real(funcdata21), -np.imag(funcdata21), 'y', label='EECM B')
# ax.plot(np.real(funcdata31), -np.imag(funcdata31), 'g', label='EECM C')
# ax.plot(np.real(funcdata41), -np.imag(funcdata41), 'r', label='EECM D')
# ax.plot(np.real(funcdata51), -np.imag(funcdata51), 'm', label='EECM E')
# ax.plot(np.real(upper_mean_impedance), -np.imag(upper_mean_impedance), '-', color='k', label='upper')
# ax.plot(np.real(lower_mean_impedance), -np.imag(lower_mean_impedance), '-', color='k', label='lower')
# ax.plot(real_impedance1, -imaginary_impedance1, '*', color='k', label='0.0V nr.1')
# ax.plot(real_impedance2, -imaginary_impedance2, '+', color='k', label='0.0V nr.2')
# ax.plot(real_impedance3, -imaginary_impedance3, 'x', color='k', label='0.0V nr.3')
# ax.plot(real_impedance4, -imaginary_impedance4, '.', color='k', label='0.0V nr.4')
# ax.plot(real_impedance5, -imaginary_impedance5, '*', color='k', label='0.0V nr.5')
# ax.plot(real_impedance6, -imaginary_impedance6, '+', color='k', label='0.0V nr.6')
# ax.plot(real_impedance7, -imaginary_impedance7, 'x', color='k', label='0.0V nr.7')
# ax.plot(real_impedance8, -imaginary_impedance8, '.', color='k', label='0.0V nr.8')
ax.set_title('Nyquist Diagram of CME with Activated Carbon')
ax.set_xlabel('Re(Z) [ + r$\\Omega$ + $\\Scm^2$ ]')
ax.set_ylabel('Im(Z) [ + r$\\Omega$ + $\\Scm^2$ ]')
ax.legend()
plt.gca().set_aspect('equal', adjustable='box') # Set aspect ratio to 1:1
ax.grid(True, which='both', linestyle='--')
plt.xlim(0, 260)
plt.ylim(-130, 130)
plt.show()
# Plot the Bode magnitude plot of the impedance
fig, ax = plt.subplots()
# ax.plot(frequency10, magnitude_impedance10, 'P', color='r', label='Charge +1.0V')
# ax.plot(frequency12, magnitude_impedance12, '+', color='r', label='Charge +1.0V')
ax.plot(mean_frequency_plusoneV, mean_magnitude_impedance_plusoneV, 'P', color='r', label='Charge +1.0V')
# ax.plot(mean_frequency, mean_magnitude_impedance, '--', color='k', label='No Charge')
ax.plot(frequency8, magnitude_impedance8, 'o', color='grey', label='No Charge')
ax.plot(mean_frequency_minoneV, mean_magnitude_impedance_minoneV, '*', color='b', label='Charge -1.0V')
# ax.plot(frequency9, magnitude_impedance9, '*', color='b', label='Charge -1.0V')
# ax.plot(frequency11, magnitude_impedance11, '.', color='b', label='Charge -1.0V')
# ax.plot(mean_frequency_minoneV, np.sqrt(np.real(funcdata11)**2+np.imag(funcdata11)**2), 'b', label='TLM: Charge -1.0V')
# ax.plot(mean_frequency_minoneV, np.sqrt(np.real(funcdata21)**2+np.imag(funcdata21)**2), 'y', label='Inhomogeneous TLM')
# ax.plot(mean_frequency_minoneV, np.sqrt(np.real(funcdata31)**2+np.imag(funcdata31)**2), 'g', label='TLM with holes')
# ax.plot(mean_frequency_minoneV, np.sqrt(np.real(funcdata41)**2+np.imag(funcdata41)**2), 'r', label='Inhomogeneous TLM with holes')
# ax.plot(mean_frequency_minoneV, np.sqrt(np.real(funcdata51)**2+np.imag(funcdata51)**2), 'm', label='R//C-circuit')
# ax.plot(mean_frequency_plusoneV, np.sqrt(np.real(funcdata12)**2+np.imag(funcdata12)**2), 'r', label='TLM: Charge +1.0V')
# ax.plot(mean_frequency_plusoneV, np.sqrt(np.real(funcdata22)**2+np.imag(funcdata22)**2), 'y', label='Inhomogeneous TLM')
# ax.plot(mean_frequency_plusoneV, np.sqrt(np.real(funcdata32)**2+np.imag(funcdata32)**2), 'g', label='TLM with holes')
# ax.plot(mean_frequency_plusoneV, np.sqrt(np.real(funcdata42)**2+np.imag(funcdata42)**2), 'r', label='Inhomogeneous TLM with holes')
# ax.plot(mean_frequency_plusoneV, np.sqrt(np.real(funcdata52)**2+np.imag(funcdata52)**2), 'm', label='R//C-circuit')
# ax.plot(frequency8, np.sqrt(np.real(funcdata13)**2+np.imag(funcdata13)**2), 'k', label='TLM: No Charge')
# ax.plot(frequency8, np.sqrt(np.real(funcdata23)**2+np.imag(funcdata23)**2), 'y', label='Inhomogeneous TLM')
# ax.plot(frequency8, np.sqrt(np.real(funcdata33)**2+np.imag(funcdata33)**2), 'g', label='TLM with holes')
# ax.plot(frequency8, np.sqrt(np.real(funcdata43)**2+np.imag(funcdata43)**2), 'r', label='Inhomogeneous TLM with holes')
# ax.plot(frequency8, np.sqrt(np.real(funcdata53)**2+np.imag(funcdata53)**2), 'm', label='R//C-circuit')
ax.set_xscale('log')
ax.set_yscale('log')
ax.set_title('Bode magnitude plot of CME with Activated Carbon')
ax.set_xlabel('Frequency [Hz]')
ax.set_ylabel('|Z| [ + r$\\Omega$ + $\\Scm^2$ ]')
ax.legend()
ax.grid(True, which='both', linestyle='--')

```

```

plt.xlim(1e-3, 1e5)
plt.ylim(1e1, 1e4)
plt.show()
# Plot the Bode phase angle plot of the impedance
fig, ax = plt.subplots()
ax.plot(mean_frequency_plusoneV, -mean_phase_angle_plusoneV, 'P', color='r', label='Charge +1.0V')
# ax.plot(frequency10, -phase_angle10, 'P', color='r', label='Charge +1.0V')
# ax.plot(frequency12, -phase_angle12, '+', color='r', label='Charge +1.0V')
# ax.plot(mean_frequency, -mean_phase_angle, '--', color='k', label='No Charge')
ax.plot(frequency8, -phase_angle8, 'o', color='grey', label='No Charge')
ax.plot(mean_frequency_minoneV, -mean_phase_angle_minoneV, '*', color='b', label='Charge -1.0V')
# ax.plot(frequency9, -phase_angle9, '*', color='b', label='Charge -1.0V')
# ax.plot(frequency11, -phase_angle11, '.', color='b', label='Charge -1.0V')
# ax.fill_between(mean_frequency, upper_mean_phase_angle, lower_mean_phase_angle, alpha=0.20, facecolor='k')
# ax.plot(mean_frequency_plusoneV, -np.angle(funcdata12, deg=True), 'r', label='TLM: Charge +1.0V')
# ax.plot(mean_frequency_plusoneV, -np.angle(funcdata22, deg=True), 'y', label='Inhomogeneous TLM')
# ax.plot(mean_frequency_plusoneV, -np.angle(funcdata32, deg=True), 'g', label='TLM with holes')
# ax.plot(mean_frequency_plusoneV, -np.angle(funcdata42, deg=True), 'r', label='Inhomogeneous TLM with holes')
# ax.plot(mean_frequency_plusoneV, -np.angle(funcdata52, deg=True), 'm', label='R//C-circuit')
# ax.plot(frequency8, -np.angle(funcdata13, deg=True), 'k', label='TLM: No Charge')
# ax.plot(frequency8, -np.angle(funcdata23, deg=True), 'y', label='Inhomogeneous TLM')
# ax.plot(frequency8, -np.angle(funcdata33, deg=True), 'g', label='TLM with holes')
# ax.plot(frequency8, -np.angle(funcdata43, deg=True), 'r', label='Inhomogeneous TLM with holes')
# ax.plot(frequency8, -np.angle(funcdata13, deg=True), 'm', label='R//C-circuit')
# ax.plot(mean_frequency_minoneV, -np.angle(funcdata11, deg=True), 'b', label='TLM: Charge -1.0V')
# ax.plot(mean_frequency_minoneV, -np.angle(funcdata21, deg=True), 'y', label='Inhomogeneous TLM')
# ax.plot(mean_frequency_minoneV, -np.angle(funcdata31, deg=True), 'g', label='TLM with holes')
# ax.plot(mean_frequency_minoneV, -np.angle(funcdata41, deg=True), 'r', label='Inhomogeneous TLM with holes')
# ax.plot(mean_frequency_minoneV, -np.angle(funcdata51, deg=True), 'm', label='R//C-circuit')
ax.set_xscale('log')
ax.set_title('Bode phase plot of CME with Activated Carbon')
ax.set_xlabel('Frequency [Hz]')
ax.set_ylabel('Phase angle(Z) [°]')
ax.legend()
ax.grid(True, which='both', linestyle='--')
plt.xlim(1e-3, 1e5)
plt.ylim(-20, 90)
plt.show()
#####
print("")
print("      "+ "\033[4m" +"The values for +1.0V:" + "\033[0;0m")
print("EECM A --> The optimal values for TLM are: R is", R_opt12, "Ohm*cm^2, and C is", C_opt12, "F/cm^2.")
print("  The goodness of the fit for TLM is:", chi_square_sum12*10**3, "* 10^-3")
print("")
print("EECM B --> The optimal values for inhomogeneous TLM are: R1 is", R1_opt22, "Ohm*cm^2, C1 is", C1_opt22, "F/cm^2, R1 is",
R2_opt22, "Ohm*cm^2, and C2 is", C2_opt22, "F/cm^2.")
print("  The goodness of the fit for inhomogeneous TLM is:", chi_square_sum22*10**3, "* 10^-3")
print("")
print("EECM C --> The optimal values for TLM with holes are: R1 is", R_opt32, "Ohm*cm^2, C1 is", C_opt32, "F/cm^2, R_M is", R_M_opt32,
"Ohm*cm^2.")
print("  The goodness of the fit for TLM with holes is:", chi_square_sum32*10**3, "* 10^-3")
print("")
print("EECM D --> The optimal values for inhomogeneous TLM with holes are: R1 is", R1_opt42, "Ohm*cm^2, C1 is", C1_opt42, "F, R2 is",
R2_opt42, "Ohm*cm^2, C2 is", C2_opt42, "F/cm^2, and R_M is", R_M_opt42, "Ohm*cm^2.")
print("  The goodness of the fit for inhomogeneous TLM with holes is:", chi_square_sum42*10**3, "* 10^-3")
print("")
print("EECM E --> The optimal values for R//C-circuit are: R is", R_opt52, "Ohm*cm^2, and C is", C_opt52, "F/cm^2.")
print("  The goodness of the fit for R//C-circuit is:", chi_square_sum52*10**3, "* 10^-3")
print("")
print("")
print("      "+ "\033[4m" +"The values for No Charge:" + "\033[0;0m")
print("EECM A --> The optimal values for TLM are: R is", R_opt13, "Ohm*cm^2, and C is", C_opt13, "F/cm^2.")
print("  The goodness of the fit for TLM is:", chi_square_sum13*10**3, "* 10^-3")
print("")
print("EECM B --> The optimal values for inhomogeneous TLM are: R1 is", R1_opt23, "Ohm*cm^2, C1 is", C1_opt23, "F/cm^2, R1 is",
R2_opt23, "Ohm*cm^2, and C2 is", C2_opt23, "F/cm^2.")
print("  The goodness of the fit for inhomogeneous TLM is:", chi_square_sum23*10**3, "* 10^-3")
print("")
print("EECM C --> The optimal values for TLM with holes are: R1 is", R_opt33, "Ohm*cm^2, C1 is", C_opt33, "F/cm^2, R_M is", R_M_opt33,
"Ohm*cm^2.")
print("  The goodness of the fit for TLM with holes is:", chi_square_sum33*10**3, "* 10^-3")

```



```

print("
")
print("EECM D --> The optimal values for inhomogeneous TLM with holes are: R1 is", R1_opt43, "Ohm*cm^2, C1 is", C1_opt43, "F/cm^2,
R2 is", R2_opt43, "Ohm*cm^2, C2 is", C2_opt43, "F/cm^2, and R_M is", R_M_opt43, "Ohm*cm^2.")
print(" The goodness of the fit for inhomogeneous TLM with holes is:", chi_square_sum43*10**3, "* 10^-3")
print("
")
print("EECM E --> The optimal values for R//C-circuit are: R is", R_opt53, "Ohm*cm^2, and C is", C_opt53, "F/cm^2.")
print(" The goodness of the fit for R//C-circuit is:", chi_square_sum53*10**3, "* 10^-3")
print("
")
print("
")
print(" "+ '\033[4m' +"The values for -1.0V:" + "\033[0;0m")
print("EECM A --> The optimal values for TLM are: R is", R_opt11, "Ohm*cm^2, and C is", C_opt11, "F/cm^2.")
print(" The goodness of the fit for TLM is:", chi_square_sum11*10**3, "* 10^-3")
print("
")
print("EECM B --> The optimal values for inhomogeneous TLM are: R1 is", R1_opt21, "Ohm*cm^2, C1 is", C1_opt21, "F/cm^2, R1 is",
R2_opt21, "Ohm*cm^2, and C2 is", C2_opt21, "F/cm^2.")
print(" The goodness of the fit for inhomogeneous TLM is:", chi_square_sum21*10**3, "* 10^-3")
print("
")
print("EECM C --> The optimal values for TLM with holes are: R1 is", R_opt31, "Ohm*cm^2, C1 is", C_opt31, "F/cm^2, R_M is", R_M_opt31,
"Ohm*cm^2.")
print(" The goodness of the fit for TLM with holes is:", chi_square_sum31*10**3, "* 10^-3")
print("
")
print("EECM D --> The optimal values for inhomogeneous TLM with holes are: R1 is", R1_opt41, "Ohm*cm^2, C1 is", C1_opt41, "F/cm^2,
R2 is", R2_opt41, "Ohm*cm^2, C2 is", C2_opt41, "F, and R_M is", R_M_opt41, "Ohm*cm^2.")
print(" The goodness of the fit for inhomogeneous TLM with holes is:", chi_square_sum41*10**3, "* 10^-3")
print("
")
print("EECM E --> The optimal values for R//C-circuit are: R is", R_opt51, "Ohm*cm^2, and C is", C_opt51, "F/cm^2.")
print(" The goodness of the fit for R//C-circuit is:", chi_square_sum51*10**3, "* 10^-3")
print("
")

```

Appendix E: EIS measurement Procedure for the CME meter

E.1 Procedure for placing the CME inside the CME-cell

1. Remove the crocodile clamps from the titanium current collectors after the EIS measurement is done.
2. Turn the hotplate stirrer on *OFF* by turning the temperature knob counterclockwise until you hear a clicking sound. Remove the SCT2 temperature probe from the beaker.
3. Turn the pump off by pressing the *play/stop* button. Remove the tube where the electrolyte flows into the tube.
4. Remove the CME-cell from the beaker by first removing silicone pink hood from the beaker and then removing the hood included with the CME-cell and other tube from the beaker.
5. Put the SCT2 temperature probe back into the beaker with electrolyte and turn the temperature knob on the hotplate stirrer clockwise until you hear a clicking sound to turn the temperature sensor on. The electrolyte temperature does not drop when the CME is replaced.
6. Remove the tubes from the CME-cell by loosening the two adapters where the tube is connected and the tube stop.
7. Remove the PMMA rods from the CME-cell.
8. Open the CME-cell by losing the four M6 bolts. Pull the PMMA plates from each other. The contents inside the cell fall on the desk.
9. Replace the old CMEs with new CMEs. Put the CME-cell back together. Place a 4mm pons in the M5 hole in one of the PMMA plates and stack the components in the according sequence: PMMA plate, rubber o-ring, titanium current collector for end electrodes, end electrode, spacer, titanium current collector for CMEs, CME, spacer, spacer, CME, titanium current collector for CMEs, spacer, end electrodes, titanium current collector for end electrodes, rubber o-ring, PMMA plate.
10. While leaving the pons inside the cell, tighten the four M6 bolts “loosely” and place the PMMA rods back.
11. Tighten the M6 bolts until the index finger could not tighten the bolts anymore.
12. Place the tubes back on the CME-cell by tightening the two M5 adapters.
13. Place the hood on the CME-cell by inserting the titanium current collector strips and PMMA rods inside the 3D printed entrances.
14. Turn the hotplate stirrer on *OFF* by turning the left knob counterclockwise until a clicking sound is heard. Remove the SCT2 temperature probe from the beaker.
15. Place the hood include with CME-cell and tube inside the beaker and place the hood over the edge of the beaker.
16. Put the SCT2 temperature probe through entrance of the hood into the beaker and turn the temperature knob on the hotplate stirrer to the clockwise to turn the temperature sensor on.
17. Place the tube, where the electrolyte flows into the tube, back in the electrolyte in the beaker via the 3D printed entrance in the hood.
18. (Optional) and place the Ag/AgCl reference electrode inside the beaker through the 3D printed entrance in the hood.
19. Set the temperature in the electrolyte by setting the temperature with the SCT2 temperature sensor, turn the mixing button until the desired mixing rate is achieved, and change the rpm on the Lead Fluid pump until the desired flowrate is reached.

E.2 Procedure for performing EIS measurement on CME sample

- Place the clamps of the BioLogic® potentiostat on the titanium current collectors. The end electrodes get P1 and P2, while the CMEs get the sensing probes S1 t/m S3. Table 12 shows the connection between the probe and electrode for the 4-point and 2-point measurements.
- Turn the BioLogic® potentiostat on. Open the EC-Lab® software on the computer. Click on the plus sign and choose *potentiostatic electrochemical impedance spectroscopy (PEIS)*. Now fill the specification in according to the results of TEST 2 in the *Parameters Settings* (see Figure 71):
 - Click at *Excitation signal mode* for the option *Multi sine*
 - Set the potential at 0V vs E_{OC} .
 - The *drift correction* box must be checked to get EIS data which generate a smooth line.
 - Set the applied frequency range between 10^5 and 10^{-3} ($f_i = 100.0$ kHz and $f_f = 1.000$ mHz).
 - Set the *sinus amplitude* at 10mV.
 - Keep the E_{range} at $-5V; 5V$
 - For VSP-300 systems, the *bandwidth* must be set on 9Bd.
 - Other specifications should not be changed because they have no influence on the generated impedance data
- Click on *Safety/Advanced settings* and uncheck the checkbox at *EIS quality indicators*. Click on *play*.
- Give the file a name and save it in a specified folder. Click on *OK*.
- The EIS measurement starts. The colour on the bottom of the screen is pink during the EIS measurement. The measurement is done when the bottom of the screen turns white.

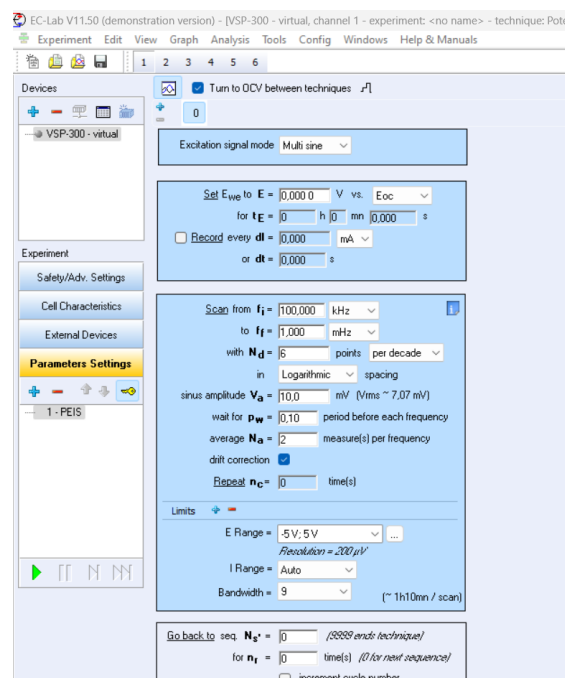


Figure 71: Specifications of the *Parameters Setting* to perform an EIS measurement at a frequency range of 100kHz to 1.00mHz. Screenshot of the EC-Lab® programme on the computer.







Table 12: The connection of the cables clamps of the BioLogic® VSP-300 potentiostat on the different electrodes in the CME-cell.

Cable clamp potentiostat	Connection for 2-point measurement (Standard connection)	Connection for 4-point measurement (Standard connection)
P1	CME [1]	End electrode [1]
P2	CME [2]	End electrode [2]
S1	CME [1]	CME [1]
S2	CME [2]	CME [2]
S3	CME [2]	CME [2]
Ground	Not connected	Not connected





E.3 Procedure for converting the EIS data to EIS graphs

1. The potentiostat measures the EIS data of the system.
2. The EC-Lab® file, with the EIS data, is transported from the PC of the potentiostat to the personal laptop. This is done by inserting the EC-Lab® file in the attachment of an email which is send to the person itself. The email is opened and the file is stored on the laptop.
3. The EIS data in the EC-Lab® file is copied from the EC-Lab® file to an Excel file. Only the following 7 columns are required: frequency, real impedance, negative imaginary impedance, impedance magnitude, negative impedance phase angle, real capacitance, and imaginary capacitance.
4. Copy the name of the Excel file in the Python file (Appendix D) and run the Python script.
5. The Python script generates the five impedance plots, which could be copied and placed inside the Report for data analysis.

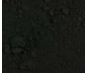
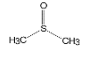


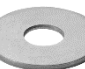





Appendix F: Bill of Materials

#	Name component	Company	Product number	Picture	Amount needed	Amount Ordered	Price per piece	Price	Website link	Ordered?
Potentiostat system										
1	Voltcraft laboratory power supply ps-2403d	Conrad.com	Item no.: 1629372		1	0	€ 430,00	€ -	https://www.conrad.com/p/voltcraft-vlp-2403-usb-bench-psu-adjustable-voltage-0-40-v-001-3-a-273-w-ovp-no-of-outputs-4-x-1629372	No
2	Biologic VSP-300 multichannel potentiostat	Biologic	Power requirement: 300 W		1	0	€ 10.000,00	€ -	https://www.biologic.net/products/vsp-300/	No
Pump										
3	BT100S Basic Variable-Speed Peristaltic Pump	alibaba.com	SKU: BT100S		1	0	€ 500,00	€ -	https://www.alibaba.com/product-detail/Economic-Time-Dispensing-Peristaltic-Pump-BT100S_1600134593661.html?spm=a2700.details.0.0.3208301aNA3v9F	No
4	Siliconen slang transparant 8x14mm	rubbermagazijn.nl	Artikelnummer: 98000814		1	0	€ 7,50	€ -	https://www.rubbermagazijn.nl/siliconen-slang-transparant-8x14mm-l-50m_transparant_14784.html	No
5	Verloopstuk 4mm naar 10mm	IWS 3ME	SLA printed on standard speed		2	0	€ -	€ -	https://www.tudelft.nl/studenten/faculteiten/3me-studentenportal/voorzieningen/werkplaat-sen-en-labs/iws-aws	No
6	Siliconen slang transparant 2x4mm	rubbermagazijn.nl	Artikelnummer: 98000204		2 meter	5	€ 5,81	€ 29,05	https://www.rubbermagazijn.nl/siliconen-slang-transparant-2x4mm_transparant_14761.html	Yes
CME-cell										
5	Plexiglas helder - dikte 10 mm	plexiglasstunter.nl	18cmx10cmx 10mm		2	2	€ 2,00	€ 4,00	https://plexiglasstunter.nl/plexiglas-gegoten-glashelder	Yes
6	Plexiglas Rondstaf Helder 2 Meter - diameter 10 mm	plexiglasstunter.nl	diameter 10mm x 2m		320m	1	€ 12,50	€ 12,50	https://plexiglasstunter.nl/plexiglas-rondstaf-helder-1-meter	Yes
7	Ag/AgCl (3M NaCl) Reference Electrode	sigma aldrich	SKU: BASMF2052-1EA		1	1	€ 121,00	€ 121,00	https://www.sigmaaldrich.com/NL/en/product/aldrich/basmf2052	Yes
8	Titaniumband Grade 1 0,1-0,5x100 mm Titanium Grade 1 3.7025 Titaniumfolie 0,1-50 meter	Evek GmbH	grootte 0,05 mm & 100mm, lengte 1 meter (gr-1)		1	1	€ 95,40	€ 95,40	https://eveks.nl/titanium/706-titaniumband-grade-1-01-05x100-mm-titanium-grade-1-37025-titaniumfolie-01-50-meter.html	Yes
9	Normaplast T-stuk 90°, 3x slangtule, 4 mm	Wildkamp.nl	Artikelnr. 610712		1	0	€ 1,55	€ -	https://www.wildkamp.nl/product/normaplast-t-stuk-90-3x-slangtule-4-mm/610712	No
10	slangpilaar 4 x ø2.5mm, M5 voor nylon	Eriks	Artikelnummer: M-SAN-4		3	10	€ 1,03	€ 10,30	https://www.pneumatiek.nl/pneumatiek/smc-pneumatics/koppeling/fittingen/miniatur/slangpilaar-4-x-o2-5mm-m5/	Yes
11	Benson Krimpkous - Krimpsok 127 delig Zwart	bol.com	EAN: 8718026587857		1	0	€ 6,89	€ -	https://www.bol.com/nl/nl/p/benson-krimpkous-krimpsok-127-delig-zwart/9200000041262169/7b1tgh=ua1qwBHG48sEAVflaFL9w.2_56.57.ProductTitle	No







Appendix F: Bill of Materials

12	RS PRO Nitrile Rubber O-Ring, 4mm Bore, 5mm Outer Diameter	RS-online	RS-stocknr.: 196-5361		2	50	€ 1,05	€ 52,45	https://nl.rs-online.com/web/p/gaskets-o-rings/1965361	Yes
13	Festo PBT Blanking Plug for 4mm	RS-online	RS-stocknr.: 121-6154		1	10	€ 1,26	€ 12,60	https://nl.rs-online.com/web/p/pneumatic-fitting-accessories/1216154?cm_mmc=NL-PLA-DS3A-_-google-_-PLA_NL_NL_Pneumatics_%26_Hydraulics_Whoop-_-_(NL:Whoop!)+Pneumatic+Fitting+Accessories-_-1216154&matchtype=&pla=308255531427&gclid=CjwKCAjwp6CkChB_EiwAlQVyxTMMVW9lZvyyXbsOB0HZwlQGZVBjv4PZ_-J1dqpqO8ZcrwRcM2AcxoC0qMQAvD_BwE&gclid=aw.ds	Yes
Reservoir										
13	Bekerglas 3000 ml laag model Ø 152 mm, h=210 mm	BOOM	Artikelnummer: 21106680 Merk: Duran		1	1	€ 49,15	€ 49,15	https://www.boomlab.nl/product/21106680+duran-bekerglas-3000-ml-laag-model-oe-152-mm-h-210-mm-21106680	Yes
14	Statiefklem 150 mm, gietijzer verchroomd Ø 25 mm, ronde bek	BOOM	UNSPSC Code: 30191502		2	0	€ 14,99	€ -	https://www.boomlab.nl/product/19126225+bochem-statiefklem-150-mm-gietijzer-verchroomd-oe-25-mm-ronde-bek-19126225	No
15	Accessories for Stuart Magnetic stirrers and Hotplates Type: SCT 2	Häberle	Article number: 468 2259		1	2	€ 316,90	€ 633,80	https://www.haerberle-lab.de/en/accessories-for-stuart-magnetic-stirrers-and-hotplates-type-sct-2/4682259	Yes
16	Verwarmings- en magnetische roerder SHP-200-C/S-serie Modellen met LED-display, Aluminium/siliconen gecoat, SHP-200D-S	Carl Roth	SHP-200D-S		1	0	€ 610,00	€ -	https://www.carlroth.com/be/nl/magnetische-roerder-met-verwarming/verwarmings-magnetische-roerder-shp-200-c-s-serie-modellen-met-led-display/p/cha5.1	No
17	ÖVERMÄTTVoedselbeschermer, set van 2, silicone	Ikea	Artikelnummer: 304.979.23		1	1	€ 5,99	€ 5,99	https://www.ikea.com/nl/nl/p/overmattvoedselbeschermer-set-van-2-silicone-30497923/#content	Yes
Conductivity meter										
17	EPU357 Conductivity isoPod™ with USB	eDAQ.com	EPU357		1	0	€ 685,00	€ -	https://www.edaq.com/EPU357	No
18	ET908 Flow-Thru Conductivity Electrode (93 µL)	eDAQ.com	ET908		1	0	€ 399,00	€ -	https://www.edaq.com/ET908	No
Chemicals										
19	Potassium Chloride	sigmaaldrich.com	CAS Number: 7447-40-7	KCl	1	0	€ 50,50	€ -	https://www.sigmaaldrich.com/NL/en/product/sigald/p3911	No
20	Active Carbon	sigmaaldrich.com	CAS Number: 7440-44-0	C	1	0	€ 89,10	€ -	https://www.sigmaaldrich.com/NL/en/product/sial/05105	No
21	KETJENBLACK EC-600JD Conductive Carbon Black	Nanografi Nano Technology	CAS number 1333-86-4		100g	0	€ 82,00	€ -	https://nanografi.com/microparticles/ketjenblack-ec-600jd-conductive-carbon-black/	No
22	Poly(vinylidene fluoride)	sigmaaldrich.com	CAS Number: 24937-79-9		5	0	€ 12,88	€ -	https://www.sigmaaldrich.com/NL/en/product/aldrich/182702?gclid=CjwKCAjw9J2iBhBPEiwaErwpeRt	No

Appendix F: Bill of Materials

									HiACvkCJa0WhrcZAYp46i3kW6e4cymTqI340fpF_dqZM1lft2xoCdQQAvd_BwE&gclsrc=aw.ds	
23	GRAFIET POEDER - ZWART	labshop.nl	Artikelnummer: K4771-1000		1	0	€ 14,16	€ -	https://www.labshop.nl/grafiet-poeder-zwart/?attribute_pa_gewicht=1-kg&gad=1&gclid=CjwKCAjw9I2i8h8PEiWAErwpeQGRU_VPC1KLpqp4GZMCYY2zeOew6jB9EDmRX4_A5ZqSD7NHs8sEgxoCJEUQAvd_BwE	No
24	DIMETHYLSULFOXIDE (DMSO)	labshop.nl	Artikelnummer: O1007		1	0	€ 19,95	€ -	https://www.labshop.nl/dimethylsulfoxide-dmsol/	No
Bolts and more										
24	Zeskantbout, DIN933, ISO 4017, RVS316 (A4)	rvsland.nl	Artikelnummer: 933-4-6x30_20x		4	20	€ 0,20	€ 4,04	https://rvsland.nl/ze-skantbouten-din933-rvs316	Yes
25	Mini slangkleem 7-9 mm (W1)	prolech.nl	Productcode: 2017922141615		4	0	€ 0,29	€ -	https://www.prolech.nl/webshop/ijzerwaren/slangklemmen/mini-slangklemmen/detail/1501/mini-slangklem-7-9-mm-w1.html	No
26	Sluitring 3xd M6, DIN9021, RVS316 (A4), 100 stuks	rvsland.nl	Artikelnummer: 9021-4-6.4_100x		4	100	€ 0,07	€ 6,88	https://rvsland.nl/sluitring-din9021-m6-rvs316-100stuks	Yes
27	igus GFM-1012-10 Glijlager Boordiameter 10 mm	Conrad	Artikelnummer: 1416575-8J		4	0	€ 0,43	€ -	https://www.conrad.nl/nl/p/igus-gfm-1012-10-glijlager-boordiameter-10-mm-1416575.html?utm_medium=affiliate&utm_source=tradetracker&utm_campaign=316050&utm_content=ShopForward+NL+Shopping&refresh=true	No
28	Griffon Water Afdichtingstape	gamma.nl	Productnummer: 419620		1	0	€ 3,49	€ -	https://www.gamma.nl/assortiment/griffon-water-afdelingstape/p/B419620?store=%7Bstore_code%7D&gclid=CjwKCAjw9I2i8h8PEiWAiwA_473dGtE2hwa3aqH2kLPwafSdRILDUYs_RCu09XA0B0CU2naLj_jvnW8FhoCeLsQAvd_BwE&gclsrc=aw.ds	No
29	HBM 9 Delige Penuitdrijverset 1,6 - 8,0 mm	HBM machines	Artikelnummer: 6074185		1	1	€ 6,00	€ 6,00	https://www.hbm-machines.com/nl/p/hbm-9-delige-penuitdrijverset-16-80-mm?kb=ga_pm_19587892072_&gclid=CjwKCAjw9I2i8h8PEiWATgviXLMCXD1kTnSkIEq7_LhX8zvYU3-X3QRJTeXdWwfvEiMsNc7xT_AtRoCu2MQQAvd_BwE	Yes
30	Unisex Laboratoriumjas Maat XXXL	bol.com	EAN: 8720514070666		1	1	€ 34,95	€ 34,95	https://www.bol.com/nl/p/unisex-laboratoriumjas-maat-xxxl/9300000025050495/?s2a=&bltgh=IDU8jr-e-afxSA-DufhEQ.2_31_32.33.FeatureListitem#productTitle	Yes
32	RS PRO Safety Knife with Snap-off Blade, Retractable	rs-online.nl	RS-stocknr.: 789-4600		1	0	€ 4,32	€ -	https://nl.rs-online.com/web/p/safety-knives/7894600?tp=1	No

Appendix F: Bill of Materials

33	Potassium chloride solution	sigma aldrich	SKU: 60137-250ML		1	1	€ 25,40	€ 25,40	https://www.sigmaaldrich.com/NL/en/product/sial/60137	Yes
34	RS PRO Nitrile Rubber O-Ring, 5.1mm Bore, 8.3mm Outer Diameter	RS-online	RS-stocknr.: 196-5539		3	50	€ 0,08	€ 3,75	https://nl.rs-online.com/web/p/gaskets-o-rings/1965539	Yes
35	Greisinger G1710 Temperatuurmeter - 70 - +250 °C Sensortype Pt1000	Conrad.nl	Artikelnummer: 1592162 - 8J		1	1	€ 124,99	€ 124,99	https://www.conrad.nl/nl/p/greisinger-g1710-temperatuurmeter-70-250-c-sensortype-pt1000-1592162.html?utm_source=google&utm_medium=surfaces&utm_campaign=shopping-feed&utm_content=free-google-shopping-clicks&utm_term=1592162&adcampaign=google&tid=17213980048_pla-1592162&gad=1&gclid=CjwKCAjwhdWkBhBZEiwA1bLmA24LhVAITGhhV6gU8WyDsHU0OyQtHKc_3dXhyFFpQx3tRoQxwrqjxoCr0oQAvD_BwE&refresh=true	Yes
36	Dispensing Gun, For 50 ml cartridges	struers.com	Product no.40900066		1	0	€ 110,00	€ -	https://webshop.struers.com/en/product/40900066	No
37	RepliSet-F5, 5 cartridges of 50 ml	struers.com	Product no.40900046		1	0	€ 250,00	€ -	https://webshop.struers.com/en/product/40900046	No
38	Static-mixing Nozzles, 35 pcs.	struers.com	Product no.40900088		1	0	€50,00	€ -	https://webshop.struers.com/en/product/40900088	No

Appendix G: Additional Literature - CDI and ED

G.1 Different cell architectures of CDI

Some of the current drawbacks and limitations of CDI could actually be regarded as avenues for further maturation of the technique. For example, different researchers have already shown that these limitations could be overcome by designing different CDI cell architectures, flow arrangements or electrodes [5,15,18]. Some alternative designs will be briefly described below.

G.1.1 Flow arrangements: flow-by vs flow-through

The conventional CDI cell is analogous to the flow-by (or flow-between) CDI, as depicted in Figure 72a. The potential field is perpendicular to the flow direction. When the feedwater flows through the porous electrodes, as depicted in Figure 72c, thus the potential field is parallel to the feedwater direction, then the cell is called a flow-through CDI cell [170]. Benefits over flow-by CDI cells are that the flow-through CDI cell uses a porous separator which thickness can be minimized instead of a separator for the flow-by CDI where a smaller thickness would result in a smaller feed flow [171]. Flow-through CDI cells are compacter cells and compacter cells allow for improved desalination rates and higher charge efficiencies [6]. However, larger pressures are required to push the feed water through the porous electrodes of the flow-through CDI cells. The electrodes of flow-through CDI cells additionally have larger pores than the porous electrodes of a flow-by CDI cell which results in less surface area where ions could be adsorbed [171]. The SAC of the flow-through CDI cell is thus lower than the SAC of the flow-by CDI cell.

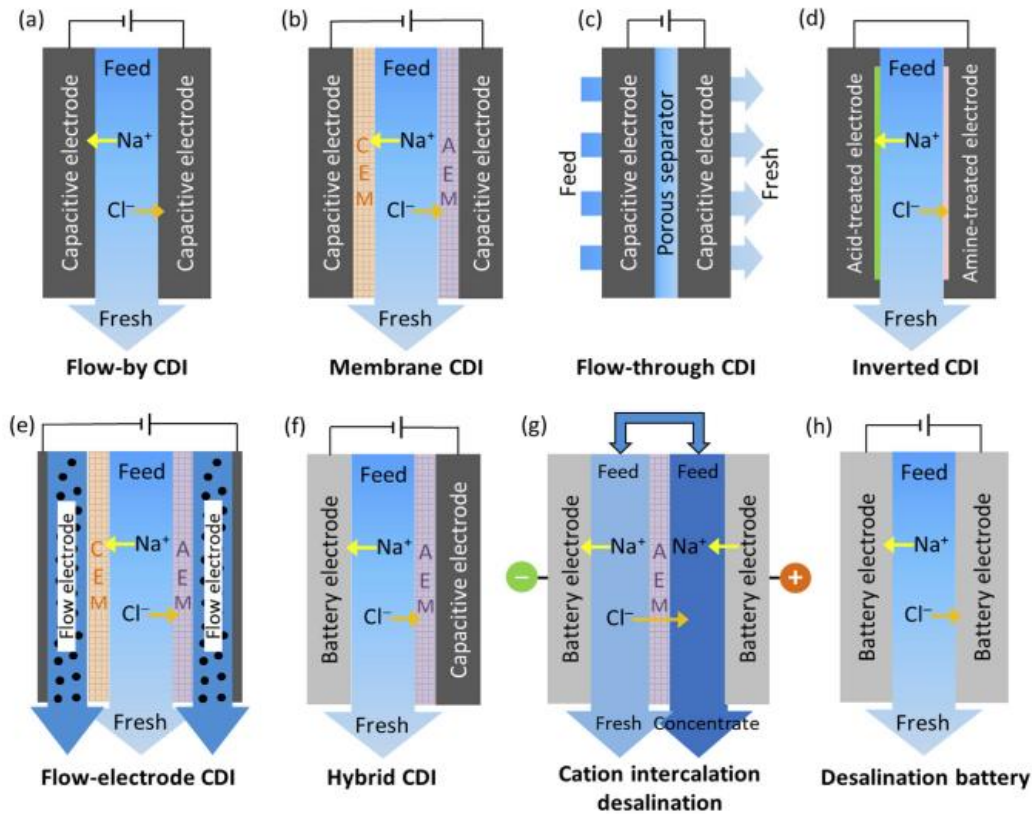


Figure 72: Cell architectures and flow arrangements of CDI systems: (a) Flow-by CDI, (b) Membrane CDI (MCDI), (c) Flow-through CDI, (d) Inverted CDI (i-CDI), (e) Flow-electrode CDI (FCDI), (f) Hybrid CDI (HCDI), (g) Cation intercalation desalination (CID), and (h) Desalination battery. Source: Tang et al. (2019) [6].

G.1.2 Cell architectures: Membrane CDI, Inverted CDI and Flow-electrode CDI

There are many developed CDI cell architectures. The most mentioned CDI cell architectures of the literature are: Membrane CDI, Inverted CDI and Flow-electrode CDI.

Membrane CDI (MCDI) is a flow-by CDI cell with ion exchange membranes in front of the porous electrodes to enhance the charge efficiency and the salt adsorption capacity, see Figure 72b [5,15]. The process of flow-by CDI and MCDI are similar, the only difference is that the ion exchange membranes block the co-ions that would be repelled by the potential field. An ion exchange membrane (IEM) is a membrane with charged ionic groups in the backbone of the material which allows for the flow of counter-ions and blocks the flow of co-ions [6]. Assuming that the ions are monovalent, i.e. having the same charge as an electron, but either positive or negative, then one electron can either be used to attract one positive charge or to repel one negative charge ion during charging of the electrode. The reverse is true for holes, i.e. the absence of an electron in the carbon backbone of the electrode. So, the addition of an IEM blocks the co-ions from moving out of the macropores of the electrode, then the energy of the electron could be used to attract a counter-ion. As a result, more counter-ions are attracted with the same amount of electrons, increasing the charge efficiency and the SAC during charging [15]. Another advantage of MCDI is that the occurrence of faradaic reactions at the electrode surfaces are decreased relative to flow-by CDI systems [18]. The degradation of the porous electrodes and the energy losses due to faradaic reactions reduces. However, because of the added ion exchange membranes, there are some mentionable drawbacks: the added ion exchange membranes are relatively expensive and have a higher electrical resistance [6].

Overall, MCDI increases the SAC and charge efficiencies while the effects of faradaic reactions are reduced relative towards flow-by CDI, however, MCDI is still a batch operation. Continuous systems are more cost-efficient than batch operating systems, and continuous systems do not require an extra

separation step which reduces the cost and energy consumption. Jeon et al. came in 2013 with a modification of the MCDI by utilizing flow electrodes: Flow-electrode CDI (FCDI) [172]. In FCDI, the static porous electrode is replaced by a slurry of activated carbon particles which flows in a separate channel. There is an anode channel and a cathode channel. The current collector is placed alongside the anode and cathode channels (See Figure 72e) [6]. When a voltage or current is applied on the current collectors, the activated carbon particles are charged. The counter-ions in the feed stream move through the IEMs towards the activated carbon particles where they are adsorbed. The greatest advantage of this system is that the MCDI cell is continuous. An additional advantage is that the continuous supply of activated carbon particles leads to a higher specific surface area which leads to a higher salt adsorption capacity than the static electrode [15].

MCDI reduces the faradaic reactions (formation of oxides) relative to CDI systems, but unfortunately, those reactions still occur. Preventing these reactions from happening is key for increasing the lifetime of the porous electrodes. Gao et al. (2015) proposed a new cell architecture: inverted CDI (i-CDI) [173]. In i-CDI, the cathode surface is charged with a positive surface charge by anion-exchanging and the anode surface is charged with a negative charge by acid-treating. The charge-discharge processes occur reversed relative to other CDI cells (see Figure 72d) [6]. When a voltage or current is applied, the cell desorbs the ions in the electrode, and during discharging, the cell adsorbs ions in the micropores of the electrode. During operation, an oxidation reaction occurs at the anode. The oxide protects the rest of the carbon material against faradaic reactions. The parasitic losses are reduced, the electrode degradation is reduced and the working voltages are much higher but at the costs of reduced ion removal capacity of the electrode which is limited by increasing anode resistances due to the oxide layer [6].

G.1.3 CDI architecture based on faradaic reactions: Hybrid CDI, Cation intercalation desalination, and Desalination battery

The previous mentioned CDI cell architectures utilize capacitive electrodes which adsorb ions in their electrical double layers (non-faradaic reactions) and not use redox reactions to chemisorb ions (faradaic reactions) onto their surface. Still, these faradaic reactions do occur which is the important cause of the degradation of the electrodes and energy losses in CDI cells [170]. So, the faradaic reactions were a point of concern for researchers until Lee et al. (2014) came to the idea to use the faradaic reactions as pseudo-capacitance to increase the total capacitance of the CDI system [174]. This novel CDI architecture is called the Hybrid CDI (HCDI) and is depicted in Figure 72f [6]. This CDI architecture has a higher capacitance by additionally allowing ions to be removed with redox reactions at one faradaic electrode, which results in a SAC almost twice as large as the SAC of conventional CDI cells [15,174]. Other cell architectures which utilize faradaic reactions are: faradaic CDI (FarCDI), Cation intercalation (CID) and Desalination battery (Figure 72g and Figure 72h) [6]. More details regarding these technologies can be found in, for example, the articles of Tang et al. (2019) or Volfkovich (2020) [6,18].

G.2 Relation between physical properties and CDI performance

The EDL theory helps understand why certain physical parameters of the electrode influence the performance of the electrode and thus the performance of the CDI system. Factors that influence the performance of the electrode, according to Jia & Zhang (2016): the nature of the electrode material, applied electrical potential and electrolyte conditions [47]. The operating parameters also influence the performance of the CDI system, which was explained in more detail in Section 2.1.2.3.

G.2.1 Nature of the electrode material

With the nature of the electrode material is meant the pore size distribution (PSD), the average pore size, and material types of the electrode [47,77].

- The average pore size and PSD determine the adsorption performance of the electrode. As explained earlier, the macropores and mesopores facilitate the transportation of ions to the micropores where the counter-ions can be adsorbed in the EDL of the micropores. Increasing the micropores in the electrode, increases the specific surface area, so more ions could be adsorbed, increasing the SAC. Still, a larger SAC does not directly mean a large ASAR. Macropores and especially mesopores should be increased to increase the diffusion of ions to the extra micropores, consequently, increasing the wettability. Thus, macro- and mesopores increase the wettability, which increases the ASAR. Finding the pore size distribution which induces a large ASAR is determined with experiments and testing of different electrode materials. Yang et al. (2002) and Noked et al. (2012) suggested that mesopores as entries of the micropores is the best pore distribution to improve both the SAC and the salt adsorption rate (ASAR) [175,176].
- Increasing micropores in the PSD increases the specific surface area of electrodes to a certain extent. Some micropores are not able to adsorb ions due to EDL overlapping. When the Debye length is much larger than the pore size, the EDLs overlap [57]. This phenomena reduces the capacity of the electrode because pores with overlapping EDLs do not contribute to the total active sites of the electrode surface because the ions simply do not fit in the pores. So, the capacity of the electrode is reduced if the pore sizes are too small. Yang et al. (2002) defined the cut-off pore size as the smallest width that contributed to the electrical double layer [175]. Fabricating electrodes with pore diameters larger than cut-off pore size or fabricating electrodes with more meso- and macropores would reduce the risk of overlapping EDLs. Also, high concentrated electrolytes have short Debye lengths that reduce the EDL thickness which reduces the amount of overlapping EDL micropores.
- The pore size of the micropores also have an effect on the charge efficiency. How smaller the pores, how larger the specific surface area, however, this could also increases the energy loss. Ions need to (partially) remove their solvation shell to enter the micropores. This process cost energy which adds to the electrical work needed to charge the micropores [177]. If, during discharging, this energy dissipates as heat, then the charge efficiency decreases. Also, if the average pore size becomes smaller than the ion radius, then the adsorption into the micropores is hindered. The SSA and thus EDL is reduced. Consequently, the pore size determines which ions are favoured for adsorption and which not. Ions with a smaller hydrated radius are more favoured to be adsorbed in smaller pore sizes, while ions with a larger hydrated radius are more prone to be adsorbed in larger pores [178]. This trait of the pore size is utilized for the selective separation of ions.

- The electrode material has a major influence on the resistance of the electrode. A dominant energy loss in CDI systems are the resistive losses due to ohmic resistances in the system. Electronic and ionic resistances can be reduced by changing the electrode material by adding respectively more electron conductive additives or active carbon powder [27]. Section 2.5 explains in more detail how the modification of the electrode material and composition changes the conductivity of the ions and electrons in the electrode.

G.2.2 Applied potential

The applied potential is an operational parameter. Higher applied potentials increases the electric charge of the electrode resulting in more active sites for the ions to be adsorbed on [40]. The ASAR increases with increasing applied potential [179]. However, the applied potential could not be increased indefinitely, because faradaic reaction will occur at the electrode surface which reduces the charge efficiency. Additionally, the capacity of the electrode convergence to a constant value, increasing the applied potential does not induce a higher SAC [40].

G.2.3 Electrolyte conditions

Electrolyte conditions, like salt type and concentration, influence the selectivity and the ionic resistances.

- As was explained for the average pore size, the type of ion in the electrolyte, especially if there are multiple ion types inside the electrolyte, also determines the ion adsorption rate [9,10]. The size of the hydration radius of the ion must be smaller than the average pore size for the ion to be adsorbed into the EDL. The average pore size and the pore size distribution determine the selectivity of ions [10]. The selectivity of ion types lies outside the scope of this report and will not be investigated in depth.
- High concentrations in the electrolyte improve the conduction of ions, thus reduces the ionic resistances. The energy losses in the CDI system due to resistive losses is reduced resulting in higher charge efficiencies. However, CDI does not work effectively for high salt concentrations because the CDI system is not able to remove all the salt from the stream. The Helmholtz capacity is dominant for high electrolyte concentrations, and does not depend on the concentration in the electrolyte [40]. If the concentration increases, there eventually will be a concentration where the EDL capacity is lower than the amount of salt in the stream. The applied potential could be increased to increase the capacity, however, as stated before, it could not be increased indefinitely.

G.3 Relation between physical properties and ED performance

G.3.1 Ion-exchange capacity

The number of fixed charges per unit of dry polymer weight is denoted with the ion-exchange capacity (IEC). Increasing the IEC results in increasing the permselectivity. According to the Donnan theory, more fixed charged functional groups per membrane mass increase the amount of mobile counter-ions in the membrane and enhances the co-ion exclusion, resulting in an increased counter-ion concentration within the structure of the membrane [68]. Enhancing IEC, by including more fixed charge groups inside the membrane, thus, improves the permselectivity of the IEM.

G.3.2 Tortuosity and swelling

The tortuosity is an indication of the pathlength of the ions to diffuse through the structure of the ion exchange membrane. The tortuosity depends on the hydration of the IEM, which is indicated by the volume fraction of water inside the structure of the IEM [68]. The equation for the tortuosity is given as $\tau = \frac{(2-f_w)^2}{f_w}$, where f_w is the volume fraction of water in the membrane. Swelling is the phenomena

that the dry membrane is filled with water from the electrolyte [68]. Ion transport only happens in the pores of the membrane where there is water available for the ions to move through. There is no ion transport in the hydrophobic structure. Increasing the volume fraction of water in the IEM, so more swelling, reduces the diffusional pathlength for the ions, which increases the ion mobility inside the membrane [68]. Thus, swelling improves the conductivity of the IEM. Unfortunately, swelling reduces the permselectivity of the IEM. Higher water volume inside the IEM increases the water volume fraction and thus decreases the concentration of fixed charged functional groups inside the IEM. The co-ion exclusion and the counter-ion concentration inside the membrane are reduced, according to Donnan's law. As a result, the permselectivity decreases.

G.3.3 Membrane thickness

The membrane thickness has a direct effect on the resistance for the ions to diffuse through the membrane: the thinner the IEM, the lower the electrical area resistance, how easier the diffusion through the membrane is [66]. The tortuosity is smaller for thinner IEMs and thus improves the mobility of the ions through the membrane [68]. The conductivity improves for thinner membranes while the permselectivity remains unchanged [68].

G.3.4 Initial salt concentration and Applied potential

The current efficiency and permselectivity depend on the applied voltage. The current efficiency and permselectivity decrease when the applied potential on the electrodes is increased, while the conductivity stays approximately constant [68]. A higher applied voltage results in higher counter- and co-ion fluxes, however, the driving force of the counter-ion flux decreases.

The conductivity in the IEM increases with increasing concentration in the electrolyte and eventually reaches a plateau [67]. At low concentrations, the resistance in the DBL is the dominant contributor to the conductivity, while at high concentrations, the membrane resistance is the dominant contributor [180]. Fontananova et al. (2017) explains this effect with the Debye length: EDL thickness, and thus the Debye length, increases when the concentration inside the electrolyte is lower, resulting in higher EDL resistance and lower double layer capacitance [100]. The contribution of the resistance of the EDL to the conductivity is reduced, so that the resistance of the DBL becomes dominant. At low concentrations, the resistance in the DBL is the dominant influence of the conductivity, resulting in diffusion limitations to be the factor causing the convergence of the conductivity [67]. A lower initial salt concentration in the feed stream, however, has a positive influence on the permselectivity and current efficiency. Decreasing the concentration, decreases the co-ion concentration in the bulk solution, resulting in a decrease of co-ions in the IEM (Equation 2.17). The selectivity of the IEM increases because the exclusion of co-ions is increased [68]. Thus, the permselectivity and current efficiency are higher for lower initial feed stream concentrations. However, the conductivity decreases when the initial concentration of the feedwater stream decreases, establishing the trade-off between permselectivity and conductivity.

G.4 Transport equations for membranes

The ionic transport through mesopores has been explained in detail in the paper of Xin et al. (2019) [42]. A short summary of their findings will be given below.

The ionic flux of every ion in a solution through a charged mesopore is given by the Nernst-Planck equation,

$$N_i = uc - D_i(\nabla c_i + \frac{z_i F c_i}{RT} \nabla \phi), \quad (G.1)$$

where N_i is the ionic flux of an ion ($\text{mol}/\text{m}^2\text{s}$), D_i is the diffusion coefficient of the ion (m^2/s), c_i is the ion concentration (mol/m^3), z_i is the charge number of the ion, and T is the temperature (K) [42]. The Nernst-Planck equation describes the movement of the ions through the mesopores due to respectively convection, diffusion and electromigration. The effect of convection can be neglected

because that effect is very small when the driving force is a potential gradient (as in CDI and ED) [73]. Also, the diffusion term is relatively smaller than the electromigration term because IEMs are dense membranes [73]. The change in electrochemical potential ($\nabla\bar{\mu}_i = \nabla(\mu_i + z_i F\varphi)$) is the driving force for the transport of ions. The Poisson equation,

$$\nabla^2\varphi = -\frac{F}{\epsilon} \sum z_i c_i, \quad (\text{G.2})$$

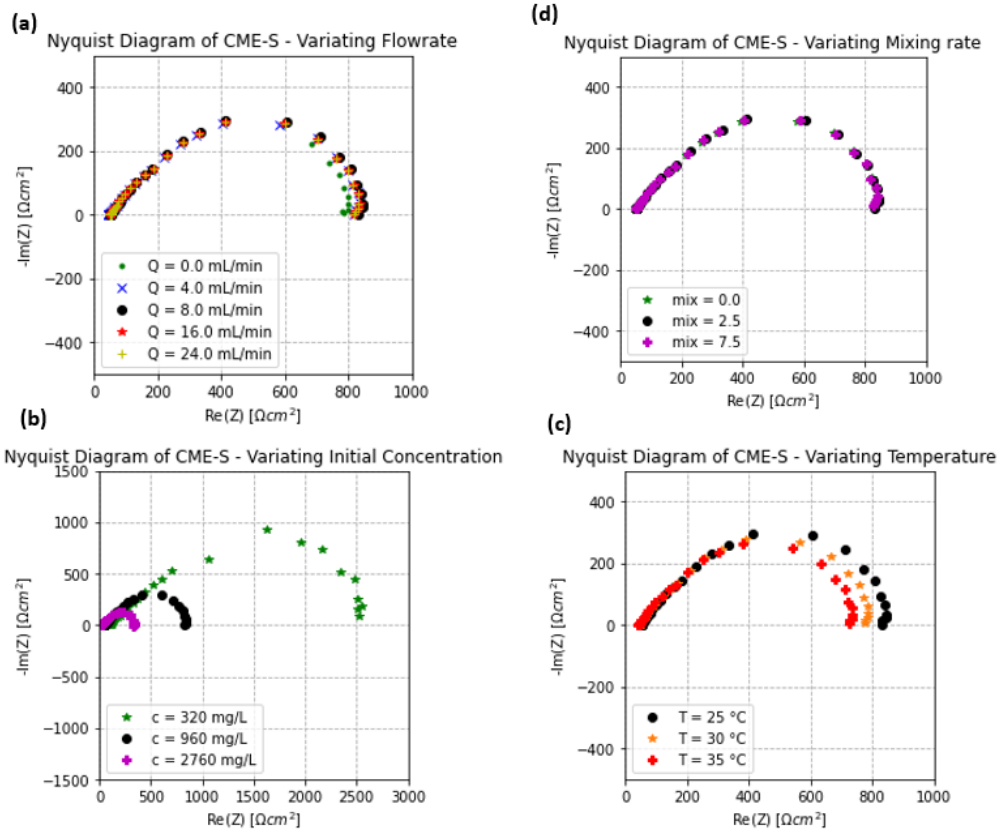
describes the electric potential distribution along the mesopore due to ion concentrations [42]. Herein, c_i is the ion concentration (mol/m^3), z_i is the charge number of the ion, and φ is the electrical potential (V) [42]. The continuity equation is used when a steady-state is assumed,

$$\nabla \cdot \mathbf{N} = 0, \quad (\text{G.3})$$

where \mathbf{N} is the ionic flux ($\text{mol}/\text{m}^2\text{s}$) [42]. The ionic flux of every ion in the solution could be calculated with these three equations and with the correct boundary conditions. The field of detailed calculation of the ion transport within the pores of the IEM is large and complex and is beyond the scope of this thesis.

Appendix H: Additional Results - Graphs and Tables

H.1 Quality of fit values of EECMs through EIS data of CME-S



Quality of fit values (χ^2 [10^{-3}])		EECM A: R//C-circuit	EECM B: TLM	EECM C: Inhomogeneous TLM	EECM D: TLM with holes	EECM E: Inhomogeneous TLM with holes
Varying the flowrate	0 mL/min	316	2.34	2.05	2.24	1.90
	4.0 mL/min	298	2.07	1.86	2.09	1.69
	8.0 mL/min	321	2.04	1.85	2.05	1.73
	16 mL/min	334	2.53	2.32	2.51	2.04
	24 mL/min	331	2.40	2.15	2.36	1.98
Varying the mixing rate	0	336	1.77	1.37	1.70	1.53
	2.5	321	2.04	1.85	2.05	1.73
	7.5	308	1.87	1.54	1.84	1.46
Varying the concentration	320 mg/L	2153	13.2	13.4	13.2	13.8
	960 mg/L	321	2.04	1.85	2.05	1.73
	2760 mg/L	239	3.53	3.08	3.53	3.94
Varying the temperature	25 °C	321	2.04	1.85	2.05	1.73
	30 °C	222	1.61	1.40	1.66	1.26
	35 °C	177	1.61	1.35	1.61	1.35

Figure 73: Nyquist plots of the EIS data of CME-S when the operational parameters are varied. Impedance equations of five EECMs (EECM A: R//C-circuit, EECM B: TLM, EECM C: Inhomogeneous TLM, EECM D: TLM with holes, EECM E: Inhomogeneous TLM with holes) have been fitted through the EIS data (not visible) and the quality of fit value was calculated. The χ^2 -values of the five EECMs have been displayed in the table below the Nyquist plots. The Nyquist plots are equal to the ones in Figure 41a to Figure 44a.

Looking at the Nyquist plots of Figure 73, the fits of the impedance equations of the TLM and the EECMs with TLM features show that those EECMs fit accurately through the EIS data of the Nyquist plot, Bode magnitude plot and Bode phase plot, at least more accurate than the R//C-circuit. What is also noticeable between the impedance equations is that there is almost no difference between the fit of the TLM and the TLM with hole (EECM B vs EECM D) and the fit of the inhomogeneous TLM with hole and without hole (EECM E vs EECM C). The quality of fit values in the tables below Figure 73 also shows this effect. The values of R and C are equal while the resistance in the macropores R_M is very large. This means, looking at the electric circuit, that the ions are more prone to move through the blocks of the TLM (z_A) and not through the resistor R_M because the value of that resistor is too high. This means that there were probably no holes large enough inside the CME which could act as macropores. So, the extra resistor in the EECM is obsolete and should be removed to improve the simplicity. What is made clear by the values of χ^2 for every EECM is that the fit of the more complex TLM of EECM C is never an order more accurate than the simpler TLM of EECM B. Therefore has been chosen to furtherly use the Transmission-Line Model of EECM B to fit the impedance data of the CMEs.

H.2 Impedance plots of charged CME-AC

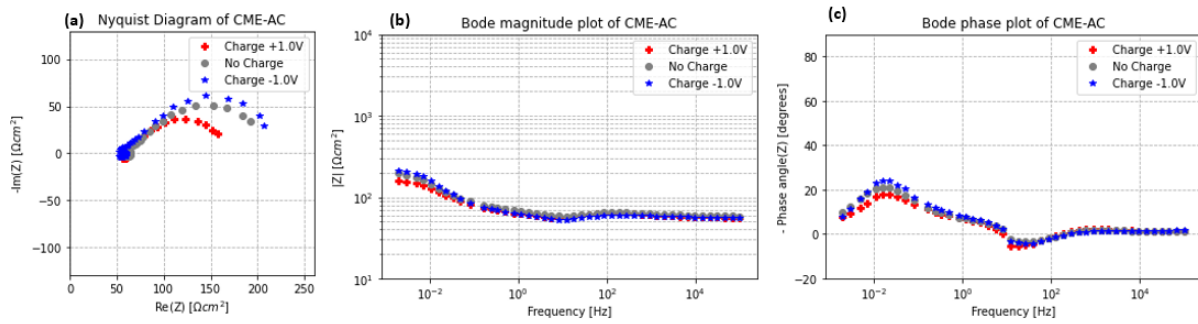


Figure 74: Electrochemical impedance spectroscopy performed on the CME with activated carbon instead of graphite as active material (AC:CB:PVDF=45:8:47wt%). The CMEs were made selective for anions by placing a potential between the CMEs and the end electrodes of +1.0V for 30 minutes. The CMEs were made selective for cations by charging them with the electrons of the end electrodes by placing a potential between them of -1.0V for 30 minutes. The EIS data is visualised as the (a) Nyquist diagram of the CME-AC, the (c) Magnitude Bode Plot of CME-AC, and the (d) Phase Bode Plot of CME-AC. The uncharged CME-AC has been included in the figure for comparison with the charged ones.

Table 13: Values retrieved by fitting the impedance equation of the Transmission-Line Model in the EIS data of the CME with activated carbon as active material at different potentials. χ^2 is the quality of fit, R is the membrane resistance in Ωcm^2 , C is the membrane capacitance in F/cm^2 , τ_t is the transport time constant in s, and P is the calculated permselectivity when the CME is positively charged by placing a potential of +1.0V or negatively charged by placing a potential of -1.0V between the CMEs and the end electrodes.

CME-AC	R [Ωcm^2]	C [F/cm^2]	χ^2 [10^{-3}]	τ_t [s]	P [-]
+1.0V	97.2	0.950	50.4	139	-0.27
0.0V	133	1.10	37.6	146	-
-1.0V	158	0.881	37.0	92	+0.19

H.3 Impedance plots of charged CME-PVDF

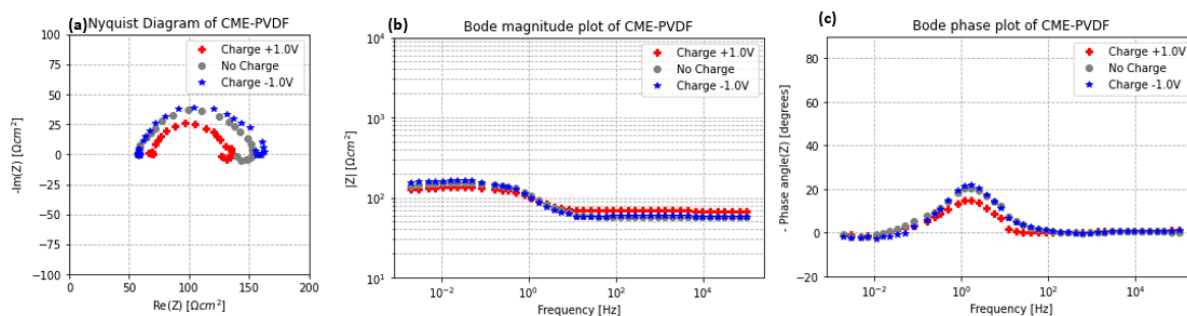


Figure 75: Electrochemical impedance spectroscopy performed on CMEs with a lower mass percentage of the binder PVDF than CME-S. The slurry mass composition of CME-PVDF is G:CB:PVDF=60:10:30wt%. The CMEs were made selective for anions by placing a potential between the CMEs and the end electrodes of +1.0V for 30 minutes. The CMEs were made selective for cations by charging them with the electrons of the end electrodes by placing a potential between them of -1.0V for 30 minutes. The EIS data is visualised as the (a) Nyquist diagram of the CME-PVDF, the (b) Magnitude Bode Plot of CME-PVDF, and the (c) Phase Bode Plot of CME-PVDF. The EIS data of the uncharged CME-PVDF has been included in the figure for comparison with the charged ones.

Table 14: Values retrieved by fitting the impedance equation of the Transmission-Line Model in the EIS data of the CME with half the amount of polymeric binder PVDF in the slurry as CME-S at different potentials. χ^2 is the quality of fit, R is the membrane resistance in Ωcm^2 , C is the membrane capacitance in F/cm^2 , τ_t is the transport time constant in s, and P is the calculated permselectivity when the CME is positively charged by placing a potential of +1.0V or negatively charged by placing a potential of -1.0V between the CMEs and the end electrodes.

CME-PVDF	R [Ωcm^2]	C [F/cm^2]	χ^2 [10^{-3}]	τ_t [s]	P [-]
+1.0V	65.9	0.033	51.5	2.2	-0.28
0.0V	91.6	0.024	47.2	2.2	-
-1.0V	104	0.030	16.5	3.1	+0.14

H.4 Impedance plots of charged CME-CB

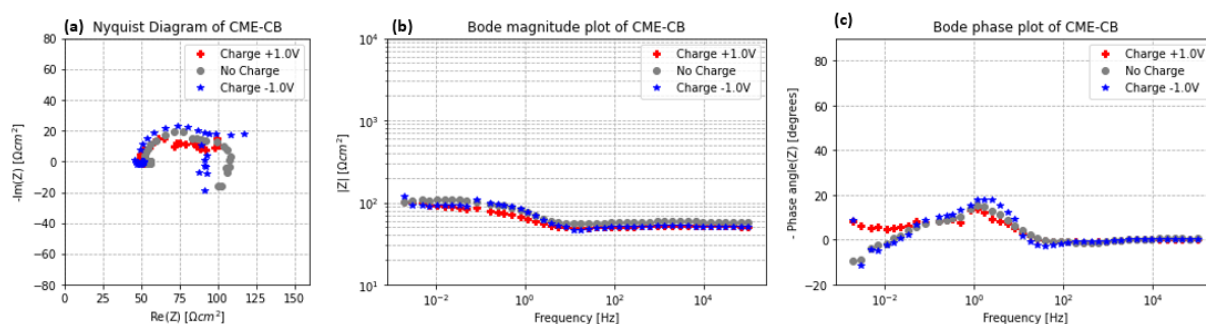


Figure 76: Electrochemical impedance spectroscopy performed on CMEs with a higher mass percentage of carbon black (CB) than CME-S. The slurry mass composition of the CME-CB has twice as much carbon black in the slurry as CME-S (G:CB:PVPDF=43:14:43wt%). The CMEs were made selective for anions by placing a potential between the CMEs and the end electrodes of +1.0V for 30 minutes. The CMEs were made selective for cations by charging them with the electrons of the end electrodes by placing a potential between them of -1.0V for 30 minutes. The EIS data is visualised as the (a) Nyquist diagram of the CME-CB, the (b) Magnitude Bode Plot of CME-CB, and the (c) Phase Bode Plot of CME-CB.

Table 15: Values retrieved by fitting the impedance equation of the Transmission-Line Model in the EIS data of the CME with twice as much carbon black in the slurry as CME S at different potentials. χ^2 is the quality of fit, R is the membrane resistance in Ωcm^2 , C is the membrane capacitance in F/cm^2 , τ_t is the transport time constant in s, and P is the calculated permselectivity when the CME is positively charged by placing a potential of +1.0V or negatively charged by placing a potential of -1.0V between the CMEs and the end electrodes.

CME-CB	R [Ωcm^2]	C [F/cm^2]	χ^2 [10^{-3}]	τ_t [s]	P [-]
+1.0V	41.9	0.143	97.8	6.0	-0.12
0.0V	47.7	0.103	141	4.9	-
-1.0V	45.9	0.043	452	2.0	-0.04

H.5 Impedance plots of charged CME-G

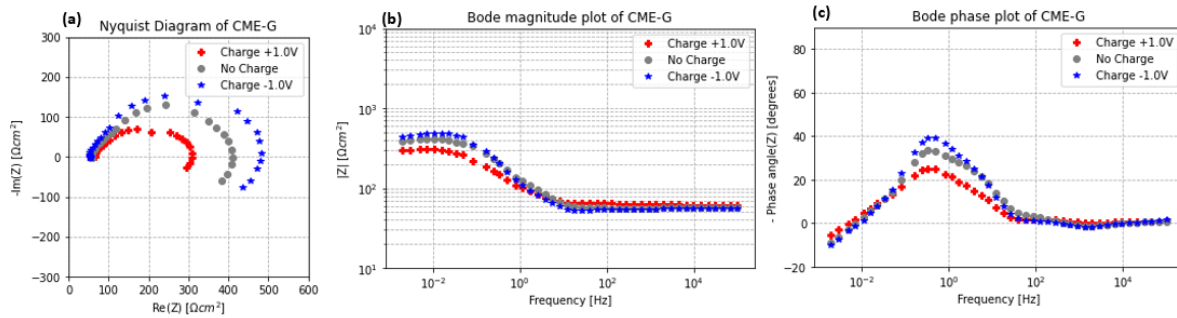


Figure 77: Electrochemical impedance spectroscopy performed on CMEs with a lower mass percentage of graphite than CME-S. The slurry mass composition of CME-G has twice less graphite in the slurry than CME-S (G:CB:PVDF=29:11:60wt%). The CMEs were made selective for anions by placing a potential between the CMEs and the end electrodes of +1.0V for 30 minutes. The CMEs were made selective for cations by charging them with the electrons of the end electrodes by placing a potential between them of -1.0V for 30 minutes. The EIS data is visualised as the (a) Nyquist diagram of CME-G, the (b) Magnitude Bode Plot of CME-G, and the (c) Phase Bode Plot of CME-G. The EIS data of the uncharged CME-G has been included in the figure for comparison with the charged ones.

Table 16: Values retrieved by fitting the impedance equation of the Transmission-Line Model in the EIS data of the CME with half the amount of graphite in the slurry as CME-S at different potentials. χ^2 is the quality of fit, R is the membrane resistance in Ωcm^2 , C is the membrane capacitance in F/cm^2 , τ_t is the transport time constant in s, and P is the calculated permselectivity when the CME is positively charged by placing a potential of +1.0V or negatively charged by placing a potential of -1.0V between the CMEs and the end electrodes.

CME-G	R [Ωcm^2]	C [F/cm^2]	χ^2 [10^{-3}]	τ_t [s]	P [-]
+1.0V	242	0.064	13.9	16	-0.29
0.0V	341	0.034	55.9	12	-
-1.0V	417	0.037	63.0	16	+0.22